Università degli Studi di Torino

Doctoral School

PhD in Physics

Development of a SiPM-based camera for the Large Size Telescope of CTA and study of its performance

Davide Depaoli

Tutor:
Prof. Andrea Chiavassa
Co-Tutor:
Dr. Federico di Pierro

Examination Committee:
Prof. Marco Costa
Prof. Mosè Mariotti
Dr. Richard White

17 February 2022

Contents

Introduction

Very high energy (VHE) cosmic gamma rays provide clues to understanding the origin of cosmic rays, the mechanisms of particle acceleration in extreme environments and the nature of cold dark matter. Imaging atmospheric Cherenkov telescopes (IACTs) are nowadays the standard detectors for VHE gamma-ray astronomy. Multiple telescopes take Cherenkov-light stereoscopic images of extensive air showers (EAS) induced by gamma rays entering the atmosphere. The Cherenkov Telescope Array (CTA) is the next generation VHE gamma-ray observatory, with one site in each hemisphere and up to 100 telescopes of three different types. The Large-Sized Telescopes (LSTs) have a 23 m mirror dish and target the low-energy range (20 GeV - 3 TeV). Their baseline camera has 1855 photomultiplier tubes (PMTs) as photon detectors, divided into 265 modules of 7 PMTs each.

While the PMT technology is mature and reliable, Silicon Photomultipliers (SiPMs) are recently emerging as promising competitors also in IACT applications. Indeed, they have many advantages, such as lower operating voltage and tolerance to high illumination levels (e.g. moonlight); on the other hand they have some disadvantages, like higher dark count rate and optical crosstalk.

This work is inserted in a project to study the possibility of installing a SiPM-based camera in the LST, instead of the PMT-based one. The goal of this work was the construction of a SiPM-based module that has the same electrical and mechanical characteristics of the PMT module, using the LST electronics for readout.

Compared to small-sized telescopes, in large-sized telescopes the background light due to the night sky background is considerably higher: this aspect must be carefully considered during the design. This work is therefore a useful test bench both to study possible front-end solutions and to develop a slow control circuit which can be used in a SiPM-based camera for LST, or more in general in any other SiPM application characterized by a high background noise and/or requiring the use of a medium-large pixel.

The work started from studying the problem, finding possible solutions, up to the realization of a working detector, covering all the steps of its realization. After choosing the SiPMs, possible front-ends were studied, both based on discrete component circuits and on Application Specific Integrated Circuits (ASICs). The decision was to rely on the Multiple Use SiPM Integrated Circuit (MUSIC) ASIC, a 500 MHz SiPM front-end and summation circuit developed by the Institute of Cosmos Sciencies - University of Barcelona (ICCUB) group in Barcelona. To solve the high background problem, a technique to limit the SiPM current was developed, using an active transistor-based current limiter instead of the standard protection resistor approach; in addition, an AC filter was added to remove the DC background. A digital thermometer detects the temperature on the sensor and a voltage regulator controlled by a slow control software keeps the SiPM overvoltage constant during the operations. After having reached the final version of the circuit, a six-layer printed circuit board (PCB) was designed; the board hosts both the slow control circuit, the MUSIC chip and a microcontroller, necessary to configure the ASIC at each start up. The result of these developments is an end-to-end working module, equipped with 7 SiPM-based photon detectors equivalent to the PMTs, and using the standard LST electronics.

In order to evaluate the potential performance improvement with respect to standard PMT cameras, a detailed simulation work has been performed in parallel with the hardware studies. This work is also fundamental to optimize the various parameters which characterize a complete SiPM camera, such as the pixel dimensions and the signal duration.

This thesis is divided as follows:

- *Chapter 1: High Energy Gamma-Ray Astronomy*
  In this chapter we introduce the basic concepts of the High Energy Gamma-Ray Astronomy. We start with a brief excursus on how high energy photons are radiated from astrophysical sources: these objects behave as huge and energetic accelerators, and they can emit gamma rays via different mechanisms. Then we describe how gamma rays propagate to the Earth, and how they interact with matter. An excursus on the various gamma-ray detection techniques follows, both from space and from ground. The Imaging Atmospheric Cherenkov Telescope (IACT) technique, the one used by CTA, is discussed more in detail at the end of the chapter.

- *Chapter 2: Cherenkov Telescope Array*
  In this chapter we introduce the CTA project. After analyzing the science themes it will study, we illustrate the characteristics of the various types of telescopes that will populate the observatory.

- *Chapter 3: Silicon Photomultipliers*
  This chapter is a short introduction to SiPMs. We start recalling the basic concepts of the PN junction, then we briefly describe the principles and operation of photodiodes, analyzing the various operating regimes. So we describe the SiPMs and their various characteristics, such as photon detection efficiency, dark count rate, cross talk and so on. Thanks to an accurate equivalent circuit, we study how the SiPM output signal varies according to some device characteristics (e.g., cell size, number of cells) and to the load to which it is connected. Such work is fundamental for the development of a front-end circuit for such devices. Then we discuss our use case for SiPMs, i.e. IACT applications. We analyze the night sky background and how SiPMs are more sensitive to this noise than PMTs. The chapter ends with some examples of already existing Cherenkov telescopes using SiPMs as photodetectors.

- *Chapter 4: Development of a SiPM Pixel Prototype*
  This chapter deals with the main work of this thesis, which is the development of the SiPM module for LST. Since the project starts from the photomultiplier tube readout system designed for LST, the first part of the chapter is a brief discussion of its main characteristics. Then we introduce the MUSIC ASIC, used as front-end. After that we describe in detail the SiPM pixel: at the beginning we talk about the general idea, then we go into the details of each of its part, with particular attention to the development of the current limiter and the AC filter, solutions that made it possible to solve the aforementioned high background problem. After a short discussion on how the PCBs were developed, the results of the main measurements made on the used SiPMs are shown, in particular their breakdown voltages and how they vary as the temperature changes. These values are needed for the module slow control. Then we describe the Camera Control Software for the SiPM Pixel (CaCoSiPM), which is the software that takes care of the module slow control. The measurements made on the SiPM pixel are therefore illustrated, starting from current limiter tests, studies of the signals in different light backgrounds condition, up to the calibration of the pixel output signals in terms of photoelectrons. Then some comparisons with the PMT

pixel are reported. The chapter ends by illustrating some alternative solutions that have not been used, including the use of a front-end based on a discrete components circuit.

- *Chapter 5: Analysis of SiPM-Based Camera LSTs Simulations*
  This chapter describes the analysis of Monte Carlo simulations of a SiPM-based camera LSTs array. The main goal is to evaluate the potential performance improvement with respect to standard PMT cameras. Two different analysis pipelines for stereoscopic reconstruction are used for this purpose: *magic-cta-pipe* and *protopipe*. We are developing the first one to analyze MAGIC and LST observations: the two facilities are indeed built very close together, and joint observations between the two MAGIC telescopes and LST-1 (the first and currently only LST) are already performed. The second one is instead the pipeline prototype for CTA.

- *Chapter 6: Conclusions ad Future Prospects*
  Thesis concluding chapter.

Chapter 1

High Energy Gamma-Ray Astronomy

The human being, due to his curious nature, has always been attracted to what surrounds him, often giving imaginative explanations to phenomena he was not able to understand. Nowadays, thanks to the huge progress we made both in science and in technology, we can at least try to find more reasonable explanations.

The nature, the composition and the origin of the Universe is by far one of the most intriguing questions, and nowadays is only partially answered. From prehistoric times until the last century, the only available detector was the human eye, maybe helped by some instrumentation (e.g. the Galilei telescope). This means that we could probe the Universe only using a very small fraction of the electromagnetic spectrum, the visible light. Today, both thanks to scientific and technological progress, we have many more probes available; these probes, often called *messengers*, range from non-visible photons to charged particles, from neutrinos to the recently detected gravitational waves. A new and promising discipline was born, the *multi-messenger astrophysics*, which quickly became not only one of the most important chapters of high energy physics, but one of the most promising branches of physics in general.

1.1 Gamma Rays

In this scenario we will focus on gamma rays; with this identifier we refer to photons which are so energetic that they cannot be thermally generated: they are instead radiated via various electrodynamical processes which occur in the most violent particle accelerators which can be found in our Universe. These particles have a very useful peculiarity: since, like neutrinos, they do not have an electromagnetic charge, they are not deflected by galactic and extragalactic magnetic fields; thanks to this feature they point back to their sources, allowing us a very detailed study of extreme physical environments which cannot be reproduced in our laboratories. In addition gamma rays are excellent probes to study a wide range of fundamental physics problems, like studies of possible Lorentz Invariance Violation, indirect search for Dark Matter and the existence of axion-like particles.

Gamma rays are commonly classified according to their energy in the following way:

- High Energy (HE): $0.5\,\mathrm{MeV} \lesssim E \lesssim 100\,\mathrm{GeV}$
- Very High Energy (VHE): $100\,\mathrm{GeV} \lesssim E \lesssim 100\,\mathrm{TeV}$
- Ultra High Energy (UHE): $100\,\mathrm{TeV} \lesssim E \lesssim 100\,\mathrm{PeV}$
- Extreme High Energy (EHE): $E \gtrsim 100\,\mathrm{PeV}$

Depending on the gamma-ray energy, different experimental techniques are used; while High Energy gamma rays are detected before they interact with our atmosphere, thanks to properly equipped satellites, the higher energy gamma-ray detectors are built on ground. Indeed, as the gamma-ray energy increases, their flux decreases, so we need a large area detector to efficiently collect them; in addition, in order to contain as much as possible the energy of the incident photon, we need a big and heavy detector. Both requirements collide with the constraints of a satellite detector, which has to be small and light.

1.1.1 Production of High-Energy Photons

In this section we will briefly discuss how high-energy photons are radiated from astrophysical sources. These objects behave as huge and energetic accelerators, and thus they can emit gamma rays from various channels. Depending on the particles interested in the mechanism, we can divide the processes in two categories, the *leptonic* processes and the *hadronic* ones [1].

Regarding leptonic processes, we will focus on *synchrotron radiation* and the *inverse Compton scattering*, which together give rise to the *synchrotron self-Compton*, one of the fundamental processes for the production of high-energy gamma rays; then we will describe the two most important hadronic processes, i.e. the *inelastic pp collision* and *photo-hadronic* $p\gamma$ *interactions*. Finally, we will mention a couple of processes that are not described by the Standard Model, which, if observed, can be the evidence of new physics.

Synchrotron Radiation

Many quantum electrodynamical processes are responsible for the radiation of high-energy photons from the acceleration of energetic electrons; however, synchrotron radiation and inverse Compton radiation are the most important in astrophysical sources [1]. We will start briefly discussing the first one.

Synchrotron radiation is the electromagnetic radiation emitted by charged particles radially accelerated, for example the radiation emitted by a charged particle spiraling around a magnetic field line. If we consider a charged particle q in a uniform magnetic field B along a spiral path at a constant pitch angle α, the total radiation loss rate is [2]:

$$-\left(\frac{dE}{dt}\right) = \frac{q^4 B^2}{6\pi\epsilon_0 c m^2}\frac{v^2}{c^2}\gamma^2 \sin^2\alpha \tag{1.1}$$

where m is the particle mass and v is its velocity. In an astrophysical object both electrons and protons emit synchrotron radiation; however, due to the strong dependence on the particle mass ($\propto 1/m^2$), it is clear that electrons are much more subjected to this kind of energy loss.

Considering the specific case of a relativistic electron, Equation 1.1 becomes:

$$-\left(\frac{dE_e}{dt}\right) = \frac{e^4 B^2}{6\pi\epsilon_0 c m_e^2}\frac{v^2}{c^2}\gamma^2 \sin^2\alpha$$

Since $c^2 = 1/(\epsilon_0\mu_0)$:

$$-\left(\frac{dE_e}{dt}\right) = \frac{1}{c^2\epsilon_0\mu_0}\frac{e^4 B^2}{6\pi\epsilon_0 c m_e^2}\frac{v^2}{c^2}\gamma^2 \sin^2\alpha$$

If we define the magnetic energy density as $U_{mag} = B^2/2\mu_0$:

$$\begin{aligned}-\left(\frac{dE_e}{dt}\right) &= 2\frac{e^4}{6\pi c^3\epsilon_0^2 m_e^2}U_{mag}\frac{v^2}{c^2}\gamma^2 \sin^2\alpha \\ &= 2\left(\frac{e^4}{6\pi c^4\epsilon_0^2 m_e^2}\right) c\, U_{mag}\frac{v^2}{c^2}\gamma^2 \sin^2\alpha\end{aligned}$$

Defining the *Thomson cross section* as:

$$\sigma_T = \frac{e^4}{6\pi\epsilon_0 c^4 m_e^2} \tag{1.2}$$

we obtain:

$$-\left(\frac{dE_e}{dt}\right) = 2\sigma_T \left(\frac{v}{c}\right)^2 c\,U_{mag}\gamma^2 \sin^2\alpha \tag{1.3}$$

In the ultra relativistic limit (i.e. $v \to c$):

$$-\left(\frac{dE_e}{dt}\right) = 2\sigma_T c\,U_{mag}\gamma^2 \sin^2\alpha \tag{1.4}$$

Since any electron is scattered at a random pitch angle α and the α distribution for a cloud of high energy electrons is isotropic [2], we can find the average energy loss rate by averaging Equation 1.3 on a isotropic α distribution $p(\alpha)d\alpha = 1/2\,\sin\alpha\,d\alpha$:

$$-\left(\frac{dE_e}{dt}\right) = 2\sigma_T c\,U_{mag}\gamma^2 \left(\frac{v}{c}\right)^2 \frac{1}{2}\int_0^\pi \sin^3\alpha\,d\alpha = \frac{4}{3}\sigma_T c\,U_{mag}\left(\frac{v}{c}\right)^2\gamma^2 \tag{1.5}$$

The single particle spectrum has a complicated solution, described by Beissel functions, and we will not discuss it in detail. However the spectrum exhibits an exponential decay above the *cutoff frequency* ν_c:

$$\nu_c = \frac{3}{2}\gamma^2\frac{eB}{2\pi m_e}\sin_\alpha \tag{1.6}$$

and, by folding the spectrum with an electron distribution described by a power law ($N(E) \propto E^{-p}$), we obtain that the synchrotron spectrum has the following behaviour:

$$J(\nu) \propto \nu^{-\frac{p-1}{2}} \tag{1.7}$$

This radiation is responsible for the lowest part of the high energy gamma-ray spectrum, since at higher energies the radiation loss becomes predominant. This is no longer true if the source moves towards the observer at a large Lorentz factor: for example in gamma-ray bursts, the synchrotron radiation emitted by the electrons accelerated in the external ultra-relativistics shocks causes the afterglow emission [3].

Inverse Compton Scattering

In inverse Compton scattering ultra-relativistic electrons scatter low energy photons [1, 2]:

$$e^- + \gamma_b \to e^- + \gamma \tag{1.8}$$

where γ_b is a background (or seed) photon and γ is the upscattered one. In this interaction the energy is transferred from the electron to the photon, contrary to what happens in the usual Compton scattering (this is why we refer to it as inverse). Depending on the photon energy, we usually define two different regimes, the *Thomson* one and the *Klein–Nishina* one.

In the *Thomson regime* the photon energy in the electron rest frame is lower than its rest mass energy:

$$\gamma_e\epsilon_{\gamma_b}(1-\beta_e cos\theta) < m_e c^2 \tag{1.9}$$

where γ_e is the electron Lorentz factor, ϵ_{γ_b} the energy of the seed photon and θ the scattering angle. In this regime the mean energy of the upscattered photon is:

$$\epsilon_\gamma \simeq 2\gamma_e^2\epsilon_{\gamma_b} \tag{1.10}$$

and the electron radiation loss rate is:

$$-\left(\frac{dE_e}{dt}\right) = \frac{4}{3}\sigma_T U_{rad} \beta_e^2 \gamma_e^2 c \tag{1.11}$$

where U_{rad} is radiation energy density and σ_T is the Thomson cross section, as defined in Equation 1.2. Since the expression is very similar to the synchrotron radiation loss rate (Equation 1.5), often the inverse Compton radiation is treated as the synchrotron one, considering an equivalent magnetic field. Indeed, the energy loss rate depends on the field that accelerates the electrons: for the synchrotron radiation this field is the $v \times B$ one, caused by motion of the electrons in the magnetic field, while for the Compton scattering this field is the sum of the electromagnetic fields incident upon the electron. Similarly, we can consider the synchrotron radiation as the scattering on "virtual photons" observed by the electron as it gyrates around the magnetic field. In the Thomson limit the spectrum is described by a power-law distribution who has the same slope as the synchrotron spectrum:

$$J(\nu) \propto \nu^{-\frac{p-1}{2}} \tag{1.12}$$

and peaks at the mean upscattered photon energy (Equation 1.10).

In the *Klein–Nishina* regime the photon energy in the electron rest frame is higher than its rest mass energy:

$$\epsilon_{\gamma_b} \gtrsim m_e c^2/\gamma_e \tag{1.13}$$

The total cross section is given by the Klein–Nishina formula [2]:

$$\sigma_{KN} = \pi r_e^2 \frac{1}{x} \left\{ \left[1 - \frac{2(x+1)}{x^2}\right] \ln(2x+1) + \frac{1}{2} + \frac{4}{x} - \frac{1}{2(2x+1)^2} \right\} \tag{1.14}$$

where r_e is the classical electron radius:

$$r_e = \frac{e^2}{4\pi\epsilon_0 m_e c^2} \tag{1.15}$$

and x is defined as:

$$x = \frac{\hbar\omega}{m_e c^2} \tag{1.16}$$

In the ultra-relativistic limit, i.e. $\gamma \gg 1$, Equation 1.14 becomes:

$$\sigma_{KN} \simeq \pi r_e^2 \frac{1}{x} \left[\ln(2x) + \frac{1}{2}\right] \tag{1.17}$$

Therefore at the highest energies the cross-section roughly decreases as x^{-1}.

Synchrotron Self-Compton

Often the previously described processes are strictly related in astrophysical sources: indeed, in these violent environments the background photons necessary to the inverse Compton radiation are emitted by the same electrons due to synchrotron radiation. This mechanism is called *synchrotron self-Compton* process, and it is a pillar of the standard model of high-energy radiation from relativistic jets in active galactic nuclei and in gamma-ray bursts [1].

In the Thomson limit and in the case of a single Compton scattering, the ratio of the inverse Compton power P_{IC} to synchrotron power P_{syn} is:

$$\frac{P_{IC}}{P_{syn}} \simeq \frac{U_{rad}}{U_{mag}} \tag{1.18}$$

and roughly corresponds to the Compton parameter:

$$Y = \sigma_T n_e r \langle \gamma_e^2 \rangle \tag{1.19}$$

where n_e is the electron density and r the radius of the emitting region. This parameter represents the mean energy gain of photons weighted by the interaction probability.

Another useful relation is the one between the peak of the inverse Compton spectrum $\nu_{IC,peak}$ and the synchrotron one $\nu_{syn,peak}$:

$$\nu_{IC,peak} \simeq 2\langle \gamma_e^2 \rangle \nu_{syn,peak} \tag{1.20}$$

Inelastic pp Collisions

The most important hadronic processes leading to the production of high-energy photons in astrophysical objects are *inelastic pp collisions* and *photo-hadronic pγ interactions*. Protons can emit synchrotron radiation; however, compared to electrons, the emitted power is lower by a factor $(m_p/m_e)^4$, and therefore it becomes efficient only at high energies and in strong magnetic fields [1].

We will start by discussing *inelastic pp collisions*; these processes also describe the interaction between nuclei, since at high energy the process can be described as the interaction of single nucleons inside the nucleus. The common reaction is similar to:

$$p + p \rightarrow p + p + \pi + ... \tag{1.21}$$

By pp interaction we have thus the production of pions, which can decay into photons and neutrinos. The most common decay channels for pions (both charged and neutrals) are the following:

$$\begin{aligned}
&\pi^0 \rightarrow 2\gamma \\
&\pi^+ \rightarrow \mu^+ + \nu_\mu \\
&\qquad \mu^+ \rightarrow e^+ + \nu_e + \bar{\nu}_\mu \\
&\pi^- \rightarrow \mu^- + \bar{\nu}_\mu \\
&\qquad \mu^- \rightarrow e^- + \bar{\nu}_e + \nu_\mu
\end{aligned} \tag{1.22}$$

Photon production via pp collision explains for example the high-energy emission from the disk of the Milky way, where cosmic ray protons collide with the interstellar gas [4], or the non thermal photon emission in young supernova remnants, where the accelerated cosmic ray protons interact with the surrounding molecular gas [5]. It is clear that the higher the density, the higher will be the collision probability and therefore the gamma-ray emission: this is why Molecular clouds are common region where these processes occur, since they have an higher gas density, compared to the average interstellar medium [1].

Photo-hadronic pγ Interaction

The second important hadronic process which describes the emission of non-thermal photons is the *photo-hadronic pγ interaction*. The Greisen–Zatsepin–Kuzmin (GZK) cut-off is a famous example of this process: high energy cosmic ray protons ($E_p \gtrsim 6 \times 10^{19}\,\mathrm{eV}$) interacting with the cosmic microwave background give origin to lower energy protons and neutral pions:

$$p + \gamma \rightarrow p + \pi^0 \tag{1.23}$$

The neutral pion will decay in two gamma rays, as seen in Equation 1.22: this leads to a rapid degradation of the proton energy. The reaction 1.23 is kinematically allowed if:

$$\epsilon_\gamma E_p \geq \frac{m_\pi (m_\pi + 2m_p) c^4}{2(1 - \cos\theta)} \tag{1.24}$$

where θ is the angle between the incoming photon and protons in the laboratory frame [1]. Integrating over the Cosmic Microwave Background photon distribution it is possible to obtain the GZK threshold; this cut-off was detected both by the HiRes experiment [6] and by the Pierre Auger Observatory [7].

The photo-hadronic interaction is an important signature of proton acceleration to very high energies. It is expected in compact sources with intense radiation fields, such as high-energy blazars; in these objects the radiation field is commonly produced by synchrotron emission of accelerated electrons [1].

Since, as we have seen, the same decays described in Equation 1.22 occurs both in the inelastic pp collisions and the pγ interactions, we have a strong connection between high-energy gamma rays with cosmic rays and neutrino astrophysics, allowing us a multi-messenger approach.

Other Processes

All the processes described so far rely on the Standard Model; other theories (e.g. Supersymmetry) include particles which can decay in photons: for this reason gamma rays can be excellent probes for Beyond Standard Model theories. For example, great efforts are made to search for WIMP dark matter particles and for axion-like particles that might play a role in gamma-ray propagation [8].

1.1.2 Gamma-Ray Propagation

After having briefly discussed the possible gamma-ray production mechanisms, in order to fully understand the experimental observations it is necessary to study their propagation from their sources to the Earth.

Canonical Propagation

Since photons are neutral in charge, their trajectories are not affected by galactic and extragalactic magnetic fields. However during their travel from their source to the Earth, high energy gamma rays can interact with diffuse and low energy photons of the intergalactic medium, referred as *background photons* γ_{BKG}, producing e^+e^- pairs:

$$\gamma + \gamma_{BKG} \rightarrow e^+ + e^- \tag{1.25}$$

Later we will call E_γ the gamma-ray energy and ϵ the background photon energy. The background photons involved in this interaction are mainly those which contribute to the *Cosmic Microwave Background* (CMB), the relic radiation from the early stage of the Universe, and those which constitute the *Extragalactic Background Light* (EBL), the light from all the resolved and unresolved extragalactic sources, integrated over the whole time of the Universe.

If we call θ the angle between the two photons, the energy threshold for the pair creation is [9]:

$$\epsilon_{th}(E_\gamma, \mu) = \frac{2(m_e c^2)^2}{E_\gamma(1-\mu)} \tag{1.26}$$

where $\mu \equiv cos(\theta)$. The cross section is:

$$\sigma_{\gamma\gamma}(E_\gamma, \epsilon, \mu) = \frac{3\sigma_T}{16}(1-\beta^2)\left[2\beta(\beta^2-2) + (3-\beta^4)\ln\left(\frac{1+\beta}{1-\beta}\right)\right] \tag{1.27}$$

where:

$$\beta \equiv \sqrt{\left(1 - \frac{\epsilon_{th}}{\epsilon}\right)} \tag{1.28}$$

The cross section is maximized for $\beta = 0.70$, giving us the following relation at the peak:

$$E_\gamma(\mathrm{TeV}) \simeq \frac{1.07}{\epsilon(\mathrm{eV})(1-\mu)} \simeq \frac{0.86\,\lambda(\mathrm{\mu m})}{1-\mu} \tag{1.29}$$

From this relation we clearly see that the higher the gamma-ray energy E_γ, the lower the background photon energy ϵ_{th} which maximizes the cross section. For VHE gamma rays (100 GeV to 100 TeV) it peaks for EBL background photons, while for higher energies the CMB is the predominant background. While the CMB is already well known, the EBL is still poorly understood; VHE gamma rays are therefore excellent probes to study this important but largely unknown radiation [10].

If the differential number density of background photons $dn_\gamma(\epsilon)/d\epsilon$ is isotropic, the mean free path is [10]:

$$\lambda_{\gamma\gamma} = \left(\int \frac{dn_\gamma(\epsilon)}{d\epsilon} d\epsilon \int \sigma_{\gamma\gamma}(\mu, \epsilon, E)\frac{1-\mu}{2} d\mu\right)^{-1} \tag{1.30}$$

The gamma-ray mean free path decreases as the gamma-ray energy increases: for a 1 TeV gamma ray $\lambda\gamma\gamma \sim 1$ Gpc, while for a 10 TeV one $\lambda\gamma\gamma \sim 100$ Mpc. Below 100 GeV this value is negligible even at cosmological distance, therefore the Universe is almost transparent in this energy range [10].

Modification of the Canonical Propagation

What has been described so far only takes into account Standard Model physics: exotic phenomena, such as *Lorentz Invariance Violation* or the mixing between photons and *axion-like particles*, can modify the gamma-ray propagation.

Lorentz Invariance is a key concept of Special Relativity, is valid in Quantum Mechanics and has been verified at the electro-weak scale. With gamma rays we can study its applicability up to the highest observable energies. On the other hand, Quantum Gravity models predict its violation. Currently the test of Lorentz Invariance by studying gamma-ray propagation is largely performed in the high energy astrophysics community [11, 12].

To solve the strong CP problem, in 1977 Peccei and Quinn introduced the *axion* field [13]. The axion a is a spin-zero boson, and through the Primakoff effect it can couple to photons (vector bosons):

$$\gamma + \gamma^* \to a \tag{1.31}$$

where γ^* can be a virtual photon. More generally, different models predict different spin-zero bosons which have similar couplings to photons; we usually refer to them as axion-like particles (ALPs). During their travel, gamma rays cross intergalactic magnetic fields, and they can interact with their virtual photons γ^* to produce ALPs; since the Universe is transparent to the latter particles, they can travel basically undisturbed. But if they cross another strong magnetic field, they can give again origin to a gamma ray, which will undergo the EBL absorption [14]. This photon-ALP oscillation can therefore affect the measured gamma-ray spectrum of astrophysical sources, and the search for ALPs using high energy gamma rays as probes is currently ongoing [12].

1.1.3 Gamma-Ray Interaction with Matter

Before discussing the various techniques used to detect gamma rays, we will briefly describe how they interact with matter; as we will see, depending on their energy, different processes are predominant: only an in-depth knowledge of the physics involved can lead us to the best detector design for our aim.

The light attenuation in a material follows an exponential trend and is described by the *Lambert-Beer Law*:

$$I = I_0 e^{-\mu z} \tag{1.32}$$

where μ is the *linear attenuation coefficient*. Since many mechanisms describe the interaction of photons with matter, μ will be the sum of the various coefficients of each process:

$$\mu = \sum_{i=0}^{N} \mu_i \tag{1.33}$$

If ρ_m is the material mass density, we can define the *mass attenuation coefficient* α_m as:

$$\alpha_m = \frac{\mu}{\rho_m} \tag{1.34}$$

The Lambert-Beer Law can be written as:

$$I = I_0 e^{-\alpha_m \lambda} \tag{1.35}$$

where $\lambda = \rho_m z$ is the area density.

Although many are the possible gamma-ray interaction mechanism with matter, three are the most important: *photoelectric absorption*, *Compton scattering* and *pair production* [15]. The common point to all these mechanisms is the total or partial transfer of energy to electrons. The mass attenuation coefficient can be expressed as:

$$\alpha_m = \alpha_{m,\, photoelectric} + \alpha_{m,\, Compton} + \alpha_{m,\, pair} \tag{1.36}$$

We will briefly cover all of them, however, due to the energy involved, only the latter two are used in gamma-ray detection.

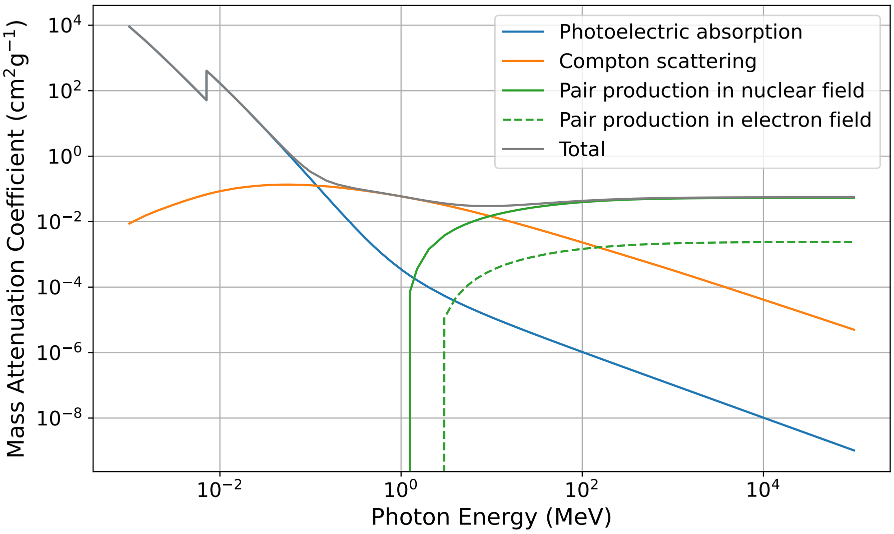

Figure 1.1: Mass attenuation coefficients of Iron for the main attenuation contributions: photoelectric absorption, Compton scattering and two types of pair production. Data taken from NIST's XCOM database [16].

As an example, in Figure 1.1 it is shown the mass attenuation coefficients of Iron for the main attenuation contributions (data taken from NIST's XCOM database [16]). From this plot we can see how the various contributions become gradually predominant as the photon energy increases.

At high energies, in particular those of the photons studied by IACTs experiments, the treatment of the interaction of photons with matter cannot be separated from that of electrons with matter. Indeed, the $e^{\pm}$ emitted by pair production are still very energetic, and lose energy in the medium mainly by *bremsstrahlung* (breaking radiation). As we will see, this process is fundamental in atmospheric shower development, and its treatment is very similar to the one of pair production.

Photoelectric Absorption

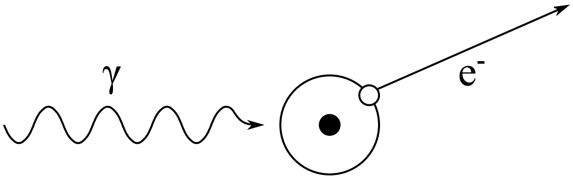

Figure 1.2: Photoelectric absorption

The *photoelectric absorption*, also known as *photoelectric effect*, is the emission of an electron, referred as *photoelectron*, induced by the interaction of a photon with an absorber atom; in this process the photon completely disappears. The mechanism is schematically depicted in Figure 1.2. The photoelectric absorption cannot take place with free electrons, but only with electrons of the bound shell of an atom: the atom recoil is indeed necessary for the conservation of the momentum (however its recoil energy is very small and usually neglected).

If ν is the photon frequency and E_b is the atom binding energy, the energy of the emitted photoelectron will be:

$$E_{e^-} = h\nu - E_b \tag{1.37}$$

Since an electron is ejected, this interaction also creates an ionized atom, with a vacancy in the outer shell; this vacancy will be quickly filled or by a free electron or by the rearrangement of other shells.

This effect is the predominant interaction mode for photons of relatively low energy, and it is more important as the atomic number Z of the material increases. Indeed, the probability of photoelectric absorption per atom can be approximated as:

$$\tau \simeq \text{constant} \times \frac{Z^n}{E_\gamma^{3.5}}, \qquad n \in [4,5] \tag{1.38}$$

For this reason high-Z material, such as lead, are commonly used as gamma-ray shields.

At low energies in the mass attenuation spectrum we can see discontinuities, which correspond to the binding energy of the various shells of the absorbed atom. In the case of iron, the discontinuity visible in Figure 1.1 is related to the K-shell: if the photon energy is higher than the K-shell binding energy, a K electron can be ejected due to photoelectric effect, while if the energy is lower, even slightly, the process is not possible and therefore the interaction probability drops.

Since for high-energy photons this process is not relevant, we will not continue further in its discussion.

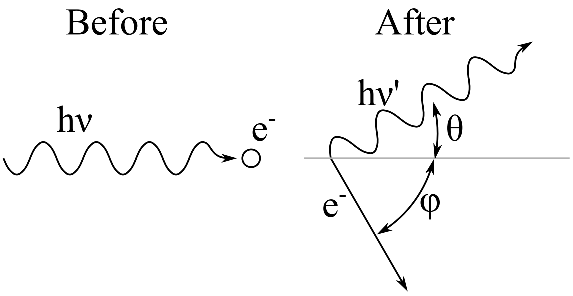

Figure 1.3: Compton scattering

Compton Scattering

In *Compton scattering* the incident gamma ray interacts with an electron in the absorbing material and is deflected by an angle θ. A schematic representation of the process is shown in Figure 1.3. We can assume the electron to be initially at rest; the photon in the interaction transfers a part of its energy to the electron, which is then referred to as *recoil electron.*

If we neglect the atomic binding energy and we assume that the photon interacts with a free electron, by applying the conservation of the energy:

$$\begin{aligned} h\nu + E_e &= h\nu' + E_{e'} \\ h\nu + m_e c^2 &= h\nu' + \sqrt{p_{e'}^2 c^2 + (m_e c^2)^2} \end{aligned} \tag{1.39}$$

Where m_e is the electron rest mass (0.511 MeV). Also the momentum is conserved:

$$\mathbf{p_{e'}} = \mathbf{p}_\gamma - \mathbf{p}_{\gamma'} \tag{1.40}$$

To obtain the square of the magnitude we can use the scalar product:

$$p_{e'}^2 = p_\gamma^2 + p_{\gamma'}^2 - 2p_\gamma p_{\gamma'} \cos\theta \tag{1.41}$$

If we multiply for c^2:

$$\begin{aligned} p_{e'}^2 c^2 &= p_\gamma^2 c^2 + p_{\gamma'}^2 c^2 - 2c^2 p_\gamma p_{\gamma'} \cos\theta = \\ &= (h\nu)^2 + (h\nu')^2 - 2h^2 \nu\nu' \cos\theta \end{aligned} \tag{1.42}$$

From Equation 1.39:

$$p_{e'}^2 c^2 = (h\nu + m_e c^2 - h\nu')^2 - (m_e c^2)^2 \tag{1.43}$$

Therefore:

$$\begin{aligned} \left(h\nu + m_e c^2 - h\nu'\right)^2 &= (h\nu)^2 + (h\nu')^2 - 2h^2\nu\nu'\cos\theta + (m_e c^2)^2 \\ 2h\nu m_e c^2 - 2h^2\nu\nu' - 2h m_e c^2 \nu' &= -2h^2\nu\nu'\cos\theta \\ h\nu'\left(h\nu + m_e c^2 - h\nu\cos\theta\right) &= h\nu m_e c^2 \\ h\nu'\left(m_e c^2 + h\nu(1-\cos\theta)\right) &= h\nu m_e c^2 \\ h\nu' m_e c^2 \left(1 + \frac{h\nu}{m_e c^2}(1-\cos\theta)\right) &= h\nu m_e c^2 \end{aligned}$$

Thus, the scattered photon energy is:

$$h\nu' = \frac{h\nu}{1 + \frac{h\nu}{m_e c^2}(1-\cos\theta)} \tag{1.44}$$

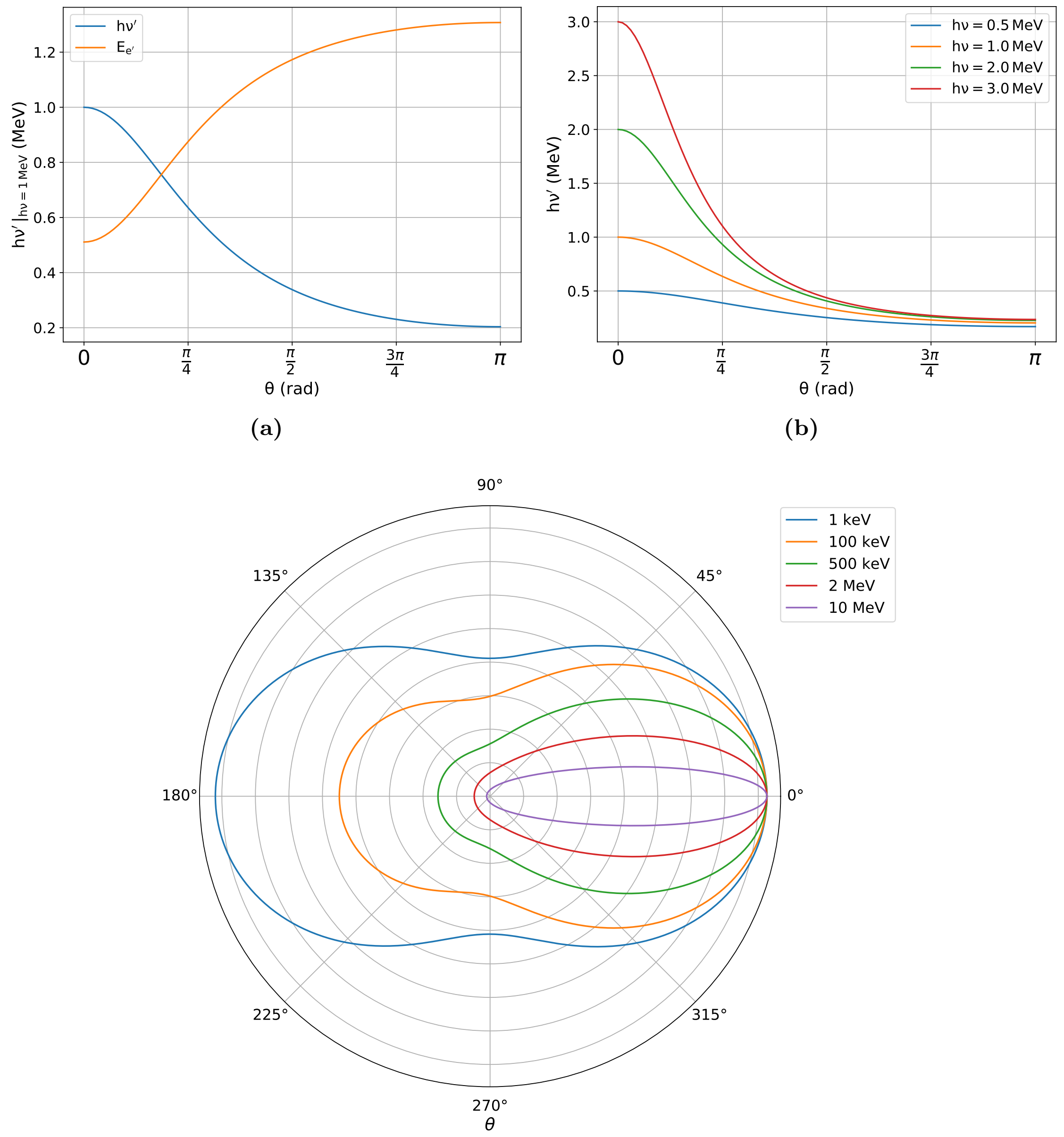

(a) **(b)**

(c)

Figure 1.4: (a) Compton scattered photon energy $h\nu'$ and scattered electron energy $E_{e'}$ by varying θ for an incident photon energy $h\nu = 1\,\mathrm{MeV}$
(b) Compton scattered photon energy $h\nu'$ by varying θ for different incident photon energies $h\nu$
(c) A polar distribution of photons Compton scattered at angle θ at different incoming photon energies; the incident photon comes from the left.

In Figure 1.4a it is shown the Compton scattered photon energy $h\nu'$ and the scattered electron energy $E_{e'}$ by varying θ for an incident photon energy $h\nu = 1\,\mathrm{MeV}$. As we can see, for very small scattered angles, there is practically no energy transfer. As θ increases, the energy transferred to the electron increases, but even for $\theta = \pi$ some energy is kept by the photon. In Figure 1.4b we can find a plot of the scattered photon energy by varying θ for different incident photon energies $h\nu$.

The Compton scattering differential cross section is described by the *Klein-Nishina formula*:

$$\frac{d\sigma}{d\Omega} = Zr_e^2 \left(\frac{1}{1+\alpha\,(1-\cos\theta)}\right)^2 \left(\frac{1+\cos^2\theta}{2}\right)\left(1+\frac{\alpha^2(1-\cos\theta)^2}{(1+\cos^2\theta)[1+\alpha(1-\cos\theta)]}\right) \tag{1.45}$$

where r_e is the classical electron radius and $\alpha = h\nu/(m_0c^2)$. By plotting the angular distribution of scattered gamma rays (Figure 1.4c) we can observe that the most probable scattering mode is the forward one as the incident photon energy increases [15].

Bremsstrahlung

Following [17], before discussing the pair production mechanism, we will describe the bremsstrahlung process.

When high energy electrons (or positrons) interact with matter, part of their energy is converted into electromagnetic radiation: this process is known as *bremsstrahlung* (from the German *bremsen* "to brake" and *Strahlung* "radiation", i.e. "braking radiation"). It is the main mechanism by which electrons and positrons lose energy in electromagnetic air showers.

When a charged particle decelerates because it is deflected by another charged particle, part of its kinetic energy is converted into electromagnetic radiation [15, 17]. In the following equation we will call E the incident $e^\pm$ energy, k the bremsstrahlung photon energy and y the fraction of the electron's energy transferred to the radiated photon ($y = k/E$). If Z is the atomic number of the absorber material, α the fine structure constant and r_e the classical electron radius, at very high energies we are in the so called "complete screening case" and the cross section can be approximated as [18]:

$$\frac{d\sigma_{br}}{dk} = \frac{1}{k}4\alpha r_e^2 \left\{\left(\frac{4}{3}-\frac{4}{3}y+y^2\right)\left[Z^2(L_{rad}-f(Z))+ZL'_{rad}\right]+\frac{1}{9}(1-y)(Z^2+Z)\right\} \tag{1.46}$$

L_{rad} and L'_{rad} are given in Table 1.1. The function $f(T)$ is the *Coulomb correction*; this function is an infinite sum, but for elements up to uranium it can be approximated with good accuracy as:

$$f(Z) = a^2\left[(1+a^2)^{-1}+0.20206-0.0369a^2+0.0083a^4-0.002a^6\right] \tag{1.47}$$

where $a = \alpha Z$ [19].

Element	Z	L_{rad}	L'_{rad}
H	1	5.31	6.144
He	2	4.79	5.621
Li	3	4.74	5.805
Be	4	4.71	5.924
Others	>4	$\ln(184.15\,Z^{-1/3})$	$\ln(1194\,Z^{-2/3})$

Table 1.1: Tsai's L_{rad} and L'_{rad} [17]

In the *infrared limit*, i.e. at small y, the cross section can be approximated as:

$$\frac{d\sigma_{br}}{dk} = \frac{A}{X_0 N_A k}\left(\frac{4}{3} - \frac{4}{3}y + y^2\right) \tag{1.48}$$

where X_0 is called *radiation length*, and is the mean distance over which a high-energy electron (or positron) loses by bremsstrahlung all but $1/e$ of its energy. If N_A is the Avogadro's number and A the material mass number, X_0 is:

$$\frac{1}{X_0} = 4\alpha r_e^2 \frac{N_A}{A}\left\{Z^2\left[L_{rad} - f(Z)\right] + Z L'_{rad}\right\} \tag{1.49}$$

The cross section in Equation 1.48 for lead is shown in Figure 1.5a. This expression is no longer accurate for $y \to 1$ (i.e. $E \to k$), where the screening may become incomplete, and for $y \to 0$, where the infrared divergence is removed by other effects [17].

If we exclude these limits and we remain in the complete screening approximation, an electron travelling at distance d much smaller than X_0 emits a number of photons with

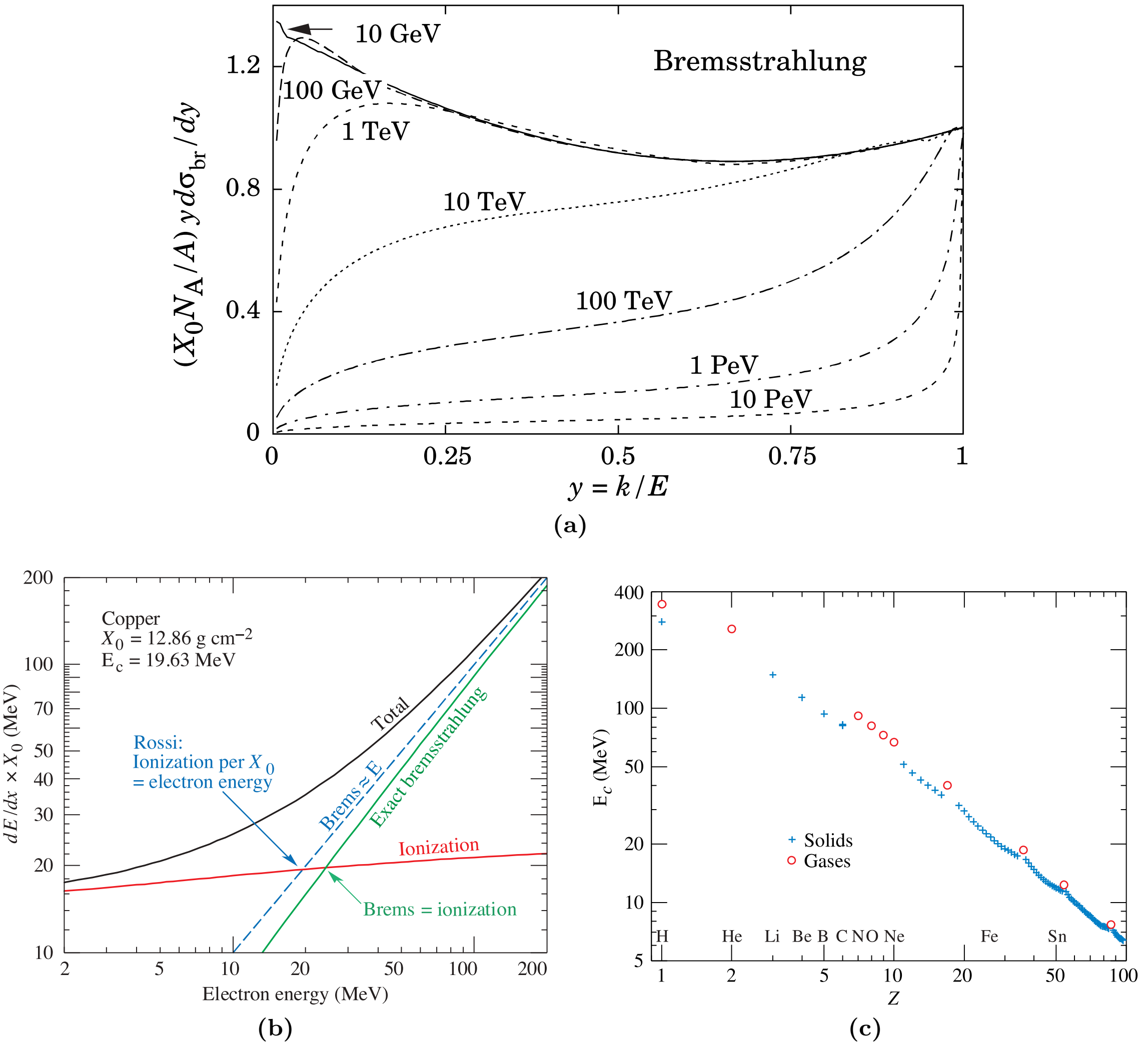

(a)

(b)

(c)

Figure 1.5: (a) Normalized bremsstrahlung cross section $k d\sigma_{br}/dk$ in lead versus $y = k/E$. The ordinate axis has units of photons per radiation length. Edited from [17]
(b) Two definitions of the critical energy [17]
(c) Electron critical energy for different elements, using Rossi's definition. Edited from [17]

energies between k_{min} and k_{max} equal to [17]:

$$N_\gamma = \frac{d}{X_0}\left[\frac{4}{3}\ln\left(\frac{k_{max}}{k_{min}}\right) - \frac{4(k_{max}-k_{min})}{3E} + \frac{k_{max}^2 - k_{min}^2}{2E^2}\right] \tag{1.50}$$

An electron (or positron) loses energy by bremsstrahlung at a rate nearly proportional to its energy, while the ionization loss varies logarithmically with the electron energy: the energy at which the two losses are equal is known as *critical energy* E_c [20]. Alternatively E_c was defined by Rossi as the energy at which the ionization loss per radiation length is equal to the electron energy [21]. This definition, which is equivalent to the first one with the approximation $-\langle dE/dx\rangle_{br} \simeq E/X_0$, has been found to describe more accurately the transverse electromagnetic shower development [17]. A comparison between the two different E_c definitions in copper is shown in Figure 1.5b, while in Figure 1.5c we can see the Rossi electron critical energy for different elements.

Pair Production

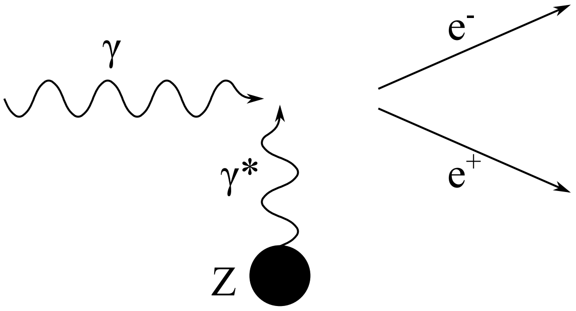

Figure 1.6: Pair production between a gamma ray and the virtual photon related to the magnetic field of an absorbing atom nucleus

The *pair production* is the production of an electron-positron pair from the interaction of two gamma rays. This process describes both the interaction of a gamma ray with a real photon (e.g. a CMB photon or an EBL one), and the interaction of a gamma ray with an intense nuclear magnetic field. It is the third important gamma-ray interaction process, and is the predominant one at high energies. In Figure 1.7 it is shown the probability that a photon interaction will result in conversion to an electron-positron pair as the photon energy increases, for different materials. One of the two photons is the virtual one related to the intense magnetic field near the protons in the nuclei of the absorbing material, as depicted in Figure 1.6. Although less likely, it is also possible to have pair production in an electron field, as shown in the plot in Figure 1.1 for iron.

The pair production can occur only if the total energy in the interaction exceeds twice the rest mass energy of an electron ($2m_ec^2 \simeq 1.02\,\mathrm{MeV}$). If the available energy exceeds this value, the excess energy goes into the kinetic energy shared by the electron-positron pair:

$$E_{e^-} + E_{e^+} = E_\gamma + E_{\gamma'} - 2m_ec^2 \tag{1.51}$$

In the complete-screening limit valid at high energies, we can express the pair production cross section as:

$$\frac{d\sigma_{pp}}{dx} = \frac{A}{X_0 N_A}\left[1 - \frac{4}{3}x(1-x)\right] \tag{1.52}$$

In this case $x = E/k$, where E is the energy of the pair-produced electron (or positron) and k is the energy of the incident photon. The cross section is very similar to the bremsstrahlung one, since the processes are one the variant of the other. In Figure 1.8

we can see the normalized pair production cross section as a function of x for different incoming gamma-ray energies; as expected it is symmetric between x and $1-x$.

By integrating Equation 1.52 we can find the high-energy limit for the total σ_{pp}:

$$\sigma_{pp} = \int_{x=0}^{x=1} \frac{A}{X_0 N_A} \left[1 - \frac{4}{3}x(1-x)\right] dx = \frac{7}{9}\frac{A}{X_0 N_A} \tag{1.53}$$

This Equation is accurate for photon energies above 1 GeV [17].

In this case the radiation length is defined as the average distance after which the photon will convert into a pair; this quantity is strictly linked with the radiation length for bremsstrahlung according to the following relationship:

$$X_{0,pp} = \frac{9}{7} X_{0,br} \tag{1.54}$$

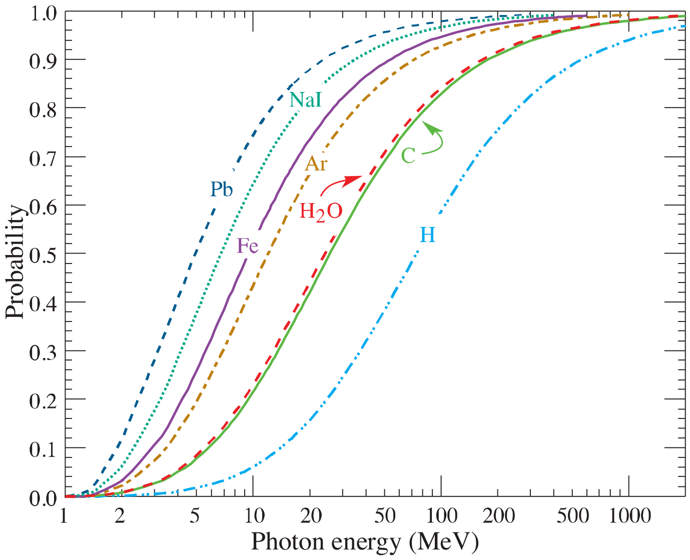

Figure 1.7: Probability that a photon interaction will result in conversion to an electron-positron pair as the photon energy increases, for different materials

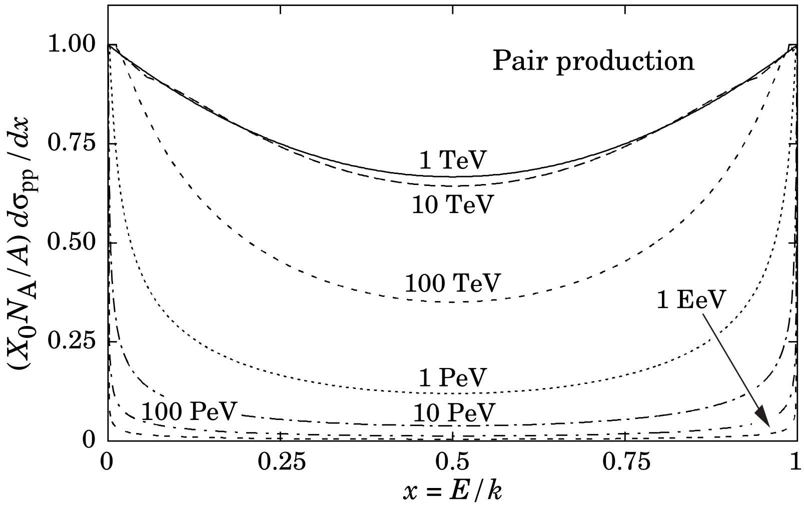

Figure 1.8: Normalized pair production cross section as a function of x for different incoming gamma-ray energies

1.1.4 Gamma-Ray Detection

Depending on the gamma-ray energy, different detection techniques were developed. In the lower energy regime ($E_\gamma \lesssim 10\,\mathrm{GeV}$) the gamma-ray flux is high enough that even a small detector can be successfully used: these observations are usually performed with satellite-based detectors. As the gamma-ray energy increases, the flux decreases, therefore a small detector becomes less efficient: in this energy regime gamma-ray observation is performed with ground-based facilities. We will briefly describe the various techniques, and then go into the details of the one used by CTA.

Direct Detection

Direct detection is the best choice for gamma rays in the lower energy range. These observations are carried out by satellites hosting proper detectors. The interaction of photons with matter is dominated by different processes, depending on the energy of the photons themselves: therefore for different gamma-ray energies, different detection techniques are used.

In the lower energy range ($1\,\mathrm{MeV} \lesssim E_\gamma \lesssim 30\,\mathrm{MeV}$) the detection is based on Compton scattering. This range is the bridge between X-ray and gamma-ray astrophysics; although here we can find hints of many production processes, such as nuclear de-excitations, radioactive decays, synchrotron and thermal emissions, few were the experiments built to study this energy range. The difficulties associated with this technique are the main reason for the low number of instruments.

The first satellite that used this technique was the *Compton telescope* (*COMPTEL*), one of the four instruments on board the *Compton Gamma-Ray Observatory* (*GRO*), launched on April 5, 1991. Its field of view was about 1 sr, with an angular resolution of $\simeq 1°$; its effective area was between 10 and $50\,\mathrm{cm}^2$. It was able to detect sources 20 times weaker than Crab with a 14 days observation. In Figure 1.9a it is shown the schematic view of the telescope; it is made by two detector arrays, called D1 (on the top) and D2 (on the bottom). D1 is an array of low-Z liquid scintillators (NE 213), while D2 is made of a high-Z material (NaI(Tl)). The light generated in the scintillators, both for D1 and for D2, is collected and converted into an electrical signal by photomultipliers. When a gamma ray of the target energy enters the telescope's field of view, it can interact by Compton scattering in D1, then the resulting gamma ray can reach D2, where it is absorbed. The location and energy loss of both interactions are measured, as well as the time of flight, fundamental to confirm the detection. All around the telescope an anticoincidence module is installed to discard non-gamma events [22].

More recent and modern is the *e-ASTROGAM* satellite, not yet launched [23]. A schematic view of the module, built to be sensitive in the gamma-ray energy range between 150 keV and 3 GeV, is shown in Figure 1.9b. It is mainly made by a silicon tracker, in which the gamma rays can interact via Compton scattering or pair conversion, and a Calorimeter, to absorb the secondary particles and measure their energy. An anticoincidence system acts as a veto for charged cosmic rays.

As energy increases, the interaction of photons with matter is dominated by pair production. Among all the various noteworthy experiments who study and have studied this energy range, we will briefly describe only the *FERMI Large Area Telescope* (*LAT*), sensitive to gamma rays with energy $20\,\mathrm{MeV} \lesssim E_\gamma \lesssim 300\,\mathrm{GeV}$. Together with the *Gamma-Ray Burst Monitor* (*GBM*), specialized for gamma-ray bursts studies in the energy range between 8 keV to 40 MeV, it is host by the *FERMI* satellite, launched in 2008 and still operating. In Figure 1.9c we can see the operating principle of FERMI-LAT: an incoming gamma ray does not produce a signal in the plastic anticoincidence detector, and freely reaches the precision converter-tracker. Here it interacts with an atom in one of the thin tungsten foils, producing an electron-positron pair. These charged particles are detected and tracked by a x-y array of silicon strips, and finally are stopped by a cesium iodide calorimeter, which measures the total energy deposited. The telescope dimensions are 1.8 m × 1.8 m × 0.72 m and its field of view is very wide, about 60 deg [24].

Indirect Detection

To have an accurate energy reconstruction of the incoming gamma ray, most of the electron-positron energy should be absorbed by the calorimeter: up to a certain energy, if

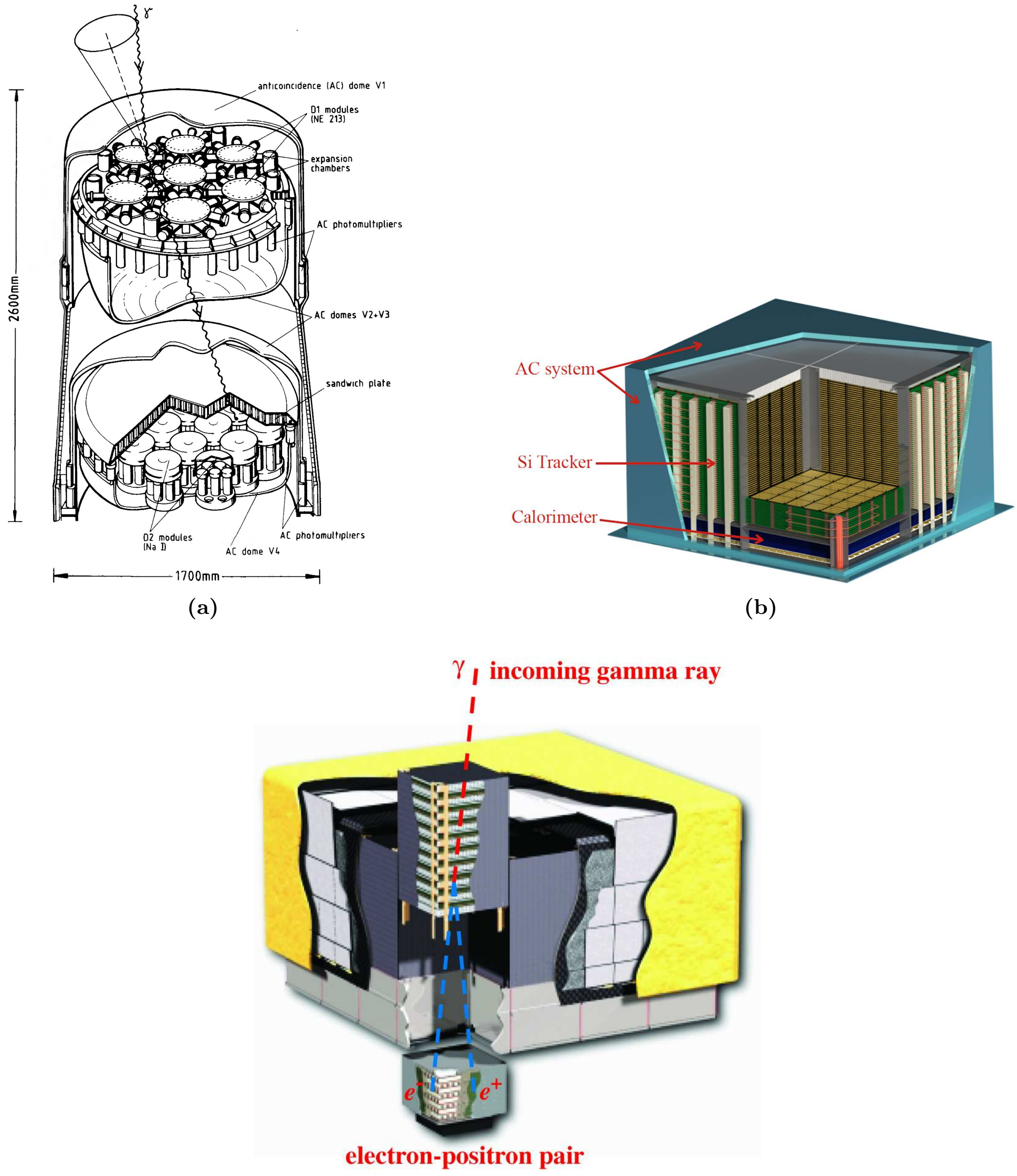

(a) (b)

(c)

Figure 1.9: Schematic views of COMPTEL (a, from [22]), e-ASTROGAM (b, from [23]) and of the Large Area Telescope (c, from [24])

we do not increase the calorimeter size and density, the direct detection becomes less sensible. Moreover, as we have already discussed, the gamma-ray flux decreases as the energy increases, thus we need a larger area detector. Due to these factors the VHE and UHE gamma-ray detection relies on ground-based experiments, which indirectly reconstruct the primary gamma-rays energies and directions by studying the air showers induced by them in the atmosphere.

When a high-energy gamma ray interacts with the atmosphere, it initiates an electromagnetic shower; we will discuss this phenomena in section 1.2. The charged particles which compose the shower, i.e. electrons and positrons, are still very energetic, and if they travel faster than the light in the medium, they emit in turn electromagnetic radiation due to *Cherenkov effect*. This radiation is detected on ground by proper telescopes, called *Imaging Atmospheric Cherenkov Telescopes* (IACT). In the following sections we will discuss this technique in more detail, since it is the one used by CTA.

Alternatively, it is possible to directly detect the electrons and positrons that make up the cascade. There are two techniques most commonly used for this purpose: the use of *Resistive Plate Chambers* and the *Water Cherenkov Detection*. Such facilities are known as wide-field of view gamma-ray observatories, to distinguish them from IACTs, which generally offer greater instantaneous sensitivity but a much smaller field of view.

The *Astrophysical Radiation with Ground-based Observatory* (ARGO-YBJ) is one of the most important examples of the first technique. The experiment has been taking data with its full layout from November 2007 till February 2013 at the YangBaJing Cosmic Ray Observatory (4300 m a.s.l.) in Tibet. Its detector was an array of RPCs covering an area of about 6700 m^2, divided in modules of 12 RPCs each; the setup is shown in Figure 1.10. It was designed to study a wide number of topics in astrophysics and cosmic-ray physics, ranging from very high energy gamma-ray astronomy to cosmic-ray and helio-physics [25].

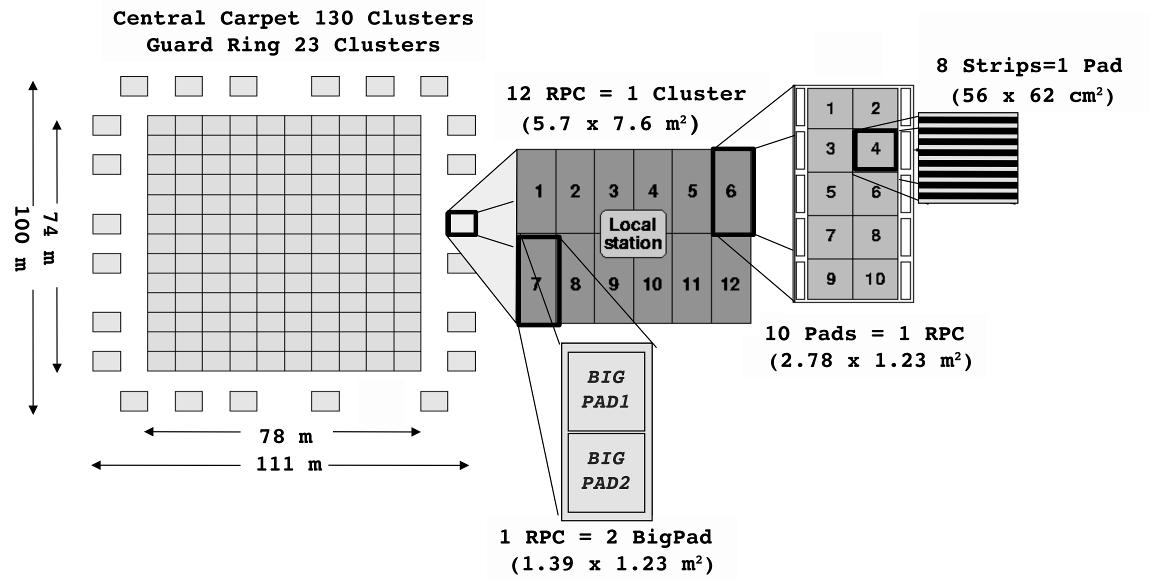

Figure 1.10: The ARGO-YBJ detector setup. The 12 RPCs Cluster is the basic module [25]

The *The High-Altitude Water Cherenkov Gamma-Ray Observatory* (HAWK) is probably the major example for the Water Cherenkov Detection technique. Built at 4100 meters above sea level on the northern slope of the volcano Sierra Negra, Mexico, it is an array of large water Cherenkov detectors (WCD) sensitive to gamma rays and hadronic cosmic rays in the energy range between 100 GeV and 100 TeV. The main array is composed of 300 WCDs, each of them is a cylinder of 7.3 m in diameter and 4.5 m in height. This array is surrounded by 345 smaller WCDs (1.55 m in diameter and 1.65 m in height); the layout is shown in Figure 1.11a. Its instantaneous field of view is about 2 sr, with a duty cycle higher than 95% [26, 27]. When a charged particle enters the detector, if it has enough energy it emits Cherenkov light; this light is collected by photomultipliers, which convert it into an electrical signal. With this technique it is possible to study both electromagnetic and hadronic showers. In Figure 1.11b it is shown a simulation of a 1 GeV muon (red line) passing through a HAWC detector and emitting Cherenkov light (green lines).

Another great example of a wide-field of view facility is the *Large High Altitude Air Shower Observatory* (LHAASO), located at 4410 m above sea level at Mount Haizi, China. It is designed to detect air showers induced both by gamma rays and by cosmic rays with energy ranging from a few tens of GeV to a few EeV. It consists of a 1.3 km^2 extensive air shower detector (KM2A) array made by 5195 scintillator counters (ED) and 1188 muon detectors (MD). In the center there is a Water Cherenkov Detector Array (WCDA) covering 78 000 m^2 and the Wide Field-of-view air Cherenkov/fluorescence Telescope Array (WFCTA), made by 18 telescopes. All these three detectors (KM2A, WCDA and WFCTA) are interconnected among themselves. A schematic view of the LHAASO layout is shown in Figure 1.12, where the small red dots are the scintillator counters, the big blue dots are the muon detectors, the three light-blue rectangles in the center is the WCDA and the small black rectangles near the WCDA are the 18 telescopes of WFCTA [29].

Nowadays the construction of a wide-field of view observatory in the southern hemisphere is under study; its name is *Southern Wide-Field Gamma-Ray Observatory* (SWGO) [30]. Being the only wide-field of view observatory sensitive to the southern sky, it would complete current and future instruments in the gamma-ray astronomy. Covering the southern sky, SWGO would allow us to deeply study the Galactic Center and give access to the full sky for transient phenomena, fundamental also for providing follow-up alerts to IACTs.

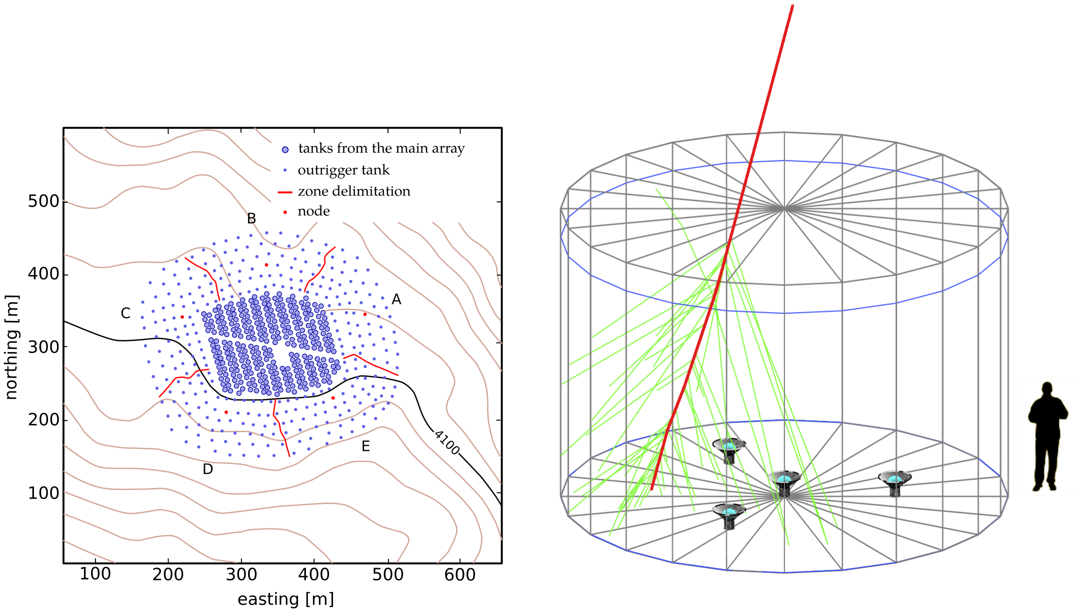

(a) **(b)**

Figure 1.11: (a) Top view sketch of the HAWC array [27]
(b) simulation of a 1 GeV muon (red line) passing through a HAWC detector and emitting Cherenkov light (green lines), from [28]

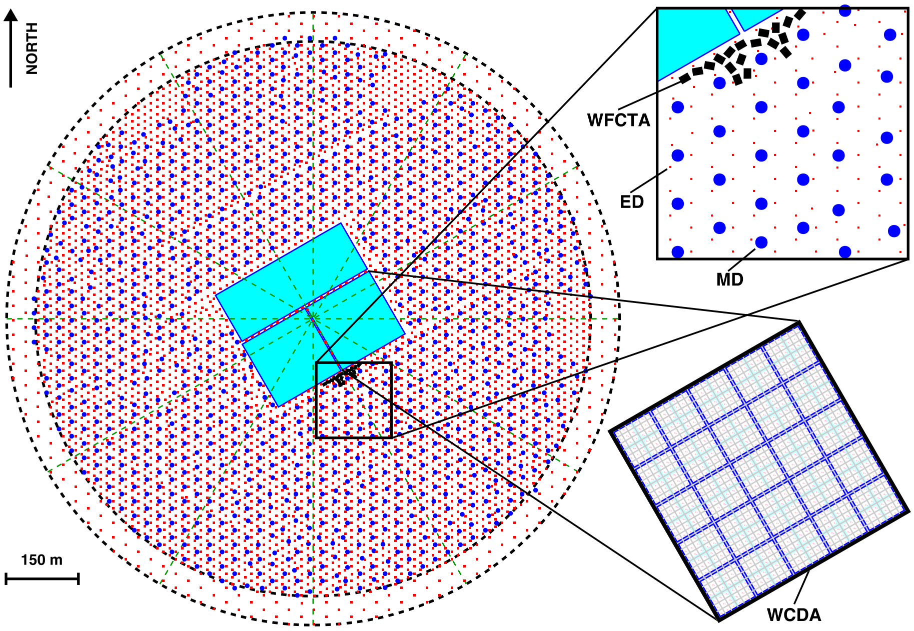

Figure 1.12: Schematic view of the LHAASO layout [29]

1.2 Air Showers

When a primary particle enters the atmosphere, it may interact with an atom's nucleus and give origin to an extensive particle cascade. Depending on the primary particle, which can be a charged cosmic ray or a gamma ray, we have different kinds of air showers; different are indeed the particles and the processes (interactions and decays) involved. We distinguish them into *Electromagnetic* and *Hadronic showers*.

1.2.1 Electromagnetic Showers

Electromagnetic showers are initiated by a primary high-energy gamma ray or by an electron interacting with the atmosphere. Since the processes which describe them are the same, the propagation and extinction of a cascade initiated by a gamma ray or by an electron follow the same treatment. The main physical processes involved are:

- *pair production*: when a high-energy photon interacts with the field a nucleus, it can generate and electron-positron pair

- *bremsstrahlung*: radiation emitted by an electron (or a positron) decelerating due to the interaction with a nucleus

The easier model built to understand the development of an electromagnetic shower is the *Heitler model* [31]. When a high-energy gamma ray interacts with the atmosphere, it will generate an electron-positron pair; each charged particle will generate in turn a gamma ray due to bremsstrahlung, and each gamma ray will generate another electron-positron pair. It is clear that the shower develops exponentially as long as the energy of the particles allows it to self-sustain. A schematic view of the model is shown in Figure 1.13a; in this case the primary particle is a gamma ray, but it is clear that except for the first step, the representation would be the same if the primary particle were an electron.

For simplicity, we assume that at each interaction the energy is distributed equally among the particles produced. In addition, we assume that the radiation lengths for pair production and bremsstrahlung are the same, and we call it λ_T (in air $\lambda_T \simeq 37\,\mathrm{g cm^{-2}}$).

Since the energy loss by bremsstrahlung follows an exponential decay, we can find the average distance d after which we have an interaction as follows:

$$e^{-\frac{d}{\lambda_T}} = \frac{1}{2} \quad \Rightarrow \quad -\frac{d}{\lambda_T} = \ln\left(\frac{1}{2}\right) \quad \Rightarrow \quad \frac{d}{\lambda_T} = \ln(2)$$

Therefore:

$$d = \lambda_T \ln(2) \tag{1.55}$$

After n interactions, we will have 2^n particles, each one with an energy of $E_0/2^n$, where E_0 is the primary particle energy. On average, the shower is made of 1/3 photons and 2/3 electrons and positrons. The shower development ends when the energy is too low for pair production or bremsstrahlung; we refer to this limit as *critical energy* E_c^e, the energy below which the electron will lose energy by ionization rather than for bremsstrahlung. In air $E_c^e = 85\,\mathrm{MeV}$.

If we consider a shower initiated by a primary particle with energy E_0, if will reach its maximum size N_{MAX} when all the particles have energy E_c^e, which means:

$$E_0 = E_c^e N_{MAX} \tag{1.56}$$

If we call n_{MAX} the steps after which the shower is formed by N_{MAX} particles:

$$N_{MAX} = 2^{n_{MAX}} = \frac{E_0}{E_c^e} \tag{1.57}$$

Therefore:

$$n_{MAX} = \frac{\ln\left(\frac{E_0}{E_c^e}\right)}{\ln(2)} \tag{1.58}$$

The total shower propagation is:

$$X_{MAX} = n_{MAX} d = \frac{\ln\left(\frac{E_0}{E_c^e}\right)}{\ln(2)} \lambda_T \ln(2) = \lambda_T \ln\left(\frac{E_0}{E_c^e}\right) \tag{1.59}$$

We can define the *elongation rate* Λ^γ as the rate of increase of X_{MAX} with E_0:

$$\Lambda^\gamma = \frac{dX_{MAX}}{d\log_{10} E_0} \tag{1.60}$$

Replacing Equation 1.59 we obtain:

$$\Lambda^\gamma = \frac{\lambda_T}{\log_e} \simeq 2.3\lambda_T \tag{1.61}$$

which means that in an electromagnetic shower the depth of its maximum increases logarithmically with energy at a rate $\Lambda^\gamma = 85\,\mathrm{gcm}^{-2}$ per decade of primary particle energy E_0.

The Heitler model, despite being very simple, describes quite well the shower development, but its results must be interpreted carefully. Indeed, it underestimates the photon to electron ratio, since the number of $e^\pm$ predicted by the model is too large; for example multiple photons are often emitted during bremsstrahlung. In addition, many electrons or positrons can escape the shower during its development. To extract the number of electron N_e from the Heitler prediction N, we use a correction factor g:

$$N_e = \frac{N}{g} \tag{1.62}$$

To get an order of magnitude estimate we can consider $g = 10$.

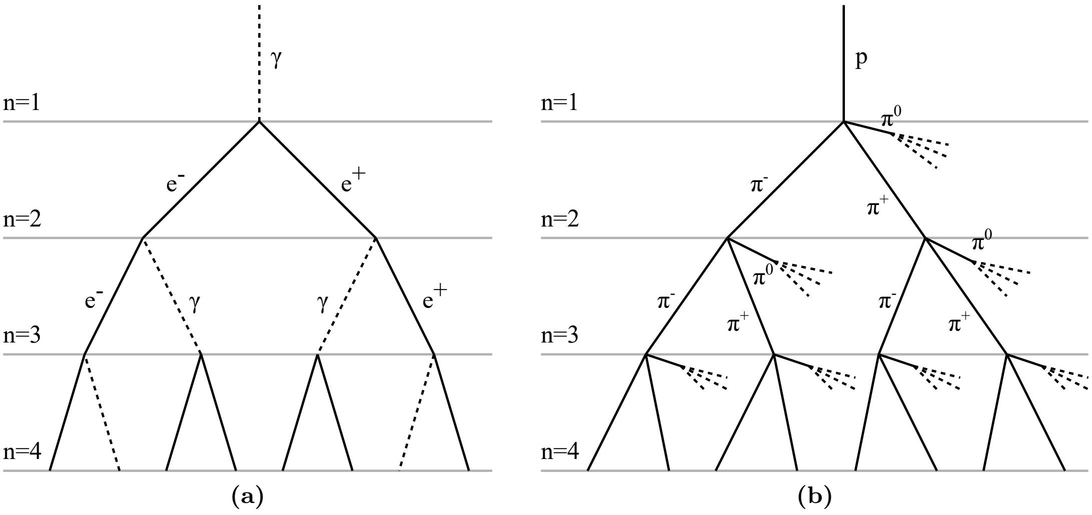

Figure 1.13: Heitler model for electromagnetic (a) and hadronic (b) showers

1.2.2 Hadronic Showers

If the primary particle is a charged cosmic ray, when it interacts with the atmosphere it can initiate an hadronic shower. The study of these showers is more complicated than in the previous case, as there are more different particles involved, and therefore more kinds of possible interactions. We will again rely on a simplistic model, applying the Heitler model also in this case [32].

Following the scheme reported in Figure 1.13b, when a primary charged cosmic ray (proton or nucleus) interacts with the atmosphere, the most produced particles are the pions, both charged $\pi^\pm$ and neutrals π^0. While the second ones decay almost immediately in photons:

$$\pi^0 \to \gamma\,\gamma \tag{1.63}$$

giving origin to electromagnetic showers, charged pions can interact again with the atmosphere, producing in turn charged and neutral pions. The process goes on until the charged pions reach the critical energy E_c^π, below which they decay emitting muons:

$$\pi^+ \to \mu^+\,\nu_\mu, \qquad \pi^- \to \mu^-\,\bar{\nu_\mu} \tag{1.64}$$

As a further approximation, let's imagine that we generate the same number of positive, negative and neutral pions: after each interaction, we will have N_{ch} charged pions and $1/2\,N_{ch}$ neutral ones; in addition we assume that the energy is equally distributed between them. As before, if λ_I is the *interaction length* of strongly interacting particles, we imagine to have an interaction every $d = \lambda_I \ln(2)$. With a good approximation we can assume that λ_I is constant and equal to $120\,\mathrm{gcm}^{-2}$.

Since we have an interaction after each layer, after n layers we will have $(N_{ch})^n$ charged pions, carrying a total energy of $(2/3)^n E_0$. The remaining part of the energy has instead gone into neutral pions, and therefore into electromagnetic showers. Even if it is a simplified model, we already have an important result: in a hadronic shower a noteworthy part of the primary particle energy gives origin to secondary electromagnetic showers.

Coming back to charged pions, after n interactions each one will carry an energy:

$$E_\pi = \frac{E_0}{\left(\frac{3}{2}N_{ch}\right)^n} \tag{1.65}$$

As we have already seen, when E_π falls below E_c^π the shower will stop: this happens after n_c interactions:

$$n_c = \frac{\ln\left(\frac{E_0}{E_c^\pi}\right)}{\ln\left(\frac{3}{2}N_{ch}\right)} \tag{1.66}$$

When the shower reaches its maximum, all the primary particle energy E_0 will be shared between N_π pions and N_{MAX} electromagnetic particles; since the number of muons N_μ is equal to the number of pions:

$$E_0 = E_c^e N_{MAX} + E_c^\pi N_\mu \tag{1.67}$$

Considering the electron number correction factor g, we have that $N_e = N_{MAX}/g$, therefore:

$$E_0 = E_c^e \frac{N_{MAX}}{g} + E_c^\pi N_\mu = gE_c^e \left(N_{MAX} + \frac{E_c^\pi}{gE_c^e}N_\mu\right) \tag{1.68}$$

From Equation 1.66 we can obtain the number of muons N_μ as a function of the energy as:

$$N_\mu = \left(\frac{E_0}{E_c^\pi}\right)^\beta, \qquad \beta = \frac{\ln(N_{ch})}{\ln\left(\frac{3}{2}N_{ch}\right)} \tag{1.69}$$

From various Monte Carlo simulations we have that β usually ranges between 0.85 to 0.92.

We can divide the total energy into electromagnetic component E_{em} and hadronic one E_h. Since $E_h = N_\mu E_c^\pi$:

$$E_0 = E_{em} + E_h = E_{em} + N_\mu E_c^\pi \tag{1.70}$$

Hence the fraction of the energy that goes into the electromagnetic part is:

$$\frac{E_{em}}{E_0} = \frac{E_0 - N_\mu E_c^\pi}{E_0} \tag{1.71}$$

Using Equation 1.69 we obtain:

$$\frac{E_{em}}{E_0} = 1 - \left(\frac{E_0}{E_c^\pi}\right)^{\beta-1} \tag{1.72}$$

The electromagnetic fraction is about 72% at $E_0 = 10^{14}\,\text{eV}$ and 90% at $E_0 = 10^{17}\,\text{eV}$.

Another fundamental quantity to describe a shower is X_{MAX}, i.e. the atmospheric depth at which the electrons and photons reach their maximum numbers. The electromagnetic component is generated from photons decaying from neutral pions; in the first interaction, one-third of the initial particle energy goes into this component. To get a proper estimation of X_{MAX}, we should consider all the electromagnetic sub-showers which compose the hadronic cascade; it's clear that this approach is anything but trivial. As an approximation, we will consider only the electromagnetic showers generated at the first interaction; in this way we will clearly underestimate the X_{MAX} value.

As we seen, the first interaction occurs at an atmospheric dept $X_0 = \lambda_I \ln(2)$, where λ_I is the primary proton interaction length. After the first interaction, we have N_{ch} photons, and each one will initiate a shower of energy $E_0/(3N_{ch})$. Using Equation 1.59, we can evaluate the depth of shower maximum as the one of an electromagnetic shower of energy $E_0/(3N_{ch})$ starting at X_0:

$$X_0^p = X_0 + \lambda_T \ln\left(\frac{E_0}{3N_{ch}E_c^e}\right) \tag{1.73}$$

The models seen so far, as mentioned above, are simple and rough; Monte-Carlo simulations are normally used to get a more complete description of the showers.

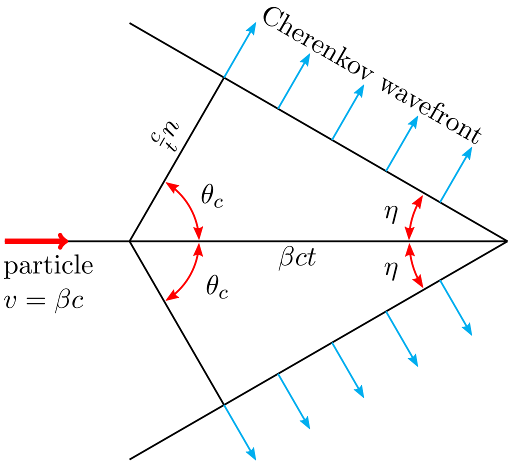

Figure 1.14: Cherenkov Light emitted by a charged particle traveling in a medium at $v = \beta c$. In a dispersive medium, $\theta_c + \eta \neq 90°$

1.3 Imaging Atmospheric Cherenkov Telescope

1.3.1 Cherenkov Radiation

The *Cherenkov radiation* is the electromagnetic radiation emitted when a charged particle passes through a dielectric medium at a speed greater than that of the light in the same medium. Most probably Pierre and Marie Curie were the first to observe this radiation, as described in Eva Curie's biography of her mother [33]; successively, between 1926 and 1928, this phenomenon was studied by Leon Mallet, without coming to a specific conclusion [34]. The first complete study of this radiation was published in 1934 by the Russian PhD student Pavel Cherenkov [35]: thanks to the discovery and the interpretation of this effect he received the Nobel Prize in 1958.

If we consider a charged particle travelling in a medium with a speed:

$$v = \beta c > \frac{c}{n}$$

where c is the speed of light in vacuum and n is the refractive index of the medium, it will emit radiation at an angle:

$$\theta_c = \cos^{-1}\left(\frac{1}{\beta n}\right) \tag{1.74}$$

A representation of the phenomenon is reported in Figure 1.14.

Practical Cherenkov radiators are dispersive material, i.e. a medium in which the refraction index depends on the photon frequency. In this case, if ω is the photon's frequency and $k = 2\pi/\lambda$ its wavenumber, the photon will propagate at a group velocity:

$$v_g = \frac{d\omega}{dk} = \frac{c}{[n(w) + \omega\left(\frac{dn}{d\omega}\right)]} \tag{1.75}$$

In a non dispersive medium the expression above is simplified to $v_g = c/n$.

The radiation is concentrated in a thin conical shell, whose vertex is in the moving particle and whose opening half-angle is η, which, in the case of a non dispersive medium:

$$\eta = 90° - \theta_c \tag{1.76}$$

This relationship is no longer valid for dispersive media.

The number of photons produced by a particle with charge ze per unit path length and per unit energy interval of the photons is [17]:

$$\begin{aligned} \frac{d^2N}{dEdx} &= \frac{\alpha z^2}{\hbar c}\sin^2\theta_c = \\ &= \frac{\alpha^2 z^2}{r_e m_e c^2}\left(1 - \frac{1}{\beta^2 n^2(E)}\right) = \\ &\simeq 370 \sin^2\left(\theta_c(E)\right)\ \mathrm{eV}^{-1}\mathrm{cm}^{-1}\ \ (\text{if } z = 1) \end{aligned} \tag{1.77}$$

or equivalently:

$$\frac{d^2N}{dxd\lambda} = \frac{2\pi\alpha z^2}{\lambda^2}\left(1 - \frac{1}{\beta^2 n^2(\lambda)}\right) \tag{1.78}$$

1.3.2 Atmospheric Cherenkov Radiation

History

In 1947, the British physicist P. M. S. Blackett predicted that relativistic cosmic rays passing through the atmosphere should produce Cherenkov light and slightly contribute to the night sky background [36]. The atmospheric Cherenkov light was detected for the first time in 1953 by B. Galbraith and J. V. Jelley [37]. They used a very simple detector: a light mirror seen by a photomultiplier (PMT), hosted in a garbage can to shield the stray light (Figure 1.15a). By setting a threshold of around four times the night sky noise level, they observed signals with a rate of about one event per two to three minutes: this was the first demonstration that Cherenkov light can be generated also in gases. Since these events were in coincidence with the ones detected by the Harwell air shower array, they demonstrated that these signals were actually induced by air showers [38]. The setup and the results of this historical detection are shown in Figure 1.15b.

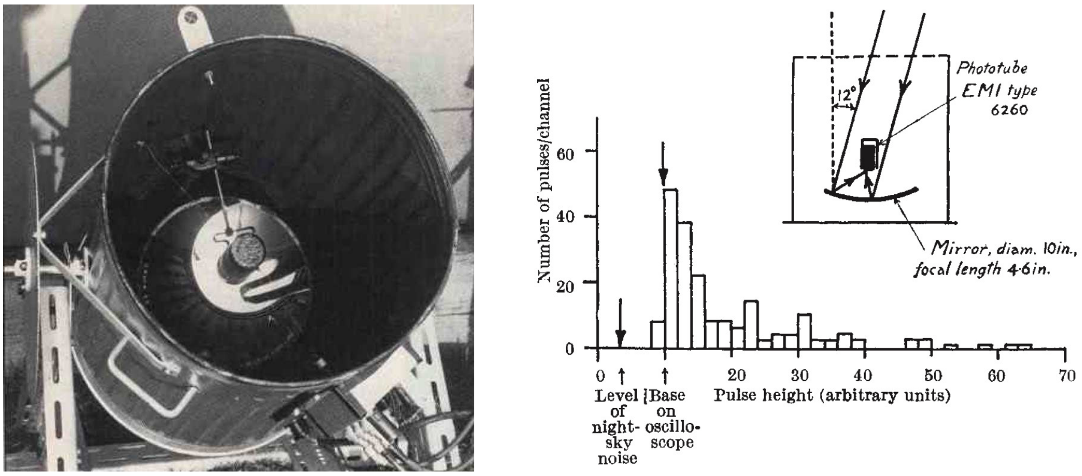

(a) (b)

Figure 1.15: (a) The first Cherenkov detector used by B. Galbraith and J. V. Jelley, made by a light mirror seen by a photomultiplier and hosted in a garbage can [37].
(b) Setup and results of the B. Galbraith and J. V. Jelley observations [37]

In the following years the technique was refined by using larger mirrors, photomultipliers array instead of a single one, coincidence between few telescopes and tracking of the source under study. This technique offers great advantages when compared to the air shower arrays. In particular, since it is possible to collect the light generated by the

Figure 1.16: Photo of the Whipple 10 m telescope at Mount Hopkins [38]

whole shower it is possible to better reconstruct the energy of the primary particle; in addition a better angular resolution can be achieved. On the other hand many were the disadvantages, such as the the limited field of view, the low duty cycle (it is possible to operate these telescopes only during clear and moonless nights), the many uncertainties induced by an imprecise knowledge of the properties of the atmosphere and the impossibility to discriminate between hadronic and electromagnetic showers. All these factors have caused that for a long time there were no great discoveries. In 1968 a 10 m telescope was completed at the Fred Lawrence Whipple Observatory in Arizona, USA, shown in Figure 1.16; in the first phase the camera was only composed of a single PMT [38]. Then both the instrument and the analysis methods were developed to increase the sensitivity. The single PMT in the focal plane was replaced by a 37 PMTs array, in order to display the reflected images of the showers [39]. We therefore have the transition from an *Atmospheric Cherenkov Telescope* (ACT) to an *Imaging Atmospheric Cherenkov Telescope* (IACT). In addition many studies were carried out in order to develop gamma/hadron discriminating methods; the most effective, still in use, was introduced in 1985 by Hillas [40]. In 1989, 35 years after the first observation of Cherenkov light from air showers, the Whipple collaboration published the first observation of gamma-ray emission from the Crab nebula [41]: this observation was not only the culmination of protracted efforts over the previous decades, but also a true milestone in astrophysics and in high-energy physics.

The next step to increase the sensitivity was to go from a single telescope detection to a stereo one: the first successfully operating stereo system with significantly improved sensitivity was built by the HEGRA (*High Energy Gamma-Ray Astronomy*) collaboration [38] at the Roque de los Muchachos Observatory (La Palma, Canary Islands) at 2200 m above sea level.

Later there were numerous experiments aimed at the detection of high-energy cosmic gamma rays. Still working and noteworthy they are MAGIC at Roque de Los Muchachos Observatory, VERITAS at Fred Lawrence Whipple Observatory and H.E.S.S. in Namibia.

The *Major Atmospheric Gamma Imaging Cherenkov* (MAGIC) is a system of two 17 m diameter Imaging Atmospheric Cherenkov Telescopes built at about 2200 m above sea level at Roque de los Muchachos Observatory, La Palma, Canary Islands. Built at the HEGRA site, the first telescope started operating in 2004; from 2009 MAGIC is taking data in stereoscopic mode. It was designed to perform gamma-ray astronomy in the energy range between 50 GeV to 50 TeV (the lower limit can be further lowered to 30 GeV by using a special trigger, called *Sum Trigger*). It has a field of view of 3.5°.

VERITAS (*Very Energetic Radiation Imaging Telescope Array System*) is an array of four 12 m IACTs built at the Fred Lawrence Whipple Observatory (FLWO) in southern Arizona, USA. It is sensitive to high energy gamma rays between $\simeq 100$ GeV and > 30 TeV. The angular resolution is 0.08° at 1 TeV and 0.13° at 200 GeV, while its peak effective area is 100 000 m^2 and its field of view is 3.5° [42, 43].

H.E.S.S. (*High Energy Stereoscopic System*) is a system of five Cherenkov telescopes located in Namibia, near the Gamsberg mountain. The first array, operative from 2003, is a 120 m side length array of four 12 m telescopes (H.E.S.S. I). In 2012, to improve the performances, a 28 m telescope was built in its center (H.E.S.S. II). The whole system is sensitive to gamma rays in the energy range between 30 GeV to 100 TeV. H.E.S.S. I has a field of view of 5°, while H.E.S.S. II of 3.2° and the global angular resolution can go down to 0.05° [44, 45].

In conclusion, the *Cherenkov Telescope Array* (CTA) will be the next generation ground based gamma-ray observatory; since it is the main topic of this thesis, it will be described in detail later.

Atmospheric Cherenkov Radiation from Gamma Rays

In Figure 1.17 it is shown the Electromagnetic opacity of the Earth's atmosphere as a function of the photon wavelength. While radio waves and visible light can reach the ground, and are therefore directly observable from Earth, for X-rays and gamma rays the atmosphere is almost totally opaque. For this reason X-rays and (low energy) gamma rays are observed from space by properly equipped satellites. However, if the photon carries enough energy, when it interacts with the atmosphere it can generate an *Electromagnetic Shower*; this is the case with Very High Energy (VHE) gamma rays. If the charged particles forming the shower (mainly e^- and e^+) travel faster than that of the light in the atmosphere, they emit Cherenkov Light: this light can be observed from ground and allow us to reconstruct the direction and energy of the incident photon.

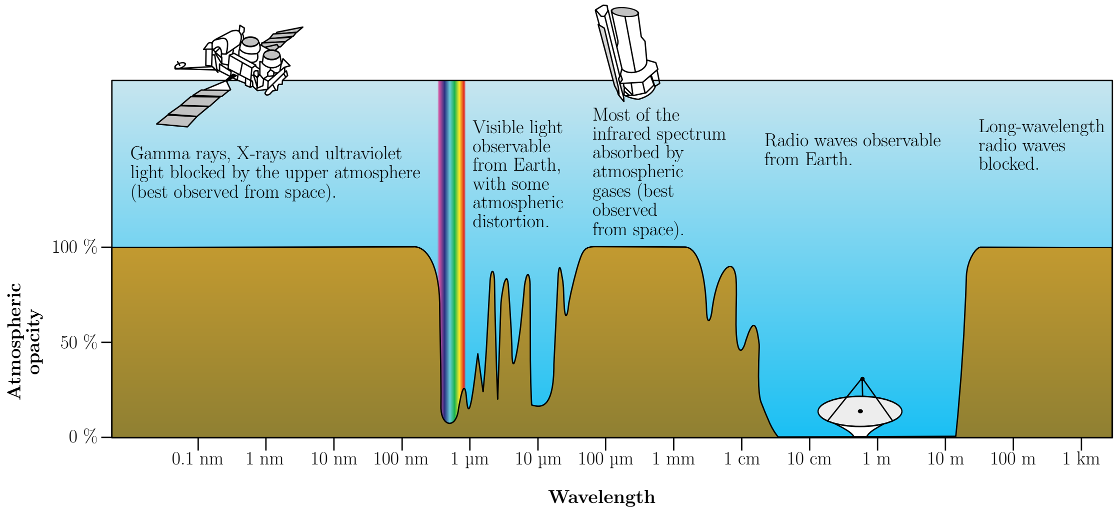

Figure 1.17: Electromagnetic opacity of the Earth's atmosphere (modified from[46])

A typical spectrum of Cherenkov light generated by vertical TeV air showers at an altitude of 2200 m is shown in Figure 1.18; as we can see, the most of the emission is in the ultraviolet band: this information is fundamental to correctly choose the sensor that will be used to detect this radiation.

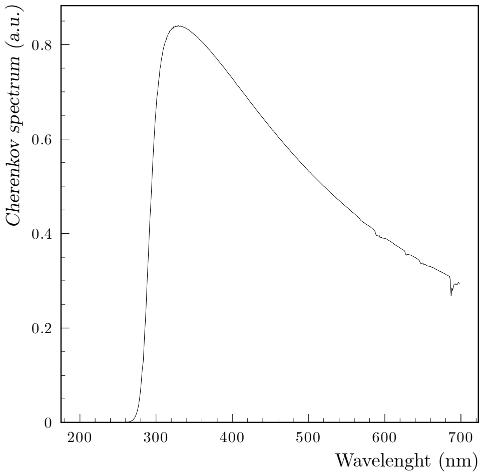

Figure 1.18: Typical spectrum of Cherenkov light generated by vertical TeV air showers at the altitude 2200 m (modified from [47])

Moreover, the refraction index changes with altitude, making the Cherenkov angle θ_C to increase during the shower propagation ($\theta_C \simeq 0.66°$ at 10 km, $0.74°$ at 8 km, $1.3°$ at sea level): the light is thus collimated in a so called *Cherenkov Pool* while it reaches the ground (Figure 1.19a). The simulated Cherenkov photon lateral density at the CTA North altitude (2200 m) for different energy of the primary gamma ray is shown in Figure 1.19b; as we can see these light pools have a radius between 120 m and 130 m.

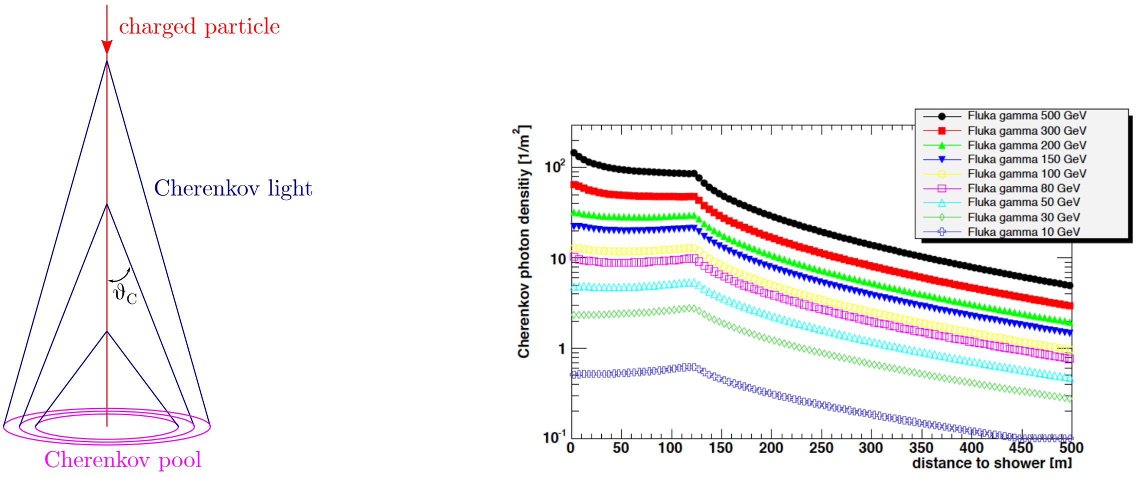

(a) **(b)**

Figure 1.19: (a) Cherenkov pool generation due to the dependence of the atmospherics refraction index with the altitude
(b) Cherenkov photon lateral density at the CTA North altitude (2200 m) for different energy of the primary gamma ray

Most of this Cherenkov light arrives at ground within few ns, as we can observe from the simulated Cherenkov photons time distribution for a 1 TeV vertical gamma-ray induced air shower shown in Figure 1.20a. This information is fundamental both for choosing the needed electronics and for rejecting the night sky background (NSB) detected by the camera, since we can be focused only on events that last a few nanoseconds.

Since we want to focus only on gamma-rays induced showers, it is necessary to reject hadronic shower events. Considering primary particles with the same energy, hadrons produce less Cherenkov light (about one third) if compared to gammas. Furthermore, gamma-ray induced showers show less fluctuations and they are compact and uniform

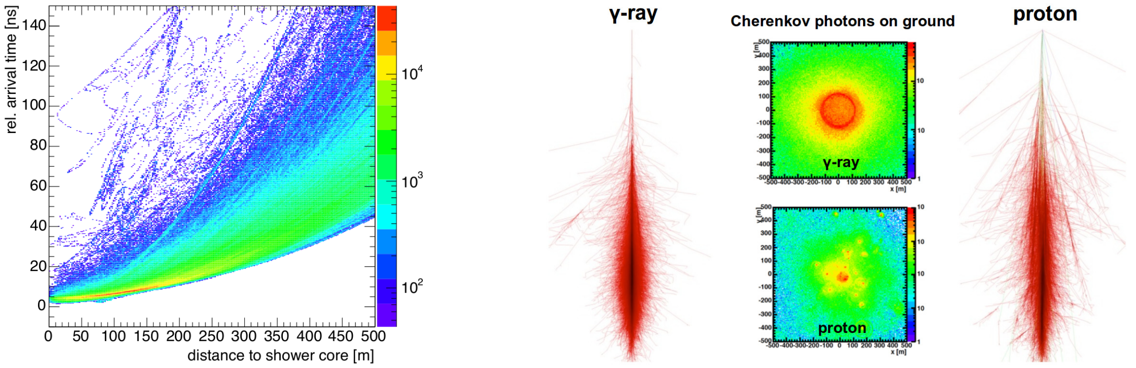

(a) (b)

Figure 1.20: (a) Cherenkov photon time distribution for a 1 TeV vertical gamma-ray induced air shower. Most of the photons arrives within $\simeq 10$ ns
(b) Difference between Cherenkov emission for gamma-induced showers and proton-induced ones

both in space and in time. Moreover, the Cherenkov pools due to primary protons (or other hadronic particles) are characterized by clusters, mainly generated by their secondary electromagnetic showers. An example of the difference between Cherenkov emission for gamma-induced shower and a proton-induced one is reported in Figure 1.20b.

The Cherenkov light emitted by the charged particles composing the EAS is reflected by the telescope segmented mirror and focused on the camera. The resulting geometry is an elliptic (or comet-like) shape with the head that points to the source position (Figure 1.21a). Its angular dimension ranges from 1° to 5° and the total number of photons detected for an event is $10^2 - 10^5$; the signal lasts for $(5 - 100)$ ns. An example of a Cherenkov event induced by a gamma ray detected at the Major Atmospheric Gamma Imaging Cherenkov Telescopes (MAGIC) is shown in Figure 1.21b. In addition the event shape depends on many other factors, for example the type and the energy of the primary cosmic ray, the core distance and the arrival direction.

Although it is possible to determine the arrival direction using a single telescope, with a *stereoscopic view* it is possible to improve the sensitivity on the reconstruction of the

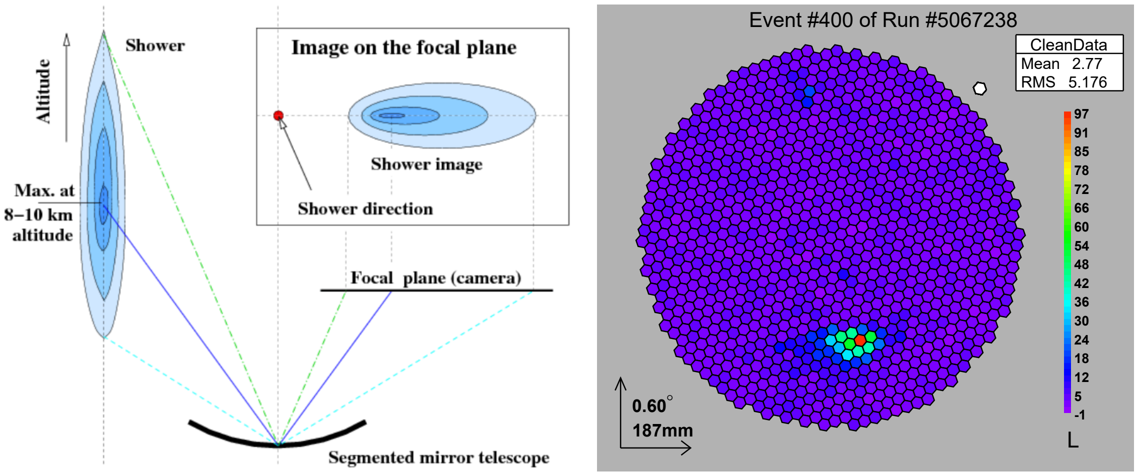

(a) (b)

Figure 1.21: (a) Cherenkov event shape on the camera
(b) An example of a gamma-ray event detected by MAGIC

core position (i.e. the intersection between the shower axis and the ground) and of the *arrival direction* (i.e. the sky coordinates that correspond to the arrival direction of the primary ray). For a stereoscopic view at least two telescopes are needed (e.g. *M1* and *M2* for the MAGIC experiment). A representation of a stereo reconstruction using four different telescopes is shown in Figure 1.22.

A pictorial representation of the Imaging Atmospheric Cherenkov technique is shown in Figure 1.23.

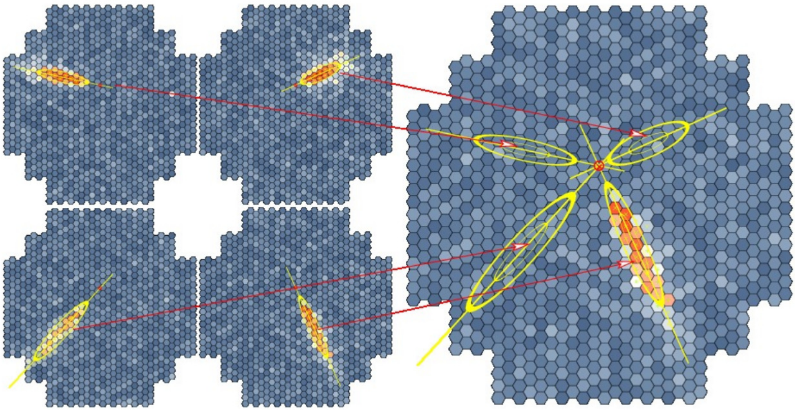

Figure 1.22: Stereo reconstruction using four different telescopes

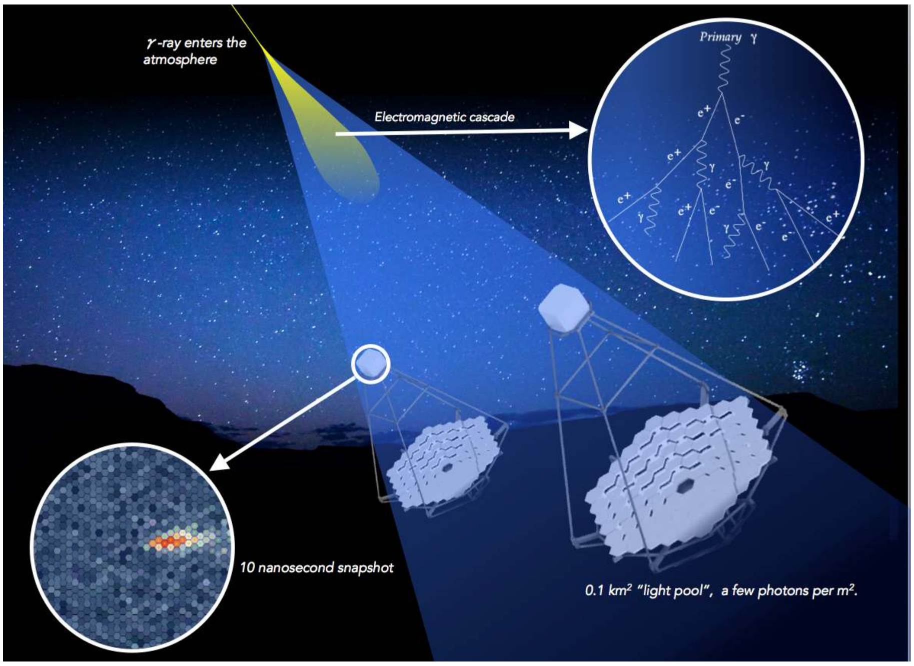

Figure 1.23: Representation of the IACT technique [48]

Chapter 2

Cherenkov Telescope Array

2.1 The CTA Project

The Cherenkov Telescope Array (CTA) will be the major global observatory for VHE gamma-ray astronomy over the next decade and beyond [8]. Ground-based gamma-ray astronomy is a very young field but it has proven to have enormous potential. In 1989 the Whipple 10 m imaging atmospheric Cherenkov telescope (IACT) detected a clear signal from the Crab nebula above 1 TeV [41], demonstrating the possibility of astrophysical measurements at teraelectronvolt energies. Since then the IACTs' instruments and techniques have strongly evolved, leading to the detection of more than 200 VHE sources [49] and making a great impact in astrophysics and more widely in physics. The current major arrays of IACTs are H.E.S.S., MAGIC and VERITAS, which have demonstrated the great physics potential and the maturity of this technique.

CTA will cover a wide energy range between 20 GeV and 300 TeV and will have a sensitivity far superior to current experiments. Thus the scientific potential of CTA is extremely broad: from understanding the role of relativistic cosmic particles to the search for dark matter [8].

2.1.1 CTA Performance

CTA will cover energies from few tens of GeV up to few hundreds of TeV with very high sensitivity, making a big step forward compared to current experiments. The performances that follow are obtained by detailed Monte Carlo simulations [48].

The expected CTA *differential sensitivity* is reported in Figure 2.1, and it is defined as the minimum flux required to obtain a 5-standard-deviation detection of a point-like source in a 50 hour observation [48]. The sensitivities of the three main IACT experiments currently operating (MAGIC, VERITAS, H.E.S.S.) and the 10 year Fermi-LAT and 5 year HAWC sensitivities are shown for comparison. With CTA there will be an increase of an order of magnitude regarding sensitivity, when compared to current IACT facilities. In the lower energy range the IACT sensitivity is limited by background noise, while in the higher range by the low gamma-ray flux.

There will also be a clear improvement in *angular resolution*, as we can see in Figure 2.2 [48]; this quantity is defined as the angle in which 68 % of reconstructed gamma rays fall, in relation to their true direction.

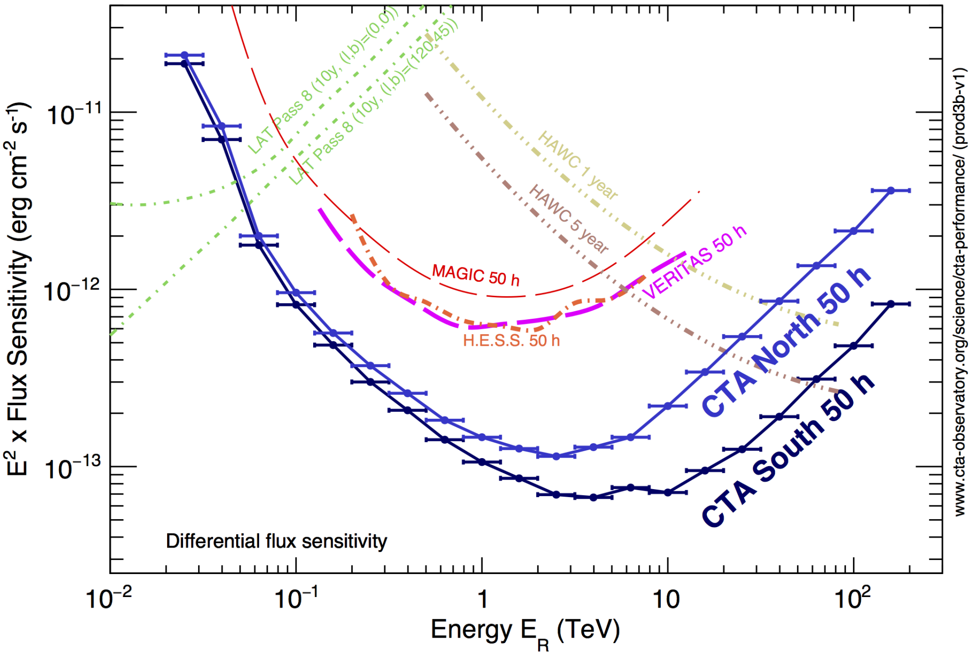

Figure 2.1: CTA differential flux sensitivity compared to other experiments [48]

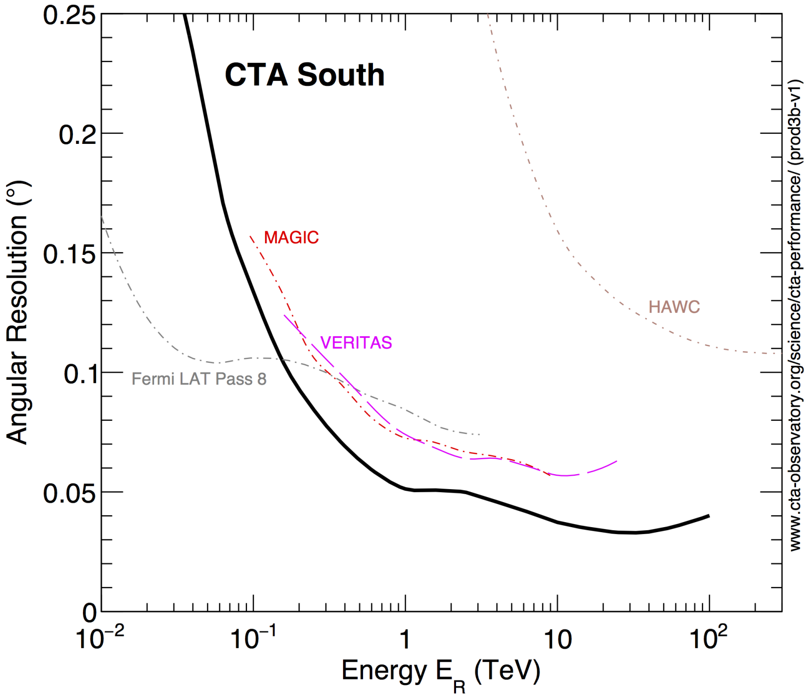

Figure 2.2: CTA angular resolution compared to other experiments [48]

2.1.2 Telescopes

CTA will consists of three different telescope types, which cover gradually higher energies: Large Size Telescopes (LSTs), Medium Size Telescopes (MSTs) and Small Size Telescopes (SSTs).

As the energy of the primary gamma-ray increases, the number of Cherenkov photons produced in the electromagnetic shower increases, so a smaller mirror is sufficient to collect enough light. On the other hand, in order to be sensitive to primary gamma rays of lower energy it is necessary to use larger telescope mirrors. Moreover, since the gamma-ray flux decreases as the energy of the gamma ray increases, it is fundamental for the telescopes sensitive to the highest energy to cover a wider area: for this reason the small telescopes are distributed over a wider array than that of the large ones. We will discuss in detail the three types of telescope in the section 2.3.

Figure 2.3 shows the CTA differential sensitivity for the three different telescope types, derived from detailed Monte Carlo calculations and standard data analysis techniques [50]. As already discussed, the first part of the gamma-ray energy range is dominated by the LSTs, while as the gamma-ray energy increases, the MSTs and then the SSTs become dominant. From this plot we can understand that the slight difference in sensitivity in the higher energy rage between the CTA North and CTA South Array in Figure 2.1 is due to the absence of the small telescopes in the north.

2.1.3 Locations

The CTA Observatory will consist of two sites, one in the southern and one in the northern hemisphere, in order to allow full-sky coverage and, consequently, access to more potential gamma-ray sources, to rare source classes and to rare events, such as VHE-rich GRBs or supernova explosions [50]. From now on they will be called CTA South and CTA North respectively. The chosen site for CTA North is Roque de los Muchachos, La Palma Island, where the MAGIC experiment is still operating (Figure 2.4), while CTA South will be built in Chile, less than 10 km southeast of the European Southern Observatory's (ESO's) in the Atacama Desert (Figure 2.5). The southern site covers the central part of the Galactic plane and sees many nearby Galactic sources, some of which may produce PeV cosmic rays: thus it is designed in order to cover the highest possible energies. The northern site will see only a small fraction of the Galactic plane, so covering the highest energies is not such

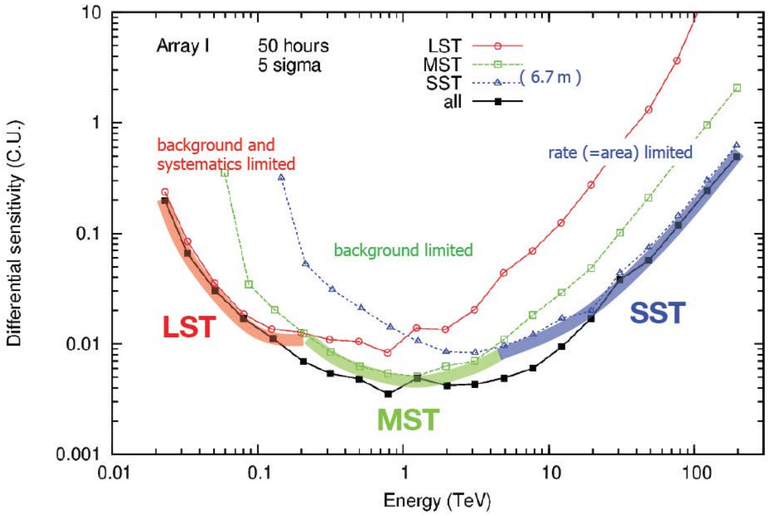

Figure 2.3: CTA differential sensitivity (in Crab Nebula units) [50]

a fundamental requirement; the gamma-ray absorption in the Universe increases as the energy of the gamma ray increases: therefore the study of the most energetic part of the spectrum is more interesting for nearby sources. For these reasons only the southern site will host the SSTs. The proposed layouts for the full arrays in the northern and southern hemisphere arrays are illustrated in Figure 2.6; in the full array configuration, CTA North will be equipped with 4 LSTs and 15 MSTs, while CTA South will host 4 LSTs, 25 MSTs and 70 SSTs. Recent agreements fixed an initial, "alpha", configuration of 4 LSTs plus 9 MSTs in the northern hemisphere and 14 MST plus 37 SST in the southern one.

Figure 2.4: Rendering of the Northern Site [48]

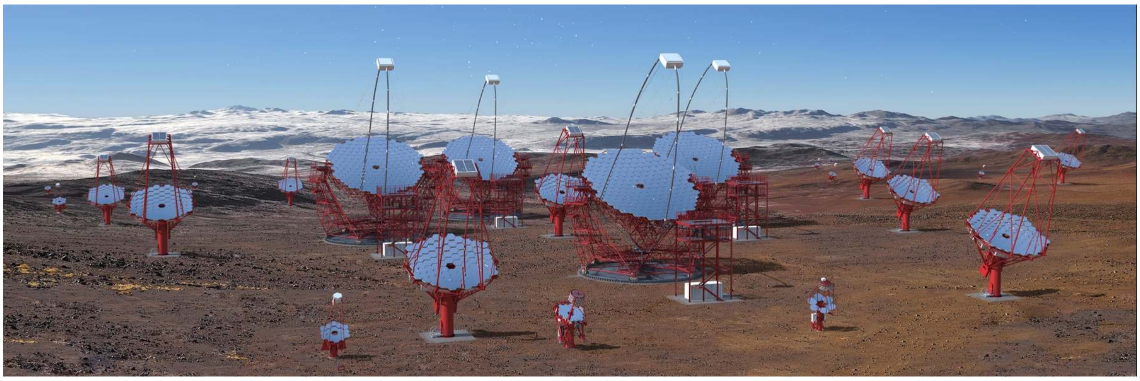

Figure 2.5: Rendering of the Southern Site [48]

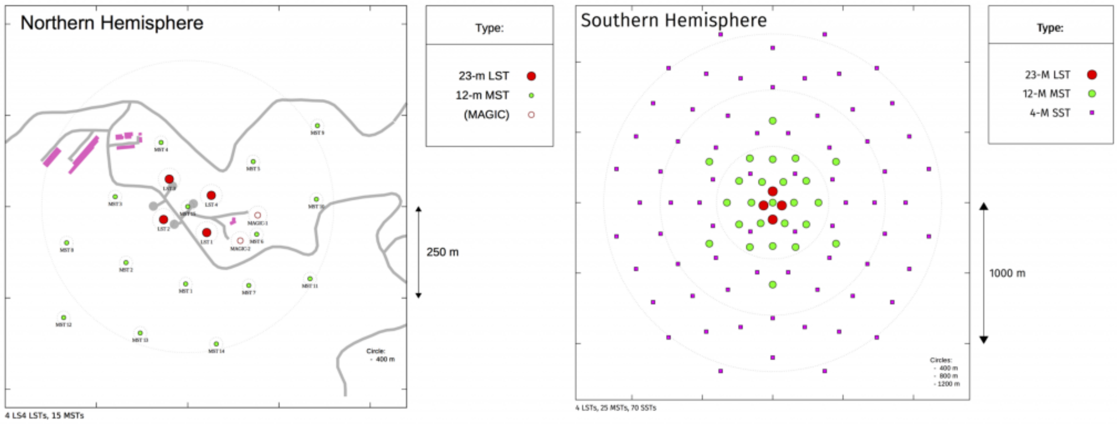

Figure 2.6: Proposed layouts of the northern and southern arrays [48]

2.1.4 State of the LST Project

The first CTA telescope (the first LST in the North Site, LST-1) was inaugurated on October 10th 2018, and now it is in the commissioning phase. A picture of the Northern Site is shown in Figure 2.7, where it's clearly visible the LST-1 close to the two MAGIC telescopes.

A picture of the PMT-based camera, mainly assembled at the Institut de Física d'Altes Energies (IFAE), Barcelona, Spain is shown in Figure 2.8a. The picture was taken in June 2018 at IFAE, during its assembly. The modules consisting of 7 PMT-pixels each are clearly visible, as well as the partially mounted light guides. One of these modules is visible in Figure 2.8b. At the time being the LST-1 is under commissioning phase.

Figure 2.7: The MAGIC and CTA site at Roque de Los Muchachos

(a) **(b)**

Figure 2.8: (a) LST PMT-based camera during during its assembly at IFAE, Barcelona
(b) A PMT module with its light guides

2.2 Science Themes

High energy primary gamma-ray initiated air showers are of particular interest to cosmic ray physicists, astrophysicists and cosmologists because gamma rays, unlike charged particles, are not deflected by the magnetic fields in the Galaxy and beyond. Moreover, as a key member of the suite of new and upcoming major astroparticle physics experiments and observatories, CTA will exploit synergies with gravitational wave and neutrino observatories as well as with classical photon observatories. Thanks to these characteristics CTA will be able to study a wide range of physical phenomena [8]:

- Understanding the Origin and Role of Relativistic Cosmic Particles
  - Identifying and studying the sites of high-energy particle acceleration in the universe
  - Studying the mechanisms for cosmic particle acceleration
  - Studying the role played by accelerated particles in star formation and evolution of galaxies
- Probing Extreme Environments
  - Studying the physical processes that are at work close to neutron stars and black holes
  - Studying the characteristics of relativistic jets, pulsar winds and stellar explosions
  - Understanding how intense are radiation fields and magnetic fields in cosmic voids, and how these evolve over cosmic time
- Exploring Frontiers in Physics
  - Studying the nature and the distribution of dark matter
  - Finding any possible quantum gravitational effects on photon propagation
  - Finding any possible axion-like particles

2.2.1 Understanding the Origin and Role of Relativistic Cosmic Particles

The primary goal of gamma-ray astrophysics until now has always been the identification of the cosmic sources in which particle acceleration takes place. In the last decade huge progress has been made in this area, thanks to the combination of Fermi-LAT and IACT data; however there are some question that still need to be answered, such as [8]:

- Are supernova remnants (SNR) the only major contributor to the Galactic cosmic rays?
- Where in our galaxy are particles accelerated up to PeV energies?
- What are the sources of high-energy cosmic electrons?
- What are the sources of the ultra-high energy cosmic rays (UHECRs)?

2.2.2 Probing Extreme Environments

Particle acceleration to very high energies typically takes place in extreme environments, such as those close to neutron stars and black holes, or in relativistic outflows or explosions: VHE emission from accelerated particles can therefore act as a probe of these environments. Three key areas within this theme where CTA data will be determining are [8]:

- Black holes and jets
- Neutron stars and relativistic outflows
- Cosmic voids

Black Holes and Jets

Active galactic nuclei are thought to host supermassive black holes, accreting material and producing collimated relativistic outflows by a still poorly-understood process. Similarly, accreting stellar mass black holes are known to produce jets, and particle acceleration seems to be universally associated with these systems.

Moreover, the discovery of gravitational wave (GW) emission associated with the mergers of massive black holes [51, 52, 53] gives us many new possibilities in observational astrophysics and in the study of the evolution of high mass binary systems [8].

Neutron Stars and Relativistic Outflows

CTA will probe the environment around neutron stars via pulsed gamma-ray emission from the magnetosphere of pulsars and analyze these systems studying for example the associated synchrotron/inverse-Compton nebula.

Furthermore binary systems including a pulsar provide a unique opportunity to study a relativistic outflow under changing physical conditions as the orbit progresses, thanks to energy-dependent light-curve measurements [8].

Cosmic Voids

Cosmic voids are extremely under-dense regions forming a large fraction of the universe. The radiation fields and the magnetic fields contained in such voids can be probed via the high energy photons that interact with these regions.

It is known that in these spaces between galaxy clusters we can find the *Extragalactic Background Light* (EBL), i.e. the integrated emission from stars and galaxies throughout the evolution of the universe, which is an important tool for cosmology; unfortunately due to the strong light background it is very difficult to measure it directly. However when a VHE gamma rays interacts with the EBL, a gamma-gamma pair production is possible: thanks to this process the EBL leaves an imprint on the measured spectra of gamma-ray sources and therefore the EBL can be more easily studied [8].

2.2.3 Dark Matter

Nature of Dark Matter

Alongside the scientific topics discussed before, CTA will play an important role in the study of fundamental physics, mainly for the search of *dark matter* and *axion-like particles.*

The nature of dark matter is one of the most important open questions for modern physics. On scales from kpc to Mpc there are numerous evidences for the existence of an unknown form of gravitating matter that is not described in the Standard Model of particle physics. This unknown matter is estimated to be dominant with respect to the baryonic matter, since the first one composes about 27 % of the total universe energy budget, while the second one only the 5 %.

Although there are many gravitational evidences for dark matter, its nature is still unknown. From cosmological calculations we obtain that the particles constituting the dark matter had to be moving non-relativistically when they stopped scattering in the early universe: thus the term *cold dark matter* (CDM). One of the most popular scenarios for CDM is that of the WIMPs, i.e. a non-baryonic and collisionless fluid of *cold* and *weakly interacting massive particles.* To be dark matter, a WIMP must have an average annihilation cross-section of $\langle \sigma v \rangle = 3 \times 10^{-26}\,\mathrm{cm}^3/\mathrm{s}$. Moreover, dark matter particles must be neutral both in charge and in color and stable on cosmological time scales [8].

In the Standard Model there is no particle that has the required properties; however theories beyond the Standard Model, built mainly to solve problems related to particle physics, such as the unification of couplings at high energy, have dark matter candidates. For the time being the most promising candidates for WIMPs come from the supersymmetric (SUSY) and extra-dimensional theories; some of these candidates are the lightest neutralino (SUSY), the first Kaluza-Klein excitation of the $B^{(1)}$ boson and the neutrino $\nu^{(1)}$ (extra-dimensional theories). Moreover, axion-like particles are popular candidates too [54].

Search Methods for Dark Matter

There are four different and complementary approaches to look for non gravitational evidence of dark matter [8]:

- Direct-detection
- Indirect-detection
- Collider experiments
- Astrophysical probes sensitive to non-gravitational interactions of dark matter

The direct-detection method looks for interactions of dark matter particles embedded in the Milky Way's dark matter halo in Earth-based detectors [55], while the indirect one looks for secondary particles emanating from dark matter annihilations or decays. Collider experiments have searched (and are nowadays searching) evidence of Dark Matter in the latest decays; many searches were carried out for example at the LEP, TeVatron and LHC colliders, and all have led to negative results but have put strong constraints on these particles. As regards the last point, non-gravitational interactions of dark matter can for example alter the cooling rate of stars [8]. The indirect method, the one that will be pursued by CTA, looks for the cosmic radiation emitted from annihilation of pair of WIMPs in region of the Universe with high dark matter density; indeed in term of WIMPs, dark matter particles can self-annihilate and give origin to Standard Model Particles. CTA will be able to detect high energy photons, and indirect detection of dark matter annihilations through gamma rays has attracted much interest due to several unique properties this particles; for example, since they are neutral, they point back to the source (where the annihilation of dark matter took place).

These different search methods are sensitive to different couplings, different masses and different dark matter candidates: thus they are complementary and essential for a complete understanding of the nature of dark matter. In Figure 2.9a is reported a comparison of models from the phenomenological minimal supersymmetric model (pMSSM) surviving or being excluded by direct-detection, indirect-detection and collider searches in the plane of scaled spin-independent cross-section versus lightest supersymmetric particle (LSP) mass.

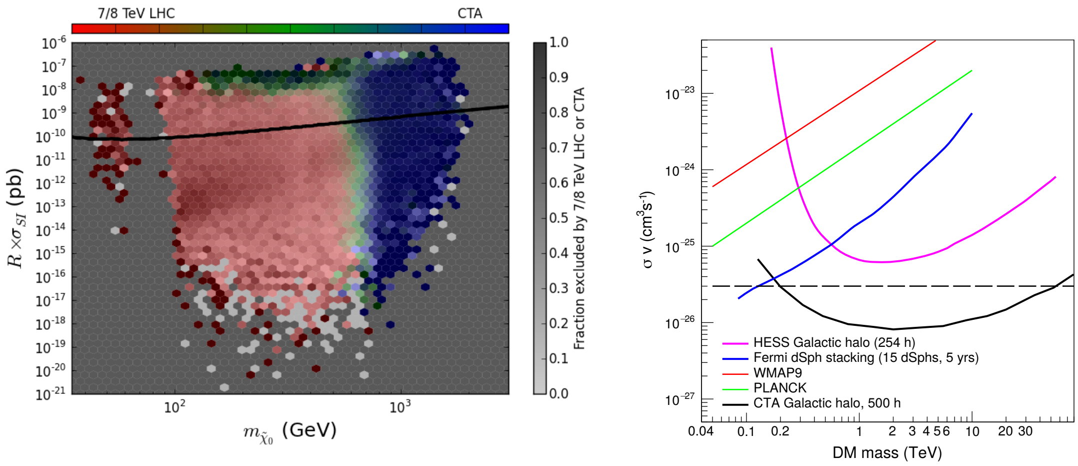

(a) **(b)**

Figure 2.9: (a) Survival and exclusion rates from various searches [56]
(b) Current best limits on the annihilation cross section compared to the projected sensitivity for CTA from observations of the Galactic halo for the Einasto profile and W^+W^- channel [8]

The spin-independent XENON1T exclusion is shown as a solid black line, while the models accessible to CTA and LHC are shown respectively in blue and red [56]; it is clear that CTA dominates for large LSP masses. In Figure 2.9b are shown the current best limits on the annihilation cross-section from indirect detection (Fermi-LAT [57] and H.E.S.S. [58]) and cosmic microwave background experiments (WMAP and Planck [59]) compared to the projected sensitivity for CTA from observations of the Galactic halo for the Einasto profile and W^+W^- channel [8].

CTA Strategy

There are several targets for the indirect search of dark matter with CTA; the most promising are [8]:

- Milky Way
- Dwarf Spheroidal Galaxies
- Large Magellanic Cloud
- Clusters of galaxies

While in the past the center of the *Milky Way* was considered as the target for dark matter searches, now the searches focus on the Galactic halo excluding the central region, because of the rich field of VHE gamma-ray astrophysical sources in the region; the inconvenience is that it is a diffuse source, the integration of the flux gives a huge instrumental background; anyway most of this background comes from known sources, so it can be relatively easy to remove it. [8].

The *Dwarf Spheroidal Galaxies* (dSphs) are galaxies where the amount of dark matter is estimated to be $\sim 10^3$ times the amount of ordinary matter, they are promising targets as well.

The *Large Magellanic Cloud* (LMC) is a nearby satellite galaxy, at a distance of only $\sim 50\,\text{kpc}$, and with a dark matter mass of $\sim 10^{10} M_\odot$. Since it is an extended source for CTA, also for the LMC the background is a challenging problem.

Clusters of galaxies are the largest and most massive gravitationally bound systems in the universe, with radii of a few Mpc and total masses of $10^{14} - 10^{15} M_{\odot}$. Since they present very high mass-to-light ratio environments they are considered as promising targets for indirect dark matter searches.

2.2.4 Quantum Gravity and Axion-like Particle Search

CTA will give an exciting possibility of detecting *axion-like particles* (ALPs) and finding evidence of *Lorentz Invariance Violation* (LIV) associated with possible *quantum gravity* effects on space-time at the Planck scale. The most promising target classes for both these searches are known to be blazars and Gamma-Ray Bursts (GRBs). Quantum gravity effects may induce time delays between photons with different energies traveling over long distances [8].

Besides being a candidate for CDM, axion-like particles (ALP) are a possible solution to the strong-CP problem of quantum chromodynamics. In presence of a strong magnetic field, a gamma ray can convert into an ALP, and in the same condition an ALP can convert into a gamma ray: thus the ALP/photon coupling can result in a detectable enhancement of the TeV photon flux [8].

2.2.5 Synergies

CTA will have important synergies with many of the new generation of astronomical and astroparticle observatories. The need for (simultaneous) multi-wavelength (MWL) and multi-messenger (MM) observations has been considered as a key factor in the site selection process for CTA and in the preparations for CTA science. MWL and MM studies using CTA can improve the knowledge of two main science cases [8]:

- Non thermal emission, to understand the origin of cosmic rays and the environments that produce them
- Source properties, such as the study of Gamma-Ray Bursts

The main areas in which synergies exists are:

- Radio to (Sub)Millimeter
- Infra-red/Optical through Ultra-violet and Transient Factories
- X-ray
- Sub-VHE Gamma-ray Energies
- VHE and UHE Neutrinos
- Gravitational Waves

A great example of the effectiveness of the multi-messenger approach was the observation of a flaring blazar coincident with high-energy neutrino IceCube-170922A, where the joint analysis allowed to establish that blazar jets may accelerate cosmic rays to at least several PeV [60].

Another great evidence of its goodness was the first Teraelectronvolt observation of a gamma-ray burst (GRB190114C), seen on ground by the MAGIC telescopes after a trigger from space experiments ([3, 61]). The multi-wavelength study of this phenomena was one of the greatest results for the understanding of these astrophysical phenomena.

2.3 Telescopes

As already mentioned, CTA will consist of three different telescope types, referred to as Large, Medium and Small Size Telescope. Two different kinds of Medium Size Telescope are under study, a Davies-Cotton [62] and a Schwarzschild-Couder [63, 64] design; there's the possibility that CTA-South will host both.

2.3.1 Large Size Telescope

The LST will have the best sensitivity in the lower energy range, i.e.:

$$E_\gamma = 20\,\mathrm{GeV} - 150\,\mathrm{GeV}$$

A computer rendering of the Large Size Telescope is reported in Figure 2.10a.

The lower structure of the telescope is made of steel tubes, while the dish structure is made of carbon fiber reinforced polymer (CFRP), steel and aluminum tubes. This structure runs on a circular rail. The Camera Support Structure is based on an almost parabolic arch geometry design, mainly built using CFRP. On the top of the arch it is mounted the Camera Frame, which has the aim to hold properly the almost 2 t camera.

Cherenkov light is reflected thanks to a tessellated mirror dish of 23 m diameter (about $400\,\mathrm{m}^2$ of area) and 28 m of focal length, composed of 198 hexagonal mirrors, each one with a surface of $2\,\mathrm{m}^2$. The reflector is equipped with an Active Mirror Control system and all the mirrors are specially coated in order to best fit the project requirements.

The camera is composed of 265 PMT modules with 7 PMTs each, for a total of 1855 PMTs; the selected photomultipliers are the Hamamatsu R11920-100. The camera also hosts the control, readout and trigger electronics [65].

Despite its large size, the low weight allows the telescope to rotate 180° in about 20 seconds, essential for fast repositioning to any position in the sky (e.g. for a Gamma-Ray Burst or any other transient alert).

The main parameters of the LST are reported in Table 2.1 [48].

Table 2.1: LST main parameters [48]

LST main parameters	
Optical Parameters	
Reflector type	1-mirror, parabolic
Focal length	28 m
Dish diameter	23 m
Mirror effective area	$370\,\mathrm{m}^2$
Camera Parameters	
Camera dimensions $L \times H \times W$	$2.8\,\mathrm{m} \times 2.9\,\mathrm{m} \times 1.15\,\mathrm{m}$
Weight	$< 2\,\mathrm{t}$
Number of pixels	1855
Pixel size	0.1°
Camera field of view	4.3°
Sampling speed	1 GS/s
Mechanical Parameters	
Total weight	103 t
Repositioning time	30 s

2.3.2 Medium Size Telescope

The Medium Size Telescopes will provide the necessary sensitivity for CTA in the core energy range:

$$E_\gamma = 150\,\mathrm{GeV} - 5\,\mathrm{TeV}$$

A computer rendering of the Medium Size Telescope is shown in Figure 2.10b.

The structure of telescopes is made of steel; the $\simeq 12\,\mathrm{m}$ diameter mirror will have two different camera designs (*FlashCam* and *NectarCAM*) which use PMTs. The optics of the MST is based on a modified Davies-Cotton design; the dish has a radius of curvature of 19.2 m and a focal length of 16 m. Camera demonstrators have been built and tested in parallel by the two camera sub-projects [48]. The main parameters of the MST are reported in Table 2.2.

Table 2.2: MST main parameters [48]

MST main parameters		
	FlashCam	*NectarCam*
Optical Parameters		
Optical design	Modified Davies-Cotton	
Focal length	16 m	
Dish diameter	11.5 m	
Mirror effective area	$88\,\mathrm{m}^2$	
Camera Parameters		
Number of pixels	1764	1855
Pixel size	0.17°	0.17°
Camera field of view	7.5°	7.7°
Mechanical Parameters		
Total weight	82 t	
Repositioning speed	90 s	

2.3.3 Schwarzschild-Couder Telescope

The Schwarzschild-Couder Telescopes are a dual-mirror version of the MSTs, proposed as an alternative type for the medium size telescopes, so they also offer the best sensitivity in the energy range:

$$E_\gamma = 150\,\mathrm{GeV} - 5\,\mathrm{TeV}$$

They are designed to better focus the light for greater imaging detail and improved detection of faint sources. They have a huge amount of pixels (more than 11 000), so they offer the opportunity for a higher angular resolution when compared to MSTs. They can cover approximately 8 degree field of view. Unlike the MSTs, their cameras are based on Silicon Photomultipliers (SiPMs).

The main parameters of the SCT are reported in Table 2.3, and a computer rendering of the SCT is shown in Figure 2.10c [48].

Table 2.3: SCT main parameters [48]

SCT main parameters	
Optical Parameters	
Optical design	Schwarzschild-Couder
Primary reflector diameter	9.7 m
Secondary reflector diameter	5.4 m
Focal length	5.6 m
Mirror effective area	$41\,\mathrm{m}^2$
Camera Parameters	
Number of pixels	11 328
Pixel size	0.067°
Camera field of view	7.6°
Mechanical Parameters	
Total weight	80 t
Repositioning speed	90 s

2.3.4 Small Size Telescope

The smaller telescopes are the ones that will focus on the higher energy range [48]:

$$E_\gamma = 5\,\mathrm{TeV} - 300\,\mathrm{TeV}$$

Three different SST structures were proposed: one single-mirror design (SST-1M) and two different dual-mirror designs (ASTRI-Horn and CHEC). A harmonization process completed in 2019 established the final structure of the SSTs, which is based on the ASTRI and CHEC design. The design is a dual-mirror Schwarzschild-Couder aplanatic configuration, and its camera uses SiPMs as light detectors. The SST main parameters can be found in Table 2.4, and a computer rendering in Figure 2.10d.

Table 2.4: SST main parameters [48]

SST main parameters	
Optical Parameters	
Optical design	Schwarzschild-Couder
Primary reflector diameter	4.3 m
Secondary reflector diameter	1.8 m
Focal length	2.15 m
Mirror effective area	$8\,\mathrm{m}^2$
Camera Parameters	
Number of pixels	2048
Pixel size	0.16°
Camera field of view	8.8°
Mechanical Parameters	
Total weight	19 t
Repositioning speed	60 s

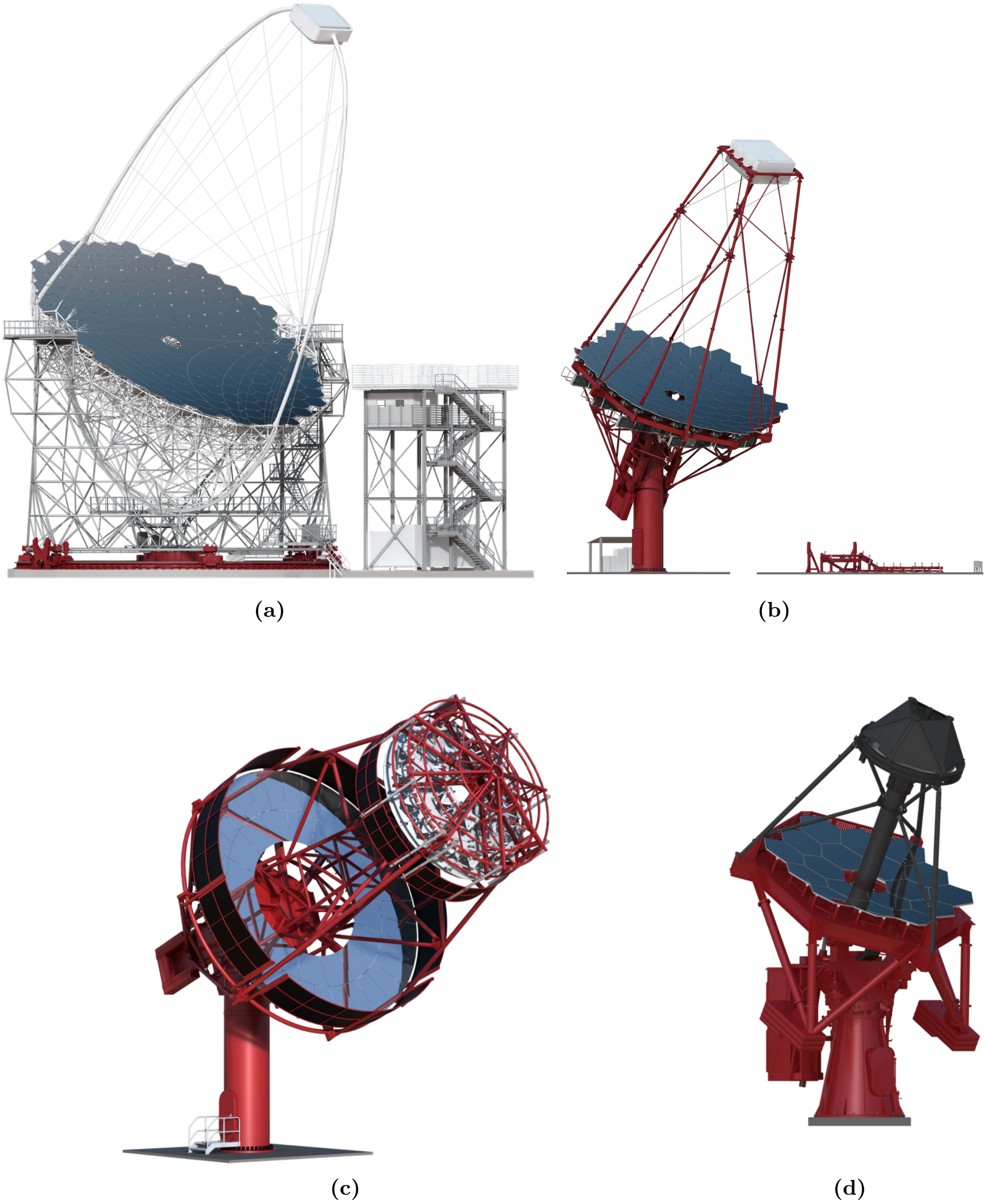
(a) (b)

(c) (d)

Figure 2.10: Computer rendering of the CTA Large Size Telescope (a), of the CTA Medium Size Telescope (b), of the Schwarzschild-Couder Telescope (c) and of the Small-Sized Telescope (d) (picture not in scale) [48]

Chapter 3

Silicon Photomultipliers

3.1 PN Junction

3.1.1 Intrinsic and Extrinsic Silicon

Pure crystalline silicon, referred as *intrinsic*, has a stable equilibrium of negative and positive charge carriers (respectively electron e^- and holes h); this state has no global charge and has quite high resistance: for these reasons it is not suitable for efficient charge collection [66].

Introducing impurities in an intrinsic silicon it is possible to modify its electrical properties; this state is called *doped* silicon. Two types of doping are possible, one with *donor* impurities (*n-type doping*) and another with *acceptor* impurities (*p-type doping*).

When a semiconductor is doped with one of these impurities, impurity energy levels are introduced in the intrinsic device; in a general way it is possible to distinguish the two types of impurities as follows: a donor impurity has a donor level which is defined as being neutral if filled by an electron, and positive if empty, while an acceptor level is neutral if empty and negative if filled by an electron [67].

Considering silicon, which has four electrons in the outermost electron shell, donor impurities are electron donors, i.e. atoms of group V elements (like Phosphorus or Arsenic) with five electrons in their more peripheral electron shell, while acceptor impurities are electron acceptors, i.e. atoms of group III elements (like Boron or Aluminum) with only three electrons in their more external electron shell.

A donor atom can share four of its more peripheral electrons to form a covalent bond with neighboring silicon atoms, and participate in the crystal lattice structure by donating its fifth outermost electron to the so called *conduction band*, i.e. the electronic band with lower energy among those not fully occupied, where an electron can freely move from one atom to another in the crystal lattice. An acceptor atom can share three of its outermost electrons with neighboring silicon atoms, and take part in the silicon lattice accepting an electron and therefore introducing a hole in the *valence band*, i.e. the electronic band with higher energy among those fully occupied, where a hole can move from one atom to another in the silicon lattice. Thanks to the presence of these charge carriers (e^- in the conduction band and h in the valence band), the electrical resistivity of the doped regions is lower than that of the intrinsic silicon [66, 67].

3.1.2 PN Junction at Equilibrium

If the same silicon is doped with donor in one region and with acceptor in one other, the interface between these two regions is called *PN junction.* As soon as this interface is formed, in order to reach electrical equilibrium, electrons from the n-side tend to diffuse to the p-side (leaving behind themselves positively charged atoms), while holes from the p-side diffuse to the n-side (leaving behind themselves negatively charged atoms). Moreover, when an electron and a hole interact with each other, they recombine and their charge is neutralized; the layer adjacent the junction is thus depleted from majority carriers (e^- in the n side and h in the p side), giving rise to the so called *depletion layer*. Since the ionized donor or acceptor atoms are immobile, the n-side of the depletion layer becomes positively charged, while the p-side negatively charged. These charges cause the formation of an electric field across the depletion layer that points from the n-side to the p-side and reaches its maximum value at the PN junction (where distance between opposing charges is minimal). During its formation, the electric field exerts a force on diffusing carriers, rejecting electrons from the p-side and the holes from the n-side of the depletion layer: this force is in the opposite direction of the carrier migration that generated this electric field and thus an equilibrium is achieved [66, 67]. A simple representation of a PN junction under equilibrium is reported in Figure 3.1.

3.2 Photodiodes

3.2.1 Unity-Gain Si Photodiodes

An external source of energy (e.g. *thermal agitation* or *photoelectric effect*) can give the sufficient energy to an electron in the depletion layer to pass from the valence band to the conduction band, leaving a hole in the latter. These electrons and holes are electrically compensated by each other and are considered to be excess charge carriers; in literature they are defined as *electron-hole pair*. A simple representation of this phenomenon is shown in Figure 3.2, where the electron-hole pair is formed by an incident photon via photoelectric effect.

Due to the presence of the depletion layer's electric field, as soon as the pair is formed, each carrier type drifts in the opposite direction towards its majority side (N for electrons and P for holes). Indeed the electron drifts in the opposite direction of the field, i.e. towards the n-side, while the hole drifts towards the p-side: this motion causes a net current across the junction. It is trivial that in this process only minority carriers (electrons generated in the depletion layer's P side and holes generated in the layer's N side) drift across the junction to arrive at the depletion layer's outer edges; majority carriers (electrons generated in the layer's N side and holes generated in the layer's P side) do not cross the junction but drift to reach the layer's outer edges.

When the excess charge carriers reach the external edge of the depletion layer, the electrons accumulate in the N region and the holes in the P one. However, if a current loop is formed between the outer side of the PN junction, the electrons and holes accumulated can travel in that loop to the opposite regions in order to recombine. Thus if the depletion layer is exposed to a flow of photons in which their energy exceeds that of the Si band gap (i.e. 1.14 eV) it is possible to observe a net current in the loop; this current is referred to as *photoelectric current*. Instead if the source of energy is thermal agitation this charge flow is commonly referred as *dark current* [66, 67].

3.2.2 Avalanche Photodiodes

When an external voltage source is applied to a PN junction, it is possible to modify the electrical characteristics of the device. It is said that a PN junction is reversely polarized if a voltage bias is applied connecting the p-type region to the negative terminal and the n-type to the positive one, as reported in Figure 3.3.

Indeed since the p-type region is connected to the negative terminal of the power supply, the holes in this region are taken away, leaving behind charged ions which cause the depletion region to increase. A similar but complementary process takes place in the

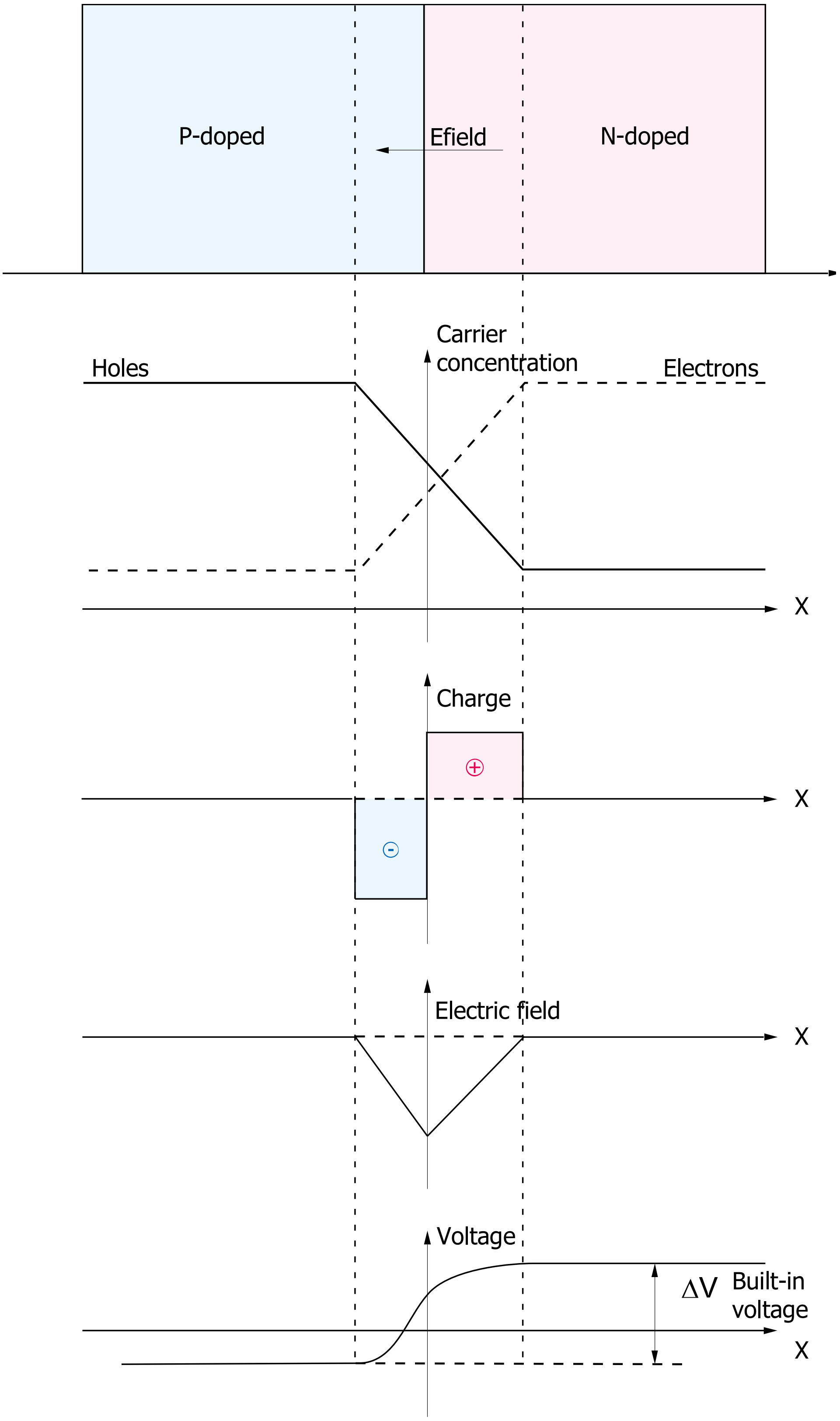

Figure 3.1: PN junction under equilibrium [66]

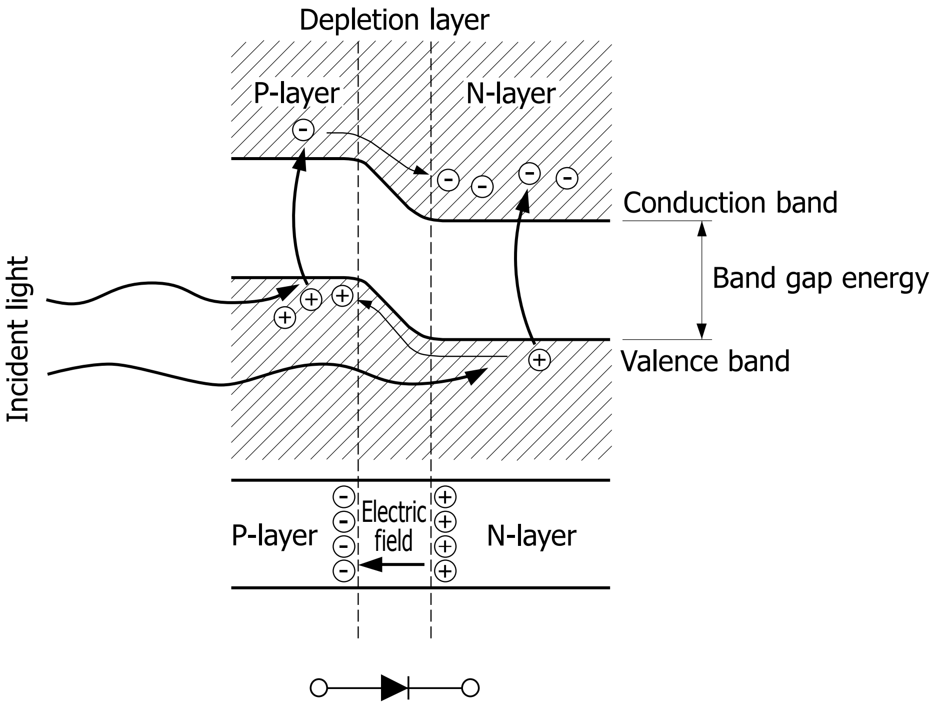

Figure 3.2: Silicon energy levels and electron-hole pair generation [66]

n-type region. The increase in width of the depletion region causes the increase of the electric field in the junction and thus the electric force applied to charge carriers.

This force accelerates the carriers, increasing their velocity and kinetic energy, until they collide with atoms in the device, losing energy through thermal vibration of the crystal lattice (referred to as *phonon vibration*). When the voltage exceeds a certain limit value, known as the *breakdown voltage*, a huge current is observed flowing into the device; this process can be clearly observed in the current versus bias voltage plot for a real diode in Figure 3.4. In this situation when an electron-hole pair is formed, each charge carrier is exposed to a high electric field, and during the average travel time in between consecutive collisions it can reach an energy that exceeds the silicon band gap: in this case charge carries can ionize lattice atoms upon impact and generate at least another electron-hole pair in the conduction and valence band respectively. This process is exponential and it is said that the junction breaks down. What is just described is know as *avalanche breakdown*; other types of breakdown are possible, but their treatment is beyond the scope of this thesis.

The breakdown voltage value strongly depends on the diode internal structure, in particular on the width of the depleted region. If, in first approximation, we suppose that inside the depleted region the electric field is constant, as the depleted region width

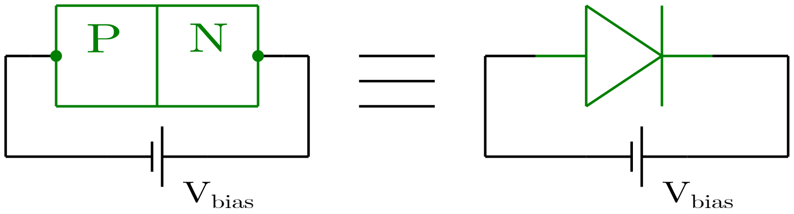

Figure 3.3: Reversely polarized PN Junction

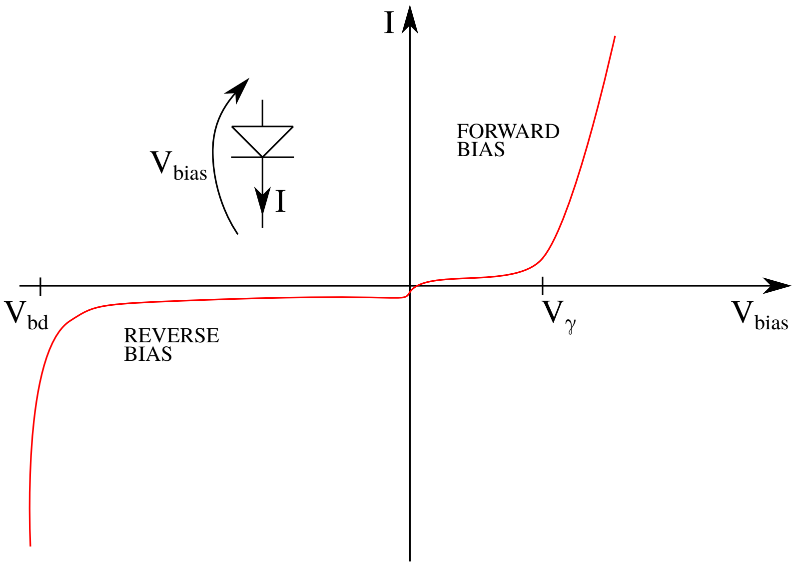

Figure 3.4: I vs V_{bias} plot for a real diode

increases, the possible number of collisions increases. Therefore, a wider depleted region has a lower critical electric field at breakdown. However, since the breakdown voltage is the integral of the electric field over the whole region, despite having a lower peak field, the breakdown voltage is higher if the depleted region is wider [68].

Thanks to the avalanche gain the magnitude of the original photoelectric signal is increased and it can exceed the noise floor, making it possible to be detected. It is trivial that this increase in magnitude is applied also to the thermal generated signals. However, due to the intrinsic randomness of an avalanching multiplication, the internal gain of an Avalanche Photodiode (APD) suffers from random fluctuations, resulting in an additional noise factor.

One peculiar aspect of these devices (and also for the Geiger mode APDs and Silicon Photomultipliers that will be discussed later) is the gain dependency on the wavelength of the incident light. When an electron-hole pair is formed by the photoelectric effect, both charge carriers can participate in the avalanche triggering; however an electron has greater ionization efficiency and hence avalanche probability in silicon than a hole. Therefore the difference in photosensitivity of these devices lies in the travel length that an electron must travel within the depletion layer before being collected; in other words the avalanche probability is higher if the electron-hole pair is generated in the depletion layer's p-side compared to being generated in the n-side. In addition an APD (and thus a GAPD and a SiPM, as we will see) can be fabricated in two different structures: N-on-P or P-on-N. Since the photon absorption in silicon increases as the wavelength decreases, in the N-on-P structure longer light wavelengths create an electron-hole pair in the P region, while in the P-on-N structure, shorter wavelengths create an electron-hole pair also in the P region: therefore P-on-N structure has higher photosensitivity in the UV/blue spectrum region, while N-on-P has higher photosensitivity in the red/NIR spectrum region [66, 69]. A visual representation of absorption of short and long wavelengths of light in a red/NIR-enhanced N-on-P APD structure is reported in Figure 3.5.

Another peculiar characteristic of an APD is its gain dependence on applied reverse voltage. Figure 3.6 shows an example of the gain vs applied reverse voltage plot for an APD. It is possible to distinguish two knees and thus three regions, which reflects the different behavior of the APD with respect to V_{bias}. In the example reported, those distinct behaviors are the first below about 50 V, the second between around 50 V and about 100 V, and the third above 100 V. Only the last two are of interest for a photodiode. While in

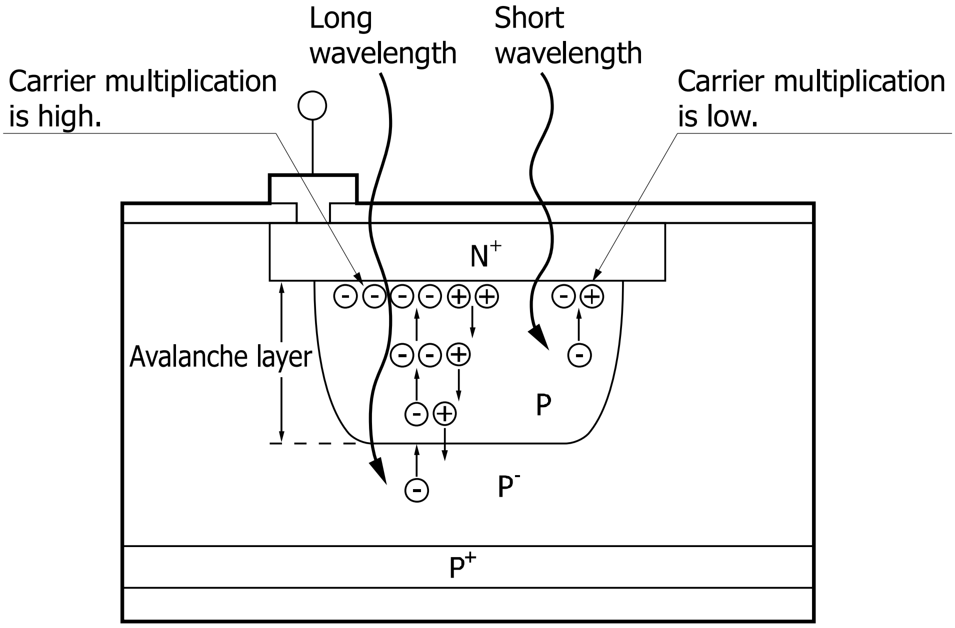

Figure 3.5: Visual representation of absorption of short and long wavelengths of light in a red/NIR-enhanced N-on-P APD structure [66]

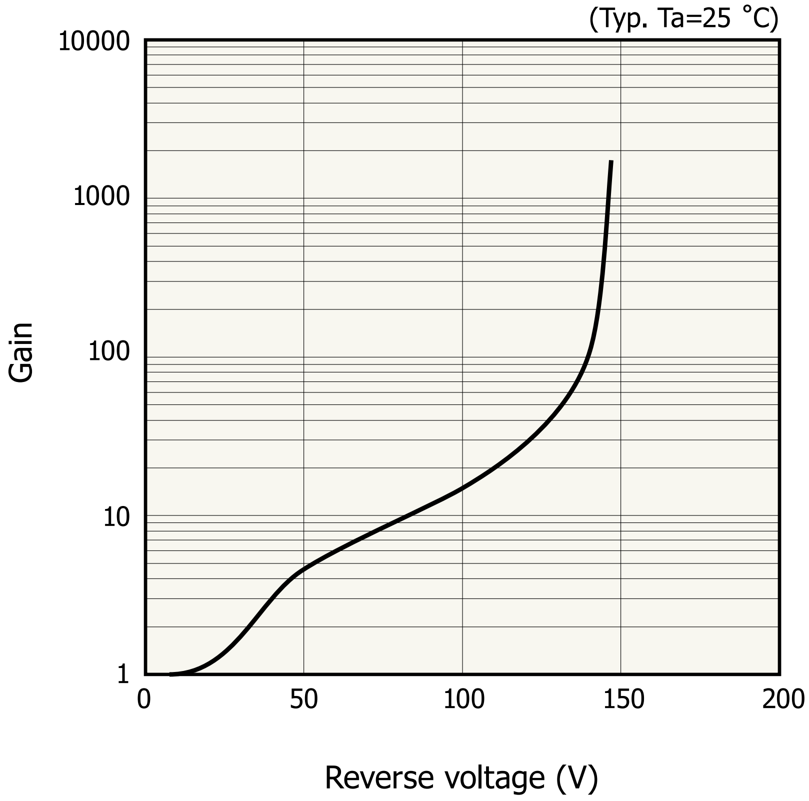

Figure 3.6: Gain vs bias voltage for an APD [66]

the second region the dependency is $\simeq 10^{\alpha V}$, it increases very steeply in the third region.

In a first approximation we can demonstrate that APD's avalanche gain is linear. Let's presume that a single photon generates an initial electron-hole pair, and both the e^- and h have the same probability P to generate a new electron-hole pair. The number of avalanching carriers N_1 resulting by a single-photon triggered avalanche after n iterations of carrier multiplication will be:

$$N_1 = 2 + 2P + 2P^2 + ... + 2P^n = 2 \cdot \sum_{i=0}^{n} P^i \tag{3.1}$$

and, if n goes to infinitive:

$$N_1 = \lim_{n \to \infty} \left(2 \cdot \sum_{i=0}^{n} P^i \right) = 2 \cdot \frac{1}{1-P} \tag{3.2}$$

Instead if the avalanche is triggered by a number m of photons (where $m > 1$):

$$N_m = 2m + 2mP + 2mP^2 + ... + 2mP^n = 2m \cdot \sum_{i=0}^{n} P^i \tag{3.3}$$

and, similarly, if n goes to infinitive:

$$N_m = \lim_{n \to \infty} \left(2m \cdot \sum_{i=0}^{n} P^i \right) = 2m \cdot \frac{1}{1-P} \tag{3.4}$$

Therefore:

$$\frac{N_m}{N_1} = m \tag{3.5}$$

and the response of the device is thus linear. We can furthermore observe from these simple calculations that if $P \to 1$, the APD gain $\to \infty$; this situation can occur under sufficiently-intense E-field. Obviously this is just a rough approximation, since the nature of the APD is more complex [66].

In a more accurate way the APD's gain M as a carrier multiplication factor can be expressed as:

$$M = \frac{(\alpha_e - \alpha_h) \cdot e^{d(\alpha_e - \alpha_h)}}{\alpha_e - \alpha_h \cdot e^{d(\alpha_e - \alpha_h)}} = \frac{1-k}{e^{(k-1)\alpha_e d} - k} \tag{3.6}$$

where α_e and α_h are the ionization efficiencies (probabilities per unit of traveled distance) of avalanching electrons and holes respectively, $k = \frac{\alpha_h}{\alpha_e}$ and d is the thickness of the avalanche layer [66].

3.3 Geiger Mode APDs

Referring to Equation 3.6, if the APD gain $M \to \infty$ the device is said to be in *breakdown*; the reverse bias voltage at which this phenomenon occurs is referred to as the APD's *breakdown voltage.*

In literature an APD that operates with an applied reverse bias voltage higher than the APD's breakdown voltage, is referred to operate in a *Geiger-mode.* This state is the previously mentioned third region in the plot shown in Figure 3.6, where the APD's gain increases steeply with the reverse voltage. In the Geiger-mode the output charge of an avalanche is the same for a given gain, and depends on the reverse bias voltage regardless of the number of the photon that initiated the considered avalanche: this situation is very far from the linear response which was obtained before with the simplistic model. A

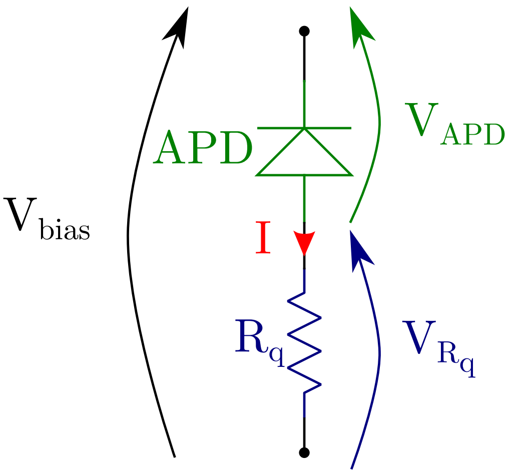

Figure 3.7: Geiger Mode APD

Geiger mode APD (GAPD) is a *digital* photodetector, since its response is binary: signal detection if the device is hit by one or more photons, and absence of signal otherwise.

Moreover, in a Geiger-mode APD the density of avalanching carriers in the depletion region is so high that the device behaves like a conductor with very low resistance under a finite bias voltage. In this situation we have that the avalanching carriers continually generate new electron-hole pairs and thus the avalanche never stops: in order to obtain discrete output pulses it is necessary to quench that current.

That quenching is done in a Geiger Mode APD using a *Quenching Resistor* R_q put in series with the avalanche photodiode APD, as shown in Figure 3.7; this cell is polarized at $V = V_{bias} > V_{bd}$. Before the photon arrival:

$$\begin{aligned} I = 0\,\mathrm{A} \qquad &\Rightarrow V_{R_q} = 0\,\mathrm{V} \\ &\Rightarrow V_{APD} = V_{bias} \end{aligned}$$

The APD is thus polarized at a $V_{APD} > V_{bd}$ and thus it is in the Geiger mode. When a photon hits the APD, there is a certain probability to form a electron-hole pair that can trigger an avalanche; if this occurs:

$$\begin{aligned} I > 0\,\mathrm{A} \Rightarrow\ &V_{R_q} > 0\,\mathrm{V} \\ \Rightarrow\ &V_{APD} = V_{bias} - V_{R_q} \end{aligned}$$

If the voltage across the APD terminations after the photon arrival:

$$V_{APD} = V_{bias} - V_{R_q} < V_{bd} \tag{3.7}$$

the avalanche stops. This happens if:

$$R_q > R_{q,lim} \tag{3.8}$$

where $R_{q,lim}$ is the minimum resistance needed for quenching the avalanche. The current I decreases until $I = 0\,\mathrm{A}$, and the cell returns in the situation where:

$$V_{APD} = V_{bias} > V_{bd} \tag{3.9}$$

i.e. in the Geiger mode; the cell is therefore again ready to detect a new incoming photon.

A more in-depth analysis can be done considering the equivalent circuit of the Geiger mode APD shown in Figure 3.8. Before the arrival of a photon, the switch is open and the capacitor C_d is charged thanks to I. When a photon hits the APD and triggers an

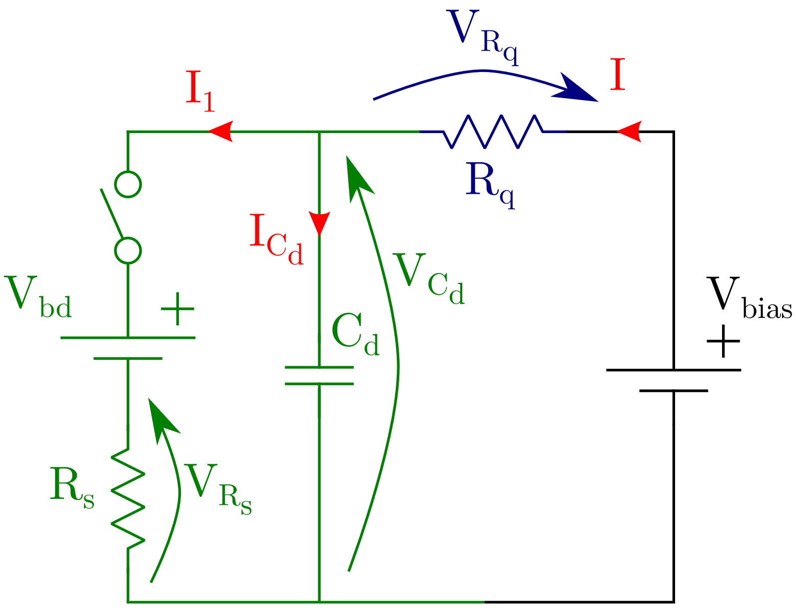

Figure 3.8: A simple Equivalent Circuit of a Geiger Mode APD

avalanche, the switch closes and the current I_1 discharges the capacitor C_d, while I charges it:

$$I = \frac{V_{R_q}}{R_q} = \frac{V_{bias} - V_{C_d}}{R_q}$$

$$I_1 = \frac{V_{R_s}}{R_s} = \frac{V_{C_d} - V_{bd}}{R_s}$$

The avalanche is not quenched while:

$$I > I_1$$

that is:

$$\frac{V_{bias} - V_{C_d}}{R_q} > \frac{V_{C_d} - V_{bd}}{R_s}$$

therefore:

$$R_q < R_s \frac{V_{bias} - V_{bd}}{V_{C_d} - V_{bd}} \triangleq R_{q,LIM} \tag{3.10}$$

Thus I can have a quenching effect only if the quenching resistor:

$$R_q > R_{q,LIM} = R_s \frac{V_{bias} - V_{bd}}{V_{C_d} - V_{bd}} \tag{3.11}$$

The most of the time it is easier to find the value of $R_{q,LIM}$ empirically.

The process just described can be seen on the voltage vs current plot of an APD (Figure 3.9a); keep in mind that now the bias voltage is defined in the opposite direction with respect to the usual definition of a biasing voltage for a common diode. The current signal I from a GAPD will be thus similar to the one reported in Figure 3.9b: it is composed of two exponentials, the rising one with a time constant $\tau_{rise} = R_s C_d$ and the following one with $\tau = R_q C_d$. The peak is when:

$$I = I_{MAX} = I_1 = \frac{V_{C_d} - V_{bd}}{R_s} \tag{3.12}$$

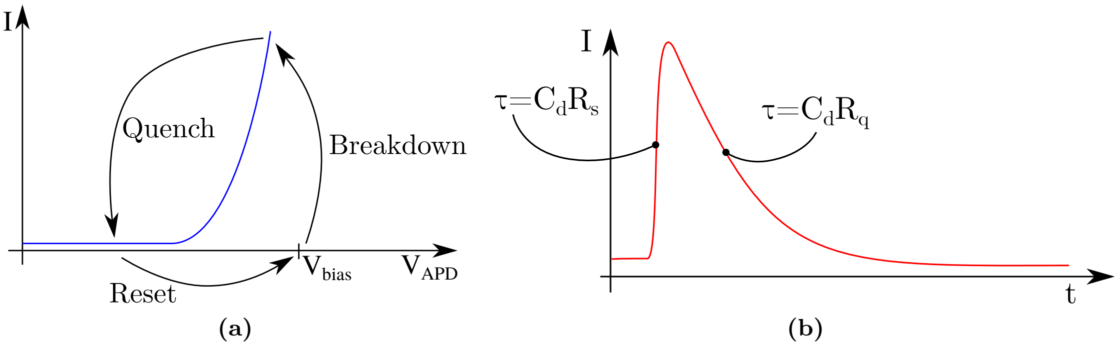

Figure 3.9: (a) Breakdown, quench and reset cycle for a GAPD
(b) Conceptual output pulse of the GAPD equivalent circuit

that is:

$$R_q = R_s \frac{V_{bias} - V_{bd}}{V_{C_d} - V_{bd}}$$
$$\Rightarrow \frac{1}{R_s} = \frac{1}{R_q}\frac{V_{bias} - V_{bd}}{V_{C_d} - V_{bd}}$$
$$\Rightarrow I_{MAX} = \frac{1}{R_q}\frac{V_{bias} - V_{bd}}{V_{C_d} - V_{bd}}(V_{C_d} - V_{bd})$$

Therefore:

$$I_{MAX} = \frac{V_{bias} - V_{bd}}{R_q} \tag{3.13}$$

From these calculations we can observe that the signal peak increases linearly with the applied bias voltage V_{bias}, or with the so called *overvoltage*:

$$V_{OV} \triangleq V_{bias} - V_{bd} \tag{3.14}$$

Please bear in mind that the equivalent circuit just mentioned is only a simple approximation of a real GAPD.

3.4 Silicon Photomultipliers

A *Silicon Photomultiplier*, often abbreviated as *SiPM*, is a common bias and common output array of Geiger mode APDs connected in parallel and fabricated on the same monolithic silicon crystal. A conceptual schematic of a SiPM is reported in Figure 3.10a. The cells which compose it are clearly visible with a SEM microscope, as shown in Figure 3.10b.

Being an array of single digital photodetectors, these sensors are capable of measuring the number of photons hitting their surface with exceptional accuracy. Their discrete behavior can be easily seen from their output signal; as an example, in Figure 3.10c it is reported the signal produced by a 1 mm × 1 mm Advansid NUV SiPM. We have to keep in mind that increasing the sensor area (and thus its capacitance) worsens the photoelectron separation.

In this section we will briefly deal with the main characteristics of these sensors.

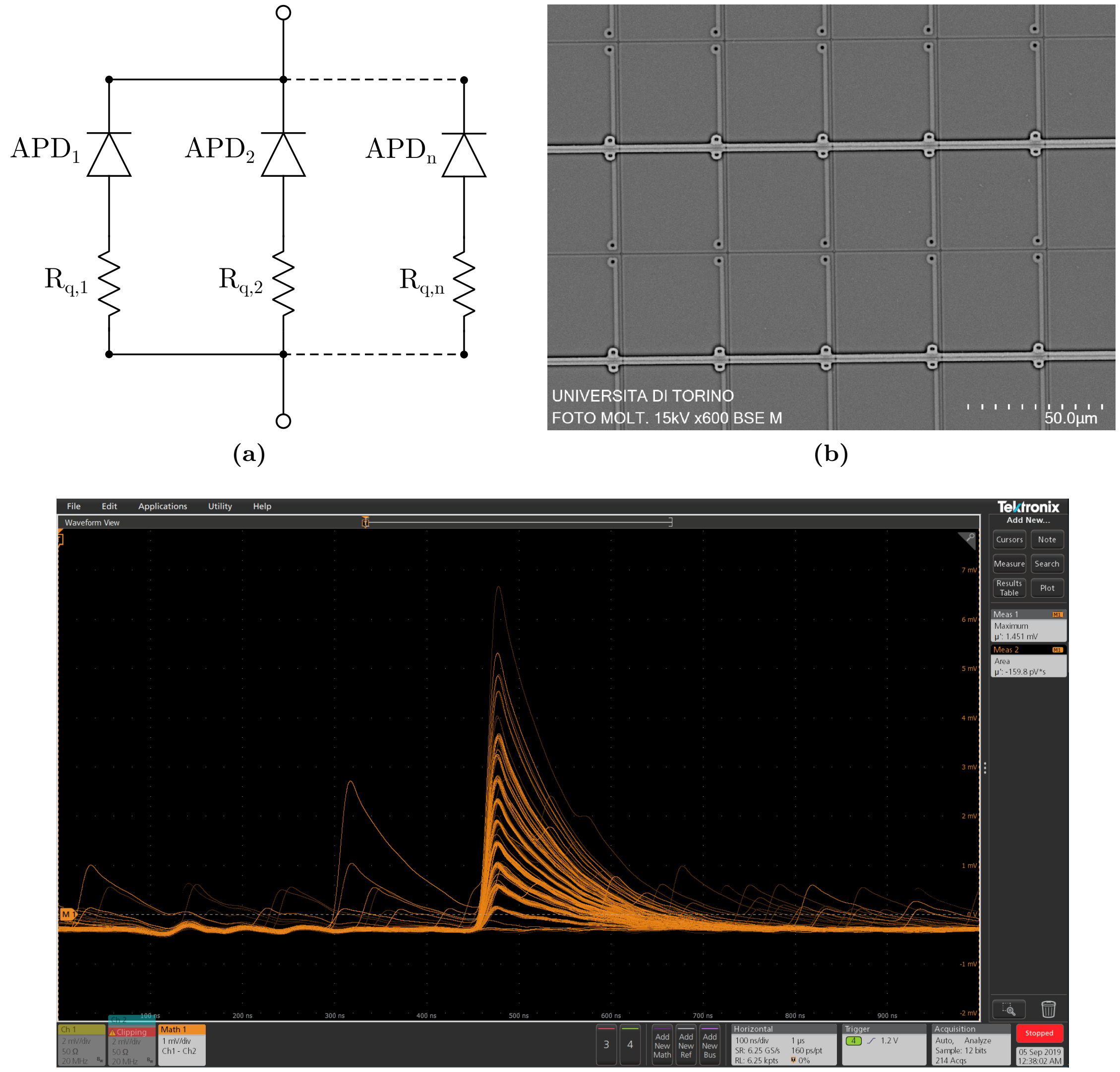

(a)

(b)

(c)

Figure 3.10: (a) SiPM as an array of GAPD connected in parallel
(b) FBK NUV HD3-2 seen with a SEM microscope
(c) Signal from Advansid NUV 1 mm × 1 mm, 20 MHz bandwidth

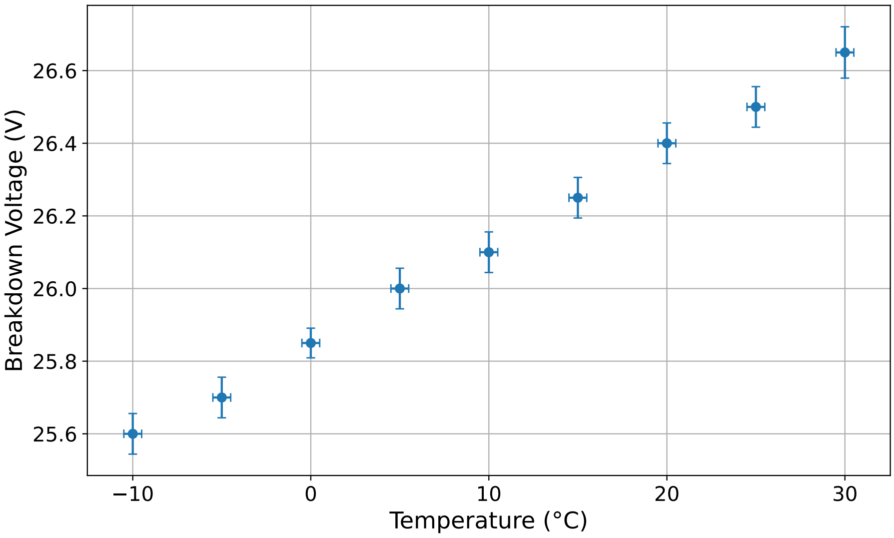

Figure 3.11: Breakdown voltage dependence on temperature for a FBK NUV HD3-2 6 mm×6 mm SiPM

3.4.1 Breakdown Voltage Temperature Dependence

All the SiPM electrical characteristics depend on the SiPM overvoltage, which, as we have seen, is the difference between the bias voltage and the breakdown voltage. However, the breakdown voltage strongly depends on the temperature: it is therefore necessary to understand how this value varies in order to be able to operate the sensor in the best possible way.

When the sensor is biased, every charge carrier (being it an electron or an hole) is accelerated by the electric field while traveling inside the depleted region. When a carrier collides with an atom of the reticle or with a phonon, there is a minimum energy, called *threshold energy*, above which we have the generation of another electron-hole pair. If we have a collision in which the accelerated carrier energy is below this threshold value, it will lose energy without generating another electron-hole pair. When all other parameters are equal, as the temperature increases, collisions are more and more likely, and therefore the average energy of the carriers decreases. Thus, we have an increase with the temperature of the minimum electric field necessary to generate a self-sustained avalanche: this explains why the breakdown voltage increases as the temperature increases [70]. This dependence is closely related to the internal structure of the sensor: the wider the depleted region, the higher the breakdown voltage dependence on temperature [68].

As an example, Figure 3.11 shows the results of the breakdown voltage dependence on temperature for a FBK NUV HD3-2 6 mm × 6 mm SiPM. The SiPM was placed in a climate chamber and the measurement was carried out after thermal stabilization. On this device we measured a variation of $26\,\frac{\mathrm{mV}}{^{\circ}\mathrm{C}}$.

The need to take this effect into account is clearly visible by observing the behaviour of the SiPM gain, measured as the difference between the average amplitude of the signals generated by two photoelectrons and that of the signals generated by one photoelectron. Results of the gain dependance on bias voltage and on overvoltage for a FBK NUV HD3-2 6 mm × 6 mm SiPM are shown in Figure 3.12a and 3.12b respectively. It is clear that by compensating the breakdown voltage temperature variation, the SiPM gain is constant at different temperatures. This also indicates that in the development of a slow control circuit for SiPMs it will be necessary to control the temperature on the sensors, in order to appropriately correct their bias voltages.

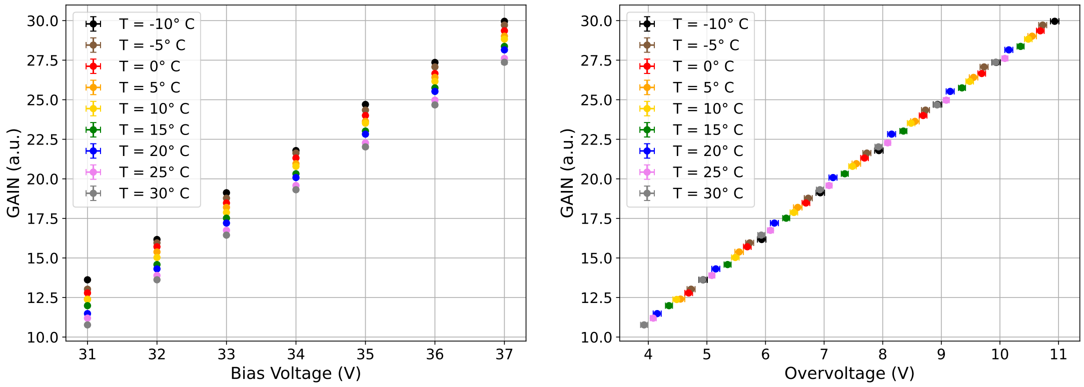

(a) **(b)**

Figure 3.12: Gain vs bias voltage (a) and vs overvoltage (b) for a FBK NUV HD3-2 6 mm × 6 mm SiPM

3.4.2 Photon Detection Efficiency

The *Photon Detection Efficiency* (PDE) is the overall conversion factor from photons to the number of detectable photoelectrons [71]; it is defined as:

$$PDE \triangleq QE \cdot FF \cdot P_{avalanche} \tag{3.15}$$

where QE is the quantum efficiency (i.e. the probability that a photon hitting the surface of the SiPM generates a electron-hole pair), FF is the Fill-Factor (i.e. the ratio of pixel photosensitive area to total area) and $P_{avalanche}$ is the Geiger-mode avalanche probability.

Similarly to APDs, two types of structures are used in SiPMs: P-on-N or N-on-P configurations, in order to be more sensitive to short wavelengths or long ones respectively [66, 69].

3.4.3 Dark Count Rate

As for the APD, thermal agitation can give sufficient energy to an electron in the depletion layer to pass to the conduction band from the valence band, leaving a hole in the latter. If this electron-hole pair triggers an avalanche, it will generate a signal that is indistinguishable from a signal generated by a photon. These counts induced by thermal energy are normally referred to as *dark counts.* The *dark count rate* is defined as:

$$DCR \triangleq \frac{N_{DCR}}{t} \tag{3.16}$$

where t is the time interval in which N_{DCR} dark counts occur.

Since it is related to thermal agitation, the Dark Count Rate increases as the temperature increases, and it is one of the most relevant drawbacks of SiPMs, since it is significantly higher than that of the traditional Photomultipliers [66].

As an example, in Figure 3.13 we can find the results of the dark count rate measurements for a FBK NUV HD3-2 6 mm × 6 mm SiPM as the overvoltage varies, at different temperatures. As expected, at constant temperature the dark count rate increases as the overvoltage increases, while at constant overvoltage it increases as the temperature increases. Measurements at different temperatures are taken at the same bias voltages; results are plotted according to the overvoltage: its variation with temperature is therefore already taken into account.

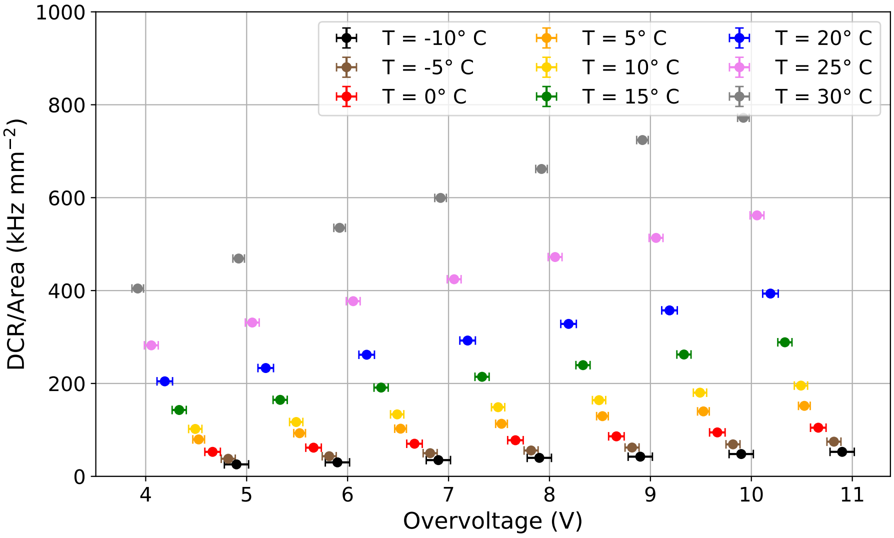

Figure 3.13: Dark count rate vs overvoltage at different temperatures for a FBK NUV HD3-2 6 mm × 6 mm SiPM

3.4.4 Optical Crosstalk

Already in 1955 it was shown that a PN junction which is reversely biased until its breakdown emits light in the visible range [72]; indeed during the avalanche process, the kinetic energy of the carriers does not necessarily take part in the continuation of the avalanche. A portion of that energy can be lost as heat in scattering collisions (phonon vibrations), and, less likely, it can be emitted as photons [66]. Lacaita et al. at the beginning of the 90s measured a photon emission efficiency of about 3×10^{-5} photons with energy higher than 1.14 eV per carrier crossing the junction [73]. Thus, assuming a typical SiPM gain of about 10^6, during a pixel breakdown on average $3 \times 10^{-5} \cdot 10^6 = 30$ photons are produced. These photons have a certain probability to reach a neighboring pixel and to trigger a new avalanche; the corresponding signal is not distinguishable from that produced by a photon that hits the surface of the SiPM [74]. This undesirable phenomenon is known as *optical crosstalk* and it is a peculiar disadvantage of SiPMs. If a crosstalk photon produces an electron-hole pair in the depletion layer of a neighboring cell and triggers an avalanche process as a result, this situation is called *prompt crosstalk*; in this case the output pulse appears simultaneously with the original pulse. Instead if the crosstalk photon creates an electron-hole pair outside the depletion layer of a neighboring pixel, the resulting electron-hole pair can only trigger an avalanche process after reaching the depletion layer by diffusion. In this situation the original pulse and the crosstalk pulse are not simultaneous, but the crosstalk signal appears after a certain time interval with respect to the genuine one. This phenomenon, less likely than the prompt one, is known as *delayed crosstalk* [66].

Figure 3.14 shows the results of the crosstalk measurements for a FBK NUV HD3-2 6 mm × 6 mm SiPM as the overvoltage varies, at different temperatures. As expected the crosstalk increases with overvoltage. Its temperature dependance is instead less clear to be understood: as the temperature increases, the DCR increases, and therefore the probability of overlapping pulses from different microcells increases, thus leading to an overestimated crosstalk measurement. If we consider a temperature range in which the DCR is low enough to made this effect negligible (let's say from $-10\,^{\circ}$C to $10\,^{\circ}$C), no particular crosstalk dependence on temperature is observed for these devices. Also in this case measures at different temperatures are taken at the same bias voltages and results are plotted according to the overvoltage.

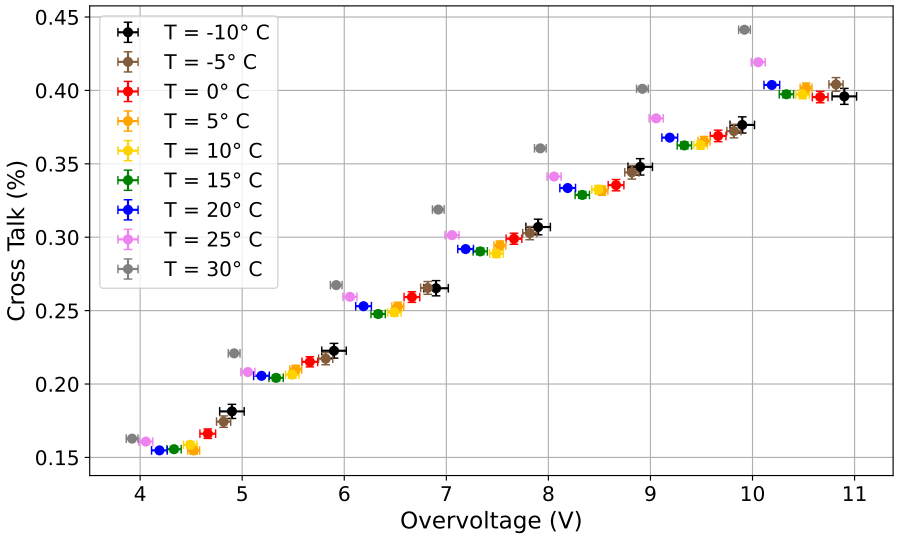

Figure 3.14: Crosstalk vs overvoltage at different temperatures for a FBK NUV HD3-2 6 mm × 6 mm SiPM

3.4.5 Afterpulses

During an avalanche process a small portion of avalanching carriers get trapped in impurity energy levels but are released after short delays upon receiving the required energy to reenter the conduction or valence band; these carriers can initiate an avalanche and thus a signal is detectable. This pulse, delayed with respect to the original one, is called *afterpulse*. If an afterpulse is released before the complete microcell recovery time, its pulse amplitude will be lower than the regular one, and can be therefore discriminated from a genuine event. Instead, if the afterpulse is released after the microcell recovery time, it will have the same shape and amplitude as a regular one-photoelectron signal [66].

3.4.6 Linearity

If the number of photons hitting the SiPM, $N_{photons}$, multiplied by the PDE is significantly smaller than the total number of sensor cells, $N_{cells,tot}$, then the number of fired cells linearly depends on the input photon signal $N_{photons}$. Please note that the number of fired cells is equal to the number of measured photoelectrons $N_{pe,measured}$. However, as $N_{photons}$ increases, the sensor goes out of linearity due to saturation effects. Indeed, in this situation there is a clear probability that more than one photon will hit the same microcell: due to the digital behavior of the SiPM microcell, always the same signal will be produced. An approximation of the number of detected photoelectrons $N_{pe\,measured}$ is given by [68]:

$$N_{pe,measured} = N_{cells,tot} \cdot \left(1 - e^{-\frac{N_{photons} \cdot PDE}{N_{cells,tot}}}\right) = N_{cells,tot} \cdot \left(1 - e^{-\frac{N_{pe,expected}}{N_{cells,tot}}}\right) \tag{3.17}$$

In Figure 3.15 we can find the non-linear behaviour of four SiPMs with different numbers of total cells: 625, 5625, 22 500 and 45 000, corresponding to 1 mm × 1 mm, 3 mm × 3 mm, 6 mm × 6 mm and 6 mm × 12 mm SiPMs with 40 µm cells.

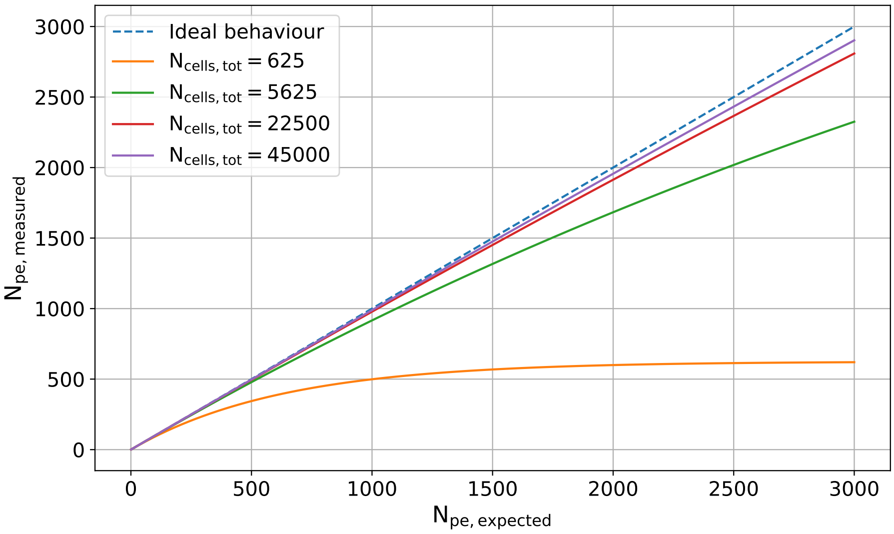

Figure 3.15: Non-linear behaviour of three SiPMs with different number of total cells: 625, 5625, 22 500 and 45 000, corresponding to 1 mm × 1 mm, 3 mm × 3 mm, 6 mm × 6 mm and 6 mm × 12 mm SiPMs with 40 µm cells

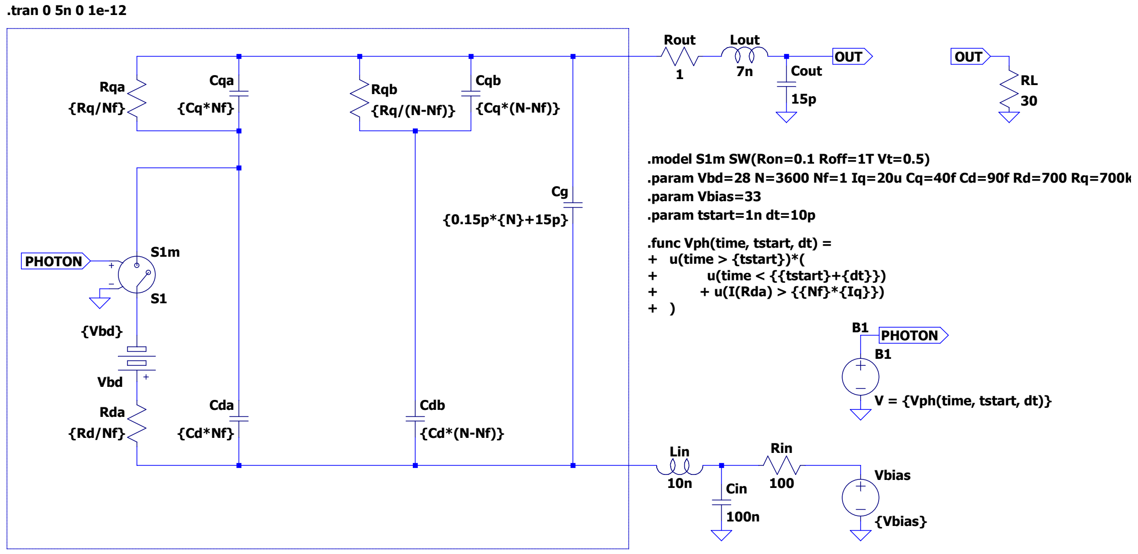

```
.tran 0 5n 0 1e-12
```

```
.model S1m SW(Ron=0.1 Roff=1T Vt=0.5)
.param Vbd=28 N=3600 Nf=1 Iq=20u Cq=40f Cd=90f Rd=700 Rq=700k
.param Vbias=33
.param tstart=1n dt=10p

.func Vph(time, tstart, dt) =
+   u(time > {tstart})*(
+           u(time < {{tstart}+{dt}})
+          + u(I(Rda) > {{Nf}*{Iq}})
+   )
```

Figure 3.16: SiPM Equivalent Circuit

3.4.7 Model of the SiPM Response

In order to better understand the SiPM signal and to find the ideal front-end electronics for our application, a usual starting point is to build an accurate equivalent circuit. We will rely on the one shown in [68], on which small changes have been made to adapt it to the used SPICE simulator (LTspice® [75]). This model, reported in Figure 3.16, takes into account the parasitics of the interconnections (both on the anode and on the cathode of the sensor), the possibility that multiple cells are fired in the same time, the avalanche ignition and its self sustaining. The load is modelled as a simple resistor.

Referring to Figure 3.16, the SiPM equivalent circuit is the one enclosed by the square box. It can be divided in two parts: on the left we have the fired cells, while on the right we have the other cells. Each cell is made by the series of a diode and a quenching resistor, similarly as previously done for a single Geiger mode APD. The diode is modelled as the series of a switch, the internal diode resistance R_d and the fixed battery that simulates the breakdown voltage potential, all in parallel with the diode capacitance C_d. For the quenching resistor R_q we also consider its parasitic capacitance C_q. N is the total number of cells, while N_f are the fired ones; these last are equivalent to a single cell with:

$$R_{d,a} = \frac{R_d}{N_f}, \qquad C_{d,a} = C_d \cdot N_f, \qquad R_{q,a} = \frac{R_q}{N_f}, \qquad C_{q,a} = C_q \cdot N_f \tag{3.18}$$

Similarly for the non-fired ones:

$$C_{d,b} = C_d \cdot (N - N_f), \qquad R_{q,b} = \frac{R_q}{N - N_f}, \qquad C_{q,b} = C_q \cdot (N - N_f) \tag{3.19}$$

Another parasitic capacitance, the grid capacitance C_g, is placed in parallel with the whole circuit.

The values used in the simulation are the one reported in [68], and are they typical for a $3\,\text{mm} \times 3\,\text{mm}$ SiPM with $50\,\mu\text{m}$ cell pitch:

$$\begin{gathered} N = 3600, \quad V_{bd} = 28\,\text{V} \\ R_q = 700\,\text{k}\Omega, \quad R_d = 700\,\Omega, \quad C_q = 40\,\text{fF}, \quad C_d = 90\,\text{fF} \\ C_g = 0.15\,\text{pF} \cdot N + 15\,\text{pF} \end{gathered} \tag{3.20}$$

A $30\,\Omega$ load is used for the firsts simulations.

As previously said, this model takes into account the avalanche ignition and its self sustaining, thanks to a switch S_1 controlled by a behavioral voltage source B_1. When the photon generates an electron-hole pair, the switch closes and triggers the avalanche; this process is self-sustaining until the current flowing in $R_{d,a}$ is greater than a threshold value, commonly referred as *latching current* [76]. The switch is open when the control voltage exceeds the threshold and closed otherwise; using the LTspice® code formatting, the S_1 switch is modelled as:

```
.model S1m SW(Ron=0.1 Roff=1T Vt=0.5)
```

which means that it has a on-resistance equal to $0.1\,\Omega$ and an open-circuit resistance equal to $1\,\mathrm{T}\Omega$, in order to have a good approximation of an ideal switch; the threshold is arbitrary set to $0.5\,\mathrm{V}$.

The control function B_1 is defined as `V = {Vph(time, tstart, dt)}`, with `Vph`:

```
.func Vph(time, tstart, dt) =
+   u(time > {tstart})*(
+             u(time < {{tstart}+{dt}})
+           + u(I(Rda) > {{Nf}*{Iq}})
+   )
```

where `u(x)` is the Heaviside step function.

The photon hits the sensor and generate an electron-hole pair at `time = tstart`; as previously described, the avalanche process is self-sustaining until the current flowing in the resistor R_d is greater than the latching current I_q. Since we are considering the equivalent circuit of all the N_f fired cells, this means that the process is self-sustaining until $I(R_{d,a}) > N_f \cdot I_q$. A latching current value of a few tens of microamps allows the correct functioning of the circuit model. The spike modelled by:

```
u(time>{tstart}) * u(time < {{tstart}+{dt}})
```

where `dt` is much smaller than the avalanche duration time, is only necessary to ensure that the process will start.

An example is reported in Figure 3.17, where in upper plot we have the output voltage V_{OUT} and the current flowing in the equivalent diode resistor ($I(R_{d,a})$), while in the lower plot it is shown the voltage controlled switch input (V_{ph}) and its threshold. The photon triggers the avalanche at $t = 1\,\mathrm{ns}$, the switch closes and the current flows in the equivalent diode resistor $R_{d,a}$. For completeness, the output voltage V_{OUT} is the one measured on the load resistor R_L, i.e. $V_{OUT} = V(R_L)$.

Looking inside the SiPM signal generation, we can distinguish two current components: a fast one, flowing through $C_{q,a}$, and a slow one, flowing through $R_{q,a}$. In Figure 3.18 it is shown the two components and their sum, which is the current generated in the fired cells. Unlike in a SPAD, all the non-fired cells act as a low-pass filter; the resulting current is the one flowing in R_{OUT}.

Different Number of Fired Cells

In Figure 3.19a we can observe how the model works with a different number of fired cells (namely $N_f = 1 - 10$). However, we must keep in mind that, since it is only a simplified model, it could lead to misinterpretations: from Figure 3.19b it would seem that the sensor is able to see without losing linearity at least up to 3000 photons (on a total of 3600 cells): likely this does not happen in reality. Indeed, what we are observing is not the signal produced by the arrival of 3000 photons, but the one produced by the ignition of 3000

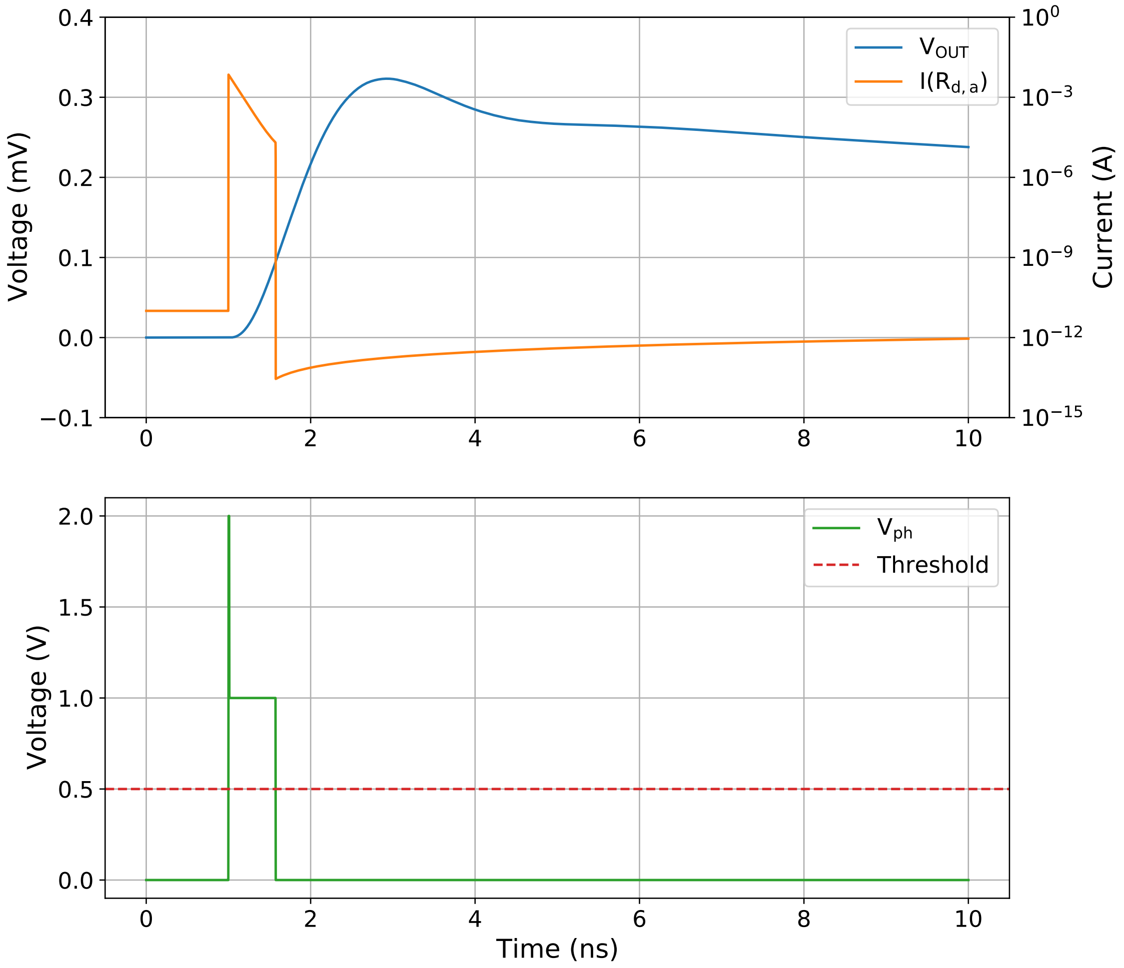

Figure 3.17: Upper plot: output voltage V_{OUT} and current flowing in the equivalent diode resistor ($I(R_{d,a})$). Lower plot: voltage controlled switch input (V_{ph}) and its threshold.

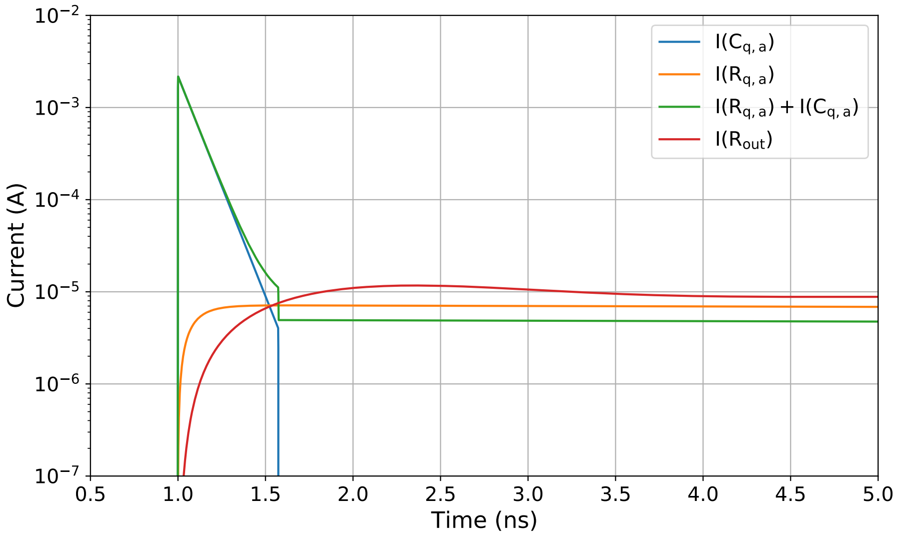

Figure 3.18: Simulation results for the fast component ($I(C_{q,a})$), slow component ($I(R_{q,a})$), current generated by the triggered cells before ($I(R_{q,a}) + I(C_{q,a})$) and after ($I(R_{out})$) the low pass filter made by the non-triggered ones

cells. Each cell is a digital sensor, therefore the signal generated by the arrival of a single photon on the same cell and the signal produced by the arrival of multiple photons at the same time on the same cell, are completely identical. The more the number of photons per area increases, the more increases the probability that more photons hit the same cell.

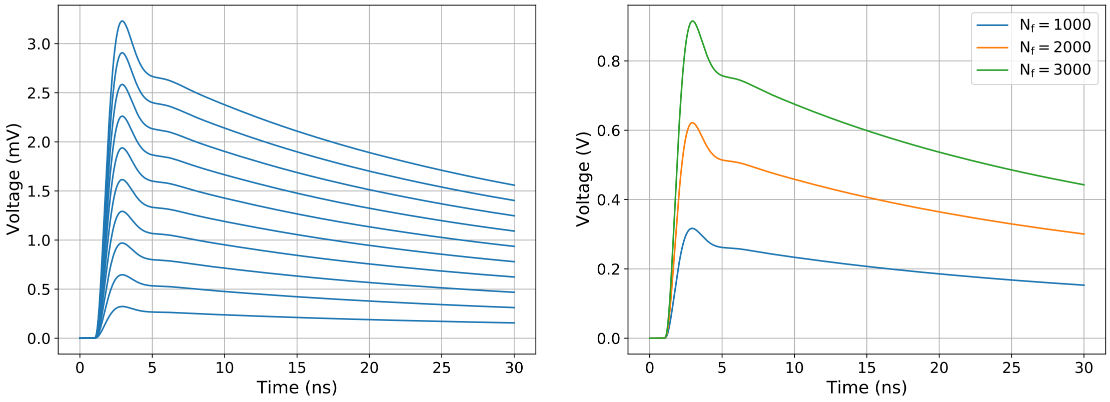

(a) **(b)**

Figure 3.19: V_{OUT} for different number of triggered cells: (a) $N_f = 1 - 10$, (b) $N_f = 1000, 2000, 3000$

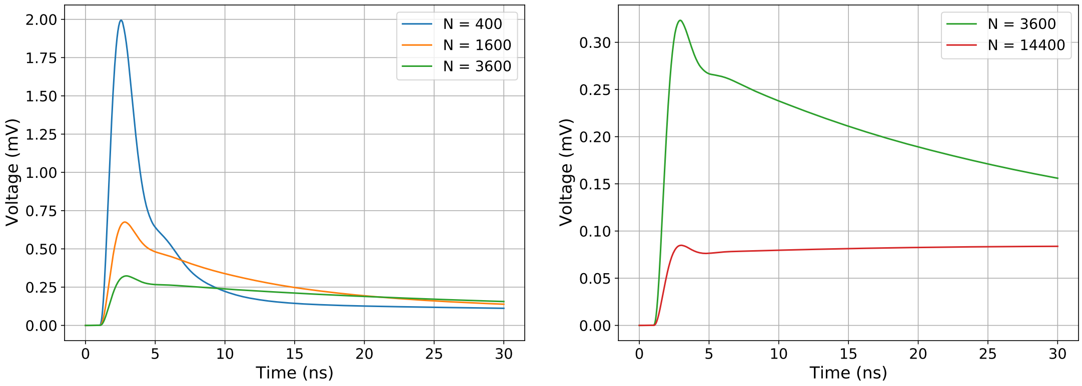

(a) **(b)**

Figure 3.20: V_{OUT} for different number of total cells

Different Number of Total Cells

In Figure 3.20 we can observe the signal generated by one firing cell for different numbers of total cell; in this way we can simulate how the sensor behaves as its area changes, keeping all its characteristics constant (in particular the size of the cells equal to $50\,\mu\mathrm{m}$): $N = 400$ for a $1\,\mathrm{mm} \times 1\,\mathrm{mm}$ SiPM, $N = 1600$ for $2\,\mathrm{mm} \times 2\,\mathrm{mm}$, $N = 3600$ for $3\,\mathrm{mm} \times 3\,\mathrm{mm}$ and $N = 14\,400$ for $6\,\mathrm{mm} \times 6\,\mathrm{mm}$. We can see that as the cell number increases, the amplitude decreases and the signal becomes longer. Indeed, the signal produced by the single cell is always the same in all the devices, but as the number of cells increases, the cutoff frequency of the low pass filter made up of the parallel of the non-triggered cells becomes lower.

If we neglect the parasitics, we can study the transfer function of the filter made by the non-triggered cells in parallel with the load resistor. The transfer function will be:

$$H(s) = \left(\left(R_{q,b} \parallel \left(\frac{1}{sC_{q,b}}\right) + \frac{1}{sC_{d,b}}\right) \parallel \frac{1}{sC_g}\right) \parallel R_L \tag{3.21}$$

We start computing Z_1 defined as:

$$\begin{aligned} Z_1 &= R_{q,b} \parallel \left(\frac{1}{sC_{q,b}}\right) + \frac{1}{sC_{d,b}} = \\ &= \left(\frac{1}{R_{q,b}} + sC_{q,b}\right)^{-1} + \frac{1}{sC_{d,b}} = \\ &= \frac{R_{q,b}}{1 + sR_{q,b}C_{q,b}} + \frac{1}{sC_{d,b}} = \\ &= \frac{1 + sR_{q,b}C_{d,b} + sR_{q,b}C_{q,b}}{sC_{d,b}(1 + sR_{q,b}C_{q,b})} \end{aligned}$$

Then:

$$\begin{aligned} H(s) &= Z_1 \parallel \frac{1}{sC_g} \parallel R_L = \\ &= \left(\frac{1}{Z_1} + sC_g + \frac{1}{R_L}\right)^{-1} = \\ &= \left(\frac{sC_{d,b}(1 + sR_{q,b}C_{q,b})}{1 + sR_{q,b}C_{d,b} + sR_{q,b}C_{q,b}} + sC_g + \frac{1}{R_L}\right)^{-1} = \\ &= \frac{R_L(1 + sR_{q,b}(C_{d,b} + C_{q,b}))}{D} \end{aligned}$$

where:

$$\begin{aligned} D = {} & s^2 R_L R_{q,b}(C_{d,b}C_{q,b} + C_{d,b}C_g + C_{q,b}C_g) + \\ & + s(R_L(C_{d,b} + C_g) + R_{q,b}(C_{d,b} + C_{q,b})) + 1 \end{aligned}$$

The transfer function has a zero in:

$$s_z = \frac{1}{R_{q,b}(C_{d,b} + C_{q,b})} \tag{3.22}$$

Using Equation 3.19:

$$s_z = \frac{1}{R_q(C_d + C_q)} \tag{3.23}$$

Considering the denominator:

$$\begin{aligned} D &= s^2 R_L R_q(C_d C_q(N - N_f) + C_g(C_d + C_q)) + \\ &\quad + s(R_L(C_d(N - N_f) + C_g) + R_q(C_q + C_d)) + 1 = \\ &= as^2 + bs + 1 \end{aligned}$$

The transfer function has two poles in:

$$s_{p1,p2} = \frac{-b + \sqrt{b^2 - 4a}}{2a} \tag{3.24}$$

where:

$$\begin{aligned} a &= R_L R_q(C_d C_q(N - N_f) + C_g(C_d + C_q)) \\ b &= R_L(C_d(N - N_f) + C_g) + R_q(C_q + C_d) \end{aligned} \tag{3.25}$$

By replacing the values shown in 3.20, and considering only one fired cell, we obtain:

$$f_z \simeq 1.75\,\mathrm{MHz} \qquad f_{p1} \simeq 1.60\,\mathrm{MHz} \qquad f_{p2} \simeq 8.85\,\mathrm{MHz} \tag{3.26}$$

where we used the relationship between the complex frequency s (rad/s) and the frequency f (Hz).

We can now study the behaviour of this filter as the number of SiPM total cells changes. In Figure 3.21a it is shown the zero and the poles frequencies trend; it is clear that for a small area SiPM the second pole plays the main role in the filter behaviour, since the first one and the zero have basically the same frequency. For a larger area device, while the zero frequency remains constant (indeed f_z is not a function of N), the first pole frequency decreases. By combining these factors, we clearly see that the filtering power increases as the total number of cells increases. The amplitude Bode Plot for the sensors studied before is shown in Figure 3.21b; these ones can be obtained whether with a SPICE simulation or by evaluating them directly from the transfer function. We can also study the behaviour of the filter at different number of firing cells, as shown in Figure 3.22a and Figure 3.22b. Although we can see a trend, it is not very pronounced: for this reason the signal produced by one or more photons will have the same shape.

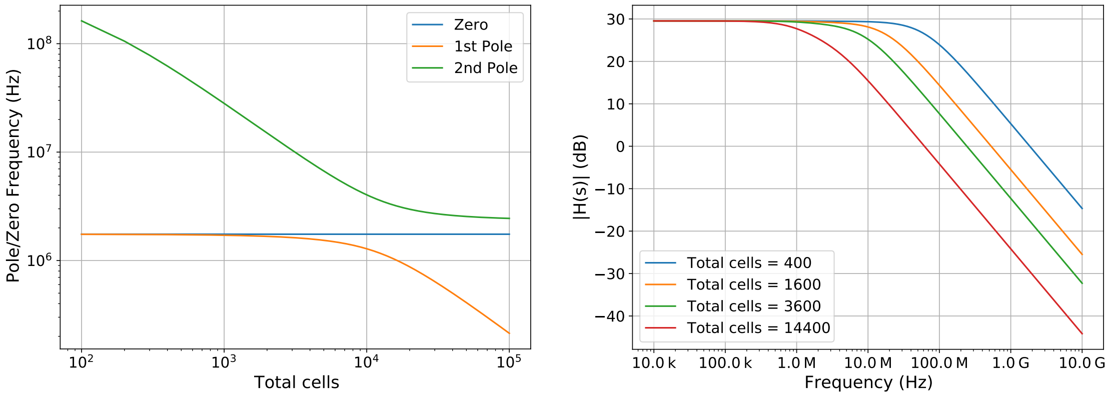

(a) (b)

Figure 3.21: Non triggered cells filter study by varying the total cells number, considering the resistors and capacitors values reported in Equation 3.20 and only one fired cell: poles and zero frequencies (a) and Bode Plot (b)

Different Quenching Resistors

In Figure 3.23 we see the SiPM behaviour at different R_q values; for clearness, the simulated signal has been divided into two time windows, in order to highlight its salient aspects. If R_q is too low, like 200 kΩ in the example, it is not able to quench the discharge, making the sensor unusable, while with higher resistor values the avalanche is correctly quenched, but in a different way according to R_q. When R_q increases, the slow component varies, unlike the fast component, which remains practically unchanged. With a very high R_q (like 10 MΩ) the signal rapidly decreases (in a faster way than with $R_q = 700\,\mathrm{k}\Omega$), but it reaches the baseline after more time.

Different Microcell Sizes

If we consider SiPMs obtained with the same manufacturing processes, their quenching capacitance values scale with the cell width, while their diode capacitance with the microcell area. Bearing this in mind, we can study how the cell dimension modifies the SiPM behavior.

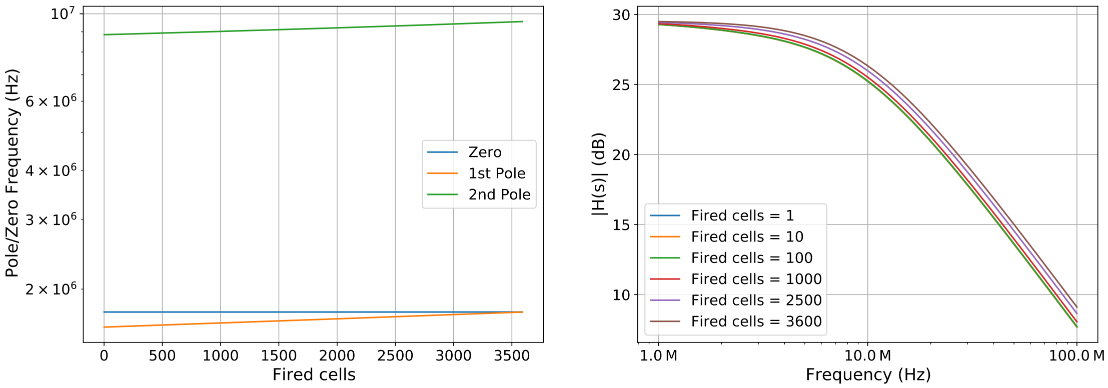

(a) **(b)**

Figure 3.22: Non triggered cells filter study by varying the fired cells number in a device composed of 3600 cells, considering the resistors and capacitors values reported in Equation 3.20: poles and zero frequencies (a) and Bode Plot (b)

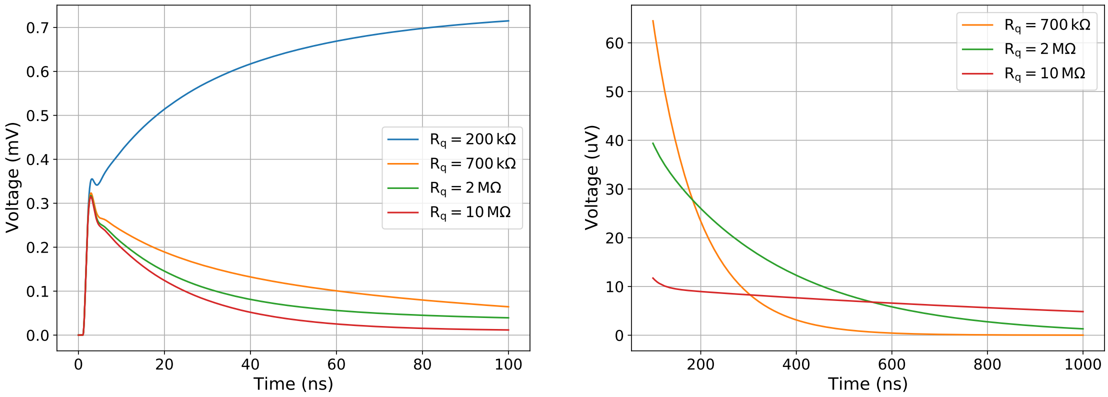

(a) **(b)**

Figure 3.23: V_{OUT} for different R_q values

In Figure 3.24a it is show the output signal of a 3 mm × 3 mm SiPM as the size of it microcells changes: the wider the cell, the higher the diode capacitance and thus the charge released in a single discharge; in addition as the size of the cells increases, the number of cells within the sensor decreases (the area is kept constant), reducing the low pass filtering effect of the non-fired cells. This results in an increase in the signal amplitude as the cell width increases, as can be seen from the simulations.

In Figure 3.24b and 3.24c it is reported the simulation results for different SiPMs, with 1 mm × 1 mm, 2 mm × 2 mm, 3 mm × 3 mm, 6 mm × 6 mm and 6 mm × 12 mm, both with 40 µm and 50 µm cell width. It is quite clear that with the used simulation parameters the signal from the 6 mm × 6 mm or 6 mm × 12 mm SiPMs cannot be used; a possible solution can be decreasing the load resistor (we will see its effect in the following section) or filtering out the lower frequencies, as shown in Figure 3.24d; later we will discuss this more in detail.

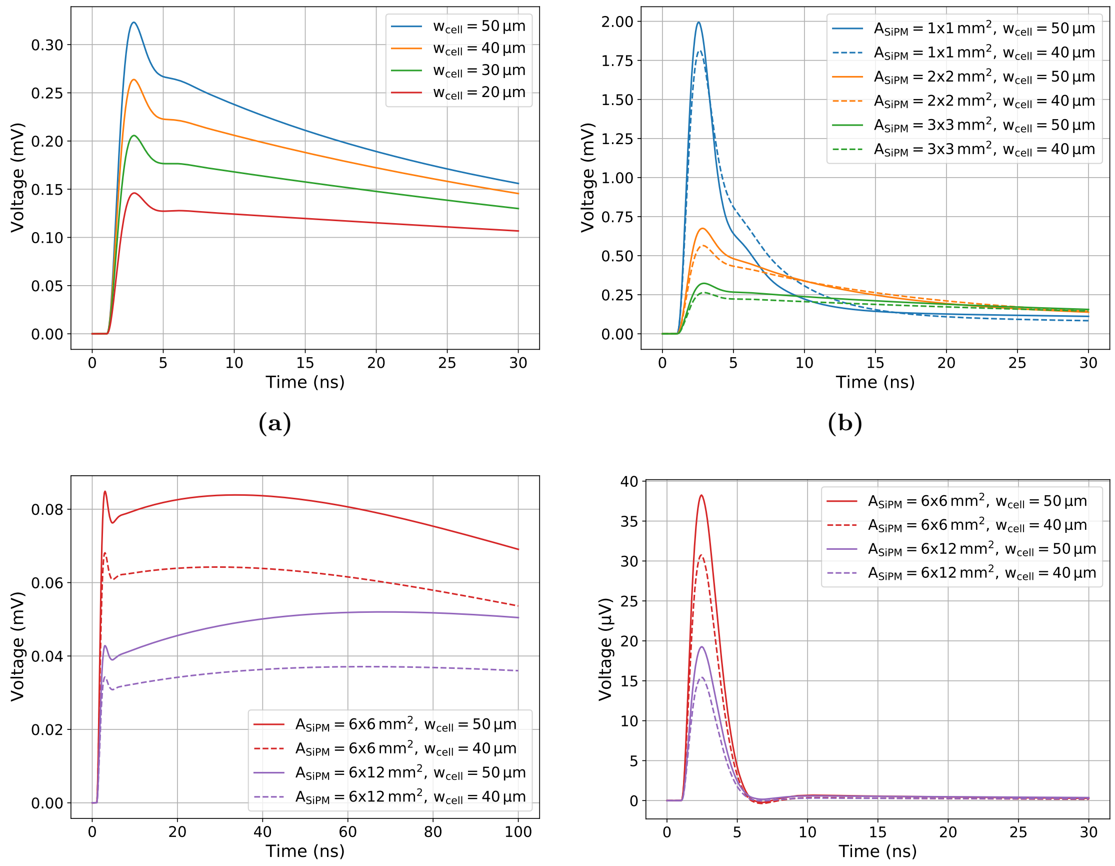

(a) (b)

(c) (d)

Figure 3.24: V_{OUT} for different SiPM areas and microcells widths:
(a) Area: $3 \times 3\,mm^2$, different cell widths
(b), (c) Different areas and different cell widths, without shaping the signal
(d) As before, but shaping the signal with a passive high pass filter

Different Load Resistors

One of the biggest goals of this equivalent model is to allow us to simulate how the SiPM signal behaves with different loads; this will allow us to find the ideal value of the front-end electronics input impedance. In Figure 3.25 it is shown the simulation results for the output signals at different resistive load values, both in voltage (3.25a) and in current

(3.25b). We can observe that by increasing the value of R_L, the voltage peak increases and the current peak decreases; integrating the signal (in a wider window than the one shown in the plot) we have that the charge remains constant. Moreover, by increasing the load value the signal becomes longer, and we can clearly see that after a certain R_L value we have a ringing after the peak signal: this is due to the parasitic interconnection between the sensor and the load, which forms a RLC filter. An oscillation in the signal can also be observed with a very low R_L value. In Figure 3.26 it is compared the output voltage and current peak at different load resistor value: we can see that up to a certain value, the V_{OUT} increasing trend (decreasing for the current) starts saturating. This, in addition with the time duration dependence, shows us that a front-end electronics must have low input impedance, but that still ensures a good signal shape.

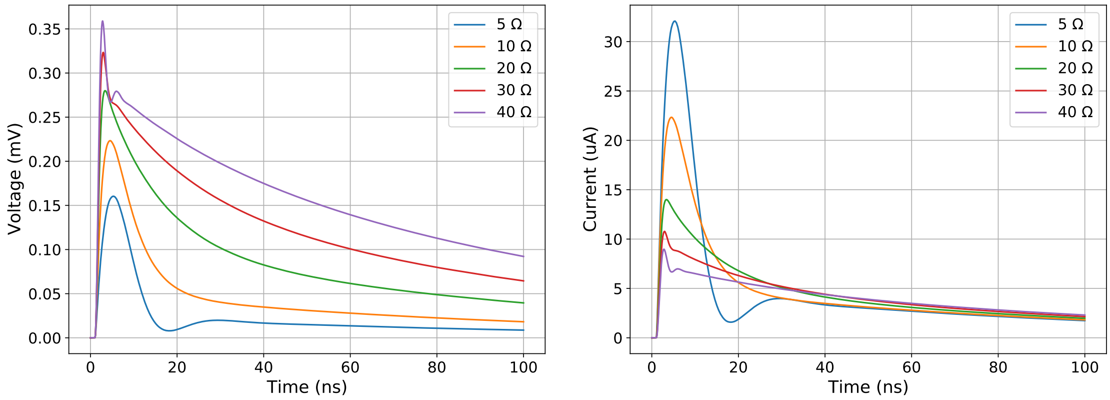

(a) **(b)**

Figure 3.25: Output signal for different R_L values: (a) $V_{OUT} = V(R_L)$, (b) $I(R_L)$

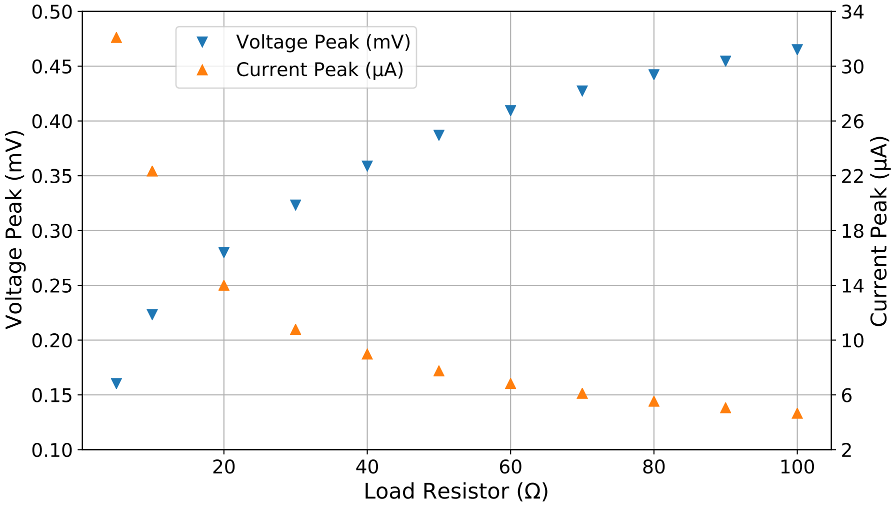

Figure 3.26: Output voltage and current peak vs different load resistor values

Two Consecutive Photons and Microcell Recharge

After a cell is hit by a photon, or after a dark event, the cell will be able to properly detect a new incoming photon only if it is completely discharged. By modifying the as control voltage B_1 as:

```
V = {Vph(time, tstart, dt)} +  {Vph(time, tstart + dtph, dt)}
```

we can study this phenomenon; the first photon triggers the avalanche at $t_0 = t_{start}$, while the second one and at $t_1 = t_{start} + dt_{ph}$. The simulation results are reported in Figure 3.27. As we can see, as dt_{ph} increases, the amplitude of the second signal increases; we will have that the signal generated at t_1 is equal to the one generated at t_0 only if dt_{ph} is long enough to allow a complete recharge of the cell.

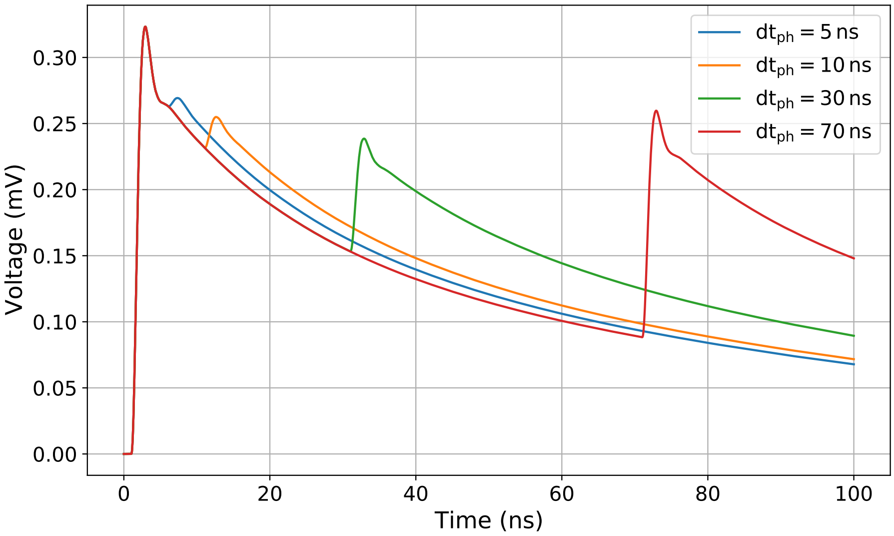

Figure 3.27: Simulation of two photons hitting the same cell at $t_0 = 1$ ns and at $t_1 = t_0 + dt_{ph}$

Different Overvoltages

Up to now we have always polarized the sensor with the same V_{bias}; in Figure 3.28 it shown the dependence of the signal voltage peak and charge at different overvoltages ($V_{OV} = V_{bias} - V_{bd}$). They both follow a line which intercepts the abscissa axis (V_{OV}) in the origin: this means that the gain is null when the sensor is polarized at its breakdown voltage, as we would expect. The extrapolation of V_{bd} from the best fit line of the gain versus overvoltage plot is one of the most used methods to evaluate this fundamental parameter.

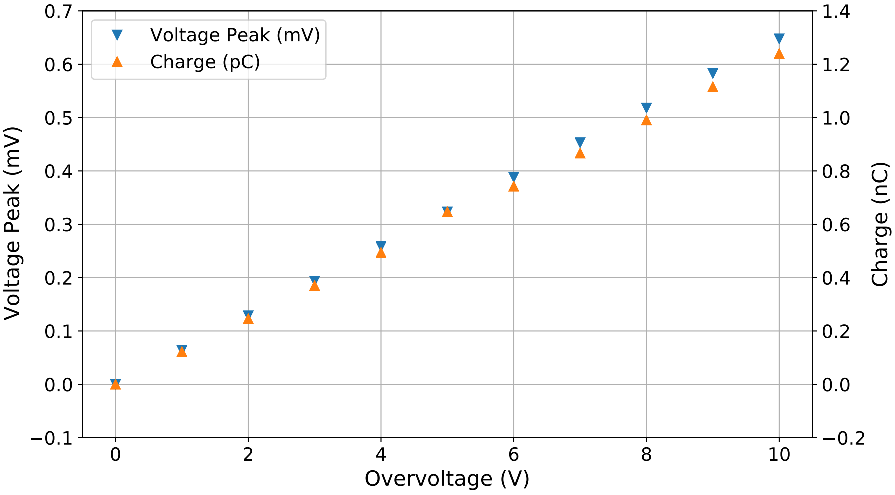

Figure 3.28: Voltage Peak and Charge for different Overvoltages

3.4.8 SiPMs vs PMTs

In recent years for many optical applications it has been chosen to use Silicon Photomultipliers instead of traditional Photomultipliers; indeed despite the PMT technology is mature and reliable, SiPMs are emerging as promising competitors.

The main advantages of SiPMs with respect to the traditional PMTs are:

- SiPMs can reach higher quantum efficiencies than the PMTs;
- SiPMs have lower operating voltages than traditional photomultipliers;
- SiPMs does not suffer from electromagnetic fields;
- SiPMs offers tolerance to high illumination levels;
- usually SiPMs are cheaper than PMTs per square millimeter, thanks to the greater cost efficiency of silicon device microfabrication and scalability of wafer processing.

However SiPMs present also some drawbacks, such as [66]:

- higher dark count rate than PMTs;
- optical crosstalk.
- gain dependance on temperature

SiPMs are particularly suitable when the pixel size is small, as they are cheaper than photomultipliers of the same size and in addition they offer better performances. As the pixel size increases, the situation becomes less clear: above a certain size, it is necessary to sum the SiPM signals, thus complicating the light detector.

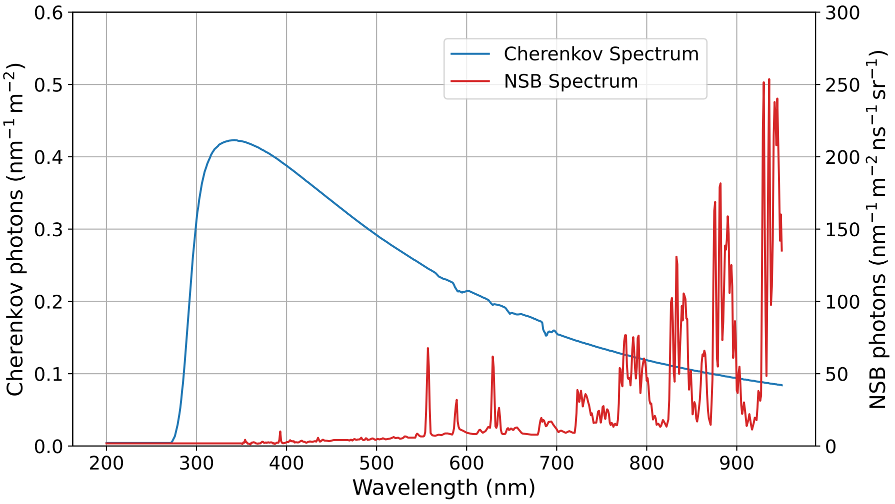

Figure 3.29: Night Sky Background measured at the Roque de los Muchachos Observatory, La Palma, Canary Islands [79], compared to the Cherenkov spectrum of a gamma-ray induced air shower.

3.5 SiPMs in IACT Experiments

The possibility that the advantages outweigh the drawbacks in IACT applications is very high: the feasibility of using a SiPM technology for these experiments has been widely demonstrated by the First GAPD Cherenkov Telescope (FACT), which has shown the stability and reliability of this solution in the long term, alongside the possibility to operate under moon light conditions, allowing a significant increase in duty cycle [77, 78].

The most important advantages of SiPMs when compared to PMTs for IACT experiments are:

- The higher quantum efficiency of SiPMs allows the telescope to lower the energy threshold, so it is possible to look deeper in the universe and to be more sensitive to lower energy phenomena;
- Since SiPMs offer tolerance to high illumination levels, it is possible to increase duty cycle. This is very advantageous for transients and for observations that require a lot of exposure time

Moreover, the higher dark count rate of SiPMs (when compared to PMTs) is often negligible, due to the considerable background photon flux from the night sky.

On the other hand, the SiPM Photon Detection Efficiency (PDE) spectrum is usually less sharp than that of PMTs: as we will see below, this makes the SiPMs more sensitive to the background noise.

3.5.1 Night Sky Background

Even on a moonless night the sky is not perfectly dark, but has a certain brightness known as *Night Sky Background* (NSB). This glow is a non-negligible source of contamination, and must be taken into account. A first effect of the NSB is that in an IACT the sensors in the focal plane will never work in dark conditions.

The main effects contributing to NSB are the *airglow* (about 65 % of the total NSB) and the *zodiacal light* (about 27 %). The airglow is the emission of atoms and molecules in the upper atmosphere which were excited by solar UV light during the day; its intensity is thus strictly related to the solar activity. The zodiacal light is the sunlight scattered by

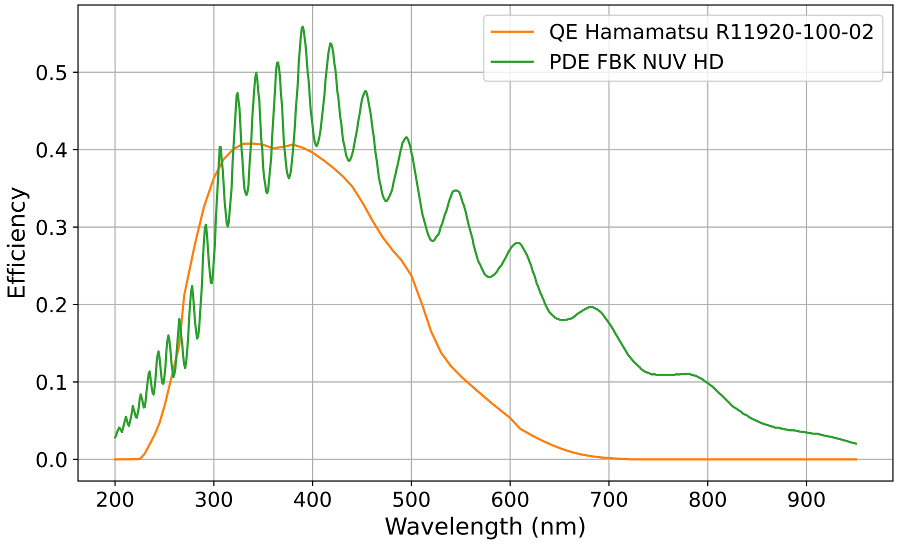

Figure 3.30: Quantum Efficiency of the Hamamatsu R11920-100-02 PMT and the Photon Detection Efficiency of a FBK NUV HD SiPM

interplanetary dust, it depends on the ecliptic latitude and its spectrum over the UV-IR range is very similar to the Sun one. In addition, less important but not negligible are the contributions of the integrated light of faint stars and the starlight scattered by interstellar dust.

A detailed study of the brightness of the moonless night sky above the Roque de los Muchachos Observatory, La Palma, Canary Islands is reported in [79]; the measurements were taken on 63 nights between 1987 and 1996 with the Isaac Newton and Jacobus Kapteyn Telescopes. This brightness is about 10 million times dimmer than the daylight sky, but it is still visible to the naked eye and can affect the observations. The results are shown in Figure 3.29 and are compared to the Cherenkov spectrum of a gamma-ray induced air shower. Looking at the two spectra, it is clear that the ideal sensor should have maximum efficiency in the UV region, and the lowest possible efficiency at higher wavelengths.

As an example, in Figure 3.30 are shown the Quantum Efficiency of the Hamamatsu R11920-100-02 photomultiplier and the Photon Detection Efficiency of a FBK NUV HD Silicon Photomultiplier. The PMT is the one used in the LST camera, and the plotted data were measured by the CTA-LST working group. The SiPM is very similar to the ones used in the prototype described in this thesis; the oscillations clearly visible in the PDE spectrum are related to the lack of coating on top of the device; see [70] for more information. It's clear that the SiPM reaches higher efficiency in the Cherenkov signal region, but integrates much more NSB than the PMT, since its response decreases less sharply as the wavelength of the incident photons increases. To better understand how these different sensor efficiency could affect the telescope performance, we can start evaluating how the signal and noise change as the wavelength of the incident photon λ changes. The signal $S(\lambda)$ is defined as:

$$S(\lambda) = \int_0^\lambda E_{sensor}(\lambda) P_{Ch}(\lambda) \tag{3.27}$$

where $P_{Ch}(\lambda)$ is the Cherenkov spectrum and $E_{sensor}(\lambda)$ is the quantum efficiency in the case of the PMT and the Photodetection Efficiency in the case of the SiPM. Similarly, if $P_{NSB}(\lambda)$ is the night sky background spectrum, we can define the noise $N(\lambda)$ as:

$$N(\lambda) = \int_0^\lambda E_{sensor}(\lambda) P_{NSB}(\lambda) \tag{3.28}$$

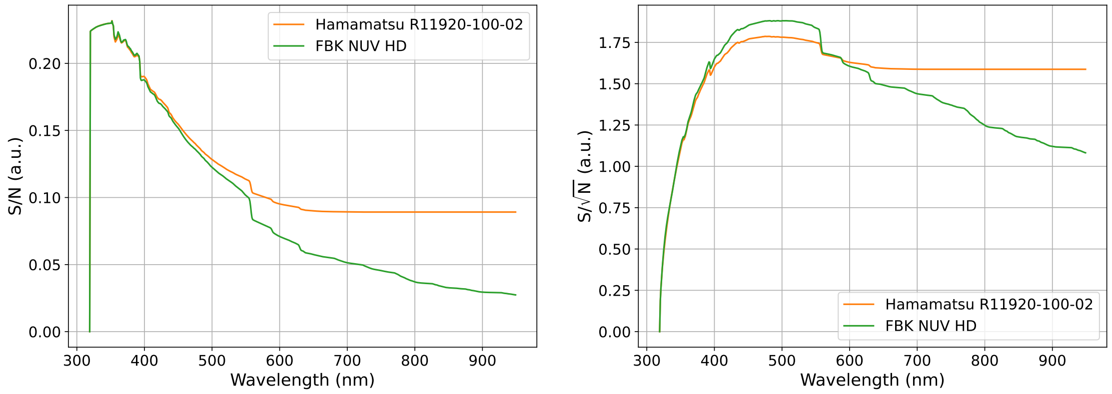

(a) **(b)**

Figure 3.31: Ratio between the signal and the noise (a) and the ratio between the signal and the square root of the noise (b) for the Hamamatsu R11920-100-02 PMT and the FBK NUV HD SiPM. See the text for more details.

We can evaluate the ratio between the signal and the noise:

$$R_1 = \frac{S(\lambda)}{N(\lambda)} \tag{3.29}$$

Results are shown in Figure 3.31a; as we would expect, the long tail in the SiPM PDE spectrum negatively affects R_1.

Since the night sky background follows a Poissonian distribution, we can introduce a quantity that takes into account the noise fluctuations: this quantity is the ratio between the signal and the square root of the noise:

$$R_2 = \frac{S(\lambda)}{\sqrt{N(\lambda)}} \tag{3.30}$$

Results are shown in Figure 3.31b, and also in this case the PMT seems to offer a better performance.

To solve the problem of the high SiPM response to longer wavelengths we can add an UV filter to the focal plane. We can divide the filters in two main categories: *transmissive filters* and *reflective filters*.

The first ones are used on top of the focal plane, and filter out the undesired wavelengths. A picture of the transmissive filter installed on the SST-1M entrance window is shown in Figure 3.32a; the filter is optimized for blue light transmission, and cuts off light beyond 540 nm. The higher wavelengths are not transmitted, and are therefore reflected by the filter window: this is the reason for the yellowish color clearly visible in the picture [80].

In order to cover a larger surface without exceeding the number and size of the sensors, often light concentrators are installed on the focal plane. In addition, these concentrators ensure that only the light coming from the mirrors reaches the sensors, thus reducing the background light contamination. One of the most used collectors are the so-called *Winston cones*; the picture of a SST-1M Winston cone can be found in Figure 3.32b, and the drawing in Figure 3.32c illustrates how they are installed in the focal plane. By means of a proper coating on the cone inner surface, it is possible to reflect only the desired wavelengths (in our case UV light); this explains the concept of a reflective filter.

In Figure 3.33 it is shown the efficiency of the reflective filter used in the SST-1M telescopes compared to the night sky background and the Cherenkov spectrum. If E_{filter}

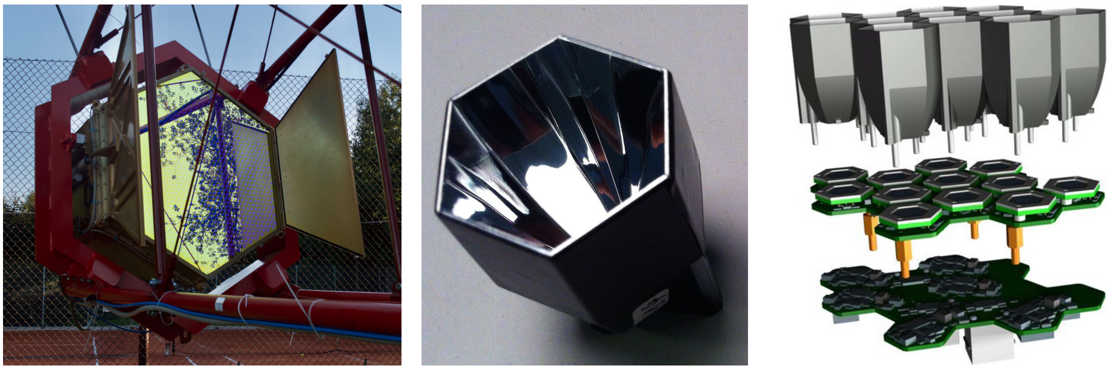

(a) **(b)** **(c)**

Figure 3.32: (a) SST-1M camera equipped with its filtering window installed in Krakow [80] (b, c) SST-1M Winston Cones [81]

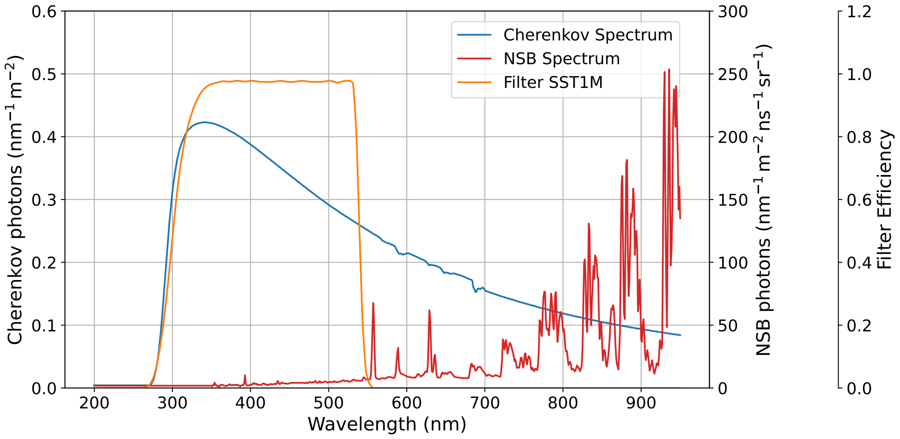

Figure 3.33: SST1M filter compared to the night sky background and the Cherenkov Spectrum. Please note that the filter transmissivity is shown on the second axis on the right.

is the filter efficiency, the signal can be evaluated as:

$$S(\lambda) = \int_0^\lambda E_{sensor}(\lambda) E_{filter} P_{Ch}(\lambda) \tag{3.31}$$

and the noise as:

$$N(\lambda) = \int_0^\lambda E_{sensor}(\lambda) E_{filter} P_{NSB}(\lambda) \tag{3.32}$$

With this approach both the ratio between the signal and the noise and the ratio between the signal and the square root of the noise are higher for the SiPM. This simple study may indicate that it would be necessary to take into account the use of a filter (being it transmissive, reflective or both together) in the design of a SiPM-based camera. However, the quantities just calculated are not sufficient to draw a conclusion. Indeed, in an IACT telescope, the trigger and the analysis are not based on the signal of a single pixel, but on the images which occur on the focal plane: for this reason having a higher signal can greatly benefit the overall performances. Only detailed Monte Carlo simulations can tell us which solution is the best one.

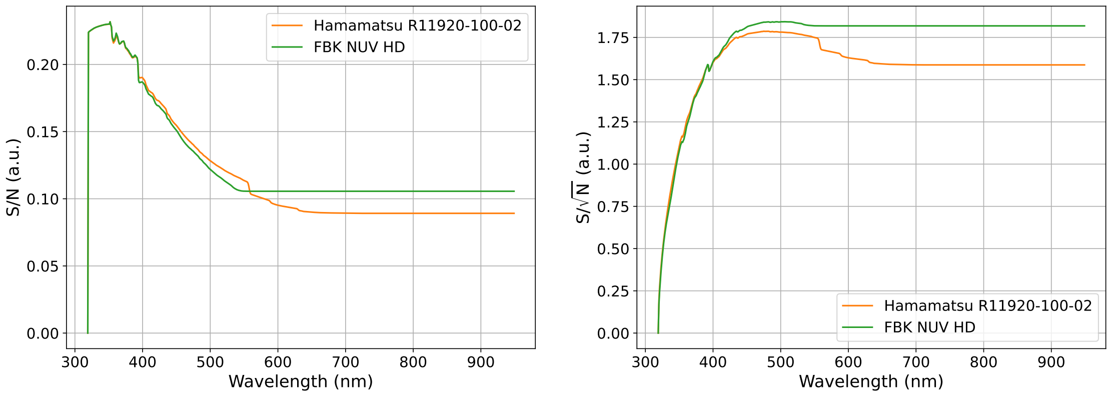

(a) (b)

Figure 3.34: Signal to Noise Ratio (a) and the ratio between the signal and the square root of the noise (b) for the Hamamatsu R11920-100-02 PMT and the filtered FBK NUV HD SiPM. See the text for more details.

3.5.2 IACT Facilities Already Using SiPMs

In this section we will briefly illustrate some of the IACT facilities hosting SiPMs in their focal plane.

FACT

The First GAPD Cherenkov Telescope (FACT) is the first Imaging Atmospheric Cherenkov telescope to use a camera based on silicon photodetectors; the detector used are solid-state Geiger-mode Avalanche Photodiodes (GAPD). It has a mirror surface of 9.51 m^2 and works mainly in TeV energy range. The telescope started operation at the Roque de los Muchachos Observatory 2200 m (La Palma, Canary Islands, Spain) in October 2011; it is operated remotely and automatically [77, 78]. Two pictures of the telescope are reported in Figures 3.35a and 3.35b.

The insensitivity of GAPDs towards strong ambient light allows the telescope to conduct observations during bright Moon and twilight. This gain in observation time is very important in many applications, such as long-term monitoring of bright TeV blazars. An example of an event while tracking the full Moon is reported in Figure 3.35c [82].

MAGIC

Also in the camera of the Major Atmospheric Gamma Imaging Cherenkov Telescopes (MAGIC) are installed a few SiPM-modules in order to study their behavior. Each camera offers six open corners for prototype installations, where these modules are installed [83].

Hamamatsu, SensL and Excelitas SiPMs are tested, in order to compare the performances of the major SiPMs suppliers.

CTA

Also in CTA SiPMs will be used: indeed the Small Size Telescopes and the Schwarzschild-Couder Telescopes will use this technology [84].

The Schwarzschild-Couder Telescopes are a dual-mirror version of the MSTs. The telescope has the primary mirror of 9.7 m in diameter and the secondary of 5.4 m. Its focal length is 5.6 m and the camera field of view is 7.6°. Its high density camera (11 328 pixels, each one with a pixel size of 0.067°) is based on 6 mm × 6 mm SiPMs. The camera is divided in 177 modules, each one with 64 SiPMs. The SCT prototype (pSCT) has been constructed at the Fred Lawrence Whipple Observatory in Arizona, USA. A picture of the telescope can be found in Figure 3.37a. For the time being only 1536 pixels are installed: 9 FBK SiPMs modules and 15 Hamamatsu modules; a picture of the preliminary focal plane is visible in Figure 3.37b. Even with a partial camera the prototype detected the Crab Nebula during an observing campaign in 2020 [85].

The Small-Sized Telescopes will focus on the CTA higher energy range (from a few TeV to 300 TeV); at this energies even a small mirror can collect enough light from the gamma-ray induced shower. The small and compact camera led to the choice of SiPMs instead of PMTs as light detectors. Three different SST structures were proposed: one single-mirror design (SST-1M) and two different dual-mirror designs (ASTRI-Horn and CHEC). A harmonization process completed in 2019 established the final structure of the SSTs, which is based on the ASTRI and CHEC design. The telescope is based on a dual-mirror Schwarzschild-Couder aplanatic configuration, with the primary mirror of 4.3 m in diameter and the secondary of 1.8 m. Its focal length is 2.15 m and the camera field of view is 8.8°. A picture of the ASTRI-Horn telescope prototype at the Catania Astrophysical Observatory (Serra La Nave, Mount Etna) can be found in Figure 3.38 on the left. The SST's camera, also known as the Compact High Energy Camera (CHEC-S) camera, is made by 2048 SiPMs. The camera is divided in 32 modules, each one with 64 6 mm × 6 mm SiPM pixels, each one with a 0.16° field of view. The camera design is in progress; for example, newer SiPMs will replace the ones used in the CHEC-S prototype, in order to reach better performances. On the right of Figure 3.38 we can see the CHEC-S camera prototype. With the ASTRI camera, the ASTRI-Horn telescope detected the Crab Nebula during an observation campaign in December 2018: this was a clear verification of the performance of the telescope structure [86]. In 2019 the CHEC-S prototype camera was installed on the ASTRI-Horn prototype telescope structure; some events taken during the ASTRI-CHEC tests campaigns carried are shown in Figure 3.39. See [87] for further information.

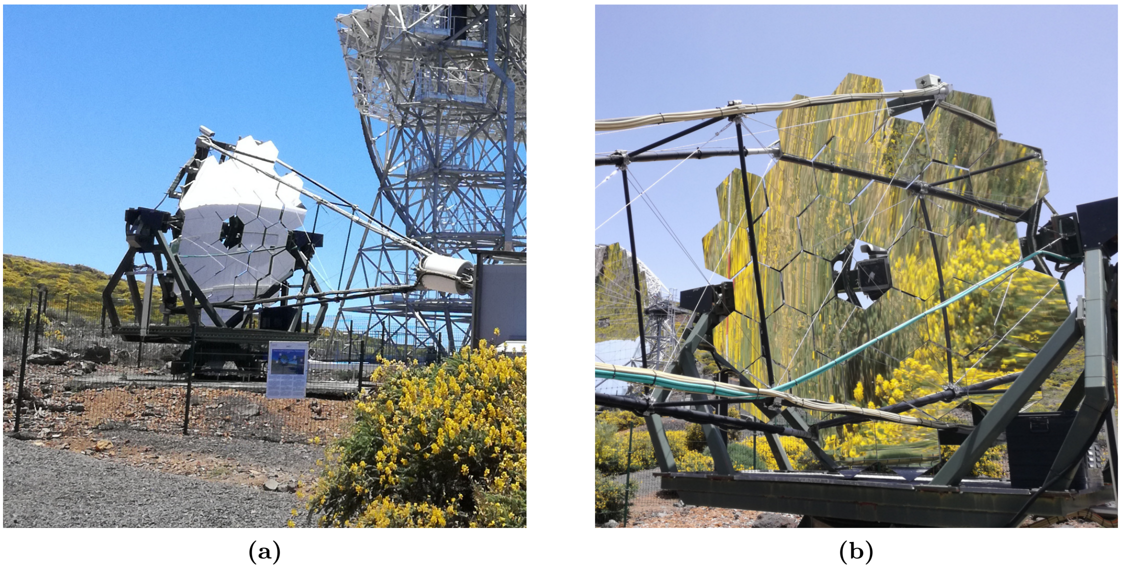

(a) **(b)**

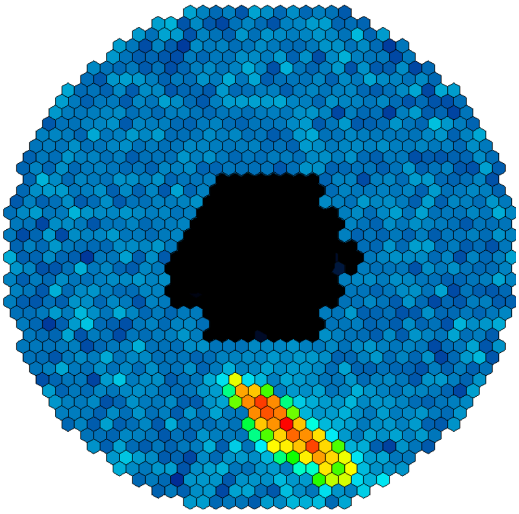

(c)

Figure 3.35: (a) The FACT telescope at the Observatorio de Roque de los Muchachos on La Palma (Canary Islands, Spain) in parking mode; its mirror diameter is about 3.5 m
(b) The mirror surface
(c) An event while tracking the full Moon on the 23th June 2013. For this measurement, the power for the central patches was disabled [82].

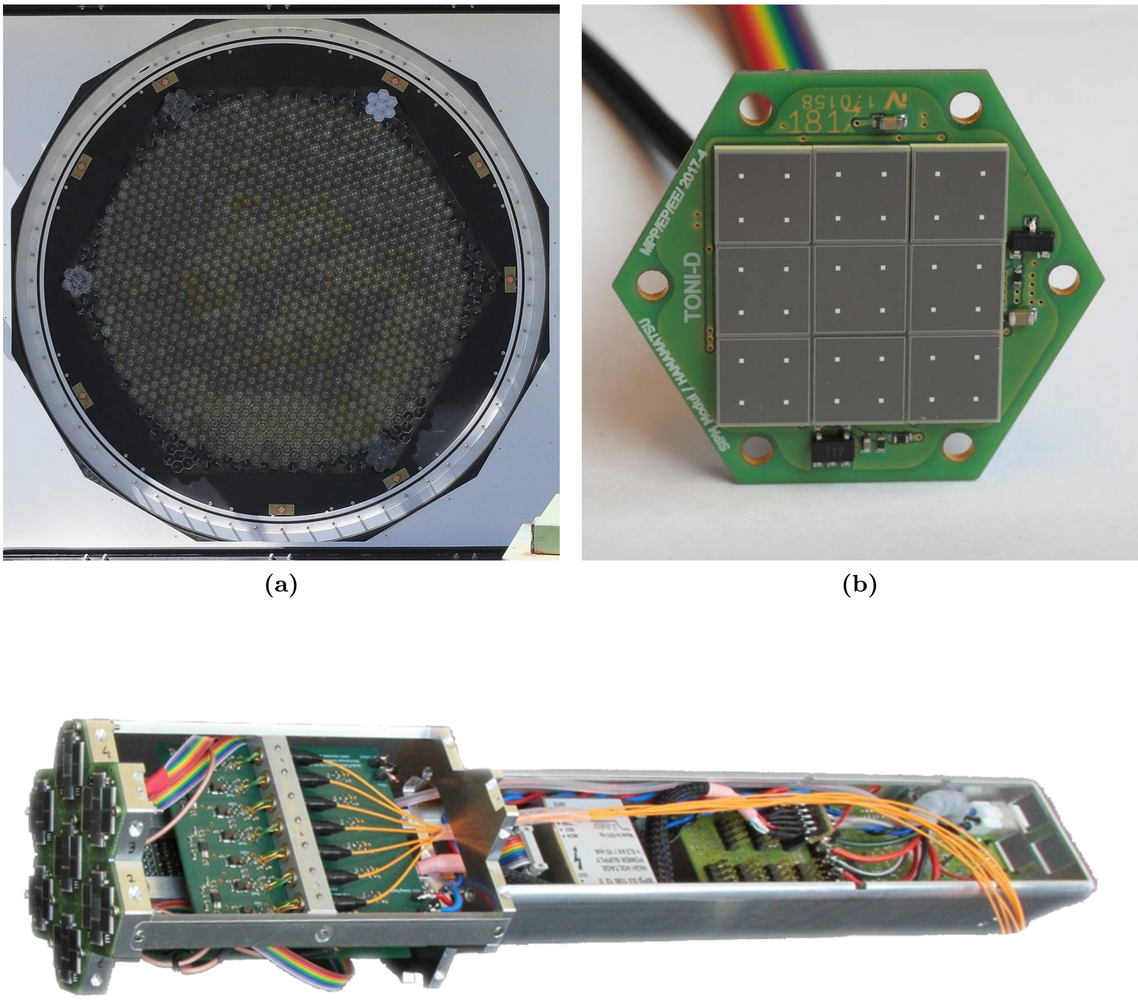

(a) (b)

(c)

Figure 3.36: (a) MAGIC M1 camera
(b) The Hamamatsu prototype installed in MAGIC M1 camera, equipped with nine Hamamatsu S13360-6075VS SiPMs (6 mm × 6 mm) [88]
(c) MAGIC SiPM cluster

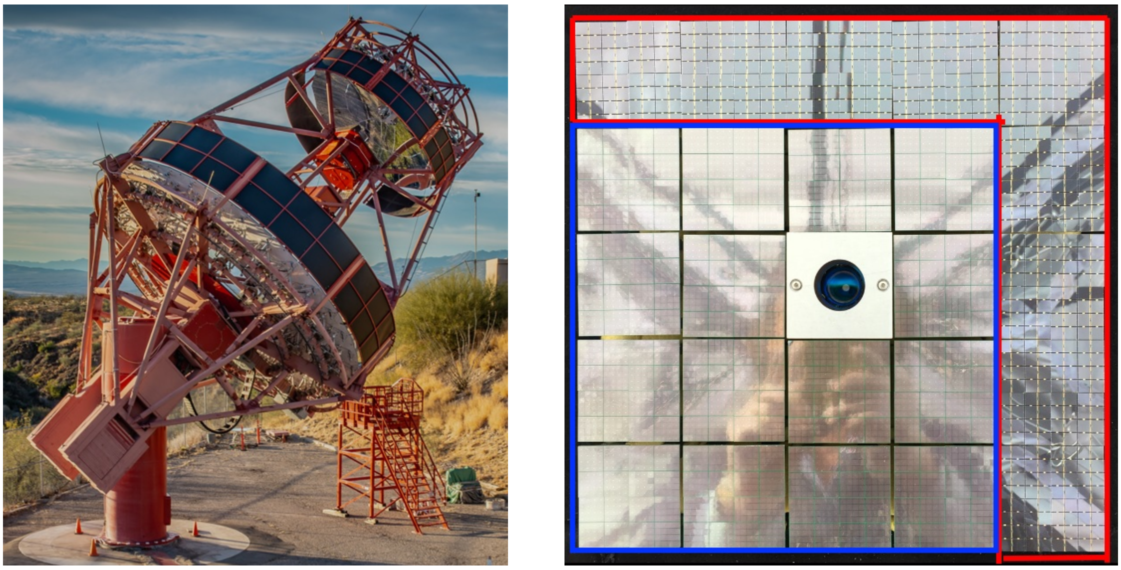

(a) **(b)**

Figure 3.37: (a) Picture of the pSCT installed at he Fred Lawrence Whipple Observatory in Arizona, USA [85].
(b) Picture of the partial pSCT camera; in red the FBK SiPM modules, in blue the Hamamatsu ones [85].

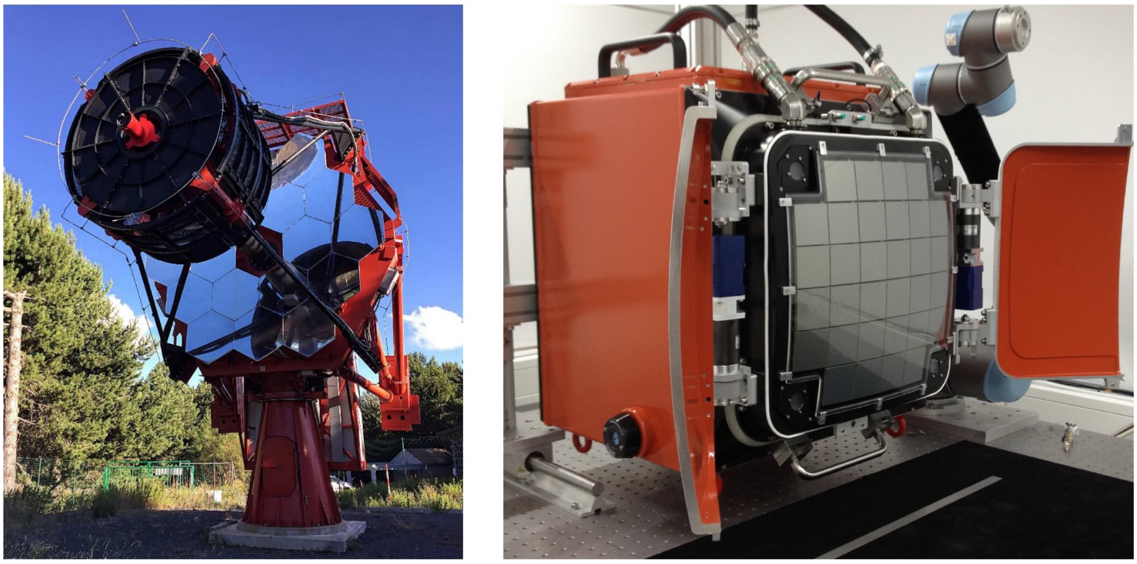

Figure 3.38: Left: the ASTRI-Horn telescope prototype at the Catania Astrophysical Observatory (Serra La Nave, Mount Etna) [87].
Right: the CHEC-S camera prototype [87].

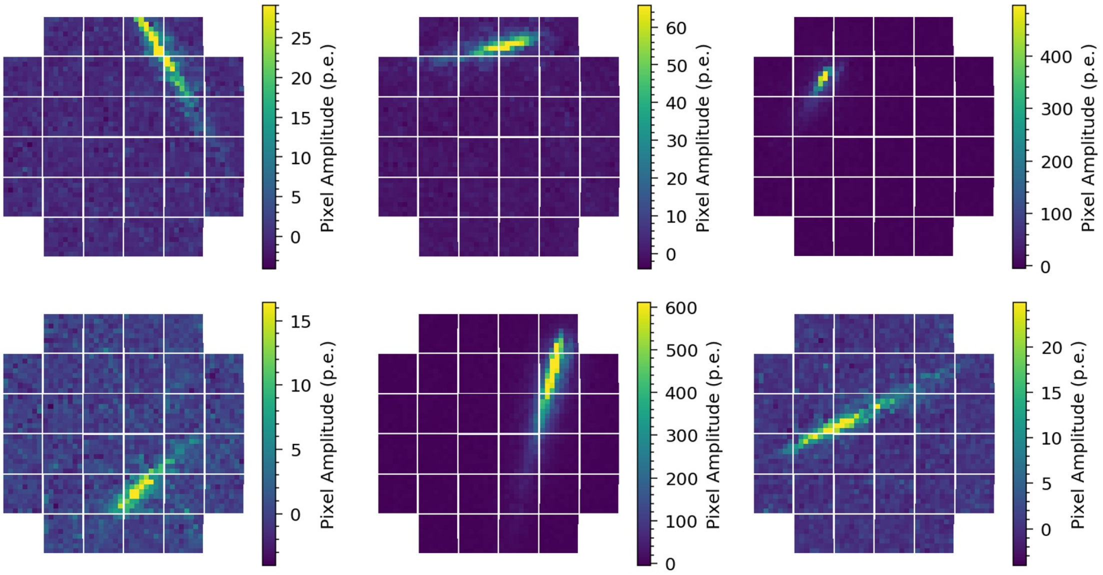

Figure 3.39: Events recorded with CHEC-S on the ASTRI-Horn telescope [87]

Chapter 4

Development of a SiPM Pixel Prototype

While photomultiplier (PMT) technology is mature and reliable, recently Silicon Photomultipliers are emerging as promising competitors also for atmospheric Cherenkov applications. The possibility that the advantages outweigh the drawbacks is very high: the feasibility of using a SiPM technology for IACT applications has been demonstrated for small scale telescopes and moreover the First G-APD Cherenkov Telescope (FACT) has shown the stability and reliability of this solution in the long term, alongside the possibility to operate under moon light conditions, allowing a significant increase in duty cycle [78]; furthermore the CTA Small Size Telescopes and the Dual Mirror Medium Size Telescopes will use this technology [84].

The aim of this work is to realize a pixel prototype for a SiPM-based camera for the LST telescope in the CTA observatory. Starting from the work done by the LST collaboration, the idea is to keep most of the existing camera readout: referring to Figure 4.1, we keep all the detector to the Slow Control Board, replacing only the so-called Pixel Unit (composed of the Cockcroft–Walton generator, the Preamplifier and the PMT) with a SiPM pixel.

This work is a useful test bench both to study possible front-end solutions and to develop a slow control circuit which can be applied on future SiPM-based cameras for IACT experiments. The use case is a large-sized telescope, where the background light on

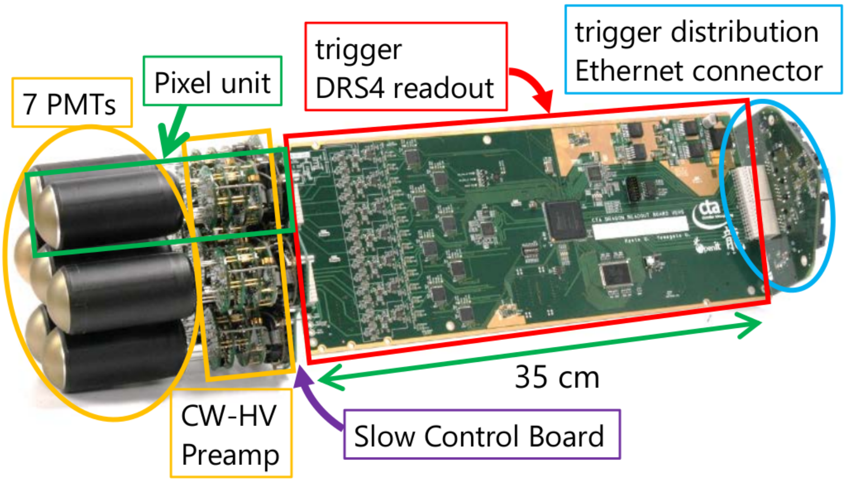

Figure 4.1: CTA-LST existing electronic chain [89]. Only the Pixel Unit (composed of the Cockcroft–Walton generator, the Preamplifier and the PMT) is replaced with a SiPM pixel

the focal place due to the NSB is higher than in the case of smaller telescopes; this aspect must be carefully considered during the design.

The development was focused to emphasize probably the main advantages of SiPMs over PMTs for our application, i.e.:

- sensor robustness;
- tolerance to high illumination levels.

It is therefore possible to observe with SiPMs in illumination conditions that are not suitable for traditional photomultipliers, thus leading to an increase in the duty cycle of the experiment. In addition, their robustness would improve the reliability of the system: indeed, exposing the PMTs to day light, even with their high voltage off, can seriously damage them.

To make the most of those features, it is necessary to build protection for the electronics, not to destroy it: indeed, although SiPMs can withstand several milliamps of current, maybe the front-end electronics cannot. In this situation the pixel would break, and the full potential of the sensors could not be exploited. In addition, it is clear that it is not enough to make sure that the pixel does not get damaged in high illumination conditions, but it is necessary to develop solutions in order to be able to see signals also in a high background environment.

From Monte Carlo simulations performed on a SiPM camera, we obtained a night sky background rate of about 1.5 GHz in dark condition and without any filter on the camera window. This high rate places constraints on the signal duration: indeed, the longer the signal, the higher the trigger threshold to be set in order not to be completely dominated by the background noise. For this reason, we will try to have the shortest possible signal; only detailed Monte Carlo simulations can more accurately fix this constraint.

In order to keep the same camera geometry (number and dimension of pixels), we need to cover an area comparable to the PMT with SiPMs; to be more precise, it is enough to cover the area below the Winston cone light guides, mounted on top of the PMT photocathodes in the LST nominal camera. The desired surface can be covered with twelve 6 mm × 6 mm SiPMs summed together. For the front-end there are two possibilities: either to rely on a discrete element circuit, or to use an existing ASIC. Given the number of channels involved and the required bandwidth, we opted for the second solution. For the realization of a future complete advanced camera, it is considered the development of a dedicated ASIC. However, especially if the pixel of the final camera will have a smaller size (and therefore it will be sufficient to sum together fewer SiPMs), a solution with discrete elements will also be carefully evaluated.

The chosen front-end circuit for this prototype is the Multiple Use SiPM Integrated Circuit (MUSIC), developed at the Institute of Cosmos Sciencies - University of Barcelona (ICCUB). We will briefly discuss its main characteristics in section 4.2.

Since the projects starts from the photomultiplier tube readout system designed for the Large-Sized Telescope, we will discuss briefly its main characteristics in the following section.

4.1 Large-Sized Telescope Camera Modules

The focal plane of the Large-Sized Telescope (LST) of the Cherenkov Telescope Array (CTA) hosts 265 modules with seven pixel units each, for a total of 1855 PMTs. A picture of a module can be found in Figure 4.1. Each module consists of seven PMT pixels, a Slow Control Board and a Domino Ring Sample 4 (DRS4) board. The module is connected to a 24 V power supply. Each pixel unit consists of a PMT, its Cockcroft-Walton high voltage supply and a preamplifier ASIC named PACTA [90]. The block diagram of a 7-PMT camera module can be found in Figure 4.2.

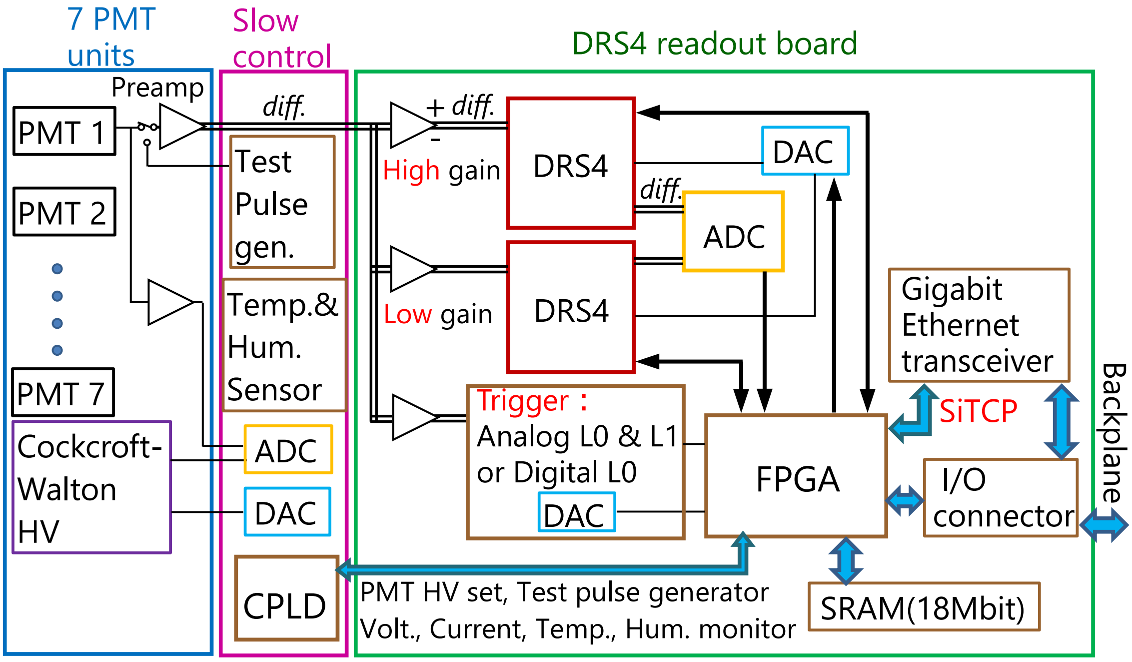

Figure 4.2: Camera module block diagram [89]

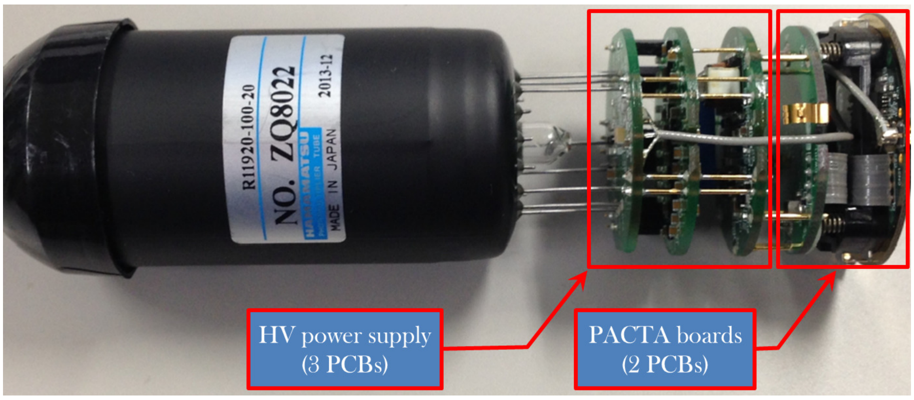

Figure 4.3: A picture of the LST PMT pixel unit [91]

4.1.1 Pixel Unit

The LST camera has 1855 pixel units, each one composed of a PMT, its Cockcroft-Walton high voltage supply and the PACTA preamplifier. A picture of the LST PMT pixel unit can be found in Figure 4.3. A Winston cone light guide (not shown) collects the light on the PMT photocathode.

Photomultiplier

The LST photomultipliers are the Hamamatsu R11900-100, developed in collaboration with Hamamatsu Photonics K.K. (Japan) for this application [92]. They have a diameter of 1.5 inch (38 mm), they contain seven dynodes and their operational bias voltage is about 1 kV.

In Figure 4.4 it is shown the quantum efficiencies of some R11920-100-20 PMTs produced for the first LST camera. Their average peak quantum efficiency is about 40 % at 340 nm – 360 nm and has almost a flat shape between 300 nm to 400 nm. The pulse width is between 2.6 ns and 3.0 ns, varying their bias voltage between 800 V and 1200 V. They have an after-pulsing rate lower than 0.02 %, evaluated with a threshold setting of 4 photoelectrons. To reduce the noise pick-up the PMT is shielded with a light aluminum foil [91].

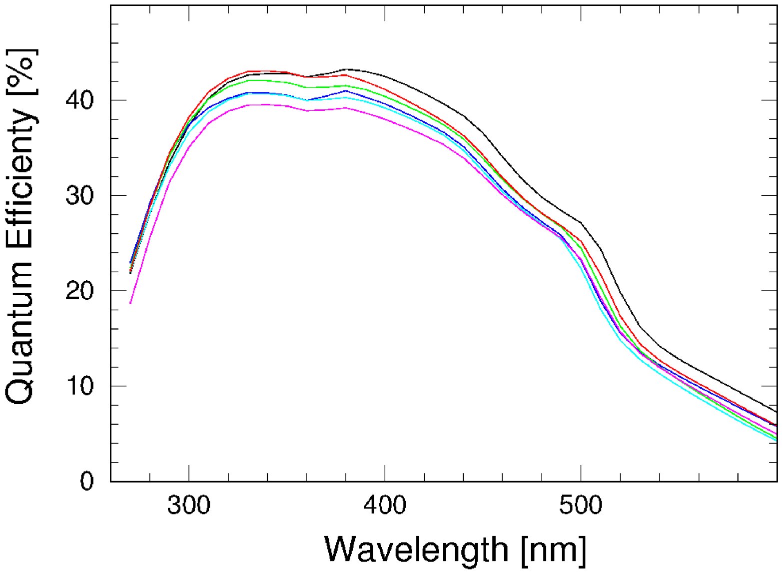

Figure 4.4: Quantum efficiencies of some PMTs R11920-100-20 produced for the first LST camera measured by Hamamatsu Photonics [91]; each color corresponds to a different PMT sample

Cockcroft-Walton High Voltage Supply

The PMT power supply electronics is based on a Cockcroft-Walton design, and is implemented on three different Printed Circuit Boards (PCBs), as we can see in Figure 4.3.

The voltage between the photocathode and the first dynode is stabilized by means of a Zener diode; in this way the gain and the photoelectron collection efficiency of the first dynode is kept constant. It is possible to set the PMT high voltage between 850 V and 1500 V by varying the a control voltage between 0.85 V and 1.5 V. The high voltage stability and ripple are within 1 V. The system includes moreover a filter for the HV power supply and a current limiter to protect the PMT in case of too high illumination (for example, a star in the field of view).

The HV power supply during standard operation sets the PMT gain at 4×10^4 to reduce the ageing of the sensor (the requirement is that the PMT should have a lifetime longer than ten years while being exposed to the night sky). The power consumption is about 35 mW [91].

Preamplifier

Due to the low gain of the PMT, it is necessary to use a preamplifier. It should be located as close as possible to the sensor: the last part of the PMT pixel unit is therefore the Pre-Amplifier for CTA (PACTA) ASIC [90]. The top and bottom layer of the PACTA board is shown in Figure 4.5; the chip is visible on the top layer (Figure 4.5a), while the connector on the bottom layer (Figure 4.5b) is the one which connects the PMT Pixel Unit to the Slow Control Board.

The PACTA ASIC is a current mode amplifier specifically designed for IACT applications. It has a bandwidth of 500 MHz and an input impedance lower than 20 Ω. The equivalent noise charge (ENC) is lower than 5000 electrons, allowing the discrimination of the single photo electrons, and its power consumption is lower than 150 mW.

It has two gain lines (1200 Ω and 80 Ω), both with differential outputs. In Figure 4.6 are shown the high gain and low gain differential output for different input pulse amplitudes; the injected input pulse has a shape comparable to the single photoelectron pulse (SPE). The high gain saturates for input peak currents higher than 1 mA, the low gain still operates properly; the global input range is about 20 mA.

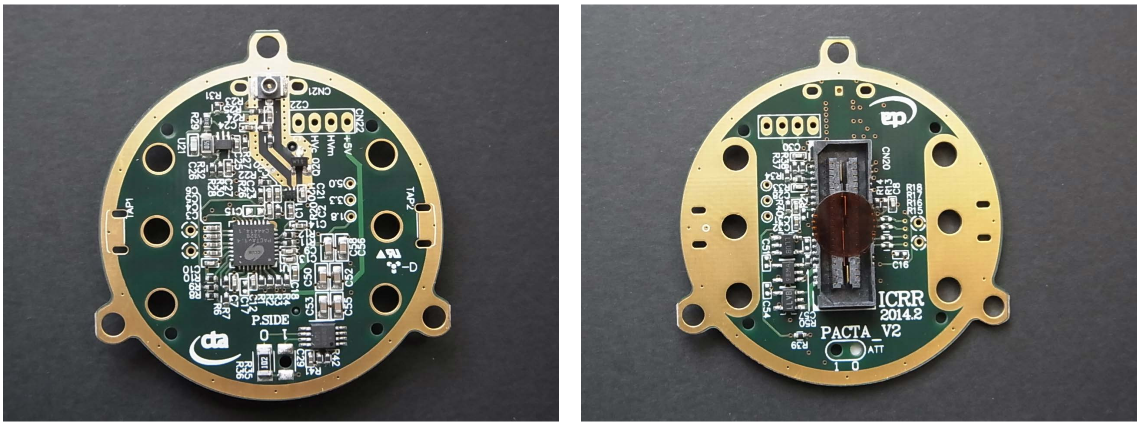

(a) (b)

Figure 4.5: Top layer (a) and bottom layer (b) of the PACTA board [91]

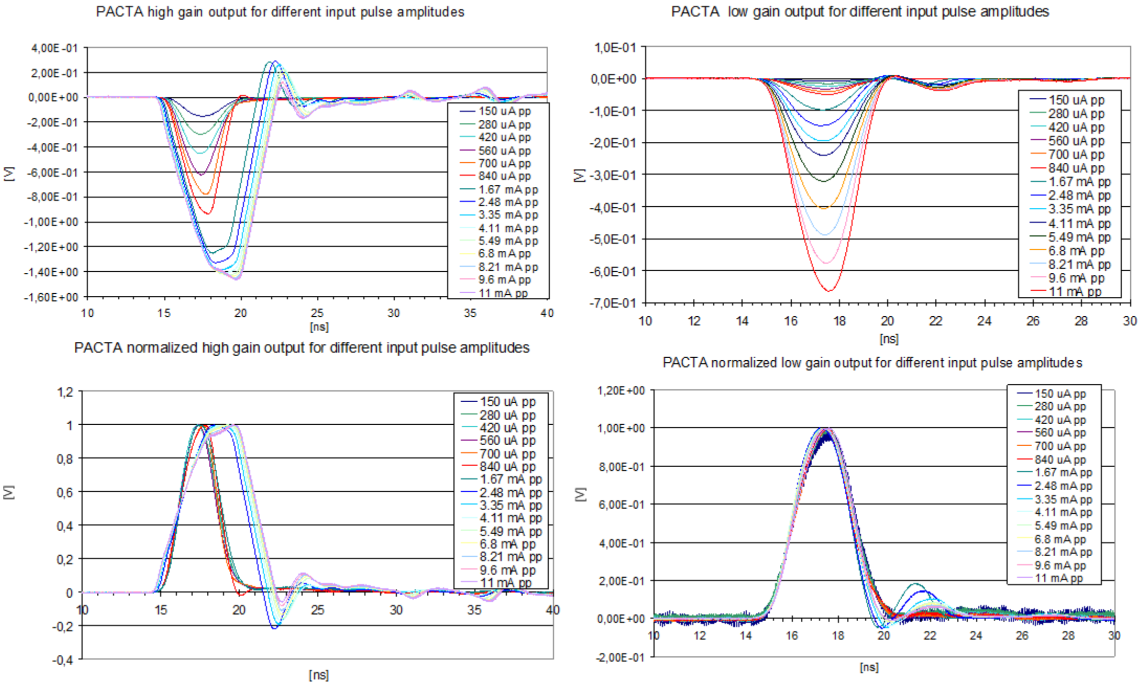

Figure 4.6: PACTA high gain (top left) and low gain (top right) differential output for different input pulse amplitudes. The injected input pulse has a shape comparable to the single photoelectron pulse (SPE). The normalized output signals are shown at the bottom [90].

4.1.2 Slow Control Board

The Slow Control Board is the board which connect the DRS4 readout board to the PMT pixel units. A picture of the two sides of the SCB is shown in Figure 4.7. Its main task is to control and monitor independently the PMT pixel units.

By means of a Digital to Analogue Converter (DAC) it controls the Cockcroft-Walton High Voltage supply, and monitors the Cockcroft-Walton High Voltage supply, the PMT anode DC currents, the pixel temperatures thanks to an Analogue to Digital Converter (ADC). In addition, a temperature and humidity sensor is installed on the board. The board hosts a Complex Programmable Logic Device (CPLD), which communicates via Serial Peripheral Interface (SPI) with the FPGA of the readout board.

The SCB can also generate a pulse similar to the PMT one for testing purposes; this pulse is injected into the preamplifier board and propagates along the whole electronic chain. With this method it is possible to carry out tests also during the day.

The SCB power consumption is about 22 mW in standard operation mode and about 1221 mW during pulse injection [93].

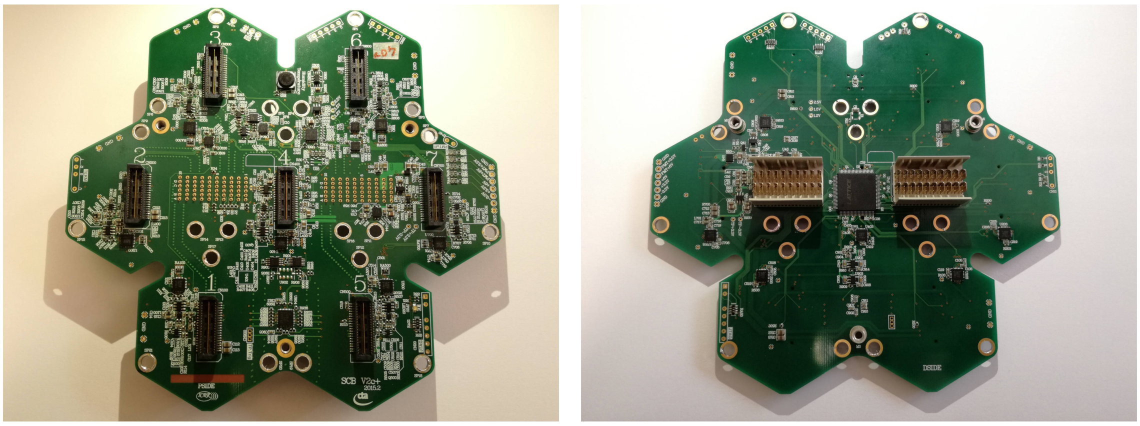

(a) **(b)**

Figure 4.7: Picture of the Slow Control Board: (a) connection to the PMT pixels; (b) connection to the DRS4 readout board

4.1.3 DRS4 Readout Board

Figure 4.8 shows the front side (top) and back side (bottom) of DRS4 readout board; its size is 35 cm × 13.6 cm. The Slow Control Board (SCB) is connected on the left and the Backplane Board on the right.

On the DRS4 readout board the differential signal coming from the PACTA preamplifiers is divided into three lines: a high gain line, a low gain line and a trigger line. Both high gain and low gain lines are sampled by the DRS4 chip (red) at 1 GHz. The trigger line, as the name suggests, is used to generate the first level trigger. When this signal is generated, the high gain and low gain stored waveforms are digitized by an external ADC (yellow) at a rate of about 33 MHz. These digitized waveforms are then transferred to a Xilinx Spartan-6 field programmable gate array (FPGA) and sent through the backplane board to the data storage server via the Gigabit Ethernet transceiver. On the board we can also find a static random access memory (SRAM) capable to store 18 Mbits of data and digital-to-analog converter (DAC) used to correct the input and output ranges of DRS4 chips. The DRS4 chips, the SRAM, the DAC and ADC are controlled by the FPGA. Moreover, the FPGA communicates with the complex programmable logic device (CPLD) host on the SCB and with another FPGA located on the backplane board via serial peripheral interface (SPI). The power consumption without pixels is about 18.48 W [89].

DRS4

The Domino Ring Sample is a Switched Capacitor Arrays (SCA) developed for the Mu to Electron Gamma (MEG) experiment at the Paul Scherrer Institute (PSI), Switzerland [94]. The chip can sample 9 differential input channels with 950 MHz bandwidth at a sampling speed which can be set from 700 MSPS to 5 GSPS. Each channel has 1024 sampling cells to store the analog waveform, a chain of inverters generates the write signal for the sampling cell with the domino principle; this domino-wave runs continuously until it is stopped by a trigger. This waveform can be later read out for external digitalization via a shift register clocked at 33 MHz. The chip offers a low noise of only 0.35 mV and a low power consumption of 17.5 mW per channel at 2 GSPS. Moreover, it is possible to cascade up to eight channels to obtain deeper sampling depth [95].

Compared to fast ADCs (FADCs), the Switched Capacitor Arrays are cheaper, smaller and less power consuming; for this reason, they are widely used in experiments which require many channels and high sampling speed. The latest version of the Domino Ring Sample chip, the DRS4, is already successfully used in the MAGIC experiment.

The readout board hosts eight DRS4 chips, each one connected to two PMT channels (high gain and low gain). Four DRS4 channels are cascaded, in order to sample each waveform with 4096 capacitors (corresponding to a sampling depth of about 4 µs at 1 GSPS) [89].

Main Amplifier

The main PMT amplifier is designed to achieve a bandwidth higher than 300 MHz and a dynamic range up to 2000 photoelectrons. Each channel has five Analog Devices ADA4927 high speed current feedback amplifiers [96]; the block diagram of the main amplifier is shown in Figure 4.9, together with a photo of the circuit. Since four DRS4 channel are cascaded, each signal line goes to four DRS4 inputs. From simulations it was demonstrated that by increasing the number of amplifiers on the signal line the capacitance load per

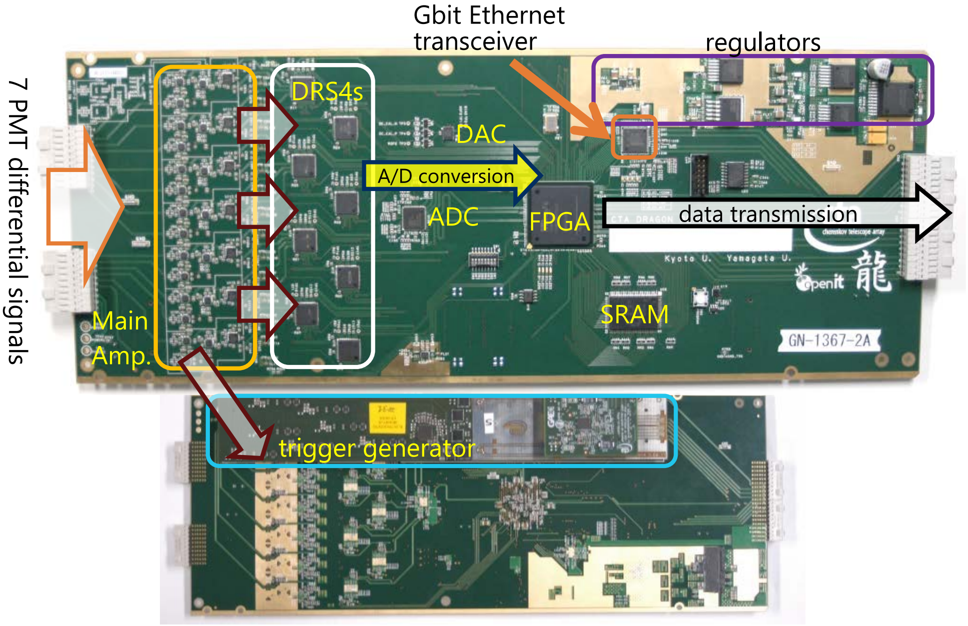

Figure 4.8: Front side (top) and back side (bottom) of DRS4 readout board [89]

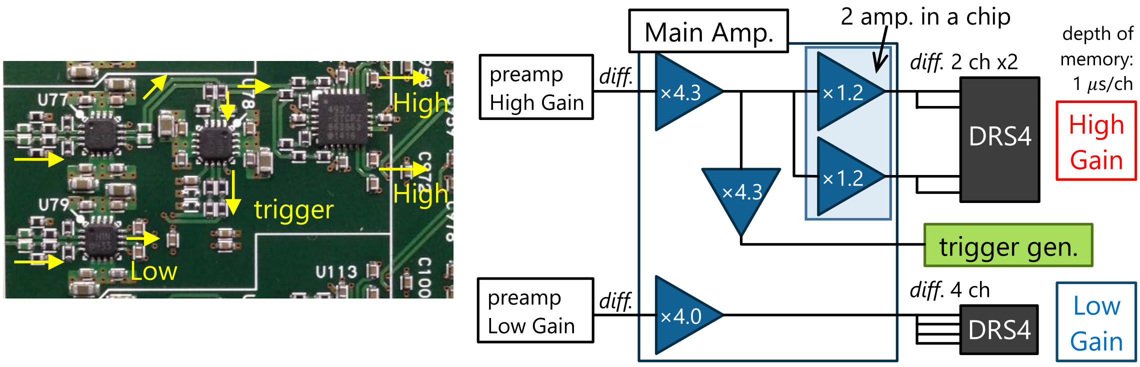

Figure 4.9: Picture of the main amplifier (left) and its block diagram (right) [89]

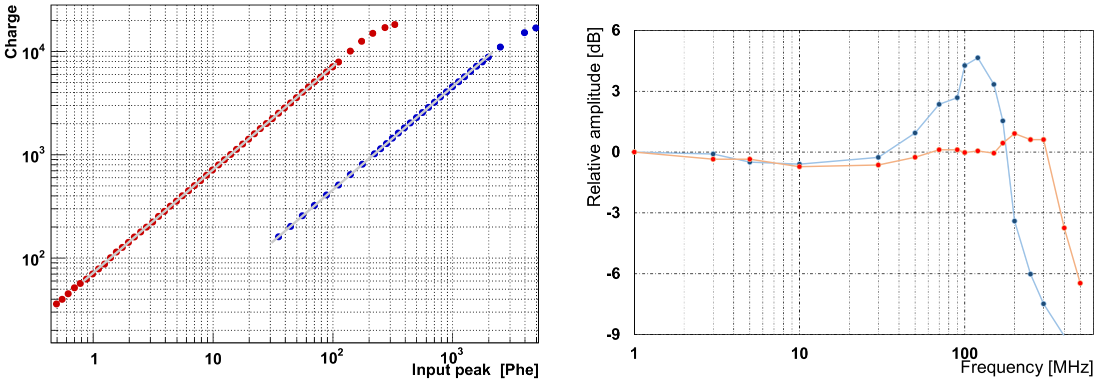

(a)

(b)

Figure 4.10: Main amplifier test results: dynamic range (a) and bandwidth (b) of high gain (red) and low gain (blue) lines [89]

amplifier will decrease, increasing in turn the bandwidth: this is the reason why the last stage of the high gain line has two separated amplifiers, each one connected to two DRS4 inputs [89].

Some test results carried out on the main amplifier circuit are below reported. Concerning the linearity, the main amplifier is linear within 5 % in the dynamic range between 1 to 2000 photoelectrons (Figure 4.10a). Figure 4.10b shows the bandwidth measurement for high gain and low gain lines. The high gain line has a bandwidth higher than 300 MHz, while the low gain one has a lower bandwidth, about 180 MHz [89].

Trigger Mezzanines

Two types of trigger logic have been developed, both an analog trigger and a digital one. Concerning the analog one, the level 0 and level 1 (L0, L1) trigger mezzanines are mounted on the DRS4 readout board (Figure 4.8). L0 trigger is the sum of the seven PMT signals, and its pulse distributed to the L1 mezzanines on neighboring modules by the backplane board. On L1 mezzanines, L0 pulses are summed and discriminated; in this way the energy threshold can be decreased. Concerning the digital trigger, only the L0 one is implemented, based on a geometrical pixel hit pattern trigger logic. The readout board is compatible with both trigger types, which can be selected by changing the mezzanines [89]. In the actual LST-1 camera only the analog trigger is used.

4.2 Multiple Use SiPM Integrated Circuit (MUSIC)

The Multiple Use SiPM Integrated Circuit (MUSIC) is an eight channel ASIC for SiPM anode readout designed for many applications, including IACT experiments. It is based on a low input impedance current conveyor and offers many functionalities for SiPM readout and summation. In the next sections we will describe briefly the MUSIC main characteristics; a more detailed description can be found in [97] and [98].

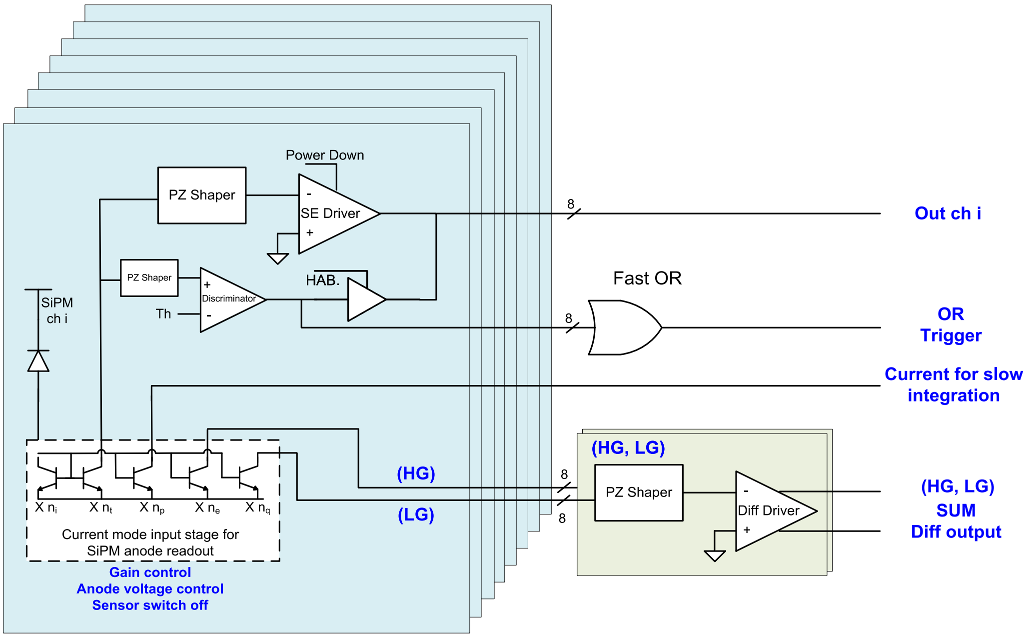

Figure 4.11: MUSIC block diagram [97]

4.2.1 Architecture

The MUSIC block diagram is shown in Figure 4.11. Below we will explain its main components, without going much into the details.

Input Stage

The first stage is an eight channels bipolar current mirror with double feedback loop, designed to provide a low input impedance, fundamental for SiPM readout. A low frequency feedback loop controls the DC voltage in the input node, while a high frequency feedback loop keeps constant the input impedance at different frequencies, in order not to affect the SiPM timing performances. In addition, its design ensures that the stability of the circuit is not compromised when a high capacitance is added at the input.

The input currents are split into different copies, each one related to a different functionality:

- Sum of signals in differential mode (two gain lines, high gain and low gain)
- Individual analog single ended channels
- Digital channels
- Fast OR signal
- Integrator current

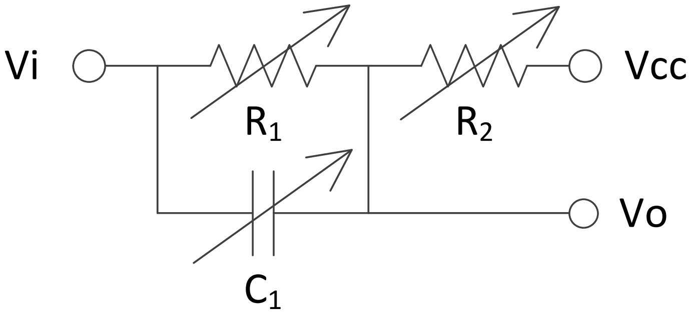

Figure 4.12: MUSIC pole-zero cancellation circuit [97]

The input stage has an input impedance of 32 Ω in the bandwidth of interest. In addition each channel offers an anode voltage control, to adjust the SiPM bias voltage; this voltage is configured by an internal DAC with 1 V (9 bit) dynamic range. This option is very useful in case of common cathode SiPM arrays connected to the same high voltage: since every SiPM will have a slightly different breakdown voltage, with this anode correction it is possible to compensate its non-uniformity, and therefore have the same gain for all SiPMs. Each channel can be individually disabled.

Pole-Zero Cancellation

The MUSIC ASIC contains a tunable pole-zero cancellation (PZ) circuit to shape the SiPM signals; with this option it is possible to reduce the peak duration of the signals and to reduce their tails. The pole-zero cancellation can be used or bypassed in any operation mode.

The PZ shaping circuit is shown in Figure 4.12. The signal after the PZ compensation will be:

$$\begin{aligned} V_O &= V_I \frac{R_2}{R_2 + R_1 \| \frac{1}{sC_1}} = \\ &= V_I \frac{R_2}{R_2 + \left(\frac{1}{R_1} + sC_1\right)^{-1}} = \\ &= V_I \frac{R_2}{R_2 + \frac{R_1}{1+sR_1C_1}} = \\ &= V_I \frac{R_2(1+sR_1C_1)}{R_2 + sR_1R_2C_1 + R_1} \end{aligned}$$

Therefore:

$$V_O = V_I \frac{R_2}{R_1 + R_2} \frac{1 + sR_1C_1}{1 + s(R_1 \| R_2)C_1} \tag{4.1}$$

The resistor and the capacitor values can be tuned to find the required signal shaping.

The resistor configuration depending on the selected resistor ladder R_{lad} are reported in Table 4.1. By increasing the pull-up resistor R_2, the current removed from input will be decreased, and therefore the signal will be less attenuated. The resistance ladder has a bit (Low Attenuation, LA) to decrease the R_1 value, and thus to decrease the signal attenuation. The value of C_1 is instead set by a 5 bit capacitance ladder which follows a linear distribution starting at 1.2 pF with steps of 0.1 pF.

Summation Circuit

One or more (up to eight) SiPM signals can be summed by means of an analog transistor circuit. Each channel, even if active, can be disconnected from the summing module.

R_{lad}	R_1 (LA OFF) (Ω)	R_1 (LA ON) (Ω)	R_2 (Ω)
0	46 500	18 600	7650
1	48 300	20 400	5850
2	50 100	22 200	4050
3	51 900	24 000	2250
4	52 350	24 450	1800
5	52 800	24 900	1350
6	53 250	25 350	900
7	53 700	25 800	450

Table 4.1: Pole-zero resistance ladder configuration [98]

Thus, it is possible to keep a channel enabled but do not sum its signal: it is therefore possible to have the single ended (SE) signal of one channel which does not enter in the summation module. The sum of the input SiPM signals is given in differential mode for two different gain configurations (low gain and high gain).

4.2.2 Functional Modes Characteristics

In this section we report the main characteristics of the various MUSIC functionalities. All these functionalities can be set and tuned via Serial Peripheral Interface (SPI).

Analog Summation

The SiPM input signals can be summed, shaped and amplified by an analog summation circuit. Each channels can be controlled individually.

The chip provides two different outputs with different gains, named Low Gain (LG) and High Gain (HG). In addition, the analog summation circuit provides two different trans-impedance gain (Zt) configurations: the sum of SiPM signals can be therefore performed with four different gains:

- High Zt configuration:
  - High Gain: 690 Ω
  - Low Gain: 90 Ω
- Low Zt configuration:
  - High Gain: 315 Ω
  - Low Gain: 45 Ω

The maximum inputs for the High Gain and Low Gain depend also on the selected trans-impedance gain configuration and are the following

- High Zt configuration:
  - High Gain: 1.8 mA peak
  - Low Gain: 13.9 mA peak
- Low Zt configuration:
  - High Gain: 3.9 mA peak
  - Low Gain: 27.8 mA peak

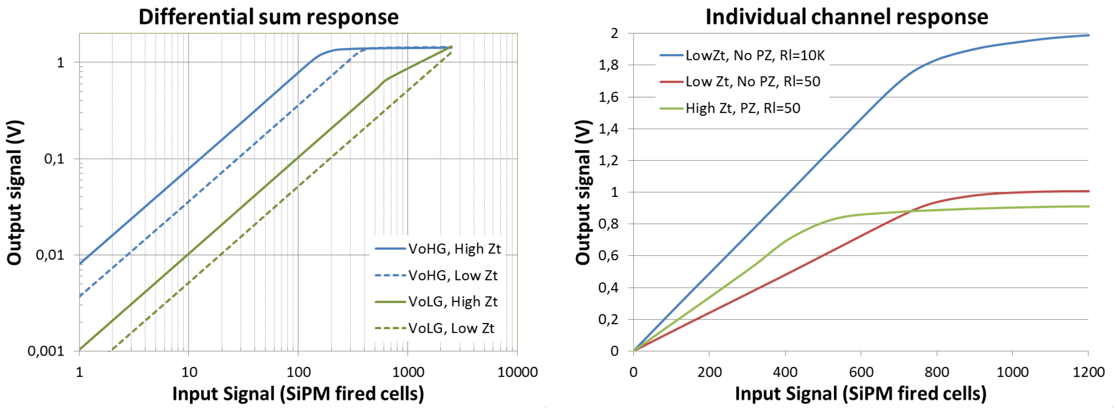

(a) (b)

Figure 4.13: (a) MUSIC sum block linearity, single cell signal is normalized to 12 µA peak [97]
(b) MUSIC SE linearity, single cell signal is normalized to 8 µA peak [97]

It is possible to configure the pole-zero cancellation to reduce the signal duration; full width at half maximum (FWHM) lower than 10 ns can be reached, depending on the used SiPM. The pole-zero cancellation can be bypassed. The bandwidth of the summation block is 500 MHz and its power consumption is about 200 mW while summing all eight channels.

The output dynamic range goes from 0 V to 1.25 V. As we can see from Figure 4.13a, the sum of signals has a linear response in the whole dynamic range. In the plot the single cell signal is normalized to 12 µA peak.

Analog Single Ended Output

The ASIC can provide also the individual SE signals of the connected SiPMs. Each channel can be shaped with the pole-zero cancellation circuit.

Also in this case we can select two different trans-impedance gains (Zt) configurations, which have the following gains:

- High Zt configuration: 480 Ω
- Low Zt configuration: 180 Ω

As for the analog summation, the single ended individual signal maximum inputs depend on the selected trans-impedance gain configuration. In addition, they also depend on the load, whether it is high impedance or 50 Ω:

- High Zt configuration:
  - High impedance load: 4.16 mA peak
  - 50 Ω load: 2.08 mA peak
- Low Zt configuration:
  - High impedance load: 11.1 mA peak
  - 50 Ω load: 5.5 mA peak

Considering the output noise, in low Zt configuration it is lower than 600 µV on high impedance loads and lower than 300 µV on 50 Ω loads. The bandwidth is higher than 150 MHz and the power consumption is about 30 mW per channel.

The output dynamic range (without pole-zero cancellation) is 2 V on high impedance loads and 1 V on 50 Ω loads. The analog single ended output has a linear response only in the first half of its dynamic range, as we can see in Figure 4.13b, where the single cell is signal normalized to 8 µA peak.

Digital Output

Each channel can be configured to give a digital output, obtained thanks to a preamplifier, a shaper and a discriminator with programmable threshold. This output is a binary signal encoding the charge collected in the duration of digital signal, using a time over threshold technique. The digitalization can be then performed on a FPGA. Since the output pad is the same both for digital and analog SE signal, it is possible to have only one of the two outputs for a given channel. Also in this case it is possible to tune the pole-zero compensation before the comparator; this option can be bypassed. By setting an aggressive shaping it is possible to perform photon counting measurements. The static power consumption is negligible.

Other Output Features

In addition to those described, the MUSIC has two additional functionalities. A current for an external slow integrator is provided for current monitoring. In addition a fast OR signal is delivered and can be used as a trigger; this signal is the logic OR of all the digital signals.

4.2.3 Application Information

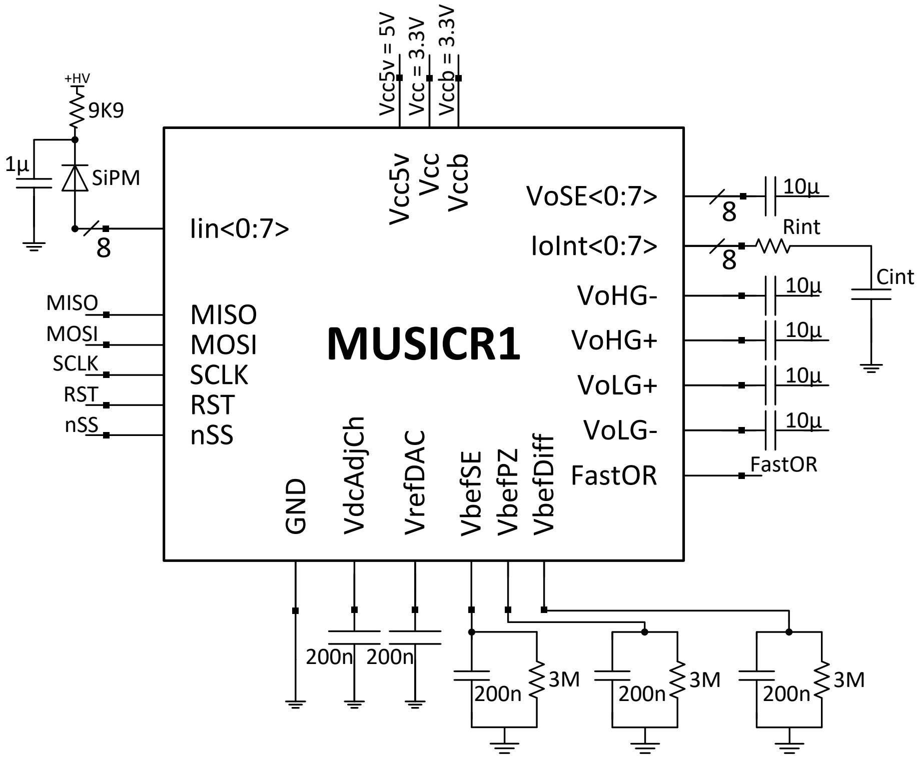

Figure 4.14: MUSIC typical application [98]

The MUSIC chip is based on the AMS 0.35 µm SiGe BiCMOS technology, and it can operate between −40° to 125°. The temperature range for storage is from −65° to 150°. It is delivered in a 64-QFN 9 mm × 9 mm package, encapsulating the 9 mm^2 (3274 µm × 2748 µm) chip. The MUSIC typical application can be found in Figure 4.14.

Eight SiPM anodes can be directly connected to the input channels; the sensors should be powered by and external voltage source. There is no precise limit for the maximum current that can flow into this MUSIC input pins. A safety limit is 1 mA shared by the eight channels; however it has been tested, after discussing with the MUSIC designers, that a current of 3 mA shared with six channels would not damage the device.

The MUSIC has three different power supply pins, two for the 3.3 V lines (V_{cc} and V_{ccb}), and one for the 5 V one (V_{cc5V}). Their maximum ratings and and typical current adsorption are reported in Table 4.2. A 1 µF capacitor should be placed as close as possible to each power pin in order to compensate transient high current consumptions.

Parameter	Maximum Voltage Rating	Typical current adsorption
V_{cc}	3.2 V to 3.4 V	47 mA
V_{ccb}	3.2 V to 3.4 V	84 mA
V_{cc5V}	4.9 V to 5.1 V	80 pA

Table 4.2: Supply voltage line maximum ratings and typical current adsorption [98]

The MUSIC ASIC is externally configurable via Serial Peripheral Interface (SPI). This connection is made by the standard four SPI signals:

- Master Input Slave Output (MISO)
- Master Output Slave Input (MOSI)
- Serial Clock (SCLK)
- Slave Select (nSS)

In addition, the device provides a reset pin RST.

The single ended (VoSE) and the two differential signals (VoHG+, VoHG-, VoLG+ and VoLG-) should be AC-coupled by means of proper external capacitors.

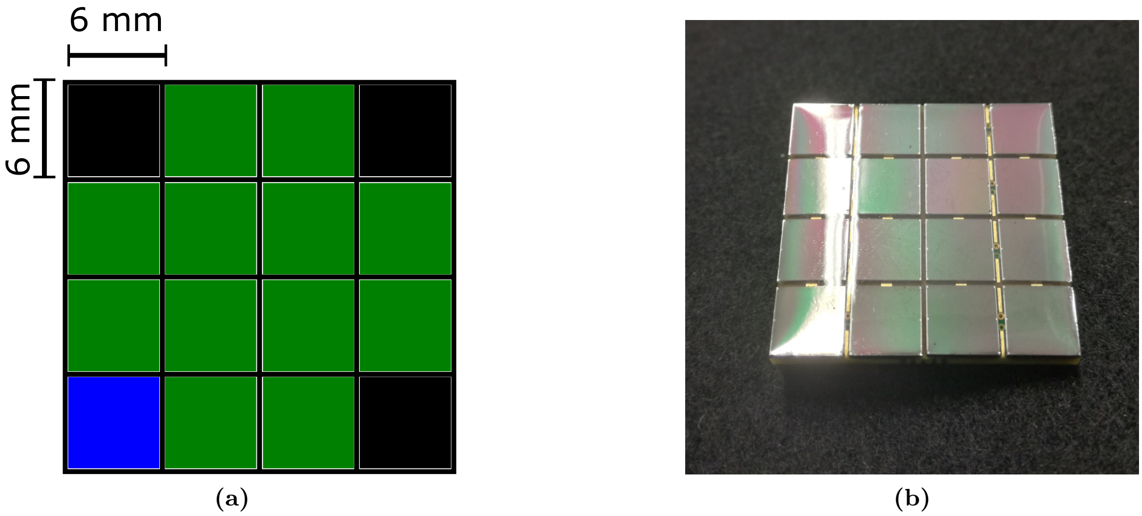

(a) **(b)**

Figure 4.15: (a) SiPM array scheme, with the pixel connected (green) and unconnected (black) during normal operation
(b) FBK NUV HD3-4 6 mm × 6 mm 4 × 4 SiPM array

4.3 SiPM Pixel Design

To cover a surface comparable to the area under the LST Winston cone light guides, at least twelve 6 mm × 6 mm SiPMs summed together should be used. To fasten the development, it was decided to use an already mounted 4 × 4 SiPM array, connecting only the inner SiPMs and discarding the outer ones. The conceptual idea is shown in Figure 4.15a, where in green are the connected pixels during normal operation, and in black the ones disconnected. The blue SiPM is used for calibration purposes: normally unconnected during standard operation, it is used as the reference sensor during the SiPM pixel calibration procedure. The SiPM arrays used in this prototype are the Fondazione Bruno Kessler (FBK) NUV HD3-4, developed for the Schwarzschild-Couder Telescope (SCT) of the Cherenkov Telescope Array (CTA). This solution was more convenient and cheaper than specifically developing a PCB hosting only the desired SiPMs. This second option will logically be followed in the construction of the full camera, where the light guides and the arrangement and shape of the sensors will be designed to fit perfectly.

Since the MUSIC ASIC has only eight channels, it is not possible to directly sum twelve SiPMs. The solution is therefore to use six MUSIC channels, each one connected to two SiPMs in parallel; in this way each channel is connected to an equivalent 12 mm × 6 mm sensor. We will refer to this connection as a *2P configuration*. It is important to point out that to solve this problem, another possibility could be to connect the sensor in series (*2S configuration*); in this case the SiPM bias voltage should set twice as normal. However, since all the SiPM cathodes in the array have the same bias voltage, this option cannot be pursued.

The global module rendering is reported in Figure 4.16. Starting from left, we find the Slow Control Board (SCB), the only part of the LST electronic chain here shown. Seven SiPM Pixel modules are connected to the board; each one is composed of:

- Pixel Main Board to SCB Adapter: a small PCB which connects the two boards; the connection is done with a Samtec connector on the SCB side and with a flat high-speed cable (not shown) on the Pixel Main Board side.
- Pixel Main Board: the PCB which hosts basically all the electronics of the pixel
- AC Filter Mezzanine: a mezzanine which can be added between the Main Board

and the SiPM array to filter the DC component of the signals

- SiPM array
- Thermometer PCB: a small board hosting a digital thermometer, in thermal contact with the back of the SiPM array (not shown)
- Power Cable PCB: a small board which acts as a mechanical adapter between the power cables and the Pixel Main Board (not shown)

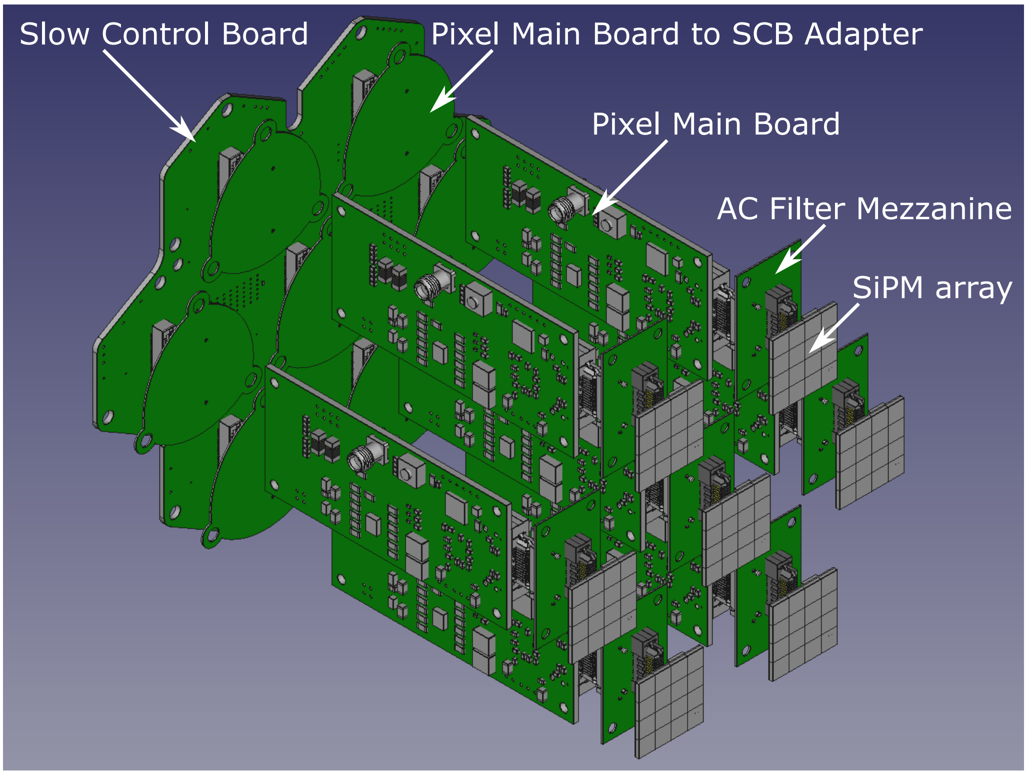

Figure 4.16: Global rendering

4.3.1 Block Diagram

The block diagram of the SiPM Pixel is shown in Figure 4.17. As already mentioned, this prototype uses most of the LST electronic chain, in particular the DRS4 readout board and the Slow Control Board (SCB).

A DC-DC Boost converter generates a voltage a few volts higher than the SiPM bias voltage; its output is connected to a *Voltage Regulator*, which is controlled by the Digital to Analog Converter (DAC) located in the SCB. The regulator output is connected to a *Current Limiter*, which takes care of limiting the current flowing in the channel, and to a two stages *Filter*. Both the current flowing in the SiPM and its bias voltage are read by two monitor circuits connected to the Analog to Digital Converter (ADC) host in the SCB. The front-end electronics is based on the MUSIC ASIC, which deals with the sum and shaping of the signals. The Regulator, the Current Limiter, the Filter, the Voltage and Current Monitors and the MUSIC are located in the Pixel Main Board. In order to be able to work even in high background environments, between the SiPM and the MUSIC it is possible to insert an AC filter, which takes care of removing the continuous component from the signals. This filter is located on a special mezzanine, which can be connected or not, in order to directly compare the DC and AC coupling in our application. The temperature near the SiPM is monitored by a digital thermometer; the value is sent to the SCB and therefore to the control software. As we know, the SiPM breakdown voltage is temperature-dependent: monitoring and appropriately correcting the bias voltage is therefore mandatory to always ensure the same sensor response.

The SiPM Pixels are more power demanding than the PMT ones. Due to their higher gain, the SiPMs will drain higher current; in addition, their signal has to be summed together with a fast (and therefore power-demanding) circuit. Considering our case, the front end (i.e. the MUSIC ASIC) cannot be powered from the LST electronics. For this prototype, an external power source is used. Concerning the DC-DC converter, it is known how these devices can affect the system noise; a lot of care has to be taken in the realization of their PCBs. Since this was outside the scope of this development, for tests based on the acquisition of signals, and therefore where an external noise could affect the results, we opted to use a low noise bench power supply.

The DRS4 Readout Board is connected to a Dummy Back Plane, which communicates via Ethernet to a computer running the LST data acquisition softwares (called *ZFitswriter* and *EventBuilder*). The acquired data are calibrated with the *cta-lstchain* [99] pipeline, developed for the LST data analysis.

The pixel development was done by using the MUSIC MiniBoard [100] as front end; this board is an evaluation board which hosts the MUSIC, an ATmega328P-AU microcontroller and other components useful for an easy ASIC evaluation. Once the best circuit solutions were found, a single board (*Pixel Main Board*) was printed; the MUSIC section of the SiPM Pixel Main Board is based on the circuit of the MUSIC MiniBoard, kindly made available by the developers. In the next sections we will describe the functionalities and the development of each block forming the SiPM Pixel.

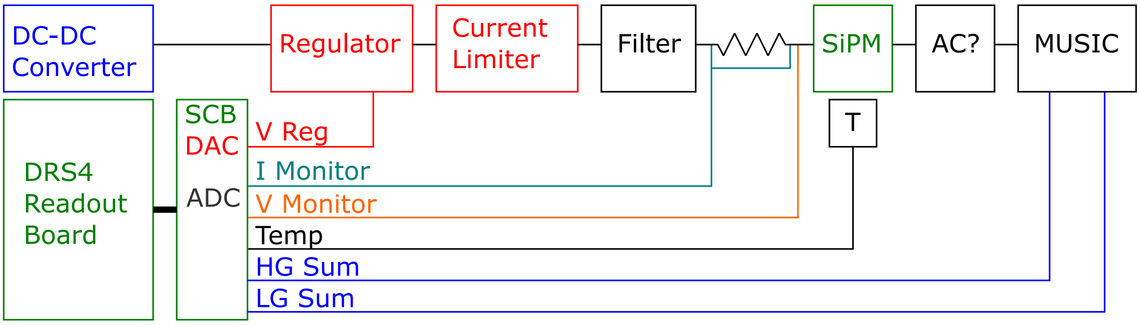

Figure 4.17: Block Diagram

4.3.2 Voltage Regulator

Since the SiPM bias voltage must be kept constant over a large range of current flowing through the sensor, a voltage regulator must be used. The output voltage of the regulator is set by the DAC located in the SCB, which is controlled by the Slow Control software.

Beissel Circuit

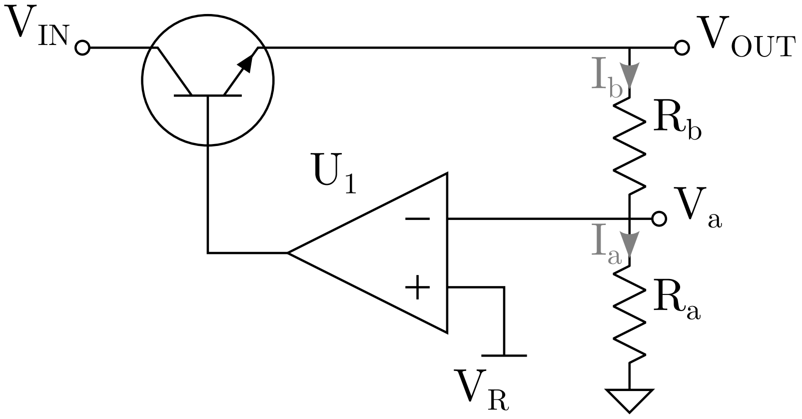

Figure 4.18: A simplified Beissel Circuit

An example of a typical Voltage Regulator is the Beissel Circuit; a simplified schematic is shown in Figure 4.18.

Considering U_1 as an ideal operational amplifier operating in the linear region:

$$V_d \triangleq V_+ - V_- = 0\,\mathrm{V}, \qquad I_+ = I_- = 0\,\mathrm{A} \tag{4.2}$$

Where V_+ and V_- are the voltages at the operational amplifier non-inverting input (+) and inverting input (-) respectively, and I_+ and I_- are the currents that flow in the operational amplifier non-inverting input (+) and inverting input (-) respectively. Thus:

$$I_a = I_b, \qquad V_a = V_R$$

Therefore:

$$I_a = \frac{V_a}{R_a} = \frac{V_R}{R_a}$$

The output voltage:

$$\begin{aligned} V_{OUT} &= V_a + I_b R_b = \\ &= V_R + I_a R_b = \\ &= V_R + \frac{V_R}{R_a} R_b \end{aligned}$$

Finally we obtain:

$$V_{OUT} = V_R \left(1 + \frac{R_b}{R_a}\right) = V_{HV} \tag{4.3}$$

The bipolar junction transistor (BJT) is necessary to give power to the circuit.

Non-Inverting Amplifier

In order not to rely only on Equation 4.3, we decide to amplify the voltage given by the DAC located the SCB V_{DAC} using a simple non-inverting amplifier; the simple schematic is reported in Figure 4.19.

Considering U_2 as an ideal operational amplifier operating in the linear region, from 4.2 we obtain:

$$I_d = I_c, \qquad V_{IN,2} = I_c R_c$$

Therefore:

$$\begin{aligned} V_{OUT,2} &= V_{IN,2} + I_d R_d = \\ &= V_{IN,2} + I_c R_d = \\ &= V_{IN,2} + \frac{V_{IN,2}}{R_c} R_d \end{aligned}$$

Finally:

$$V_{OUT,2} = V_{IN,2}\left(1 + \frac{R_d}{R_c}\right) \tag{4.4}$$

In our case:

$$V_{IN,2} \equiv V_{DAC}, \qquad V_{OUT,2} \equiv V_R \tag{4.5}$$

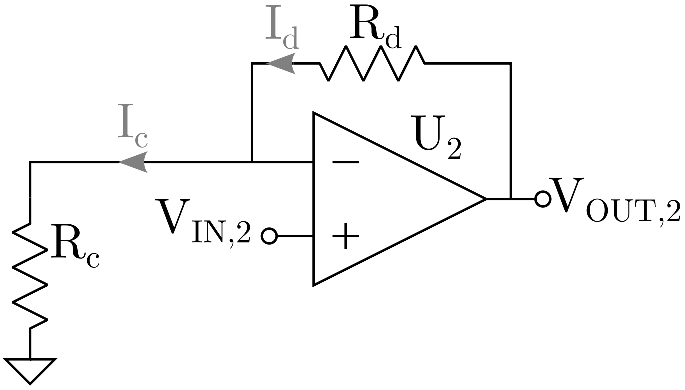

Figure 4.19: Non inverting amplifier

Modified Beissel Circuit

From Equations 4.4, 4.5 and 4.3 we obtain that for our circuit:

$$V_{HV} = V_{DAC}\left(1 + \frac{R_b}{R_a}\right)\left(1 + \frac{R_d}{R_c}\right) \tag{4.6}$$

Resistor values are chosen in order to cover the desired dynamics. Moreover, due to the voltages in our circuit, we have to modify the simple Beissel circuit reported in Figure 4.19, using a BJT cascade instead of a simple BJT. Where the DAC is connected to the Board we add a $1\,\mathrm{k\Omega}$ resistor and a $1\,\mathrm{\mu F}$ capacitor in order to prevent possible damage to the DAC.

4.3.3 Current Limiter

Protection Resistor

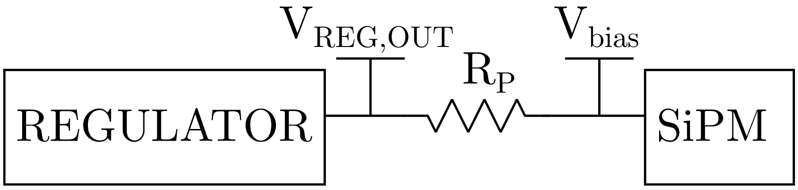

Figure 4.20: Protection Resistor

The most trivial way to limit the current in a SiPM is to use a *protection resistor*, as shown in Figure 4.20. This approach is very simple and not space-consuming, and it is the best solution for a low background detector. However, it has the huge disadvantage of making the bias voltage dependent on the current flowing into the SiPM. If we call I_{MAX} the maximum current allowed, we will have to select the resistor R_P in order to have a voltage drop across it equal to the overvoltage:

$$R_P = \frac{V_{OV}}{I_{MAX}} = \frac{V_{REG,OUT} - V_{bd}}{I_{MAX}}$$

However, the bias voltage will strongly depend on the SiPM current: indeed if I is the current which flows into the SiPM, the bias voltage is:

$$V_{bias} = V_{REG,OUT} - IR_P = V_{REG,OUT}\left(1 - \frac{I}{I_{MAX}}\right)$$

To better understand the implication of this solution, let's make an example: if we want to limit to 3 mA the current flowing into a SiPM operated at $V_{OV} = 6\,\mathrm{V}$, we will have to choose a 2 kΩ resistor. With this approach, if only 2 mA flows into the SiPM (therefore well below our operational limit), we will have a 4 V voltage drop, and the SiPM will work only at 2 V of overvoltage. Since the SiPM response strongly depends on this quantity, for high background application this solution is not feasible.

If instead the background is not very high, but enough to modify the bias voltage, it is possible to overcome the problem by fully characterizing the sensor at different value of current flowing into the device, in order to take into account the drop on the protection resistor [101].

One might think that a possible solution could be to actively change the regulator voltage $V_{REG,OUT}$, in order to keep constant the SiPM bias voltage; however in this case we would compromise the current limiting. The same problem would arise if we substitute the resistor with an actively controlled potentiometer.

Active Current Limiter

As we clearly see in the previous section, for our needs it is necessary to find a different solution. The one reported in Figure 4.21 is a typical two-BJTs current limiter circuit. When the current through R_E exceeds the design limit, Q_2 turns on, thus turning off Q_1, therefore limiting the load current. In the description, we will use the following notation:

- I_{Bi}, I_{Ci} and I_{Ei}: Q_i base, collector and emitter current, taken with positive values
- V_{BEi} (V_{CEi}): base-emitter (collector-emitter) voltage drop for Q_i
- I_{Ri}: current flowing in resistor R_i, using the passive sign convention

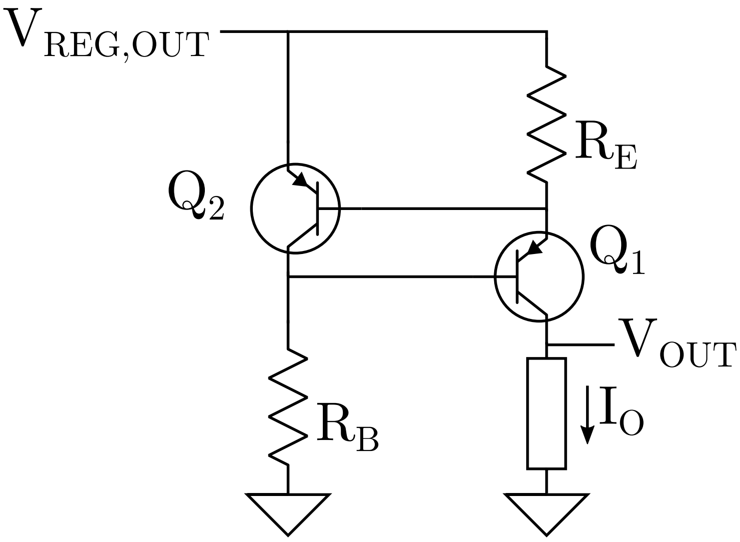

Figure 4.21: Current Limiter

The current is limited when both Q_1 and Q_2 are on; the output current I_O, which is the current flowing in the load R_L, is equal to:

$$I_O = \beta_1 I_{B1} = \frac{\beta_1}{\beta_1+1} I_{E1} = \frac{\beta_1}{\beta_1+1}\left(I_{B2} + I_{R_E}\right) \tag{4.7}$$

This current is the maximum allowed by the circuit: later we will refer it as I_{MAX}. Since $V_{RE} = -V_{BE2}$:

$$I_O = I_{MAX} = \frac{\beta_1}{\beta_1+1}\left(I_{B2} - \frac{V_{BE2}}{R_E}\right) \tag{4.8}$$

The voltage drop on the resistor R_B is equal to:

$$I_{R_B} R_B = V_{REG,OUT} + V_{BE1} + V_{BE2} \tag{4.9}$$

Let's consider only the current I_{R_B}:

$$\begin{aligned}
I_{R_B} &= I_{C2} + I_{B1} = I_{C2} + \frac{I_{E1}}{\beta_1+1} = \\
&= I_{C2} + \frac{I_{B2} + I_{R_E}}{\beta_1+1} = \beta_2 I_{B2} + \frac{I_{B2} + I_{R_E}}{\beta_1+1} = \\
&= \frac{((\beta_1+1)\beta_2+1)I_{B2} + I_{RE}}{\beta_1+1} = \\
&= \frac{((\beta_1+1)\beta_2+1)I_{B2} - \frac{V_{BE2}}{R_E}}{\beta_1+1} \\
&= \frac{V_{REG,OUT} + V_{BE1} + V_{BE2}}{R_B}
\end{aligned}$$

Therefore:

$$((\beta_1+1)\beta_2+1)I_{B2} - \frac{V_{BE2}}{R_E} = (\beta_1+1)\frac{V_{REG,OUT} + V_{BE1} + V_{BE2}}{R_B}$$

From which we can obtain I_{B2} as:

$$I_{B2} = \frac{1}{(\beta_1+1)\beta_2+1}\left(\frac{V_{BE2}}{R_E} + (\beta_1+1)\frac{V_{REG,OUT} + V_{BE1} + V_{BE2}}{R_B}\right)$$

Substituting in Equation 4.8:

$$\begin{aligned} I_{MAX} = {} & \frac{\beta_1}{\beta_1+1}\cdot \\ & \cdot\left(\frac{1}{(\beta_1+1)\beta_2+1}\left(\frac{V_{BE2}}{R_E}+(\beta_1+1)\frac{V_{REG,OUT}+V_{BE1}+V_{BE2}}{R_B}\right)-\frac{V_{BE2}}{R_E}\right) \end{aligned} \tag{4.10}$$

If Q_1 and Q_2 are the same BJTs, and are mounted nearby in the circuit, they will be basically at the same temperature, so we can say:

$$\beta_1 = \beta_2, \qquad V_{BE1} = V_{BE2} \tag{4.11}$$

Therefore:

$$\begin{aligned} I_{MAX} &= \frac{\beta}{\beta+1}\left(\frac{1}{(\beta+1)\beta+1}\left(\frac{V_{BE}}{R_E}+(\beta+1)\frac{V_{REG,OUT}+2V_{BE}}{R_B}\right)-\frac{V_{BE}}{R_E}\right) = \\ &= \frac{\beta}{\beta+1}\left(\frac{V_{BE}}{R_E}\left(\frac{1}{(\beta+1)\beta+1}-1\right)+\frac{1}{(\beta+1)\beta+1}(\beta+1)\frac{V_{REG,OUT}+2V_{BE}}{R_B}\right) = \\ &= \frac{\beta}{\beta+1}\left(\frac{V_{BE}}{R_E}\left(\frac{-(\beta+1)\beta}{(\beta+1)\beta+1}\right)+\frac{1}{(\beta+1)\beta+1}(\beta+1)\frac{V_{REG,OUT}+2V_{BE}}{R_B}\right) = \\ &= \frac{\beta}{1}\left(\frac{V_{BE}}{R_E}\left(\frac{-\beta}{(\beta+1)\beta+1}\right)+\frac{1}{(\beta+1)\beta+1}\frac{V_{REG,OUT}+2V_{BE}}{R_B}\right) \end{aligned}$$

Which means:

$$I_{MAX} = \frac{\beta}{(\beta+1)\beta+1}\left(\frac{V_{BE}}{R_E}(-\beta)+\frac{V_{REG,OUT}+2V_{BE}}{R_B}\right) \tag{4.12}$$

Thus:

$$\begin{aligned} I_{MAX}\frac{(\beta+1)\beta+1}{\beta} &= \frac{V_{BE}}{R_E}(-\beta)+\frac{V_{REG,OUT}+2V_{BE}}{R_B} \\ \frac{V_{BE}}{R_E}(-\beta) &= I_{MAX}\frac{(\beta+1)\beta+1}{\beta}-\frac{V_{REG,OUT}+2V_{BE}}{R_B} \end{aligned}$$

So:

$$R_E = \beta V_{BE}\left(\frac{V_{REG,OUT}+2V_{BE}}{R_B}-I_{MAX}\frac{(\beta+1)\beta+1}{\beta}\right)^{-1} \tag{4.13}$$

The great advantage of this solution is that (in first approximation) the output voltage $V_{OUT} = V_{bias}$ doesn't depend on the current flowing into the load:

$$V_{OUT} = V_{bias} = V_{REG,OUT} + V_{BE} + V_{CE} \tag{4.14}$$

In addition, from Equation 4.12 we can study the I_{MAX} dependance on the voltage $V_{REG,OUT}$:

$$\frac{dI_{MAX}}{dV_{REG,OUT}} = \frac{\beta}{(\beta+1)\beta+1}\frac{1}{R_B} \tag{4.15}$$

By choosing a sufficiently large R_B value, this dependency is negligible. This aspect is very useful if we need to modify the $V_{REG,OUT}$ value, for example to compensate a temperature variation on the sensor.

For the circuit realization we need to choose a transistor that has a collector-emitter breakdown voltage $V_{(BR)CEO}$ above the SiPM bias voltage in absolute value: we choose the *MMBT5401L*, whose minimum $V_{(BR)CEO}$ is $-150\,\mathrm{V}$. In addition, it has a typical $\beta_{typ} = 60$, $V_{BE,typ} = 0.65\,\mathrm{V}$ and the maximum collector-emitter voltage drop is $V_{CE,sat,MAX} = -0.2\,\mathrm{V}$. Therefore the voltage drop will be $\simeq 0.8\,\mathrm{V}$, much lower than with the protection resistor approach, and, in first approximation, it doesn't depend on the current flowing into the SiPM.

Now we can proceed with the choice of the resistance values. If we want to limit the current to 3 mA, we can choose:

$$R_B = 10\,\text{k}\Omega \qquad R_E = 220\,\Omega$$

However, we want to be able to set two different current limits in our circuit, without having to replace a resistor. This can be accomplished by adding another resistor in parallel to R_E; we will call this resistor $R_{E,2}$. If we want to set this new limit to 10 mA, we will choose (to be conservative):

$$R_B = 10\,\text{k}\Omega \qquad R_E = 220\,\Omega \qquad R_{E,2} = 100\,\Omega$$

In Figure 4.22 it is shown the maximum current dependence on the regulator voltage for the two configurations: its slight I_{MAX} vs $V_{REG,OUT}$ dependence is another advantage of this circuit.

To check the operation of the protection circuit, a LTspice® simulation was carried out; the SiPM was modelled as an active current load. The simulation was repeated for two current limiter configurations, with $V_{REG,OUT} = 34\,\text{V}$. Results as shown in Figure 4.23. Before the current limit, the little $V_{OUT} = V_{bias}$ dependence on the current flowing into the SiPM can be easily corrected thanks to a proper slow control feedback circuit, as the one used in the detector. According to the LTspice® simulations, if no slow control correction is applied, in the case of a SiPM biased at 6 V of overvoltage, the V_{bias} dependence would cause a maximum SiPM gain reduction of about 3 % and 10 % in the 3 mA and 10 mA limit respectively. Please note that the voltage value that will be set during normal operation will be slightly different from the one simulated.

We can perform a simple calculation to estimate how much current can flow in the SiPM pixel in a dark night; clearly this value depends on the sensor and on the overvoltage at which it will operate. If I_{DCR} is the dark current, R_{NSB} the NSB rate and G the SiPM gain, the current I_{DC} flowing into the sensor is:

$$I_{DC} = I_{DCR} + I_{NSB} = I_{DCR} + q \cdot R_{NSB} \cdot G \tag{4.16}$$

I_{DCR} is about 0.1 mA for the selected sensors at $V_{OV} = 6\,\text{V}$. From Monte Carlo simulations performed on a SiPM camera made by Hamamatsu LCT5 SST1-M SiPMs as big as a LST PMT pixel, and without any filter on the camera window, we obtained a $R_{NSB} \simeq 1.5\,\text{GHz}$ in dark condition. Considering a reasonable gain of 4×10^6 [102], we can conclude that we expect a $I_{DC} \simeq 1\,\text{mA}$. Clearly this is only a rough estimate, as this value depends on the sensor, its polarization, whether or not a filter is used, and so on.

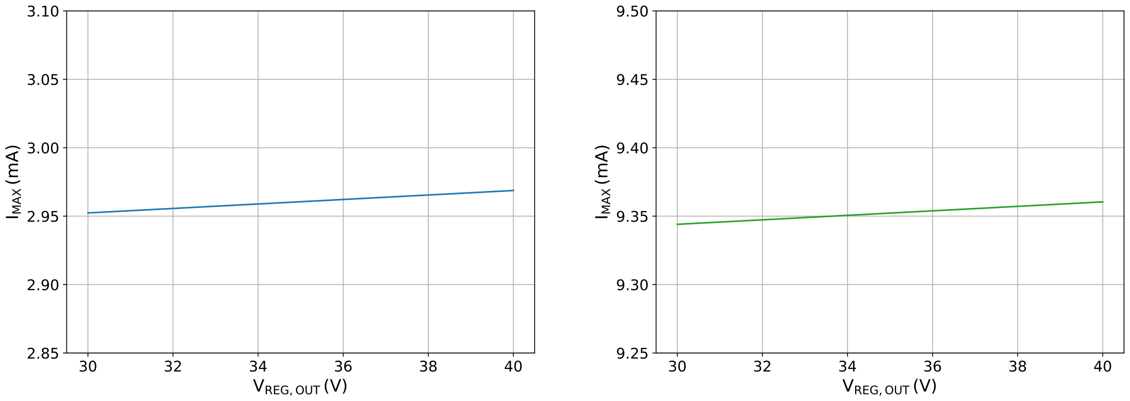

(a) **(b)**

Figure 4.22: Maximum current dependence on the regulator voltage for the two current limiter configurations

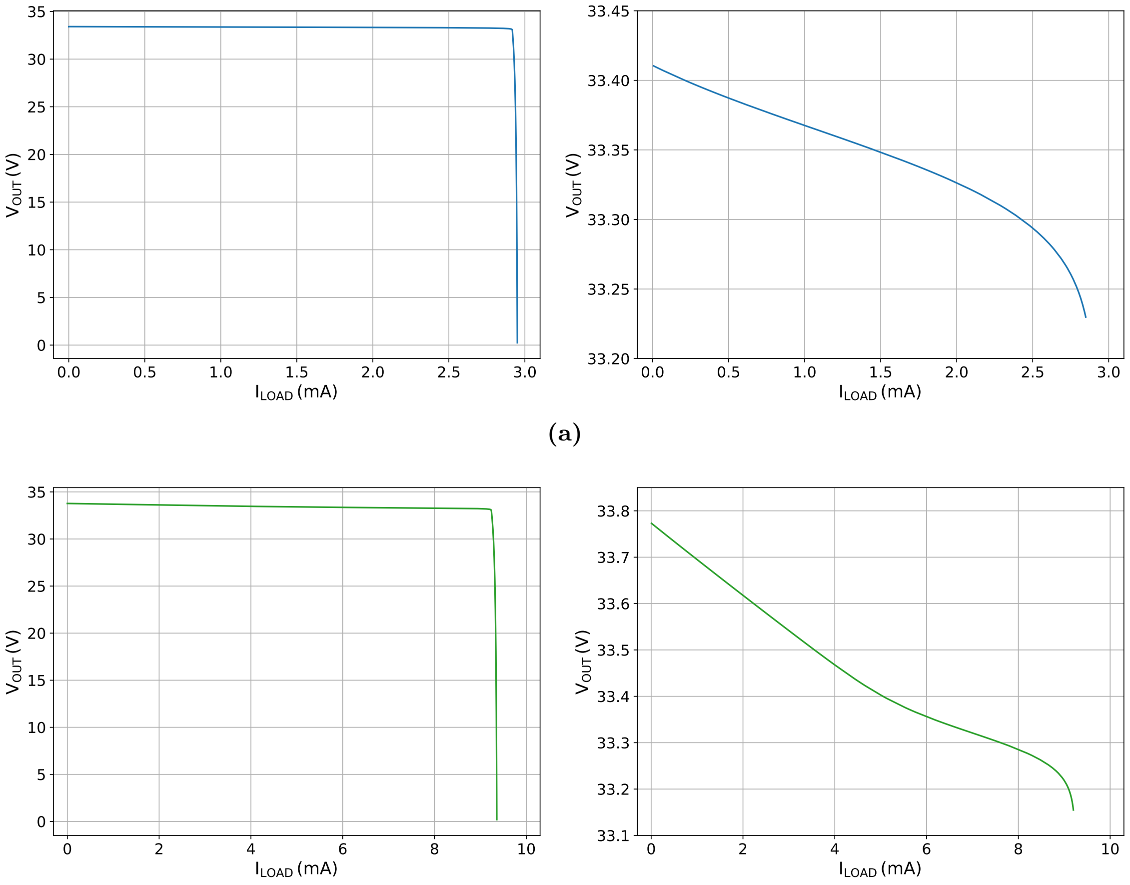

(a)

(b)

Figure 4.23: Output voltage V_{OUT} obtained from LTspice® simulations for the two current limiter configurations, with $V_{REG,OUT} = 34\,\text{V}$

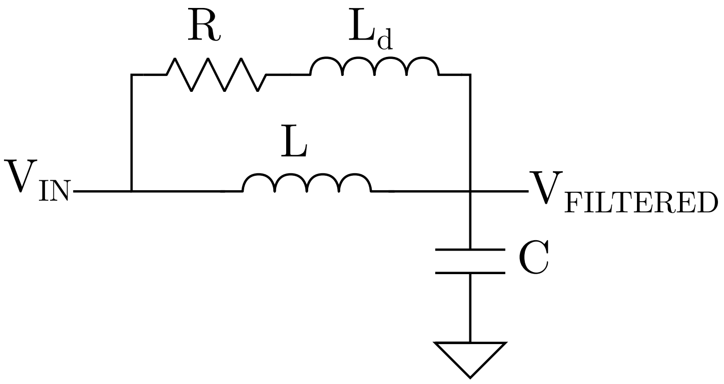

Figure 4.24: R-L_d parallel damping approach for a single-section L-C filter

4.3.4 Filter

In order to ensure optimal performance of our detector it is necessary to filter out as much as possible the noise from the SiPMs bias supply. This noise can come from the DC-DC converter, the LST electronics, the power supply, or any other part of the detector. To ensure the best performance, it must be located as close as possible to the sensors.

Since we are dealing with a bias line, where we want to avoid voltage drops as much as possible, the classical R-C low pass filter is not recommended. The easiest modification to this simple filter is done by replacing the resistor with an inductance, thus obtaining a L-C filter, one of the typical low pass filters used on power lines. However, it is well known that this second order filter presents problems at frequencies around its pole: therefore, a proper damping is necessary, in order not to run into spikes in the transfer function, which causes poor filter performance and can lead to stability problems.

In this section we will deal quickly and briefly few basics of input filter design criteria, then we show how the filter was designed. The main results are reported below, which are operationally useful for designing appropriate filters; for a more detailed discussion please refer to [103].

Single-Stage Damped Filter

The need for damping in the L-C input filters is very important and well appreciated in power electronics; an appropriate filter damping can be necessary to avoid peaks in the filter transfer function which can affect the circuit performance and stability.

Various are the possible approaches; the chosen one is the R-L_d parallel damping shown in Figure 4.24, where inductor L_d causes the filter to show a two-pole attenuation characteristic at high frequency.

We define:

$$n \triangleq \frac{L_d}{L} \tag{4.17}$$

$$Q_{opt} \triangleq \frac{R_{opt}}{R_0} \tag{4.18}$$

where R_{opt} is the optimal value of R. Moreover:

$$R_0 \triangleq \sqrt{\frac{L}{C}} \tag{4.19}$$

$$f_0 \triangleq \frac{1}{2\pi\sqrt{LC}} \tag{4.20}$$

Which is like saying:

$$L = \frac{R_0}{2\pi f_0} \tag{4.21}$$

$$C = \frac{1}{2\pi R_0 f_0} \tag{4.22}$$

The optimal damped designs, i.e. the choice of R that for a given L_d minimizes the peak output impedance is:

$$Q_{opt} = \sqrt{\frac{n(3+4n)(1+2n)}{2(1+4n)}} \tag{4.23}$$

The peak filter output impedance occurs at a frequency f_m:

$$f_m = f_0\sqrt{\frac{1+2n}{2n}} \tag{4.24}$$

and has a value:

$$\frac{\|Z\|_{mm}}{R_0} = \sqrt{2n(2n+1)} \tag{4.25}$$

Moreover, the attenuation of the filter high-frequency asymptote is degraded by the factor:

$$\frac{L}{L\|L_d} = 1 + \frac{1}{n} \tag{4.26}$$

Cascading Filter Sections

A cascade of multiple L-C filter sections allows us to achieve a certain high-frequency attenuation with less volume and weight than a single section L-C filter. Indeed, with this approach we can use higher cut-off frequencies and thus smaller inductance and capacitance values. Since we will need to damp each section of the L-C filter, we should optimize each section. As described in [103], a good approach is to stagger-tune the filter by choosing different cut-off frequencies for each stage: in this way we avoid that the two damped peaks in the transfer function are added together.

Filter Design

Our aim is to obtain the highest possible attenuation without exceeding in component weight or volume. In order to find a good compromise between filtering and footprint occupancy, we design a two-stage filter which provides an attenuation of 100 dB at $f_0 =$ 500 kHz. As we will see, we can reach this attenuation by using components easily available on the market. Concerning the capacitors, for their precision and reliability we will use only ceramic ones; in addition requiring a 100 V of maximum operating voltage reduces our choice. The filter basic schematic is shown in Figure 4.25.

In order to reduce the interactions between the filters in the cascade connection, we have just seen that it is better to stagger-tune the filter sections: we choose a smaller cut-off frequency for the first section, as suggested in [103]. We decide that the attenuations are:

- 55 dB at 500 kHz for the first section
- 45 dB at 500 kHz for the second section

Below we will refer to the first stage with the subscript “1” and with “2” for the second stage. A good compromise between damping of filter resonance and degradation of high frequency filter attenuation is given by:

$$n_1 = n_2 = \frac{L}{L_d} = 0.5 \tag{4.27}$$

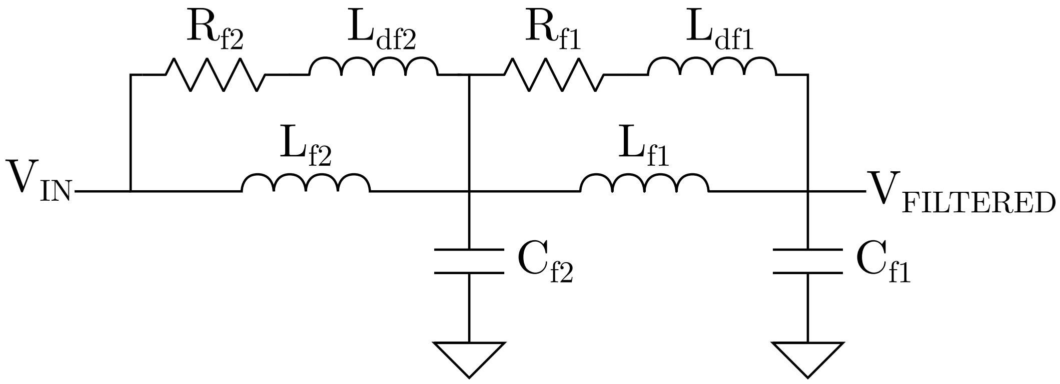

Figure 4.25: Two-stages *L*-*C* filter with *R*-L_d parallel damping

To find the components value, first we set a desired peak filter output impedance range, then we evaluate the optimal capacitor and inductor values in this range. The values found are ideal, and not all values are available on the market; therefore, first we choose a real capacitor value, then we find the corresponding inductor. It is essential to keep in mind that the capacitors must be guaranteed to support a voltage suitable for our application; logically this request limits our choice.

Let's start by asking that the peak filter output impedance should be smaller than 3 Ω. From Equation 4.25 we obtain:

$$R_0 \equiv R_{0,1} = \frac{\|Z\|_{mm}}{\sqrt{2n(2n+1)}} \tag{4.28}$$

Moreover, from Equation 4.26 we know that the *R*-L_d damping branch will degrade the high frequency attenuation by a factor of $1 + 1/n = 1 + 1/0.5 = 3$, which is equal to 9.5 dB: the section 1 undamped resonant frequency f_1 has to be chosen to ensure a $55 + 9.5 = 64.5$ dB attenuation, corresponding to:

$$Att_1 = 10^{(64.5/20)} \tag{4.29}$$

We can thus evaluate the filter frequency:

$$f_1 = \frac{f_0}{\sqrt{Att_1}} \tag{4.30}$$

and the capacitor and inductor values as (from equations 4.22 and 4.21):

$$C_{f1} = \frac{1}{2\pi R_0 f_1} \tag{4.31}$$

$$L_{f1} = \frac{R_0}{2\pi f_1} \tag{4.32}$$

In Figure 4.26a it is shown the Capacitor C and inductor L values depending on the peak filter output impedance. As mentioned, we proceed with the choice of the capacitor value: we select the value of 10 µF, which corresponds to $||Z||_{mm} \simeq 1.84\,\Omega$ and $L_{f1} \simeq 17.01\,\mu\text{H}$. For the damping branch:

$$L_{d,1} = \frac{L_{f1}}{n} \simeq 8.51\,\mu\text{H} \tag{4.33}$$

$$R_{f1} \equiv R_{opt,1} = R_0\sqrt{\frac{n(3+4n)(1+2n)}{2(1+4n)}} \simeq 1.19\,\Omega \tag{4.34}$$

The chosen value are 18 µH for L_{f1}, 8.2 µH for $L_{d,f1}$ and 1.2 Ω for R_{f1}.

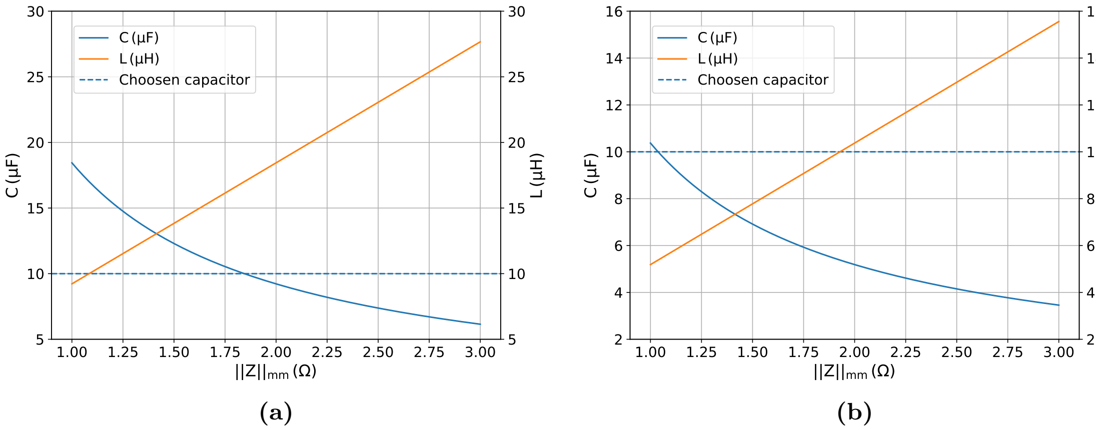

Figure 4.26: Capacitor C and inductor L values depending on the peak filter output impedance, for the first (a) and second (b) filter stages

With the same procedure we design the second stage. By selecting a 10 µF capacitor for C_{f2}, we obtain $L_{f2} \simeq 5.38\,\mu\text{H}$, $L_{df2} \simeq 2.69\,\mu\text{H}$ and $R_{f2} \simeq 0.67\,\Omega$; chosen value are 5.6 µH for L_{f2}, 2.7 µH for $L_{d,2}$ and 0.68 Ω for R_{f2}.

To check the filter design, a LTspice® [75] simulation was carried out, both by using the obtained "ideal" values and the real ones; in both cases parasitics were neglected. The magnitude Bode plot is shown in Figure 4.27; the obtained attenuation coincides with the desired one, and the difference between the ideal curve and the real one is negligible. In addition, we can appreciate the damping at the pole frequencies: in green it is shown how the filter would behave without the R-L_d branch.

Filter Placement in the Block Diagram

In the Block Diagram shown in Figure 4.17 the filter was already placed after the current limiter; this solution is the one that guarantees us the best filtering performance. To prove

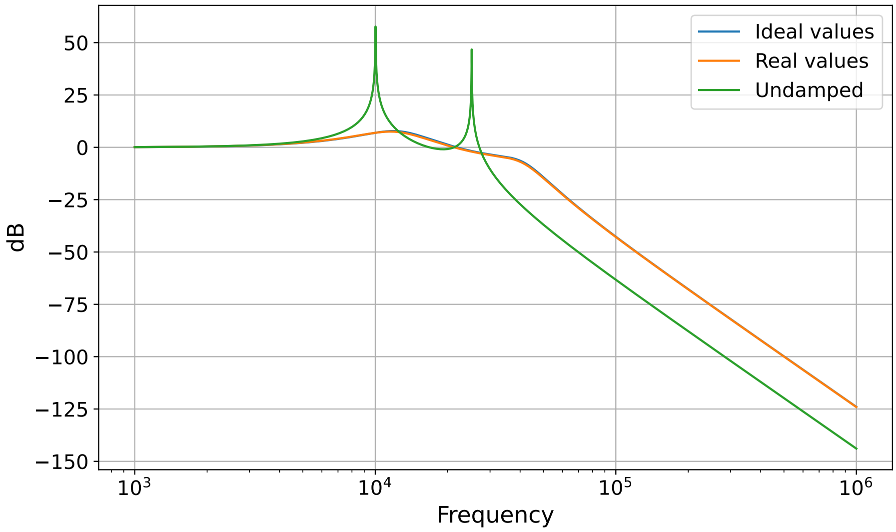

Figure 4.27: Two-stages filter magnitude Bode plot obtained by LTspice® [75] simulation, both by using the obtained "ideal" values (blue) and the real ones (orange): the two curves are almost completely overlapping. In green it is shown how the filter would behave without the R-L_d branch.

that, we can run a LTspice® simulation; we will make a qualitative simulation, which does not take into account all the variables, but which is enough for us to decide where to locate the filter. We consider three possible solutions, later referred as *Option 1*, *2* and *3*:

1. Filter between the DC-DC converter and the regulator
2. Filter between the regulator and the current limiter
3. Filter after the current limiter, i.e. between the current limiter and the voltage and current monitor

The DC-DC converter is simulated with a behavioral voltage source with value

```
V = {V_SW} + {k}*white(time*1e6)
```

where `V_SW` is the average DC-DC converter output voltage value and `k` is the scaling factor for the white noise; since we will perform a qualitative study, this value is not crucial (we can set it to 1). Then we perform a transient simulation on all the described circuits (to avoid any possible interactions, the circuits are separately simulated). The load (i.e. the SiPM) is simulated as a resistor big enough not to trigger the current limiter. The resulting output voltage subtracted by its mean is shown in Figure 4.28; it is clear that the third solution (i.e. the one shown in Figure 4.17) is the best one.

It is important to point out that we only studied the effect of the noise on the high voltage line: logically also to operational amplifier power voltages will bring noise into the system, noise that must be filtered. This simulation however would strongly rely on the operation amplifier LTspice® models' accuracy, in particular on how their model are accurate to proper simulate the noise propagation from the power lines to their outputs However, by observing where they are placed in the circuit, it is clear that also in this case the best solution would be the third one, and therefore this simulation is not needed.

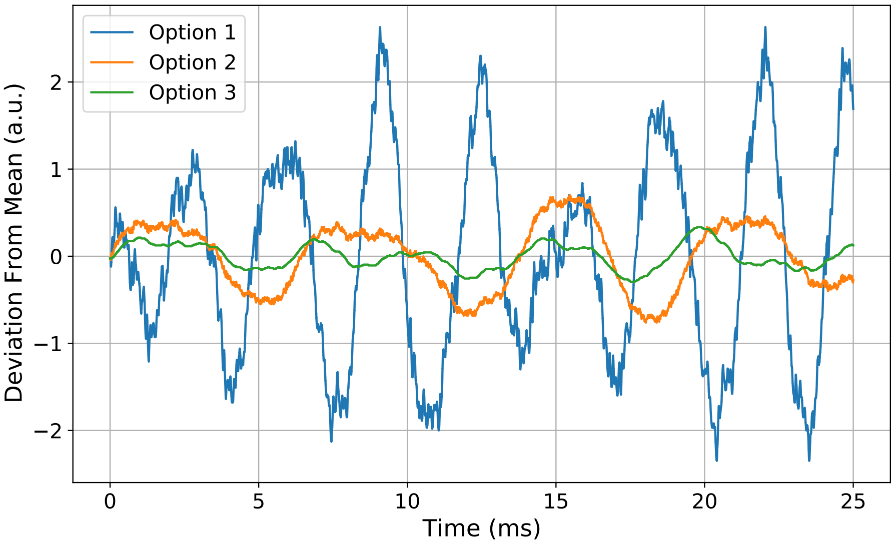

Figure 4.28: Output voltages noise for the three possible filter placement options (LTspice® simulation)

4.3.5 Voltage Monitor

The schematic of the circuit used for the voltage monitor is reported in 4.29; it is an inverting amplifier modified with a voltage divider in order to keep V_- lower than the operational supply voltage.

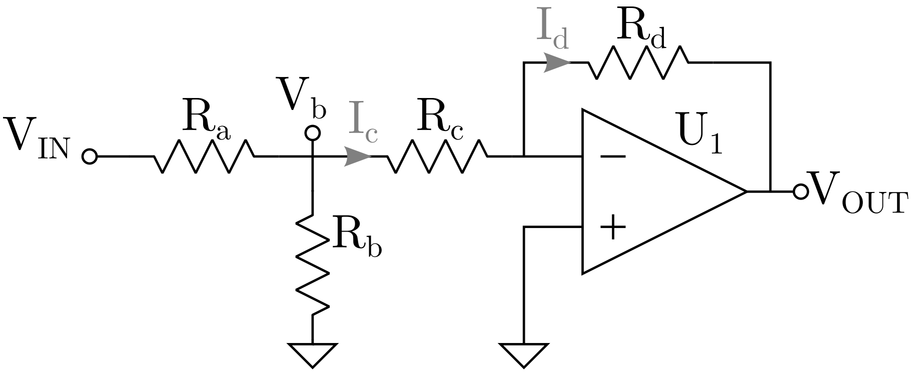

Figure 4.29: Voltage Monitor

Considering U_1 as an ideal operational amplifier operating in the linear region, from 4.2 we obtain:

$$V_+ = 0 \Rightarrow V_- = 0$$

Moreover:

$$V_b = V_{IN} \frac{R_b \parallel R_c}{R_a + R_b \parallel R_c}$$

$$I_c = \frac{V_b}{R_c} = \frac{V_{IN}}{R_c} \frac{R_b \parallel R_c}{R_a + R_b \parallel R_c}$$

$$I_c = I_- + I_d, I_- = 0A \Rightarrow I_c = I_d$$

Thus:

$$\begin{aligned} V_{OUT} &= V_- - I_d R_d = -I_d R_d = \\ &= -I_c R_d = \\ &= -\frac{V_{IN}}{R_c} \frac{R_b \parallel R_c}{R_a + R_b \parallel R_c} R_d = \\ &= -\frac{V_{IN}}{R_c} \frac{\frac{R_b R_c}{R_b + R_c}}{R_a + \frac{R_b R_c}{R_b + R_c}} R_d = \\ &= -\frac{V_{IN}}{R_c} \frac{R_b R_c}{R_a R_b + R_a R_c + R_b R_c} R_d = \\ &= -V_{IN} \frac{R_b R_d}{R_a R_b + R_a R_c + R_b R_c} \end{aligned}$$

Finally:

$$V_{OUT} = K V_{IN}, \qquad K = \frac{R_b R_d}{R_a R_b + R_a R_c + R_b R_c} \tag{4.35}$$

Resistor values are chosen in order to cover the desired dynamics.

4.3.6 Current Monitor

The schematic of the circuit used for the current monitor is reported in Figure 4.30; it is a differential amplifier modified with a voltage divider in order to keep V_- and V_+ lower than the operational supply voltage.

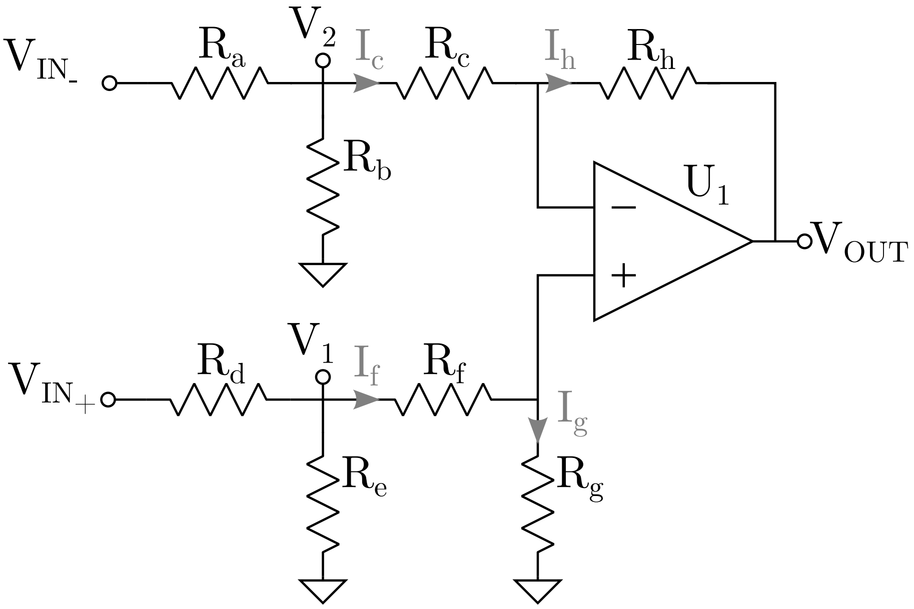

Figure 4.30: Current Monitor

Let's start considering the second stage of the circuit, i.e. from V_1 and V_2 to V_{OUT}: this stage is a conventional differential amplifier.

Considering U_1 as an ideal operational amplifier operating in the linear region, from 4.2 we obtain:

$$I_c = I_h, \qquad I_f = I_g, \qquad V_+ = V_-$$

Since we are considering a linear circuit, we can use the well known superposition principle.

If $V_1 = 0\,\mathrm{V}$ we will have:

$$V_{OUT}\Big|_{V_1=0} = -V_2\frac{R_h}{R_c}$$

While, if $V_2 = 0\,\mathrm{V}$ we will have:

$$V_+ = V_1\frac{R_g}{R_f+R_g} = V_-$$

$$I_c = -V_1\frac{R_g}{R_f+R_g}\frac{1}{R_c}$$

$$V_{OUT}\Big|_{V_2=0} = V_1\frac{R_g}{R_f+R_g}\left(1+\frac{R_h}{R_c}\right)$$

Thus:

$$\begin{aligned} V_{OUT} &= V_1\frac{R_g}{R_f+R_g}\left(1+\frac{R_h}{R_c}\right) - V_2\frac{R_h}{R_c} = \\ &= K_1V_1 - K_2V_2 = \\ K_1 &= \frac{R_g}{R_f+R_g}\left(1+\frac{R_h}{R_c}\right), \\ K_2 &= \frac{R_h}{R_c} \end{aligned}$$

In order to have $K_1 = K_2 \equiv K$:

$$\begin{gathered}
\frac{R_g}{R_f + R_g}\left(1 + \frac{R_h}{R_c}\right) = \frac{R_h}{R_c} \\
\frac{R_g R_c + R_g R_h}{(R_f + R_g) R_c} = \frac{R_h}{R_c} \\
\frac{R_g R_c + R_g R_h}{R_f + R_g} = R_h \\
R_g R_c + R_g R_h = R_f R_h + R_g R_h \\
\frac{R_g}{R_h} = \frac{R_f}{R_c}
\end{gathered}$$

A possible solution is:

$$R_g = R_h, \qquad R_c = R_f$$

Thus:

$$V_{OUT} = K\left(V_1 - V_2\right), \qquad K = \frac{R_h}{R_f} \tag{4.36}$$

Now using the same procedure we consider the whole circuit represented in Fig 4.30:

- If $V_{IN_+} = 0\,\mathrm{V}$:

$$\begin{aligned}
V_{OUT} &= -V_{IN_-} \frac{R_b \parallel R_c}{R_a + R_b \parallel R_c} \frac{R_h}{R_c} \\
&= -V_{IN_-} \frac{R_b R_h}{R_a R_b + R_a R_c + R_b R_c} = \\
&\equiv -V_{IN_-} K_-
\end{aligned}$$

- If $V_{IN_-} = 0\,\mathrm{V}$:

$$\begin{aligned}
V_{OUT} &= V_{IN_+} \frac{R_e \parallel (R_f + R_g)}{R_e \parallel (R_f + R_g) + R_d} \frac{R_g}{R_f + R_g} \cdot \\
&\qquad \cdot \left(1 + \frac{R_h}{R_c + R_a \parallel R_b}\right) = \\
&= V_{IN_+} \frac{R_e (R_f + R_g)}{R_e + R_f + R_g} \frac{1}{\frac{R_e (R_f + R_g)}{R_e + R_f + R_g} + R_d} \frac{R_g}{R_f + R_g} \cdot \\
&\qquad \cdot \left(1 + \frac{R_h}{R_c + \frac{R_a R_b}{R_a + R_b}}\right) = \\
&= V_{IN_+} \frac{R_e (R_f + R_g)}{R_e (R_f + R_g) + R_d (R_e + R_f + R_g)} \frac{R_g}{R_f + R_g} \cdot \\
&\qquad \cdot \frac{R_c (R_a + R_b) + R_a R_b + R_h (R_a + R_b)}{R_a R_b + R_a R_c + R_b R_c} = \\
&\equiv V_{IN_+} K_+
\end{aligned}$$

In order to have $K_+ = K_+ \equiv K'$:

$$R_d = R_a, \qquad R_e = R_b, \qquad R_f = R_c, \qquad R_g = R_h$$

Then:

$$\begin{gathered}
V_{OUT} = K'(V_{IN_+} - V_{IN_-}), \\
K' = \frac{R_h R_b}{R_a R_b + R_a R_c + R_b R_c}
\end{gathered} \tag{4.37}$$

Resistor values are chosen in order to cover the desired dynamics.

4.3.7 Low Dropout Regulators

To ensure that the MUSIC power lines fall within the operational limits, two Low Dropout Regulators (LDOs) are mounted on the Pixel Main Board, one for the 3.3 V line and one for the 5.0 V one. The selected ones are the MIC5205-3.3YM5-TR [104] for the first one and MIC5225-5.0YM5-TR [105] for the second one. Their maximum output current is 150 mA and their fixed output voltage is accurate enough for the MUSIC requirements.

The LDO enable pin is connected to an enable signal sent from the Slow Control Board; in this way it is possible to power off the MUSIC ASIC independently from the remaining part of the SiPM Pixel.

The LDO functionalities were tested on separated PCBs. The dependence of the output voltage from the regulator with respect to the input voltage has been studied. Tests were repeated with an open load configuration (no current I_{OUT} flowing from the LDO) and with a power resistor soldered as a load:

- 3.3 V line
  - Open Circuit ($I_{OUT} = 0\,\text{mA}$)
  - $R_L = 39 \| 56\,\Omega \simeq 23\,\Omega$ ($I_{OUT} \simeq 143\,\text{mA}$)
- 5.0 V line
  - Open Circuit ($I_{OUT} = 0\,\text{mA}$)
  - $R_L = 39\,\Omega$ ($I_{OUT} \simeq 128\,\text{mA}$)

Results are reported in Figure 4.31a and in Figure 4.31b; the second plot shows also the limits of MUSIC. If the input voltage is 1 V higher than the output voltage, we are sure to stay within the MUSIC operational limits. Therefore we will use:

- 3.3 V line: $V_{IN} = 4.3\,\text{V}$
- 5.0 V line: $V_{IN} = 6.0\,\text{V}$

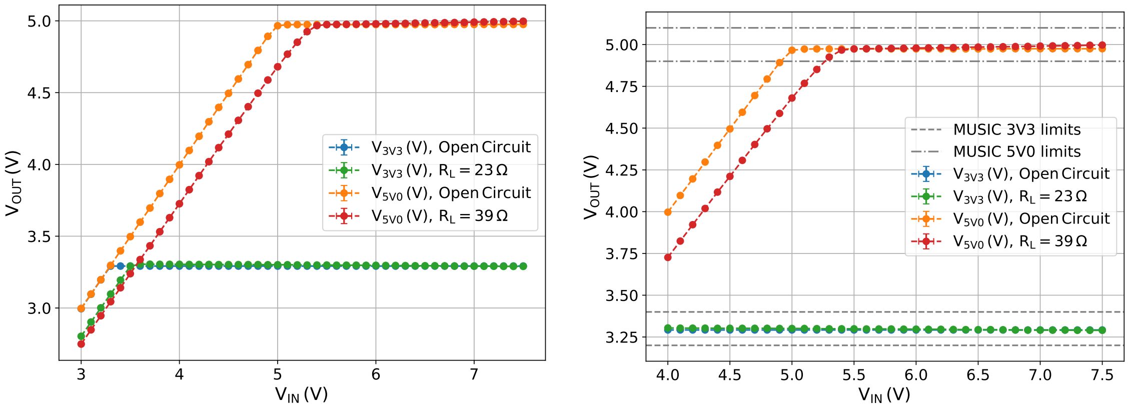

(a) **(b)**

Figure 4.31: LDO output voltage V_{OUT} dependance on the input voltage V_{IN}

4.3.8 MUSIC and Microcontroller

The MUSIC ASIC is controlled by an ATmega328P-AU microcontroller which runs the MUSIC MiniBoard [100] firmware.

The MUSIC ASIC and the microcontroller communicate via SPI interface, with the microcontroller being the master and the MUSIC chip the slave. At startup, the microcontroller sets the MUSIC operative configuration:

- Enable six channels (from 0 to 5)
- Sum the six enabled channels
- High trans-impedance configuration
- Pole-zero configuration:
    - $R_{lad} = 7$
    - $C_{lad} = 31$
    - Low Attenuation ON

The selected pole-zero configuration is the one which assures the shortest possible signal.

Since the ATmega328P-AU microcontroller factory configurations do not allow serial communication, it is necessary to pre-configure it by programming its fuses via ICSP interface. This operation is done before soldering the chip, using an Arduino UNO as ICSP programmer. In this case the microcontroller acts a slave, while in normal operation it is the master in the SPI communication with the MUSIC ASIC. Allowing this change of operation would have complicated the Pixel Main Board Circuit: we thus opted to solder the microcontroller already pre-configured. To simplify the connection between the microcontroller and the Arduino, the first one is mounted on a QFP32 to DIP adapter (see Figure 4.32). After successfully setting the microcontroller fuses, the firmware can be loaded via the UART interface.

A brief description on how to configure the microcontroller is given in appendix A; refer to [100] for more information.

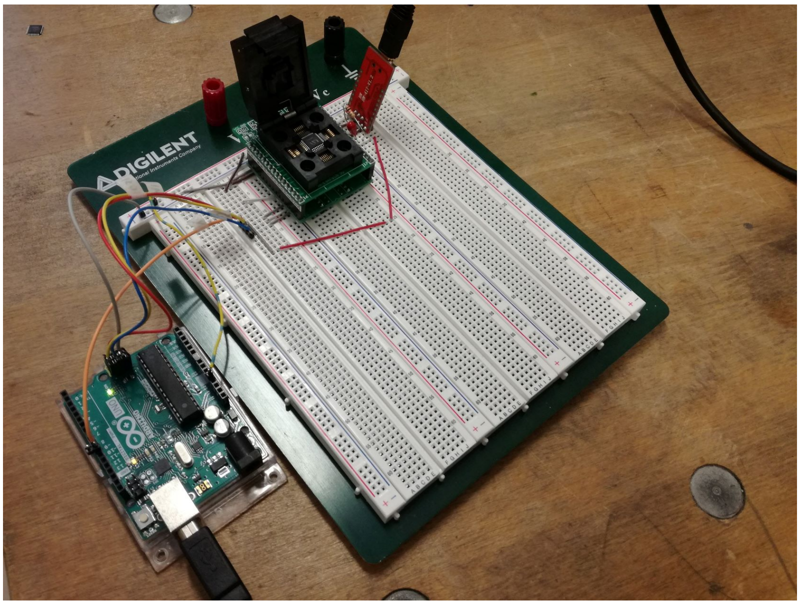

Figure 4.32: Pre-configuration of a ATmega328P-AU microcontroller

4.3.9 AC Filter

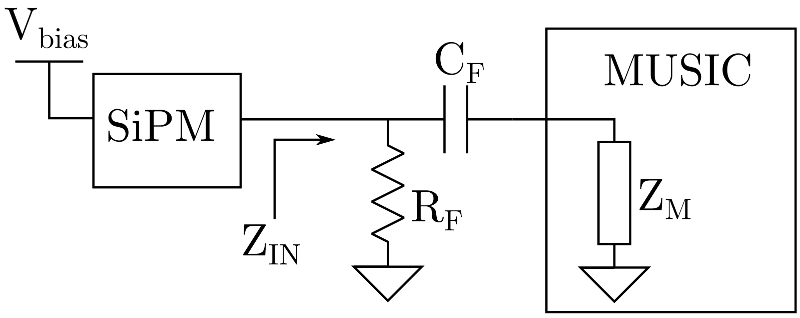

Figure 4.33: AC Filter

In high background applications, the signal lies over a quasi-DC noise. This DC baseline can be removed thanks to an AC Filter; considering our situation, it would be possible to add a high-pass filter between the SiPM anode and the MUSIC input, as depicted in Figure 4.33.

In this situation the voltage across the SiPM V_{SiPM} would be, considering only the DC component:

$$V_{SiPM} = V_{bias} - I_{SiPM} R_F \tag{4.38}$$

where V_{bias} is the SiPM bias voltage and I_{SiPM} is the current flowing into the sensor. Therefore, to keep constant the voltage across the SiPM, it is mandatory to actively adjust the bias voltage V_{bias} with a proper feedback loop, in order to compensate the voltage drop on R_F. The procedure is described in section 4.3.16.

As we have seen, particular attention must be paid to the input impedance when developing front-end circuits for SiPMs. If Z_M is the MUSIC input impedance, the equivalent impedance seen by the SiPM is:

$$\begin{aligned}
Z_{IN} &= R_F \parallel \left(\frac{1}{sC_F} + Z_M \right) = \\
&= R_F \parallel \left(\frac{1 + sC_F Z_M}{sC_F} \right) = \\
&= \left(\frac{1}{R_F} + \frac{sC_F}{1 + sC_F Z_M} \right)^{-1} = \\
&= \left(\frac{1 + sC_F Z_M + sC_F R_F}{R_F (1 + sC_F Z_M)} \right)^{-1} = \\
&= \left(\frac{1 + sC_F (Z_M + R_F)}{R_F (1 + sC_F Z_M)} \right)^{-1}
\end{aligned}$$

Therefore:

$$Z_{IN} = R_F \frac{1 + sC_F Z_M}{1 + sC_F (Z_M + R_F)} \tag{4.39}$$

The fraction of the SiPM current I_{SiPM} flowing into the MUSIC is:

$$\begin{aligned}
\frac{I_M}{I_{SiPM}} &= \frac{Z_{IN}}{\frac{1}{sC_F} + Z_M} = \\
&= sZ_{IN} \frac{C_F}{1 + sC_F Z_M} = \\
&= sR_F \frac{1 + sC_F Z_M}{1 + sC_F (Z_M + R_F)} \frac{C_F}{1 + sC_F Z_M}
\end{aligned}$$

Thus:

$$\frac{I_M}{I_{SiPM}} = \frac{sR_FC_F}{1 + sC_F(Z_M + R_F)} \tag{4.40}$$

As we know the front-end electronics should have a low input impedance, and from Equation 4.39 we have that this is achieved with a low R_F value. However we cannot use a too small R_F, otherwise we would lose too much signal; it is therefore necessary to find a compromise: for example we can use $R_F = 100\,\Omega$. At high frequency (i.e. $s \to +\infty$) the input impedance is:

$$Z_{IN,HF} = \lim_{s\to+\infty}\left(R_F\frac{1 + sC_FZ_M}{1 + sC_F(Z_M + R_F)}\right) = \frac{R_FZ_M}{Z_M + R_F} \tag{4.41}$$

We could reach the same conclusion simply by observing that at high frequencies the capacitor C_F behaves like a short circuit. With our R_F choice, and since for the MUSIC ASIC $Z_M \simeq 32\,\Omega$, we have:

$$Z_{IN,HF} \simeq 24\,\Omega \tag{4.42}$$

In the same limit the fraction of the current flowing into the MUSIC will be:

$$\frac{I_{M,HF}}{I_{SiPM}} = \lim_{s\to+\infty}\left(\frac{sR_FC_F}{1 + sC_F(Z_M + R_F)}\right) = \frac{R_F}{Z_M + R_F} \tag{4.43}$$

With our R_F choice:

$$\frac{I_{M,HF}}{I_{SiPM}} \simeq 0.76 \tag{4.44}$$

which means that about 24 % of the SiPM current will be lost.

From Equation 4.40 we have that the I_M/I_{SiPM} transfer function has a zero in the origin and a first order pole at:

$$s_p = \frac{1}{C_F(Z_M + R_F)} \tag{4.45}$$

The higher the capacitor value C_F, the smaller the pole, and therefore the shape of the signal will be less affected.

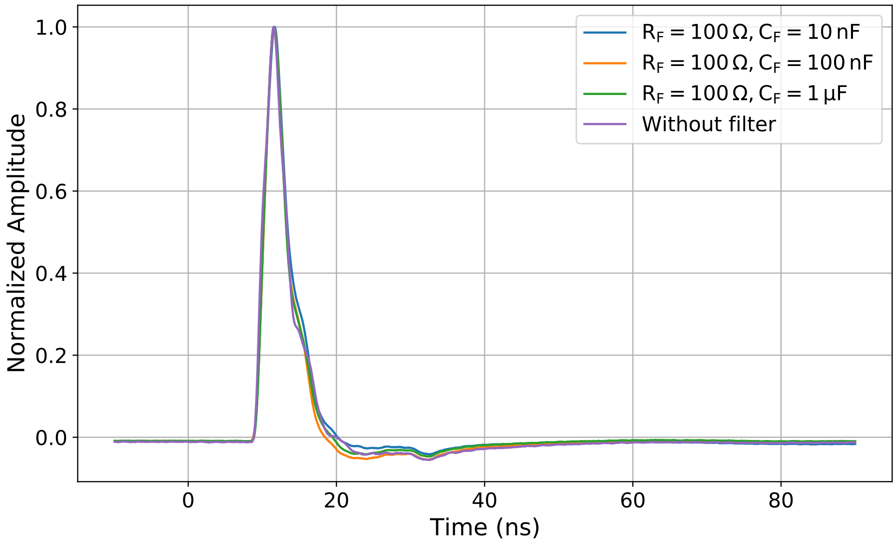

Figure 4.34: Signals for different AC Filter configurations, compared the signal obtained without any filter

Laboratory measurements were carried out to test different capacitor values. These tests were done using the MUSIC MiniBoard and a dummy AC filter board, in which for each channel different capacitors were soldered. As a reference, one channel was connected directly, without any AC filter. The comparison was done by summing only one channel at a time and acquiring the sum High Gain signal thanks to a Tektronix MSO6 Oscilloscope. Results are shown in Figure 4.34; as we can see, the shape is not particularly affected. The chosen values for the AC Filter are:

$$R_F = 100\,\Omega \qquad C_F = 1\,\mu\text{F} \tag{4.46}$$

The AC Filter is located on a mezzanine between the Pixel Main Board and the SiPM array. In this way it is possible to test the prototype with and without the filter, to compare the DC and the AC approach. Each of the six channels contributing to the sum has the R-L filter previously described; the calibration pixel is indeed directly connected. The PCB is a two layer board and has a dimension of 24 mm × 40 mm. Particular care has been taken in drawing the SiPM signal tracks, as they are not amplified. Some pictures of the board can be found in Figure 4.35.

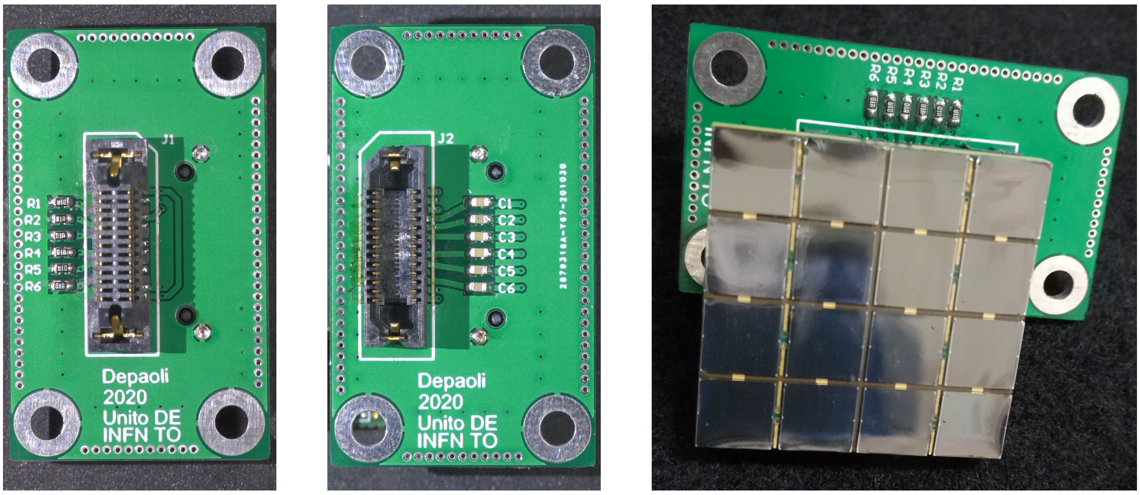

(a) (b) (c)

Figure 4.35: AC Filter PCB:
(a) connection to the SiPM array
(b) connection to the Pixel Main Board
(c) SiPM array mounted on the AC Filter PCB

4.3.10 Thermometer

As we have already discussed, most of the SiPM characteristics depends on the overvoltage $V_{OV} = V_{bias} - V_{bd}$. Due to the high temperature dependance of V_{bd}, it is necessary to strictly monitor the sensor temperature, in order to properly correct the bias voltage.

The selected one is a Maxim DS28EA00 [106], which is a digital thermometer capable to measure temperatures between −40 °C to 85 °C with a resolution selectable from 9 bit (0.5 °C) to 12 bit (1/16 °C). Its voltage bias range is between 3.0 V to 5.5 V. This device is already used in the LST PMT Pixel. The typical operation circuit is shown in Figure 4.36.

A dedicated 1 cm × 1 cm PCB is built to host this device; this small board is thermally connected to the back of the SiPM array. The thermometer resolution is kept at the factory default of 12 bit and it is powered at 3.3 V. A picture of the board is visible in Figure 4.37.

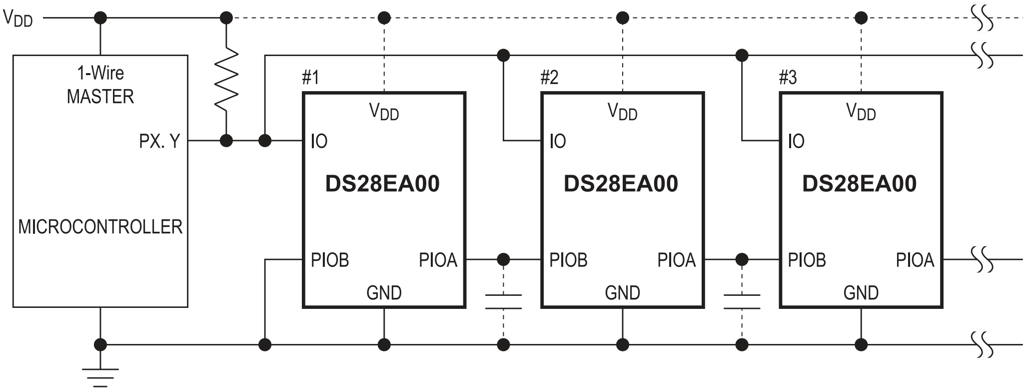

Figure 4.36: Maxim DS28EA00 typical operating circuit [106]

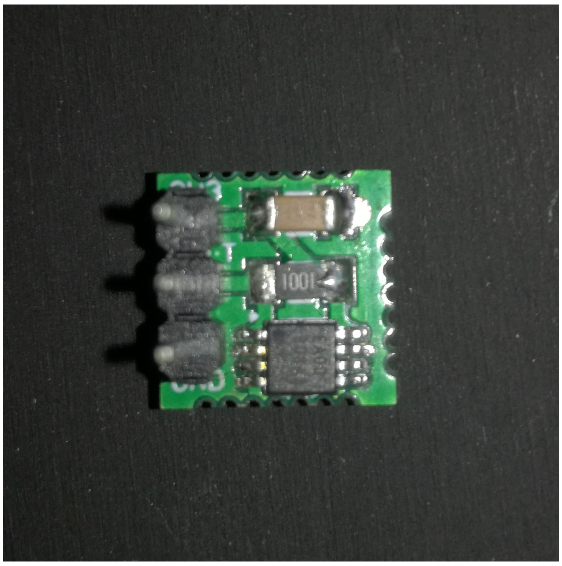

Figure 4.37: Thermometer PCB front view

4.3.11 Connection to the Slow Control Board

The Pixel Main Board connection to the Slow Control Board is performed by means of an adapter PCB as follows:

- Slow Control Board: Samtec high speed connector
- Pixel Main Board: high speed differential cable

The Samtec high speed connector is the mate of the one mounted in the Slow Control Board. The flexible connection made possible by the use of a high-speed cable allows to fit in the same mechanics both the SiPM pixel with and without the AC Filter mezzanine.

High speed differential cables can be very expensive, therefore a careful and accurate market research was carried out to find the most suitable solution. The choice fell on the 3M™ SL8801/12-10DA5-00 [107], one of the SL8800 Series 3M Twin Axial Cable. These high-speed differential shielded cables are designed for space constrained applications beyond 10 Gbps. They can be folded without significantly impacting their performances, allowing an easy 90-degree connection. These cables can be directly soldered on the PCB and their characteristics perfectly fits our needs[1]. To ensure greater strength to the connection, the cable is held in place with epoxy glue. Since the outer structure of the cable is conductive, a thin layer of Kapton has been placed under the cable.

The Pixel Main Board enable signal, which is the LDO enable, can be connected to the enable signal coming to the SCB or to the 3.5 V line. This choice is made by soldering a zero-ohm resistor (R_1 or R_2). In the prototype we soldered R_2, thus the LDO is always enabled. Figures 4.38a and 4.38b show some pictures of the board.

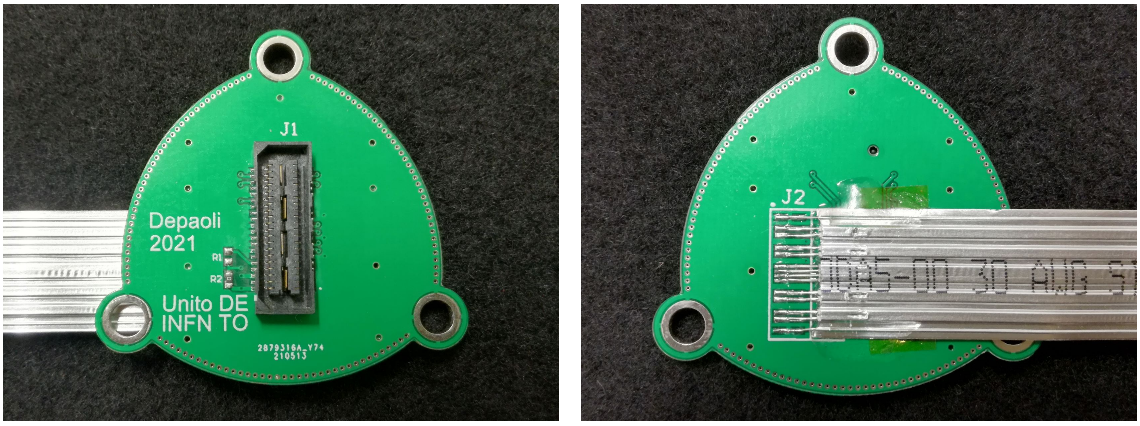

(a) **(b)**

Figure 4.38: Pictures of the PCB connecting the Pixel Main Board to the Slow Control Board

---

[1] Private communication with the dealer

4.3.12 Oscilloscope Mezzanine

For testing purposes, an Oscilloscope Mezzanine can be put between the Pixel Main Board to SCB adapter and the SCB itself. This board has four LEMO 00 connectors, corresponding to the signals of the two differential lines (High Gain and Low Gain). It is a four layer board, designed with proper impedance control. Some pictures of the board are shown in Figures 4.39a and 4.39b.

With this mezzanine it is possible to study directly the MUSIC output signals, without the LST electronics, since this board is put right before the SCB. We have to keep in mind that the Low Gain and High Gain signals are differential, but we are treating them as separated single ended signals (one for each connector). In this way we are losing the environmental noise rejection capability typical of this transmission mode. Therefore, we can only perform qualitative (but fast) measurements with this mezzanine.

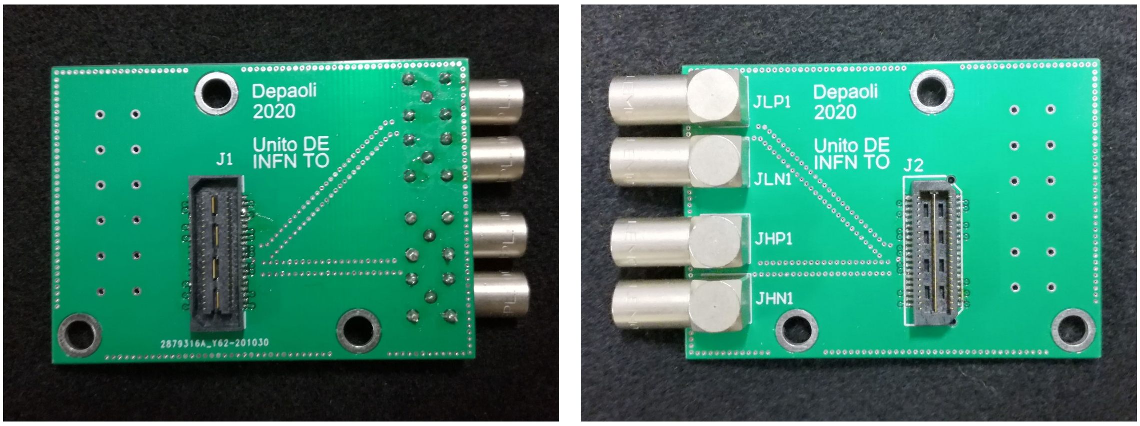

(a) (b)

Figure 4.39: Pictures of the Oscilloscope Mezzanine

4.3.13 Power Cable Board

Since the SiPM pixel is more power demanding than the PMT one, it is necessary to power it from an outside voltage generator. Three different voltages are needed for the correct functioning:

- LVL (Low Voltage Low): input voltage for the 3.3 V LDO
- LVH (Low Voltage High): input voltage for the 5.0 V LDO
- HV (High Voltage): input voltage for the SiPM bias regulator

To simplify the connection, a small PCB has been built on which the cables carrying such voltages are soldered, and which attaches directly to the Main Board. All voltages are carried independently with coaxial cables.

4.3.14 Printed Circuit Board Design

All the printed circuit boards (PCBs) composing the SiPM Pixel were designed by the Author using the Altium Designer® software package. All the boards were printed at JLCPCB, China.

Given its complexity and the fast signals involved, the board that required the most attention during its development was the Pixel Main Board. It is indeed the board where most of the components are housed, including the MUSIC. Its design started from the MUSIC MiniBoard CAD, kindly made available by the MUSIC developers; in this way it will also be possible to use the same firmware to make it work. It is a six-layer PCB, with the two inner layers dedicated only to the high speed sum signals (one for the High Gain, the other one for the Low Gain). The sum lines are adapted to 100 Ω impedance and the single ended line to 50 Ω, following the instructions given by the PCB manufacturer. Particular care was taken to shield the sum signals as much as possible, making sure to always keep at least an entire ground plane on their adjacent layers. A mechanical band has been added around the board to facilitate the assembly process; this structure was later removed. Most of the components were assembled at Asseltech Srl, Chivasso, Piedmont, Italy, and the remaining part at the Electronics Laboratory of the Istituto Nazionale di Fisica Nucleare, Turin section. Pictures of the assembled board are visible in Figure 4.40, and a picture of the Pixel Main Board connected to the Slow Control Board Adapter PCB is reported in Figure 4.41.

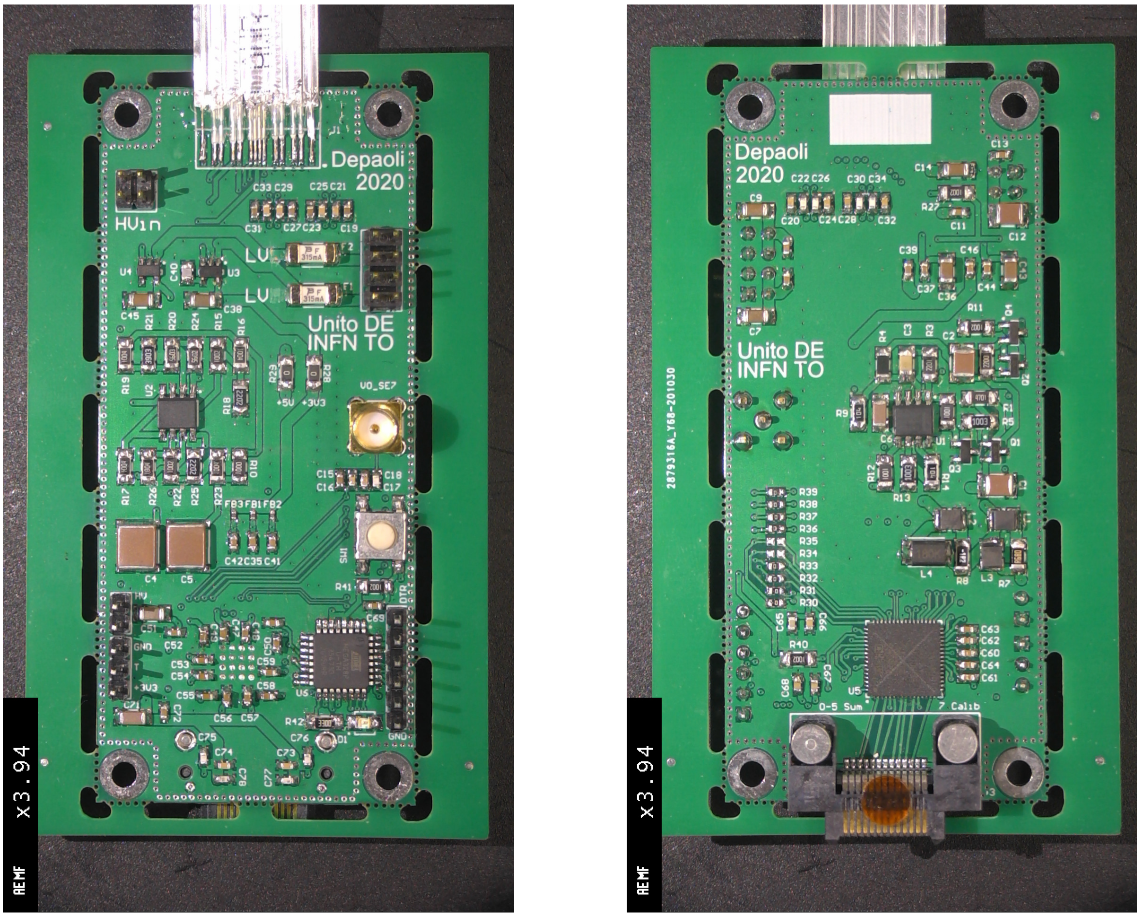

(a)

(b)

Figure 4.40: Pictures of the Pixel Main Board

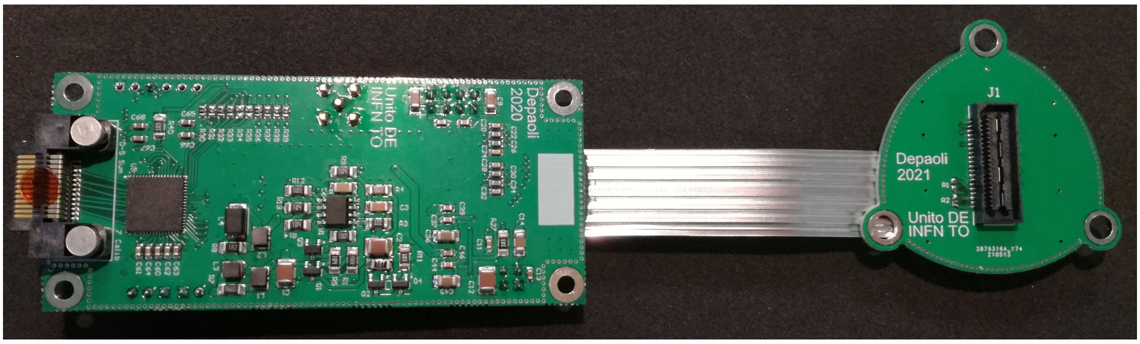

Figure 4.41: Pixel Main Board connected to the Slow Control Board Adapter PCB

4.3.15 SiPMs

The SiPM arrays used for this prototype are the Fondazione Bruno Kessler (FBK) NUV HD3-4, developed for the Schwarzschild-Couder Telescope (SCT) of the Cherenkov Telescope Array (CTA). Each array is composed of sixteen 6 mm × 6 mm SiPMs. Their cell size is equal to 40 µm, therefore each sensor has a 22 500 cells in total. Being developed for Cherenkov applications, their photodetection efficiency peaks in the ultraviolet band. A layer of epoxy resin prevents the sensors from being damaged by external events.

In the next paragraphs we will discuss the characterization of the two main values of these devices, namely the breakdown voltage and its dependence on temperature. As we will see, these values are required by the slow control software. For further measurements, carried out within the SCT collaboration, please refer to [108] and [109].

Breakdown Voltage

The breakdown voltage is the first value that has to be known when one wants to study a SiPM. Indeed, several SiPM characteristics depend on the overvoltage V_{OV}, i.e. the difference between the bias voltage V_{bias} and the breakdown voltage V_{bd}.

The easiest way to obtain the breakdown voltage is from the SiPM I-V curve: performing a voltage scan on the SiPM, at a certain voltage value the sensor will enter the Geiger regime, and the current will considerably increase. In principle, this measurement could be done in dark condition; in this case the SiPM current is only generated by thermal noise. However, experimental evidence suggests to carry out the measurement with the sensor illuminated with a dim light. Indeed, the dark current before the breakdown can be too small to be easily detected, and in addition other parasitic currents can spoil the measurement. It is important not to exceed in illuminating the sensor, otherwise an incorrect breakdown voltage value is obtained: it has been noted that V_{bd} decreases as the background light increases. Indeed, as the illuminating light increases, more electron-hole pairs will be generated in the SiPM, making the avalanche generation easier.

The experimental setup is extremely simple: the SiPM is connected to a *Keysight B2901A* source and measure unit, which is connected via USB to a computer running a LabView application. The measurement is done starting from 23 V to 30 V, with a step of 25 mV. The temperature is monitored with a thermometer, and the SiPM array is illuminated by a dim DC LED. Eight SiPM arrays have been tested; an example of the I-V curves for a FBK NUV-HD3-4 SiPM array is shown in Figure 4.42.

There are different ways to find and define the breakdown voltage; in this work, it is defined as the voltage value at which $dI/dV/I$ is maximal [70]. The procedure is shown in Figure 4.43. The first two plots at the top show the I-V characteristic of one of the SiPMs considered, both in linear and logarithmic scales, while below we find the corresponding logarithmic derivative. The resulting breakdown voltage is shown as a red vertical line.

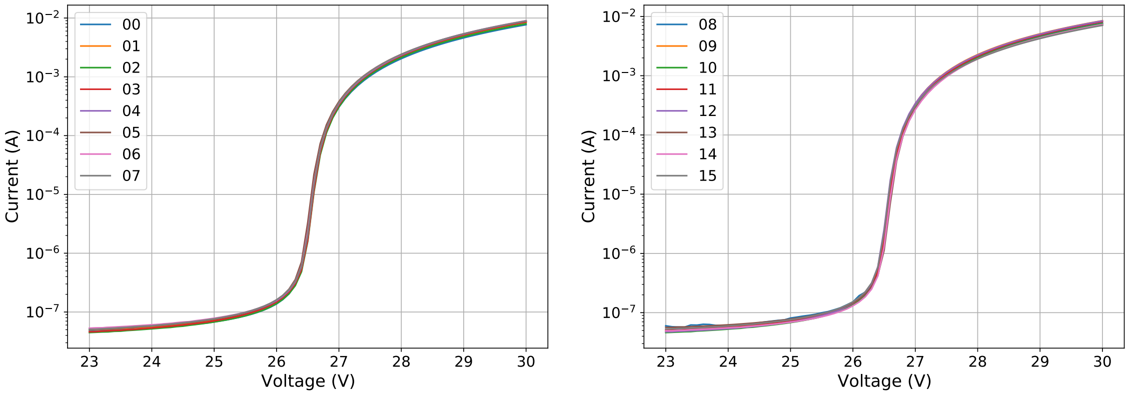

Figure 4.42: I-V curves of a FBK NUV-HD3-4 SiPM array; the numbers in the legend indicate the corresponding pixels

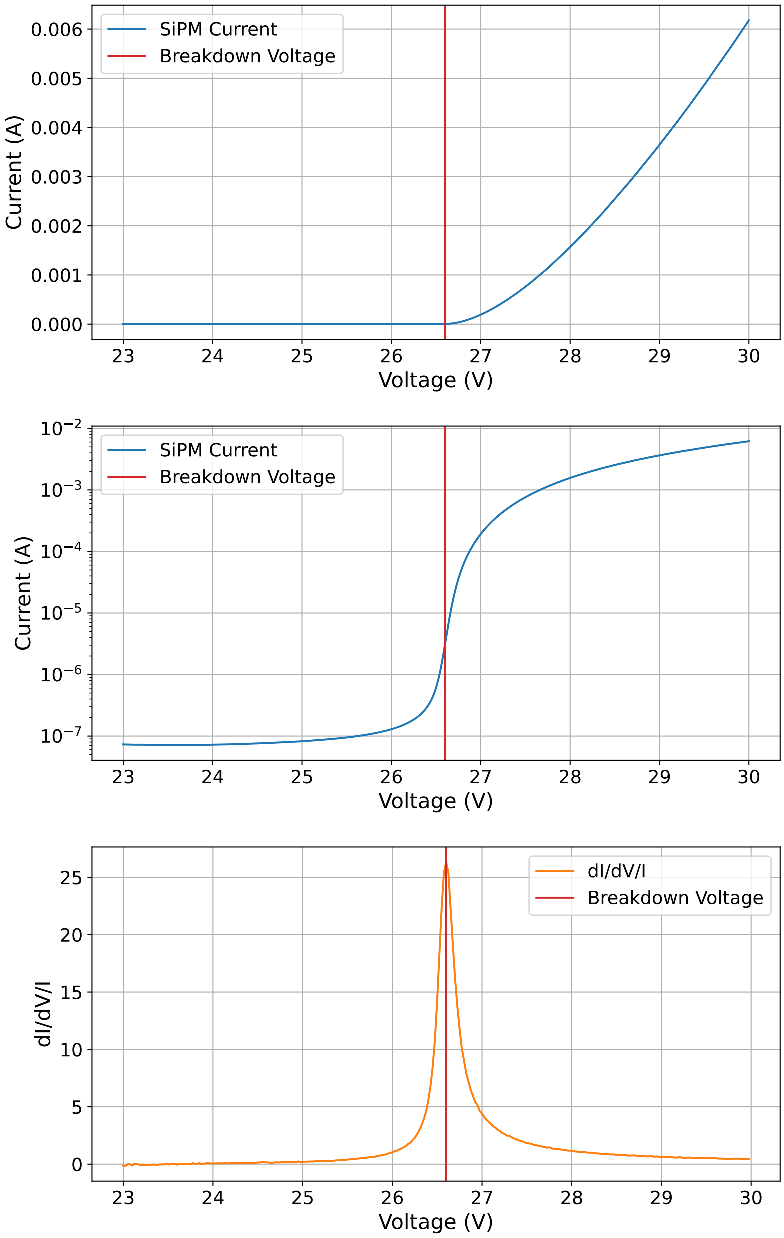

Figure 4.43: Breakdown extraction procedure from SiPM I-V curve

Breakdown Voltage Temperature Dependance

The breakdown voltage has a strong temperature dependance; since most of the SiPM characteristics depend on the overvoltage, it is necessary to monitor the temperature on the sensor and adjust properly its bias voltage. To do so, we need to know the V_{bd} dependance on temperature dV_{bd}/dT.

The sensors are kept inside a climate chamber, and the previous measurement is repeated at different temperatures, from $-10\,^{\circ}\mathrm{C}$ to $30\,^{\circ}\mathrm{C}$, with a step of $5\,^{\circ}\mathrm{C}$. The voltage scan is performed from 23 V to 30 V, with a step of 10 mV. The procedure is carried out only on two of the eight arrays; an average value will then be assumed for all the SiPMs. The breakdown voltage at each temperature is calculated for each sensor; its trend, which is linear around room temperature, is fitted with a straight line:

$$V_{bd} = \frac{dV_{bd}}{dT} T + q \tag{4.47}$$

An example of the I-V characteristics of the same SiPM taken at different temperatures and the resulting V_{bd} dependance on the temperature is shown in Figure 4.44. The distribution of the dV_{bd}/dT for the two considered FBK arrays is reported in Figure 4.45. We see how the values are slightly different for the two arrays. As anticipated, a single value will be considered for all the FBK arrays:

$$\frac{dV_{bd}}{dT} = 27\,\frac{\mathrm{mV}}{^{\circ}\mathrm{C}} \tag{4.48}$$

With this coefficient, it is possible to obtain the breakdown voltage at a generic temperature $V_{bd}(T)$ knowing its value at the measurement temperature $V_{bd}(T_0)$:

$$V_{bd}(T) = V_{bd}(T_0) + \frac{dV_{bd}}{dT}(T - T_0) \tag{4.49}$$

In Figure 4.46 it is shown the distribution of the breakdown voltages measured in the previous section, rescaled at $20\,^{\circ}\mathrm{C}$. The mean and standard deviation values of the distributions are reported in Table 4.3.

Operating Overoltage

Measurements done on these sensors in the SCT collaboration shown that the PDE increases with overvoltage up to reach a plateau, which starts at about 6 V. This value is therefore the one chosen as the operating SiPM overvoltage in this work.

However, we could choose a lower overvoltage, for example if we want to reduce the crosstalk effect. Given the many factors involved, the best and only solution to choose the optimal value is from Monte Carlo simulations.

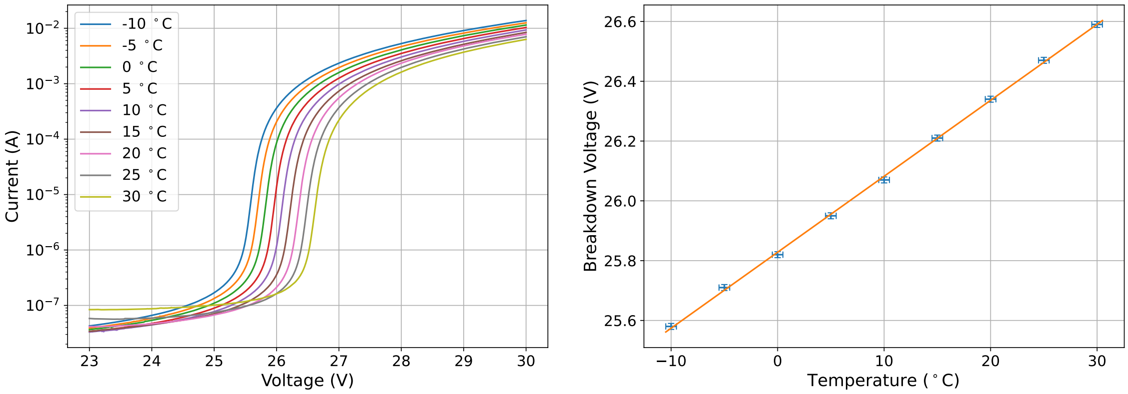

Figure 4.44: An example of the I-V characteristics of the same SiPM taken at different temperatures, and the resulting V_{bd} dependance on the temperature

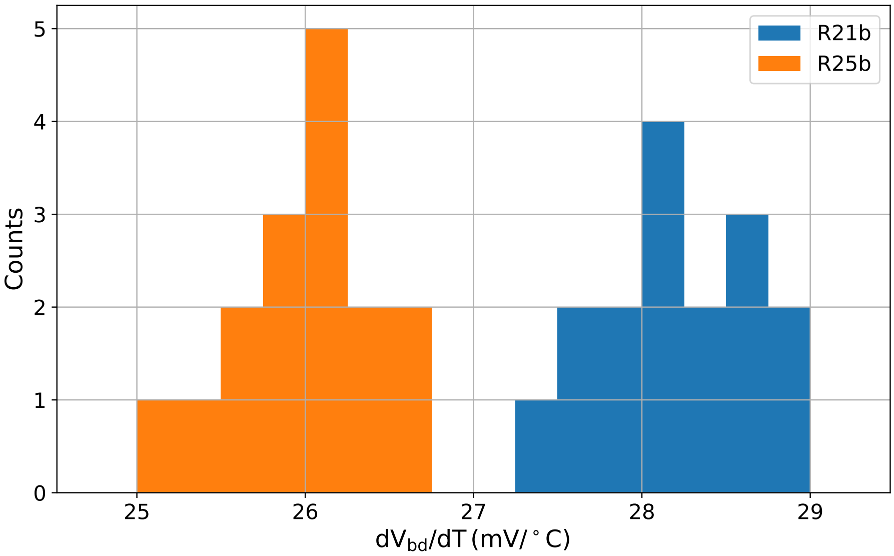

Figure 4.45: Obtained dV_{bd}/dT for the two considered FBK arrays

SiPM array	$V_{bd,mean}$ (V)	$V_{bd,std}$ (V)
R25b	26.32	0.03
R22b	26.30	0.03
L25b	26.34	0.03
R14b	27.10	0.03
L20b	27.06	0.04
L24b	27.09	0.05
R17b	26.96	0.06
R21b	27.05	0.07

Table 4.3: Mean and standard deviation of the breakdown voltage distributions at 20 °C for the SiPM arrays under study

Figure 4.46: Breakdown voltage distributions at 20 °C for the SiPM arrays under study

4.3.16 Camera Control Software

The Camera Control Software for the SiPM Pixel (CaCoSiPM) is the software that takes care of the module slow control. It runs on the Linux CentOS 7 computer connected via Ethernet to the DRS4 readout board and is based on the software developed by the collaboration to control the LST module. A python script runs the required programs using the `subprocess` library. The user can control the module thanks to a graphical interface. All the configurations are stored in a `yaml` file; an example of this file can be found in Appendix B.

User Interface

The CaCoSiPM user interface is written in python using the `tkinter` library, and is visible in Figure 4.47. Its central part is a table which shows the main pixel parameters, channel by channel:

- **OV** (V): desired overvoltage for the SiPMs. This value is set in the `yaml` configuration file
- **HV** (V): SiPM bias voltage corresponding to the desired overvoltage
- **Vmon goal** (mV): Voltage Monitor value corresponding to the desired SiPM bias voltage
- **Set (DAC)**: DAC value set by the program
- **Vmon** (mV): Voltage Monitor output voltage read by the ADC located on the Slow Control Board and converted into mV
- **HVread** (V): Regulator output voltage corresponding to Voltage Monitor value
- **Imon** (mV): Current Monitor output voltage read by the ADC located on the Slow Control Board and converted into mV
- **Iread** (mA): SiPM current corresponding to Current Monitor output voltage
- **Temp** (°C): temperature read by the digital thermometer located on the dedicated PCB

Three buttons are located at the top left:

- **START ALL**: to power on all the seven channels
- **STOP ALL**: to power off all the seven channels
- **QUIT**: to quit the program

Each pixel can be powered on independently using the check button on the side of the corresponding row. In the example reported in Figure 4.47a all the seven pixels are powered, while in Figure 4.47b only channel 2 is on; in both cases the module was illuminated by a non-uniform DC light. On the right the user finds a pictorial representation of the seven-pixel module. If a channel is powered on, its color will be related to the current flowing into it. The maximum current (10 mA in the example) is set in the `yaml` configuration file (`I_MAX`). Finally, at the top right a label shows the DRS4 readout board IP address (set in the `yaml` configuration file); its color is green if the board is connected and responding, red otherwise. The slow control programs are stored in the `script_dir` folder in the configuration file. The displayed information can be logged in a file (saved in the `log_dir` folder).

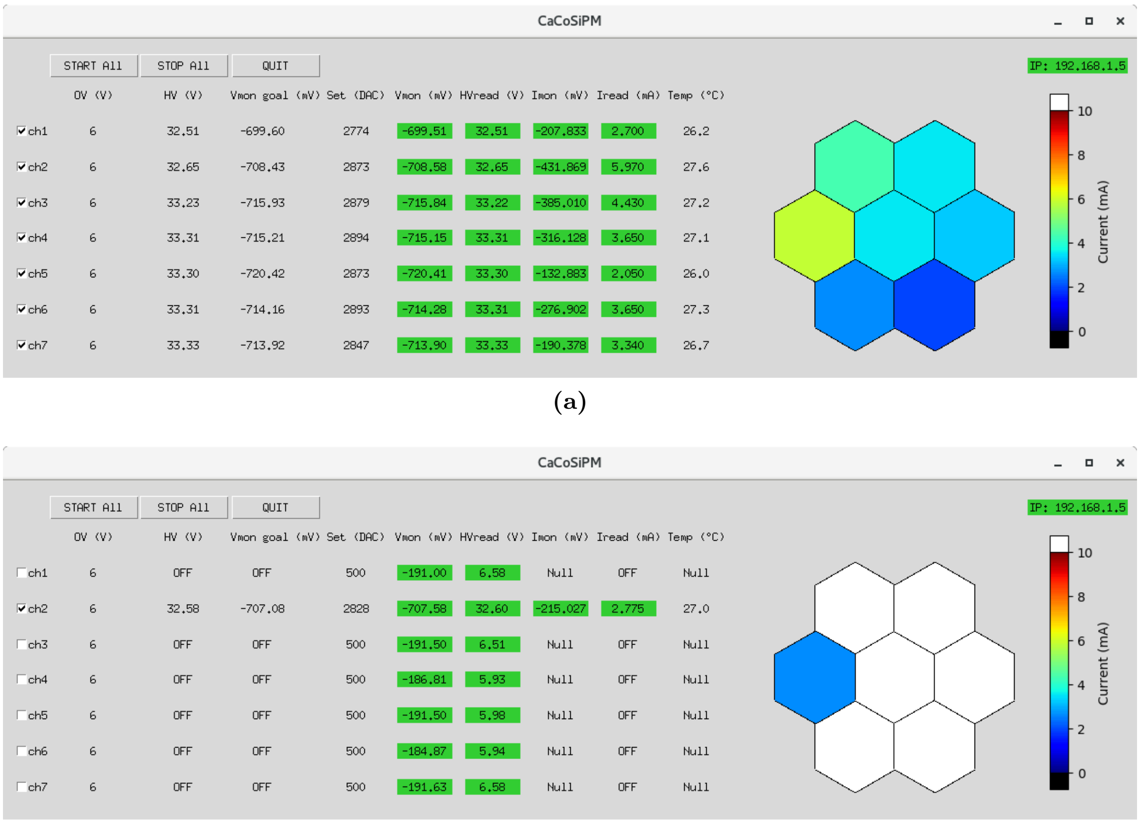

	OV (V)	HV (V)	Vmon goal (mV)	Set (DAC)	Vmon (mV)	HVread (V)	Imon (mV)	Iread (mA)	Temp (°C)
☑ ch1	6	32.51	-699.60	2774	-699.51	32.51	-207.833	2.700	26.2
☑ ch2	6	32.65	-708.43	2873	-708.58	32.65	-431.869	5.970	27.6
☑ ch3	6	33.23	-715.93	2879	-715.84	33.22	-385.010	4.430	27.2
☑ ch4	6	33.31	-715.21	2894	-715.15	33.31	-316.128	3.650	27.1
☑ ch5	6	33.30	-720.42	2873	-720.41	33.30	-132.883	2.050	26.0
☑ ch6	6	33.31	-714.16	2893	-714.28	33.31	-276.902	3.650	27.3
☑ ch7	6	33.33	-713.92	2847	-713.90	33.33	-190.378	3.340	26.7

(a)

	OV (V)	HV (V)	Vmon goal (mV)	Set (DAC)	Vmon (mV)	HVread (V)	Imon (mV)	Iread (mA)	Temp (°C)
☐ ch1	6	OFF	OFF	500	-191.00	6.58	Null	OFF	Null
☑ ch2	6	32.58	-707.08	2828	-707.58	32.60	-215.027	2.775	27.0
☐ ch3	6	OFF	OFF	500	-191.50	6.51	Null	OFF	Null
☐ ch4	6	OFF	OFF	500	-186.81	5.93	Null	OFF	Null
☐ ch5	6	OFF	OFF	500	-191.50	5.98	Null	OFF	Null
☐ ch6	6	OFF	OFF	500	-184.87	5.94	Null	OFF	Null
☐ ch7	6	OFF	OFF	500	-191.63	6.58	Null	OFF	Null

(b)

Figure 4.47: CaCoSiPM user interface examples, either with all the pixels on (a), or with just one (b); in both cases the module was illuminated by a non-uniform DC light

Normal Operation

As soon as the program is started, it checks the Ethernet connection with the DRS4 readout board; its IP value is written in the `yaml` configuration file (`IP` parameter). If the board responds, the IP label becomes green.

Each channel is brought to the initial condition in which the DAC has a safe value (`safe_dac` in the configuration file). With this DAC value the SiPM bias voltage is few volts higher than zero but well below the breakdown. This procedure is done to make sure the MUSIC ASIC will not be damaged. Indeed, in the DC connection, while the SiPM cathode is connected to the Regulator output voltage, its anode is connected to a MUSIC input pin, whose voltage is higher than zero. Therefore, if the Regulator output voltage is zero, the SiPM will act as a directly polarized diode, thus a current will flow into it. This current could damage the MUSIC: for this reason, the Regulator output voltage is always kept a few volts higher than zero, in order to have the SiPM always reversely polarized.

After enabling the channel, the software will switch it on and keep the SiPM bias voltage at the desired value thanks to a feedback loop. The procedure works as it follows: the software evaluates the desired V_{HV} corresponding to the given overvoltage, then calculates the corresponding voltage monitor V_{mon} value and changes the DAC value up to reach the desired V_{mon}. The Regulator output voltage V_{HV} is calculated as follows:

$$V_{HV} = V_{OV} + V_{bd}(T_0) + \frac{dV_{bd}}{dT}(T - T_0) + V_{anode} \tag{4.50}$$

The value of V_{anode} depends if the SiPM pixel is DC or AC coupled and is

- DC case: $V_{anode} = V_{MUSIC,IN}$
- AC case: $V_{anode} = R_{AC} * I_{mon}$

All these parameters are given in the configuration file with the following parameters:

- V_{OV}: `OV`
- $V_{bd}(T_0)$: `Vbd`
- $\frac{dV_{bd}}{dT}$: `dVbddT`
- T_0: `Def_Temp`
- $V_{MUSIC,IN}$: `V_MUSIC`
- R_{AC}: `R_ac`

V_{OV} is the desired SiPM overvoltage to which we want to operate the pixel. $V_{bd}(T_0)$ is the average of the breakdown voltages of the twelve selected SiPMs in the array; this value is obtained at the reference temperature T_0. The third term is the temperature compensation of the SiPM V_{bd}, which increases by a value dV_{bd}/dT at each degree.

The last correction depends on the SiPM coupling (AC or DC) and is introduced since in both cases the SiPM anode voltage is higher than zero. The SiPM bias voltage V_{SiPM} is:

$$V_{SiPM} = V_{HV} - V_{anode} \tag{4.51}$$

In the DC case, we have seen that the SiPM anode voltage is equal to the MUSIC input pin voltage $V_{MUSIC,IN}$.

In the AC case the situation is instead a bit more complicated. The DC current flowing in the SiPM causes a voltage drop on the filter resistor; considering the circuit in Figure 4.33, the voltage drop on the resistor R_F will be:

$$V_{R_F} = I_{SiPM} R_F \tag{4.52}$$

where I_{SiPM} is the current flowing into the SiPM. By design, the current read by the Current Monitor I_{mon} is the sum of the currents flowing into the twelve SiPMs; since they are connected two by two in parallel, we have six channels in total. With a good approximation, we can say that the current is equally split between the six channels, and thus V_{anode} will be:

$$V_{anode} = \frac{I_{mon}}{6} R_F \tag{4.53}$$

We can introduce the equivalent resistor R_{AC}:

$$V_{anode} = I_{mon} R_{AC}, \qquad R_{AC} = R_F/6 \tag{4.54}$$

This value is the one set in the configuration file.

Once obtained the desired V_{HV}, the software converts it in the V_{mon} goal value. This conversion is done thanks to proper calibration factors, later discussed. With a feedback loop, CaCoSiPM increases or decreases the DAC value up to reach the desired V_{mon} value. If V_{HV} is the desired SiPM bias voltage value and $V_{HV,read}$ is the one read by the ADC (converted from V_{mon}), at each loop the software evaluates the difference $d_{V_{HV}}$ as:

$$d_{V_{HV}} = V_{HV} - V_{HV,read} \tag{4.55}$$

This difference brings the information of how much the DAC value should be increased or decreased to reach the goal value. If $d_{V_{HV}}$ is higher than a threshold value given in the configuration file (`HV_sens` parameter, in mV), the DAC will be increased (or decreased) by a d_{DAC} value:

$$d_{DAC} = \lceil k_{DAC,V_{HV}} d_{V_{HV}} \rceil \tag{4.56}$$

where $\lceil \rceil$ is the ceil function. The value of $k_{DAC,V_{HV}}$ (`k_DAC_HV` in the configuration file) is obtained experimentally to speed up the process of achieving V_{HV}. The `HV_sens` parameter is introduced for feedback loop stability reasons. We can set also a DAC value beyond which there is no increase in V_{HV}; this value is the `max_DAC` in the configuration file. In this way we can avoid unnecessary calculations. In addition, the DAC value can never drop below the `safe_DAC` value.

For special operations (e.g. connecting a PMT pixel), it is possible to bypass the feedback loop and use a fixed DAC value. In the configuration file, the user can find the `fix_DAC` parameter, which is an array considered by the program as follows:

- if `fix_DAC[i]` is equal to zero, the bias voltage of the i-th channel will be set with the previously discussed feedback loop
- if `fix_DAC[i]` is greater than zero the DAC value of the i-th cannel will be always set to the given value

When a channel is disabled (or by unchecking the corresponding button or with the "QUIT ALL" button) the DAC is set again to the `safe_DAC` value.

If you want to run the control software more slowly, you can set the waiting time for each loop after all the operations have been carried out (`wait_time` in the configuration file, expressed in milliseconds). To prevent the software from crashing due to unsuccessful communication with the DRS4 readout board, each operation has a certain timeout (which can be set in the configuration file with the `timeout` parameter, expressed in seconds).

4.4 SiPM Pixel Measurements

4.4.1 Voltage Monitor Calibration

In order to make the CaCoSiPM software work properly, the voltage monitor must be first calibrated. This procedure is done on the bare Pixel Main Board, with the SiPM array and the AC filter mezzanine unconnected. While the software performs a DAC scan, the V_{HV} value is read by a Fluke Multimeter; to simplify this operation a two-pins header is soldered on the board. The setup is sketched in Figure 4.48, where V is the Fluke Multimeter.

Results for a single SiPM pixel are visible in Figure 4.49: on the abscissa axis we have the V_{HV} measured with the multimeter and on the ordinate axis the corresponding V_{mon} values obtained from the Slow Control Board ADC. The test was repeated for the two Current Limiter configurations, both with the limit set to 3 mA and to 10 mA. It is clear that the data follows a linear trend; a fit is therefore performed with the following equation:

$$V_{mon} = m_V V_{HV} + q_V \tag{4.57}$$

The obtained fit results are then written in the configuration file (`popt_HV` parameter) and are used to convert the desired V_{HV} to $V_{mon,goal}$ and to convert the V_{mon} value obtained from the ADC to the corresponding V_{HV}.

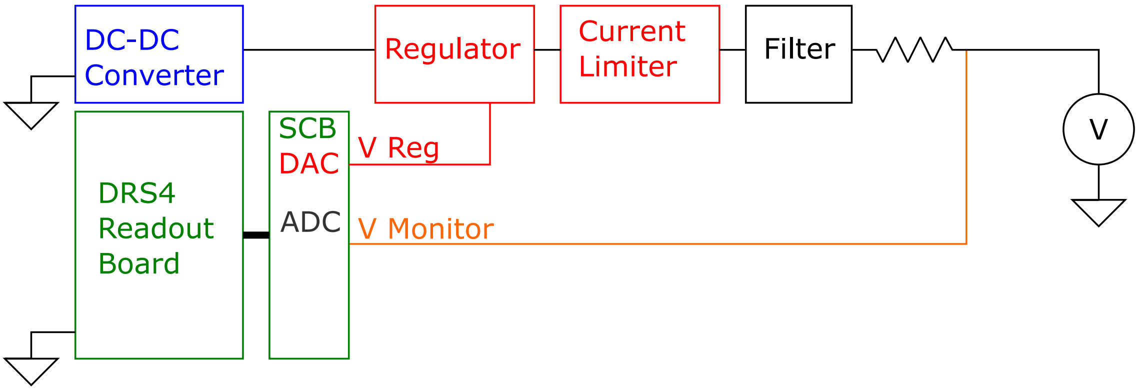

Figure 4.48: Voltage Monitor calibration setup

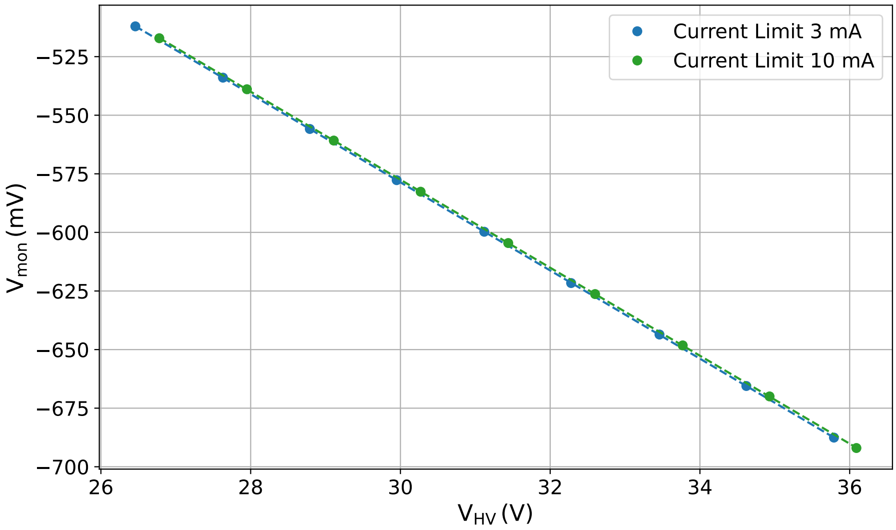

Figure 4.49: Voltage Monitor calibration results

4.4.2 Current Monitor Calibration

After the Voltage Monitor, we need to calibrate the Current Monitor. Also this procedure is done on the bare Pixel Main Board, with the SiPM array and the AC filter mezzanine unconnected; the setup is shown in Figure 4.50. A SiPM is connected to the V_{HV} pin (the same used for the Voltage Monitor calibration) and is illuminated by a LED controlled by a Power Supply. By keeping constant the DAC value and changing the Power Supply output voltage, it is possible perform a scan on I_{mon}. The current is read with a Fluke Multimeter connected between the V_{HV} pin and the SiPM.

Results for a single SiPM pixel are visible in Figure 4.51: on the abscissa axis we have the current I measured with the ammeter and on the ordinate axis the corresponding I_{mon} values obtained from the Slow Control Board ADC. Also in this case we have a linear trend, fitted with the following equation:

$$I_{mon} = m_I I + q_I \tag{4.58}$$

The obtained fit results are then written in the configuration file (`popt_I` parameter) and are used to convert I_{mon} to the real current flowing into the SiPM array.

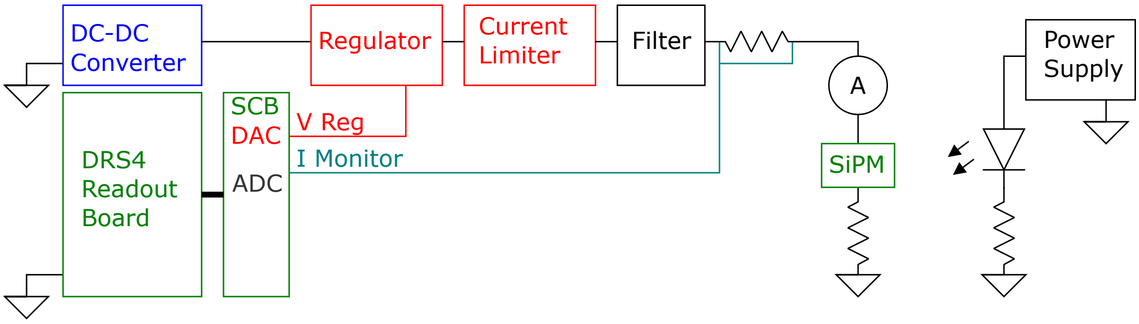

Figure 4.50: Current Monitor calibration setup

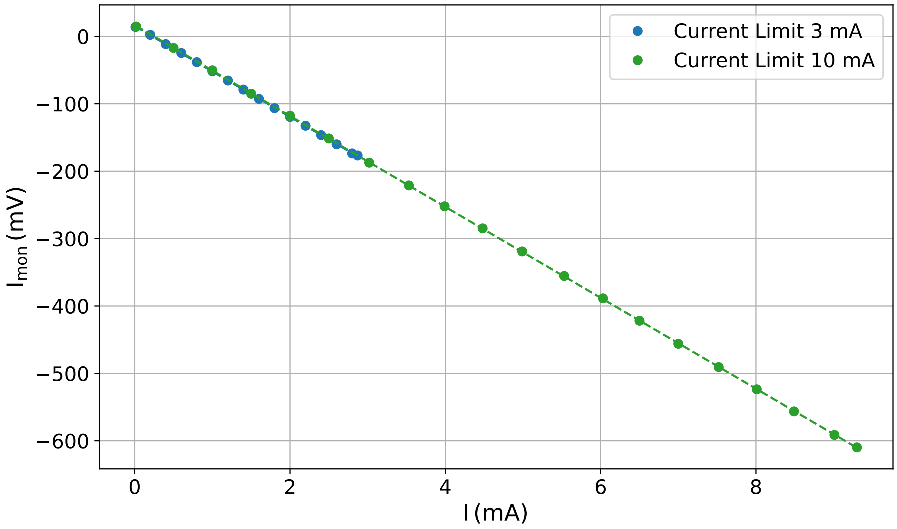

Figure 4.51: Current Monitor calibration results

4.4.3 Current Limiter Test

The Current Limiter test is done on the whole SiPM Pixel, with the AC filter mezzanine and the SiPM array connected. The detector is kept in a light-proof dark box (visible in Figure 4.55). The CaCoSiPM software runs on the CentOS 7 computer to control and monitor the SiPM bias voltage; all the measured values are saved in a log file. A DC LED controlled by a power supply simulates the night sky background; by increasing the LED polarization it is possible to scan different NSB intensities, corresponding to different currents flowing into the SiPM array. The test was repeated for the two Current Limiter configurations, with the limit set to 3 mA and to 10 mA. In the first case it would also have been possible to carry out the test in DC coupling; however, both as a precaution and because, as we will see, AC coupling is the best solution, this second configuration was chosen.

Results are visible in Figures 4.53a and 4.53b. In dark condition the DC LED is switched off, and the current is at its minimum; its value is however higher than zero due to SiPM dark counts. Turning on the LED and gradually increasing its brightness, we can see how the regulator output voltage V_{HV} remains almost constant, until it drops sharply when the hardware-set limit is reached. The last points, the ones at the lowest V_{HV} values, are taken with the dark box open, exposing the switched-on detector to daylight. The difference in the V_{HV} values is due to the fact that in the two configurations different SiPM arrays were used.

Looking more carefully at the region before the Current Limiter intervention, we observe that the V_{HV} actually slightly increases as the current flowing through the pixel increases. Indeed, this value is set by the feedback loop previously described; in particular as the current increases, the voltage drop on the AC filter resistor increases, therefore the voltage at the SiPM anodes increases: to keep the SiPM at the same overvoltage the camera control software increases the regulator output voltage. In Figures 4.53c and 4.53d it is shown the comparison between the regulator output voltage read by the monitor $V_{HV,read}$ and the target one $V_{HV,goal}$ in the pixel operative region; the difference between the two quantities is reported in Figure 4.53e and 4.53f and is negligible (corresponding to a gain modification of about 0.3 %). This difference can be tuned by changing the `HV_sens` parameter in the configuration file; however, a too small value could affect the stability of the of the feedback loop: it is therefore necessary to find a fair compromise.

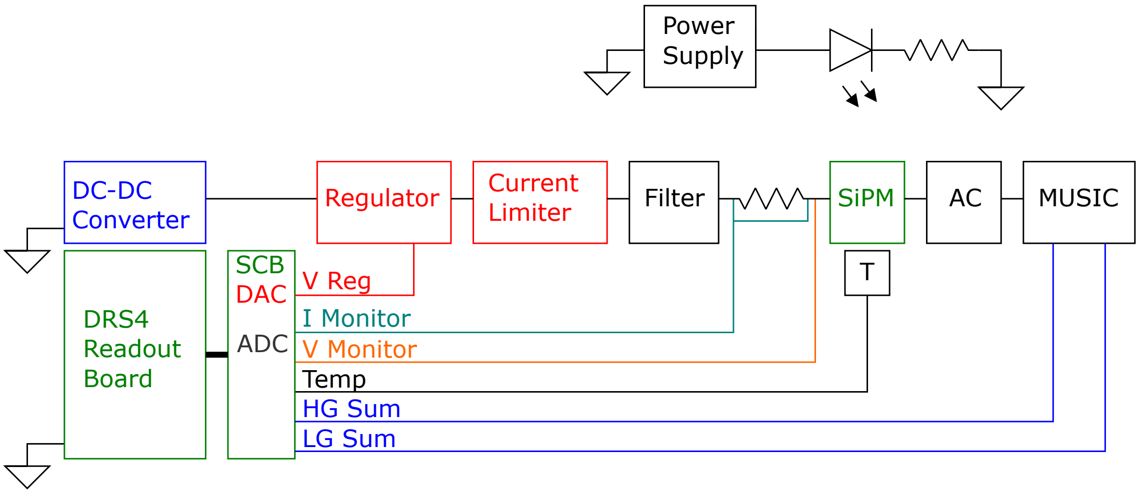

Figure 4.52: Current Limiter test setup

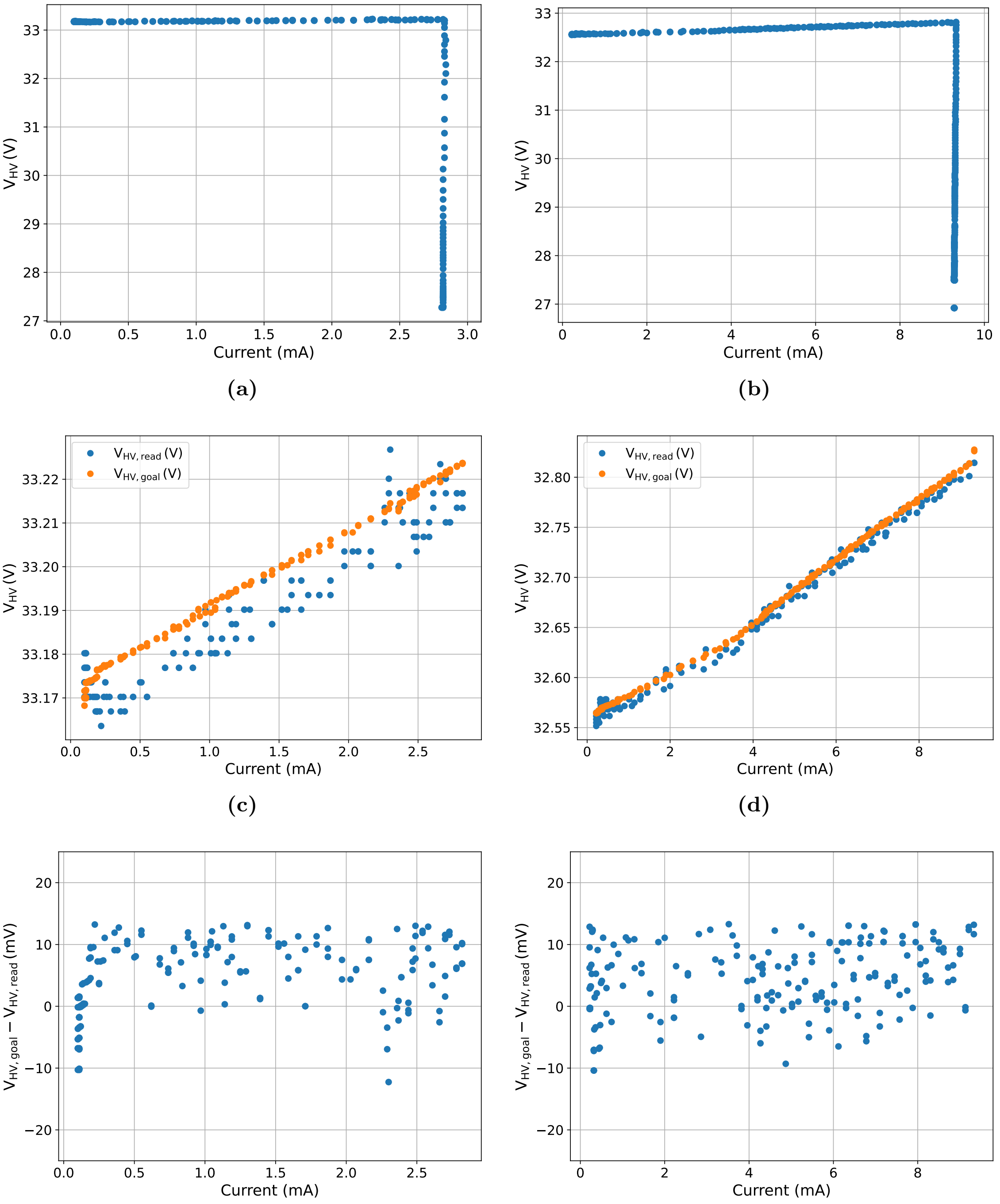

(a) **(b)**

(c) **(d)**

(e) **(f)**

Figure 4.53: Current Limiter test for the 3 mA (a, c, e) and the 10 mA (b, d, f) configuration

4.4.4 Comparison Between AC and DC Coupling

The designed SiPM Pixel allows us to quickly switch between AC and DC coupling mode by simply connecting or not the AC filter mezzanine between the Main Board and the SiPM array.

To find whether solution is the best one for our application, we can do a simple test. Being it qualitative, for simplicity the sum signals are acquired with an oscilloscope (Tektronix MS06 with 200 MHz bandwidth limit) using the LEMO Mezzanine. The setup is similar to the one used for the Current Limiter test, with the addition of a pulsed LED (Figure 4.54). A simple LED controlled by a DC power supply (DC PS in the scheme) simulates the night sky background, while the pulsed LED (Picoquant PDL 800-D with PLS 400 LED head) flashes the sensor. Pictures of the driver and of its LED head are visible in Figure 4.56. The Picoquant PDL 800-D is a driver both for picosecond pulsed laser diode heads and for sub-nanosecond pulsed LEDs; combined with a 400 nm LED head (PLS 400), it generates a sub-nanosecond pulsed light which well mimics a Cherenkov photons bunch. Tests were done also with other solutions, including a self-produced laser diode driver, but the best performances, in particular as regards the light stability, were obtained with this instrument, used for all the measurements reported in this work. An Agilent 33250A function generator triggers the pulsed LED; the output trigger from the LED is used to trigger the data acquisition. By keeping constant the pulsed LED amplitude and varying the DC LED bias voltage, it is possible to compare the pulsed LED signals with different backgrounds. In order not to damage the MUSIC ASIC during the DC coupling test, the Current Limiter is hardware set to 3 mA limit.

Results are shown in Figures 4.57a (AC coupling) and 4.57b (DC coupling). Each waveform is the average of 1000 acquisitions, and is labelled with the corresponding current flowing in the channel, measured with the Current Monitor. With the AC filter, there are basically no differences between the waveforms acquired in dark condition ($I_{mon} \simeq 0.15\,\mathrm{mA}$) and the ones acquired with the DC LED turned on ($I_{mon} \simeq 2.30\,\mathrm{mA}$). In the DC approach, instead, the MUSIC output saturates as soon as the current flowing in the ASIC exceeds a certain limit value. As anticipated, it is only a qualitative test, but enough to suggest that the AC coupling is the best solution for our application, where working in a high-brightness background environment is a critical aspect.

In addition the Current Limiter hardware settings can be relaxed if we work in AC mode, since the DC current due to the night sky background would flow to the ground trough the filter resistor. This is another reason to choose such configuration.

From now on all the reported measurements are done with the AC filter mezzanine connected.

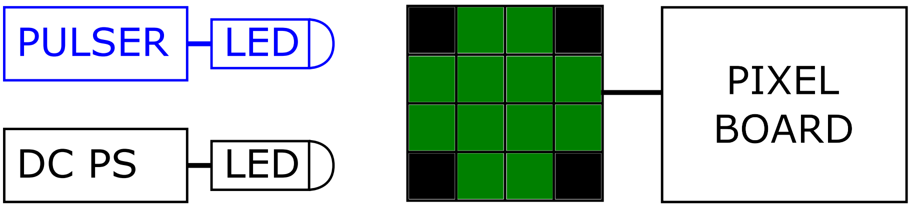

Figure 4.54: Test setup for the comparison between AC and DC coupling

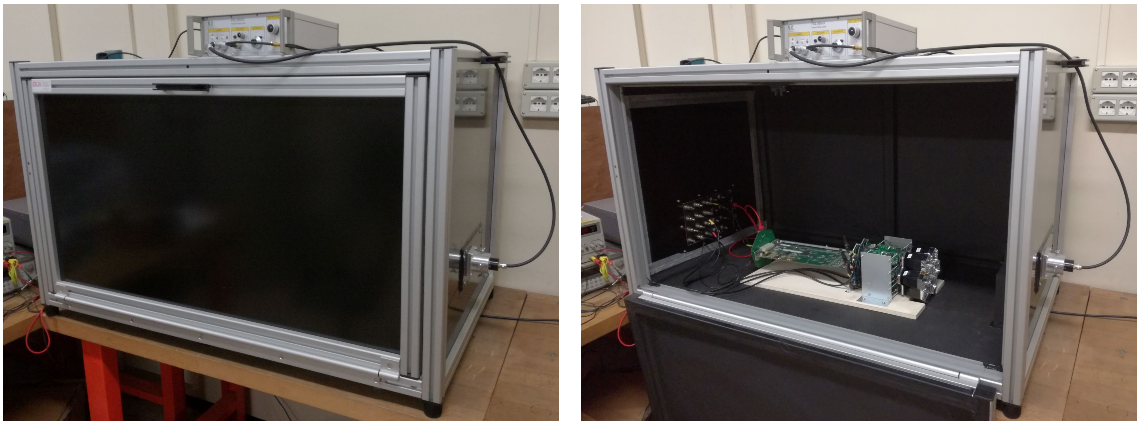

(a) **(b)**

Figure 4.55: Pictures of the light-proof black box

(a) **(b)**

Figure 4.56: The Picoquant PDL 800-D driver (a) and its PLS 400 LED head inserted in a custom made light-proof black box connector

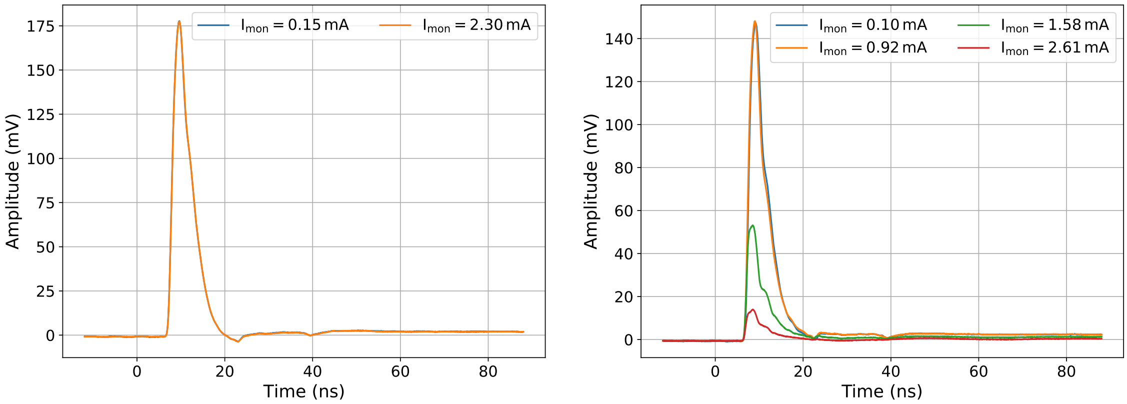

(a) **(b)**

Figure 4.57: Signals acquired in AC (a) and DC (b) coupling at different light backgrounds; in both plots the blue and orange waveforms are overlapping

4.4.5 Signal Acquisition and Processing

The SiPM Pixel signal acquisition is based on the LST readout electronics. The basic test setup is shown in Figure 4.58; all the following tests reported are based on this scheme.

The SiPM pixel is connected to the Slow Control Board, which in turn is connected to the DRS4 readout board. A dummy backplane acts as the interface to the computer. Signals are acquired with the CentOS7 computer connected via Ethernet to the DRS4 readout board, using the *ZFitswriter* and *EventBuilder* software. Raw data are later processes with the *cta-lstchain* software.

The LST board is supplied at 24 V with a Power Supply (GW GPS3030D). Another power supply (Keysight E36312A) powers the MUSIC ASIC located on the SiPM Pixel with 6 V and 4.3 V. The input high voltage for the Regulator host on the SiPM Pixel is given by a high-voltage power supply (Keysight B2901A). Some tests were done also by using a boost DC-DC converter, in particular a Texas Instruments LM5002 [110] mounted on a dedicated PCB. It is known how DC-DC converters can affect the system noise, and to avoid this problem extreme care has to be taken in the realization of their PCBs. Since this was outside the scope of our development, for tests based on signals acquisition, and therefore where an external noise could negatively affect the results, we opted to use a low noise bench power supply.

A pulsed LED (Picoquant PDL 800-D with PLS 400 LED head) flashes the SiPM pixel triggering on the output of an Agilent 33250A function generator; as previously said, this instrument well mimics a Cherenkov photons bunch. Its SYNC output is connected to the LST board for triggering the data acquisition. It is not possible to use the output trigger from the Picoquant driver for this purpose due to incompatible signal logic: the DRS4 readout board input trigger indeed follows the 0 V to 5 V TTL logic, while the Picoquant output trigger is a negative pulse going approximately from 0 V to −1 V.

Like in the Current Limiter test, a simple LED biased by another Power Supply is used to simulate the night sky background, if needed. The one just described is the basic setup; for some tests other element will be added, which will be described in due time

DRS4 Readout Board Initial Configurations

Each time the DRS4 readout board is powered on, some initial configurations as to be loaded to make it work properly. Such configurations are tailored for the laboratory measurements, and can be different from the ones used in the telescope. The loaded

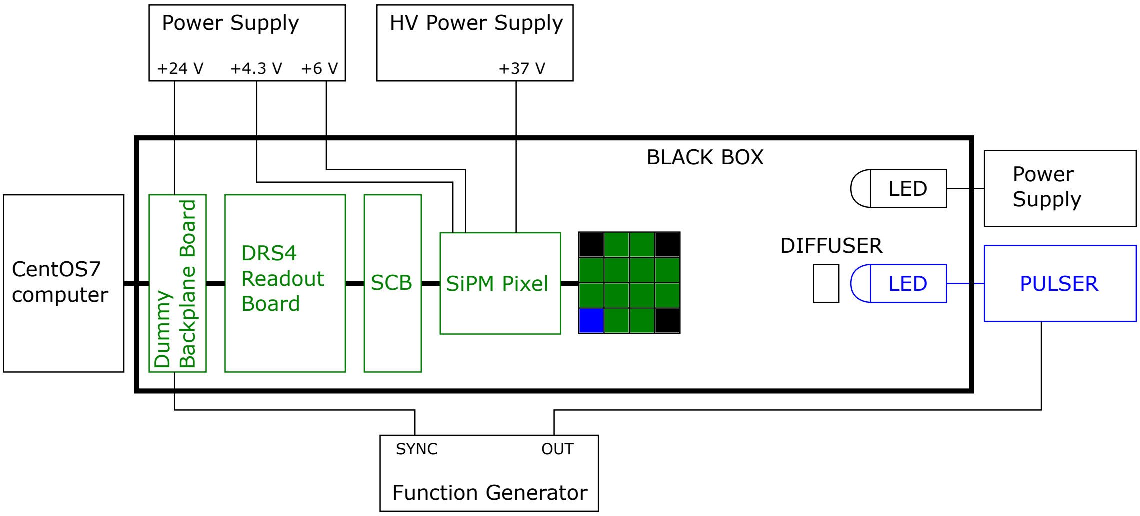

Figure 4.58: Test setup for the comparison between AC and DC coupling

settings are the following:

- Set external trigger
- Set an appropriate delay between trigger and data acquisition
- Configure baseline and DRS4 offset voltage
- Set the AD9637 ADC in offset binary output mode

Data are always taken with external trigger, therefore this option should be set; in addition a proper delay value should be written in memory, to have the pulsed LED signal inside the acquisition window. In order to use the whole 12 bits dynamic range, it is necessary to set the ADC (AD9637 from Analog Devices) in offset binary output mode (see [111]) and to configure proper baseline and DRS4 offset voltage values. A program based on the software developed by the LST collaboration is run every time the DRS4 readout board is powered on. The acquisition window and the sampling frequency are kept to the default values, namely 40 ns and 1 GSPS.

Signal Acquisition

High Gain and Low Gain signals are acquired with the CentOS7 machine connected via Ethernet to the DRS4 readout board. This machine runs the LST DAQ softwares, namely the *ZFitswriter* and *EventBuilder* softwares. These programs must be launched simultaneously to acquire and save the signals. The Dummy Backplane has only one Ethernet connector; since two different Ethernet ports are needed for this operation, an Ethernet switch is placed between the LST board and the computer.

The DRS4 output is reliable only after the chip reaches thermal stabilization. Therefore, in order to avoid data corruption, it is necessary to observe a proper warm-up time. We have to wait at least one hour after the DRS4 readout board has been turned on before taking data.

After the warm-up is finished, the first step is to take a pedestal run. This run is used to calibrate the baseline level of the DRS4 capacitors, and is taken in dark conditions, with the SiPMs powered off. To get enough statistics, about 200 000 events are acquired at 1 kHz with external trigger.

Then the interested signals are acquired. Each run is saved in a separate file, which will be later processed by the *cta-lstchain* software package.

Signal Processing

As previously said, the signal processing relies on the *cta-lstchain* software package, developed by the LST collaboration. The first step is to process the pedestal run, in order to get the pedestal file with all the baseline values of the DRS4 capacitors. Then the pipeline processes the raw data (called *r0*), to obtain the *r1* files with the calibrated waveforms. The calibration performed by the pipeline is divided in three steps. In the first one the pipeline subtracts the pedestal (baseline) of each of the DRS4 capacitors. Then it performs a time lapse baseline correction: indeed, in the DRS4, the baseline of a given cell depends also on the time elapsed since the previous reading of the same cell. In the last step the pipeline interpolates some well-known spikes which occur in the DRS4 chip. In addition for each 40 ns window, the first and last two slices are excluded, in order to reduce electronic noise.

Now we can find the signal area A of the calibrated waveforms. First the maximum value of the waveform (i.e. the peak) is found inside the signal window. Then the program opens a window which starts from d_{low} nanoseconds before the peak to d_{high} nanoseconds after the peak, and sums all the points acquired in this interval:

$$A = \sum_{t_1<t<t_2} w(t), \qquad t_1 = t_{peak} - d_{low}, \qquad t_2 = t_{peak} + d_{high} \tag{4.59}$$

where t_{peak} is the time corresponding to the waveform peak and $w(t)$ is the value of the waveform at time t. We choose d_{low} and d_{high} values in order to integrate most of the signal:

- High Gain:
  - $d_{low} = 3\,\text{ns}$
  - $d_{high} = 10\,\text{ns}$
- Low Gain:
  - $d_{low} = 3\,\text{ns}$
  - $d_{high} = 4\,\text{ns}$

Example of a High Gain (a) and Low Gain (b) calibrated waveforms are shown in Figure 4.59a and in Figure 4.59b respectively. The peak is the orange dot, while the colored area is the one considered by the algorithm. Please note that the program does not integrate the waveform with a trapezoidal algorithm, as the plot would suggest, but only sums the points of the selected waveform.

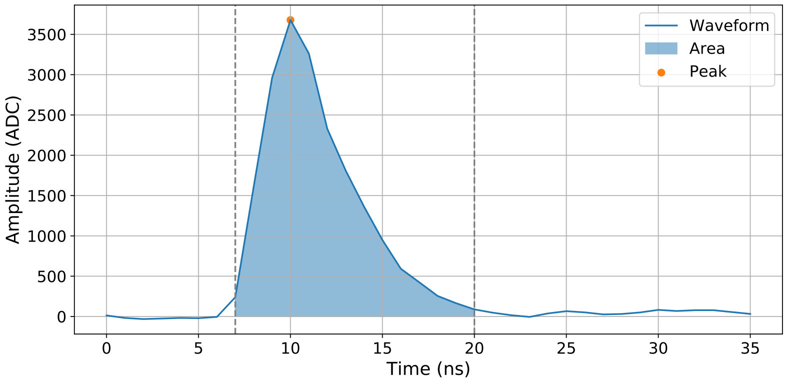

(a)

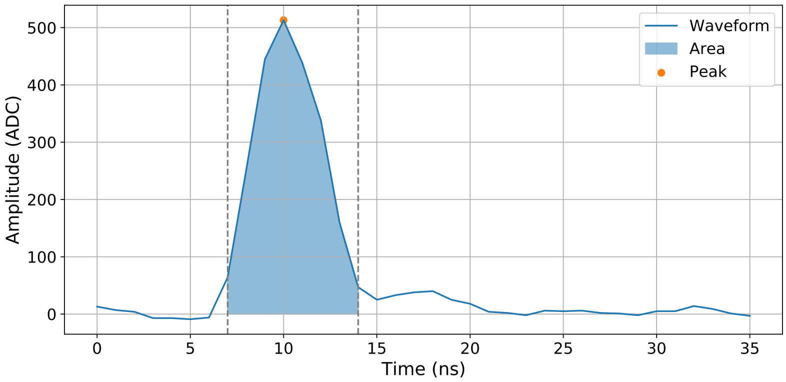

(b)

Figure 4.59: Example of a High Gain (a) and Low Gain (b) calibrated waveform acquired with the described setup

4.4.6 Full Width at Half Maximum

The SiPM Pixel is designed to work in a high-background noise environment. In this condition not only the circuit must be able to withstand the high current flowing into the sensors, but should also offer a very fast signal. Indeed, the longer the signal, the higher the trigger threshold to be set in order not to be sensitive to the background noise.

The full width at half maximum (FWHM) of the signals produced by the front-end electronics is therefore one of the most important parameter. To perform this measurement, High Gain and Low Gain waveforms are acquired in dark condition (i.e. with the LED simulating the NSB kept off) and triggering on the pulsed LED. Signals are then offline calibrated, as previously described. Then a python program interpolates with the `numpy` package the calibrated waveforms and evaluates the FWHM waveform per waveform. This is done by calculating the time difference between the two points of the interpolated waveform which have an amplitude equal to half of the signal peak.

An example of the FWHM distribution for High Gain and Low Gain signals of the same run is shown in Figure 4.60a. Despite having approximately the same mean value, the standard deviation of the Low Gain FWHM is lower; this is due to the fact that the tail of the High Gain signal is less sharp. The measurement was repeated for different pulsed LED intensities, i.e. at different area values. In Figure 4.60b it is shown the obtained FWHM mean values for High Gain and Low Gain signals at different areas. Calculating the average, we can say that:

$$\begin{aligned} FWHM_{HG} &\simeq 4.3\,\mathrm{ns} \\ FWHM_{LG} &\simeq 4.3\,\mathrm{ns} \end{aligned} \tag{4.60}$$

Despite having almost the same FWHM, it is clear from the waveforms shown in Figure 4.59 that the Low Gain signal duration is shorter. To find out if this difference can already be seen in the MUSIC output signals, or if it is due to the LST electronics, we do a simple qualitative test. We acquire the High Gain and Low Gain signals with an oscilloscope (Tektronix MSO6), thanks to the LEMO Mezzanine. For each measurement, 1000 waveforms are averaged, then the differential signal is obtained by subtracting the negative signal from the positive one, both for High Gain and for Low Gain.

Results are shown in Figure 4.61; the two signal shapes are quite similar: therefore the difference observed in the signals acquired with the LST electronics is due to the LST electronics itself.

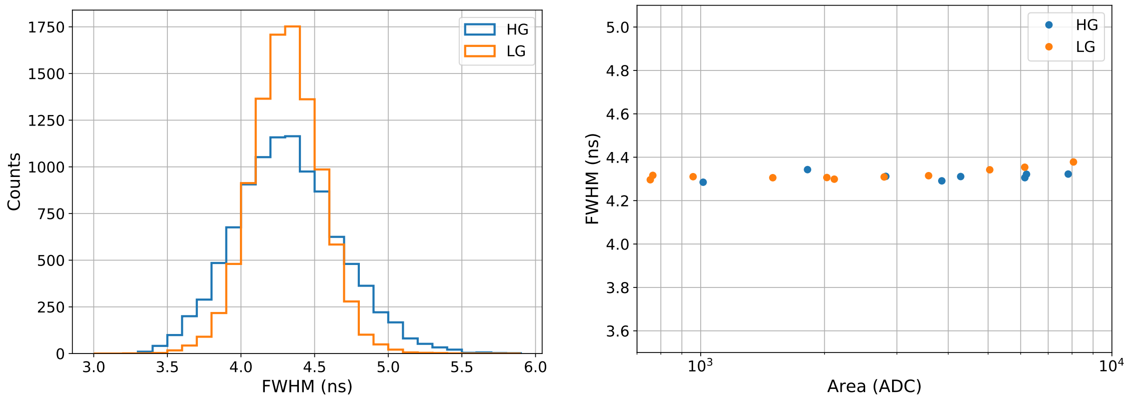

(a) (b)

Figure 4.60: (a) FWHM distribution for High Gain and Low Gain signals of the same run
(b) FWHM for High Gain and Low Gain signals at different signal areas

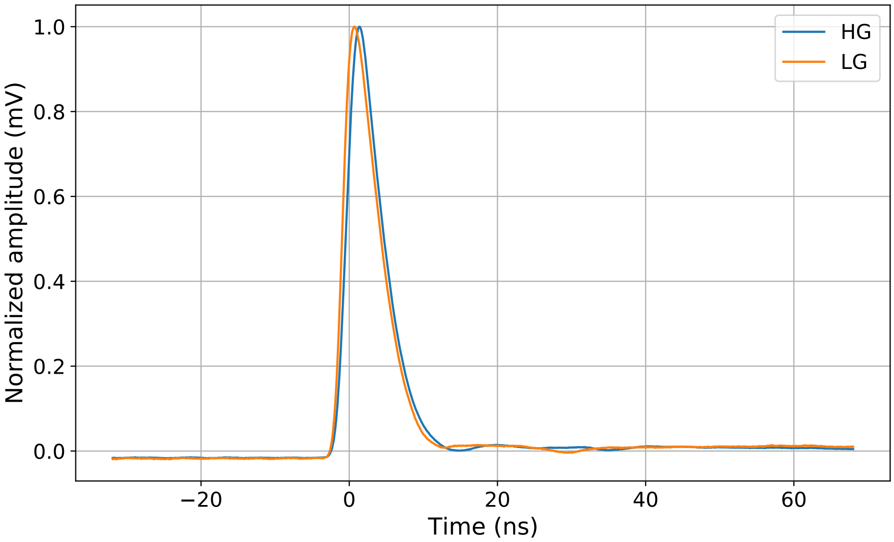

Figure 4.61: High Gain and Low Gain signal acquired on the oscilloscope thanks to the LEMO Mezzanine

4.4.7 Gain Dependance on Night Sky Background

By design, the slow control circuit should keep the SiPM at the same overvoltage, and therefore it should have the same gain at every Nigh Sky Backgrounds. However, we check if the whole SiPM pixel gain remains constant as the background varies.

The setup is the one reported in Figure 4.58. Signals are acquired triggering on the pulsed LED, at different values of light background introduced by the DC LED. To study all the possible dynamics, the Current Limiter is hardware set to 10 mA. First, five DC LED voltage values are identified to cover all the desired light background dynamics. The first measurement is done in dark condition, with the DC LED off. With the previously described procedure, 10 000 High Gain and Low Gain waveforms are acquired, and the current monitoring value is logged. Then the DC LED is set to the first voltage value, and 10 000 waveforms are again acquired. The procedure is repeated for all the DC LED voltage values. At the end, the measurement is repeated again but scanning along the DC LED polarization values in reverse, finishing with the measurement in dark condition. For each point, acquired waveforms are calibrated and the average of the areas is evaluated. For each measurement taken with the same DC LED bias voltage, the average of the two areas is evaluated, alongside with the average of the two current monitoring values, in order to compensate possible pulsed LED fluctuations.

Results are shown in Figure 4.62a for High Gain and in Figure 4.62b for Low Gain. On the abscissa axis we have the monitoring current, while in the ordinate axis the signal area. In addition the dashed green and orange lines indicate the 1 % and 5 % bands around the mean value, respectively. While the Low Gain channel is not affected by NSB, we cannot say the same for the High Gain line. Since the Low Gain response is constant as the current flowing into the SiPM increases, we can conclude that the slow control circuit works as expected. However, since the High Gain deals with the detection of signals generated by few photons, and since the trigger threshold has to be raised as the NSB increases, this suboptimal behavior of this channel is not a big problem. In this example the pulse was made of about 150 photoelectrons; similar trend was obtained at different pulsed LED intensities.

To understand if we observe the same behavior even without the LST electronics, we proceed again to carry out the measurement with the LEMO Mezzanine, as described in

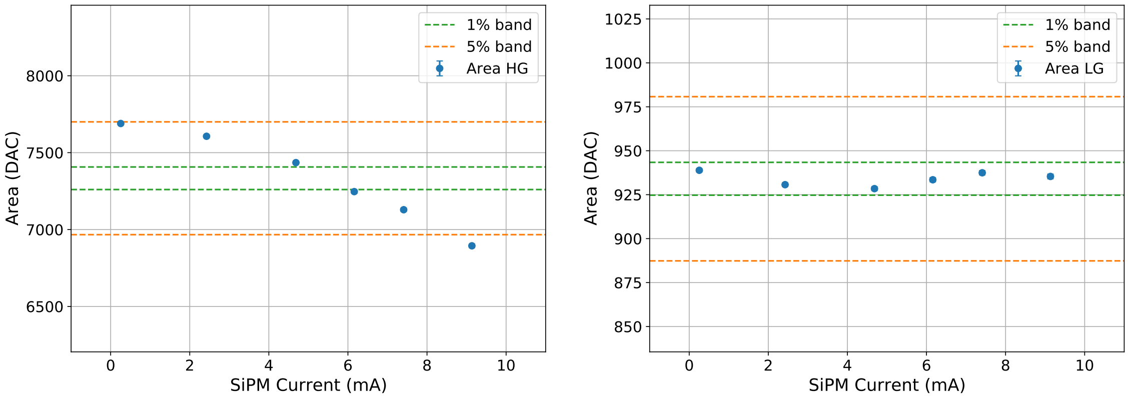

(a) **(b)**

Figure 4.62: Gain dependance on night sky background measurement results for High Gain (a) and Low Gain (b); in this example the pulse was made of about 150 photoelectrons

the previous section. As already anticipated, since we are treating differential signals as two different single ended lines, we can only perform qualitative measurements with this setup. We will only observe the signals with or without night sky background, to see whether their behavior is compatible or not with what we have just measured.

Results are reported in Figure 4.63 for High Gain and in Figure 4.64 for Low Gain. The first measurement is done in dark condition ($I_{mon} = 0.2\,\mathrm{mA}$), then the LED simulating the NSB is turned on ($I_{mon} = 8.7\,\mathrm{mA}$) and the measurement is carried out again. The procedure is repeated two times, to spot possible pulsed LED fluctuations. On the left we have the mean of the 1000 acquired waveforms, and on the right the peak to peak amplitude depending on the monitoring current. As before, the dashed green and orange lines indicate the 1 % and 5 % bands around the mean value, respectively. Results are compatible to those observed before: the higher gain variation on the night sky background in the High Gain channel is therefore related to the MUSIC ASIC behaviour.

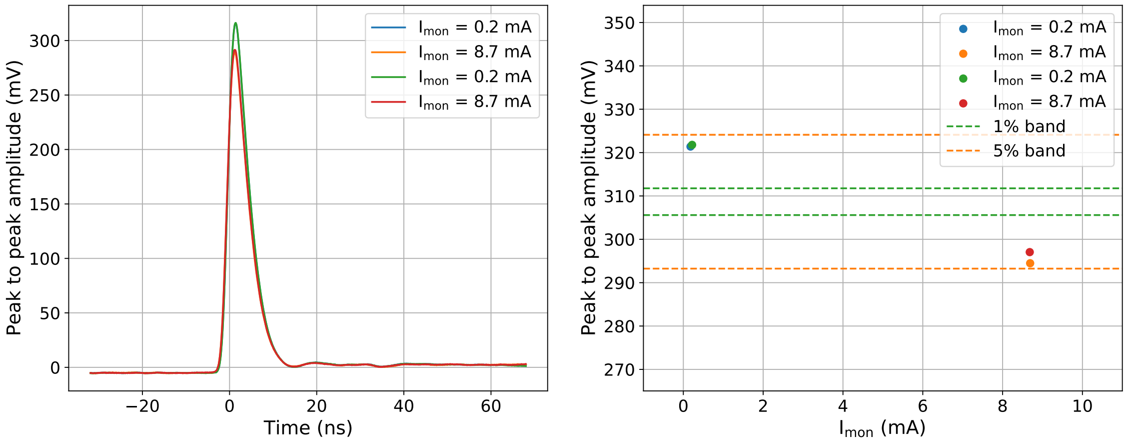

Figure 4.63: High Gain waveforms acquired at the oscilloscope thanks to the LEMO Mezzanine at different light backgrounds (left), and the resulting peak-to-peak amplitude variation (right); in the plot on the left, waveforms acquired with the same background light (i.e. same I_{mon}) are overlapping

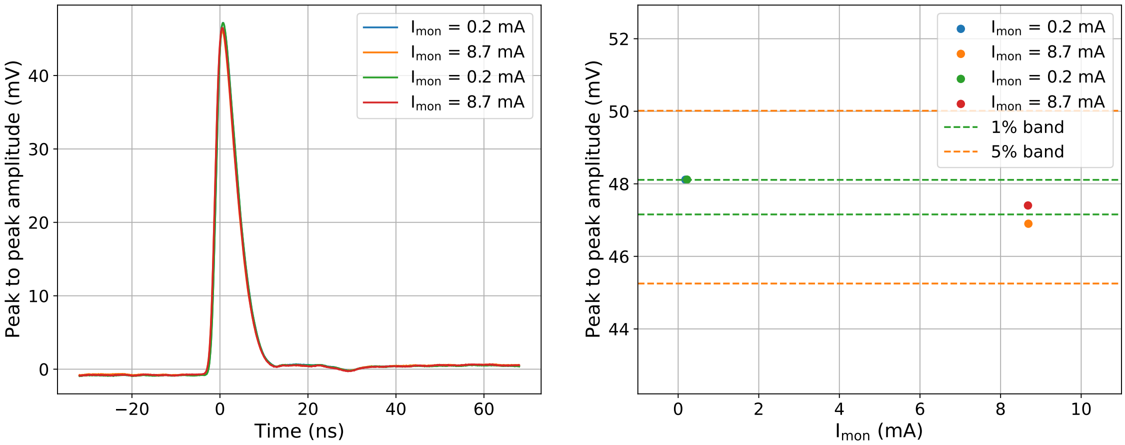

Figure 4.64: Low Gain waveforms acquired at the oscilloscope thanks to the LEMO Mezzanine at different light backgrounds (left), and the resulting peak-to-peak amplitude variation (right); in the plot on the left, waveforms acquired with the same background light (i.e. same I_{mon}) are overlapping

4.4.8 Pixel Calibration

Unluckily, it is not possible to distinguish the single photoelectron on the sum signal, neither in High Gain nor in Low Gain. It is therefore necessary to find another solution to calibrate the pixel. As we have seen, only six MUSIC channels are used for the sum signals, thus we have two channels unused during normal operations. We can connect one of these empty channels to one of the four SiPMs on the edge of the SiPM array, normally disconnected. If we are able to see the single photoelectron on this channel, we can use it to cross-calibrate the whole pixel. Its signal can be accessed from the corresponding SE MUSIC output. To improve the signal amplitude, the pole-zero cancellation on this channel is bypassed; the Differential Leading Edge Discriminator (DLED) technique, later discussed, is used to deal with the SiPM long tails.

For the calibration process, a new configuration file can be loaded through a UART connector mounted on the Pixel Main Board with an USB to UART adapter. After loading the file, the adapter must be disconnected, to avoid contaminating the system with the external noise coming from the computer. The SE signal can be accessed from the SMA connector located on the board and can be digitized by another DAQ system (e.g. an oscilloscope).

During the calibration procedure the SiPM pixel is illuminated by an uniform pulsed light; triggering on the pulsed LED, in the same time we acquire the SE reference signal and the High Gain and Low Gain sum signals. In this condition, if the reference pixel is hit by an average number of photons $n_{ph,SE}$, the SiPM pixel will be hit on average by a number of photons equal to:

$$n_{ph,SUM} = 12\, n_{ph,SE} \tag{4.61}$$

With a good approximation, we can say that the SiPM composing the pixel array have the same photon detection efficiency, therefore the same relation is also valid for the photoelectrons:

$$n_{pe,SUM} = 12\, n_{pe,SE} \tag{4.62}$$

Therefore, by knowing the average number of photoelectrons generated in the reference SiPM, we can calibrate the whole pixel. If A_{HG} and A_{LG} are the average area of the High

Gain and Low Gain sum signals, the HG and LG gains are defined as:

$$\begin{aligned} g_{HG} &= \frac{A_{HG}}{n_{pe,SUM}} = \frac{A_{HG}}{12\,n_{pe,SE}} \\ g_{LG} &= \frac{A_{LG}}{n_{pe,SUM}} = \frac{A_{LG}}{12\,n_{pe,SE}} \end{aligned} \tag{4.63}$$

Difference Between Operation and Calibration Mode

Before performing the SiPM Pixel calibration, we need to see whether the amplitudes of the sum signals change in going from operation to calibration mode. Indeed, in the second one we have a different MUSIC configuration, in which also the channel 7 is enabled, and we have a coaxial cable connected from the SMA connector to the DAQ system (Tektronix MSO6 oscilloscope, with 200 MHz bandwidth limit). In addition, during the calibration we have also the reference SiPM powered on. The current monitor, as it is designed, measures the current flowing into all connected SiPMs, without distinguishing those contributing to the sum signals to the reference one. As we have seen, the reference pixel is directly connected to the MUSIC input (DC coupling); the current value used for the anode voltage compensation is therefore overestimated. To understand if this causes non-negligible effects, and therefore if it is necessary to introduce corrective factors, we proceed with the measurement described below. In both operation modes the USB to UART adapter is unconnected, to avoid introducing extra noise into the system.

A pulsed LED (Picoquant PDL 800-D with PLS 400 LED head) flashes the SiPM pixel at 1 kHz rate with constant amplitude. High Gain and Low Gain signals are acquired with the LST data acquisition softwares (*ZFitswriter* and *EventBuilder*) and later processed with *cta-lstchain*. The measurements are repeated alternating the normal configuration with the calibration one, in order to compensate possible LED fluctuations. For each measurement, 10 000 waveforms are acquired and processed, then the average value of the found areas is computed. Results are shown in Figure 4.65a for High Gain and 4.65b for Low Gain. As a reference, a 1% band around the mean value is plotted. As we can see, there are no clear differences between the two modes, thus there is no need to add any correcting factor.

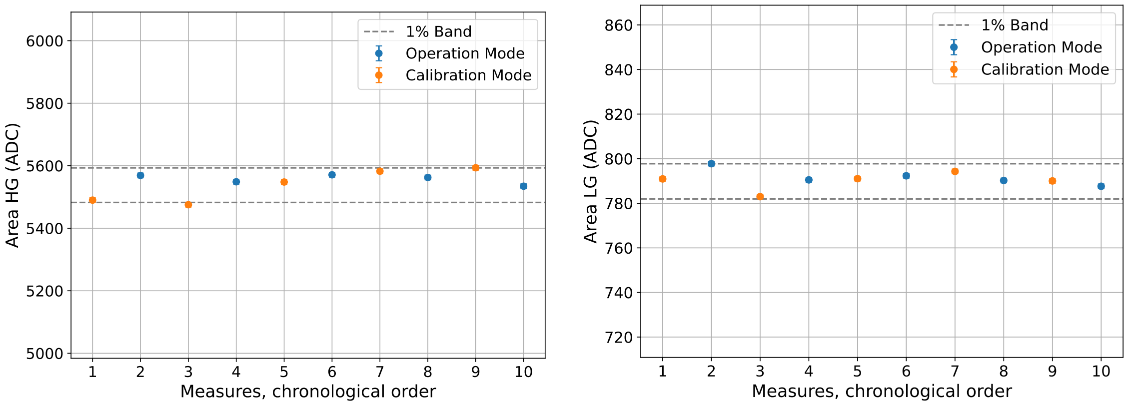

(a) (b)

Figure 4.65: Comparison between the signal area in “Operation” and “Calibration” mode for High Gain (a) and Low Gain (b)

Differential Leading Edge Discriminator Technique

Since in the SE channel we bypass the pole-zero cancellation, it is necessary to find an efficient way to remove the offset induced by the tail of the previous SiPM signals. The used technique is the so called *Differential Leading Edge Discriminator (DLED)* [112]; it is an analysis tool useful for removing offsets and finding peaks, suitable for signals in which the rise time t_{rise} is significantly shorter than its fall time t_{fall}. Considering the blue signal in Figure 4.66 as an example, this technique works as follows:

- We consider a signal $S(t)$ (blue) which has $t_{rise} \ll t_{fall}$
- We shift on the time axis the signal for a time interval dt and we reverse it: $-S(t-dt)$ (green)
- We sum the obtained signals:

$$D(t) = S(t) + (-S(t-dt)) \tag{4.64}$$

The resulting signal $D(t)$ (red) will be the analyzed signal (e.g. for peaks finding).

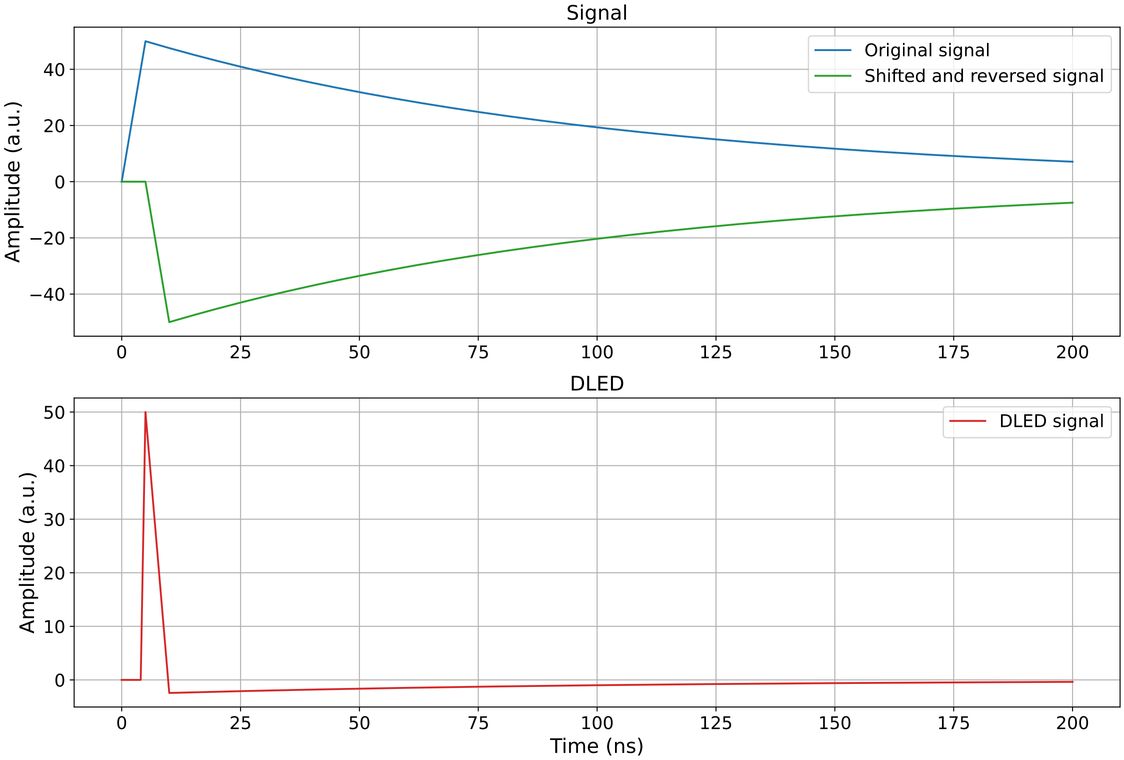

Figure 4.66: Simple example of the DLED technique: in blue the original signal, in green the shifted and reversed one, in red the resulting signal

Obviously this technique depends on the value of dt: if we use a dt equal to the rise time in first approximation we will have that the resulting signal $D(t)$ has the same peak amplitude of the original one, while if we use a $dt < t_{rise}$ or $dt > t_{rise}$ the peak obtained will be smaller. The difference in amplitude is more pronounced in the first case (i.e. $dt < t_{rise}$), since the signal is steeper during the rise time; on the other hand in the second case (i.e. $dt > t_{rise}$) we will have a higher offset. A simple simulation of these cases is reported in Figure 4.67; the signal is approximated with a steep and straight line during the rise time and an exponential during the fall time.

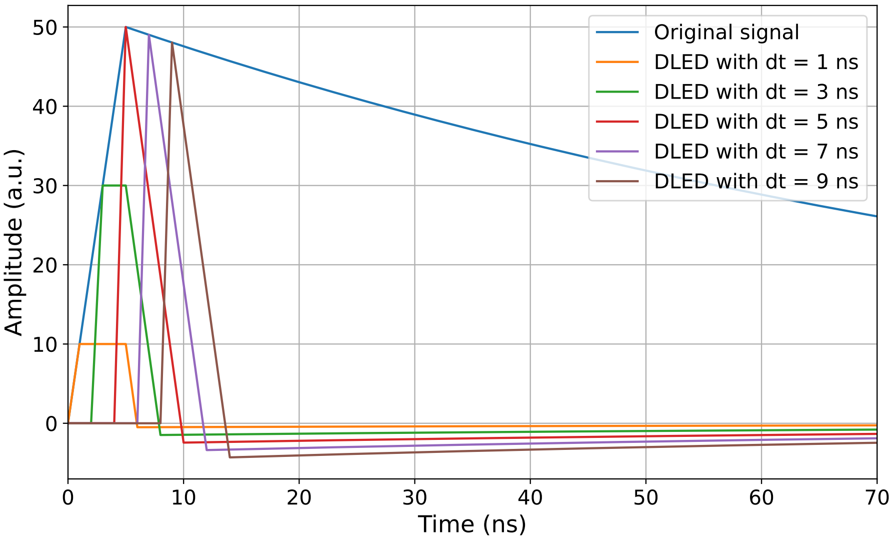

Figure 4.67: DLED using different values of dt; the original signal is shown in blue and has rise time equal to 5 ns

In our situation the signal on which we will apply the DLED technique is given by the sum of the signals generated by the APDs that compose our SiPM; two signals occurring with a delay (t_{delay}) shorter than $2 \cdot t_{rise}$ are not clearly distinguishable with this method; we have therefore a *blind gap* in peaks finding equal to $2 \cdot t_{rise}$. We can easily understand this fact observing the simple situation reported in Figure 4.68 and in Figure 4.69, where the blue signal $S_1(t)$ and the green one $S_2(t)$ are generated by two distinct APDs in the SiPM, and the black one $S(t)$ is the sum of the two, and it is the signal that will be acquired by the DAQ system:

$$S(t) = S_1(t) + S_2(t)$$

If we call t_{delay} the time interval between $S_1(t)$ and $S_2(t)$, we have that the two peaks become clearly distinguishable when $t_{delay} > 2 \cdot t_{rise}$, hence the value of the blind gap. The $t_{delay} = 2 \cdot t_{rise}$ in our approximation is the boundary condition.

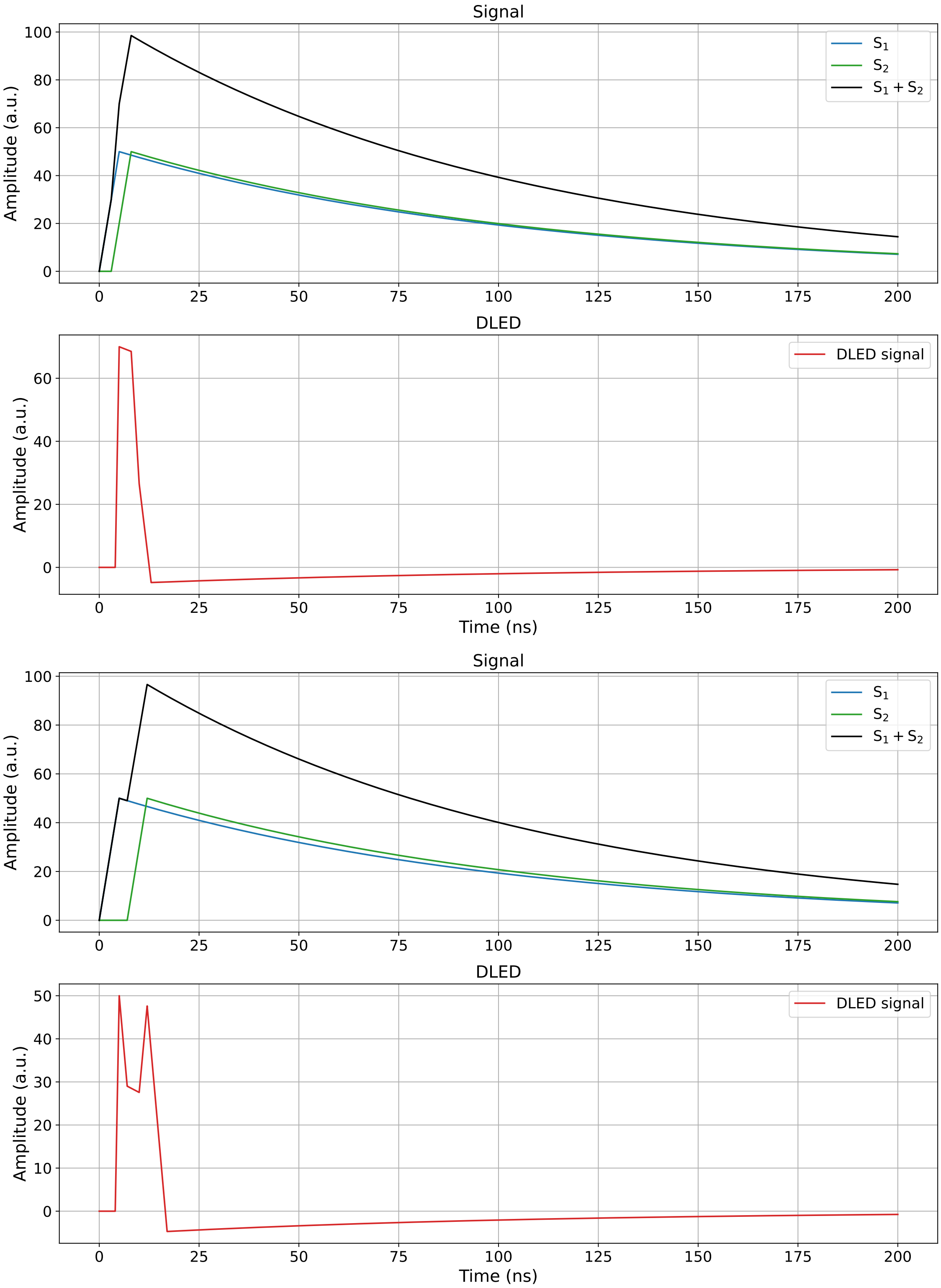

Figure 4.68: Simple DLED Simulation
(a) $0 < t_{delay} < t_{rise}$: the peaks are not distinguishable at all
(b) $t_{rise} < t_{delay} < 2 \cdot t_{rise}$: the peaks are not clearly distinguishable

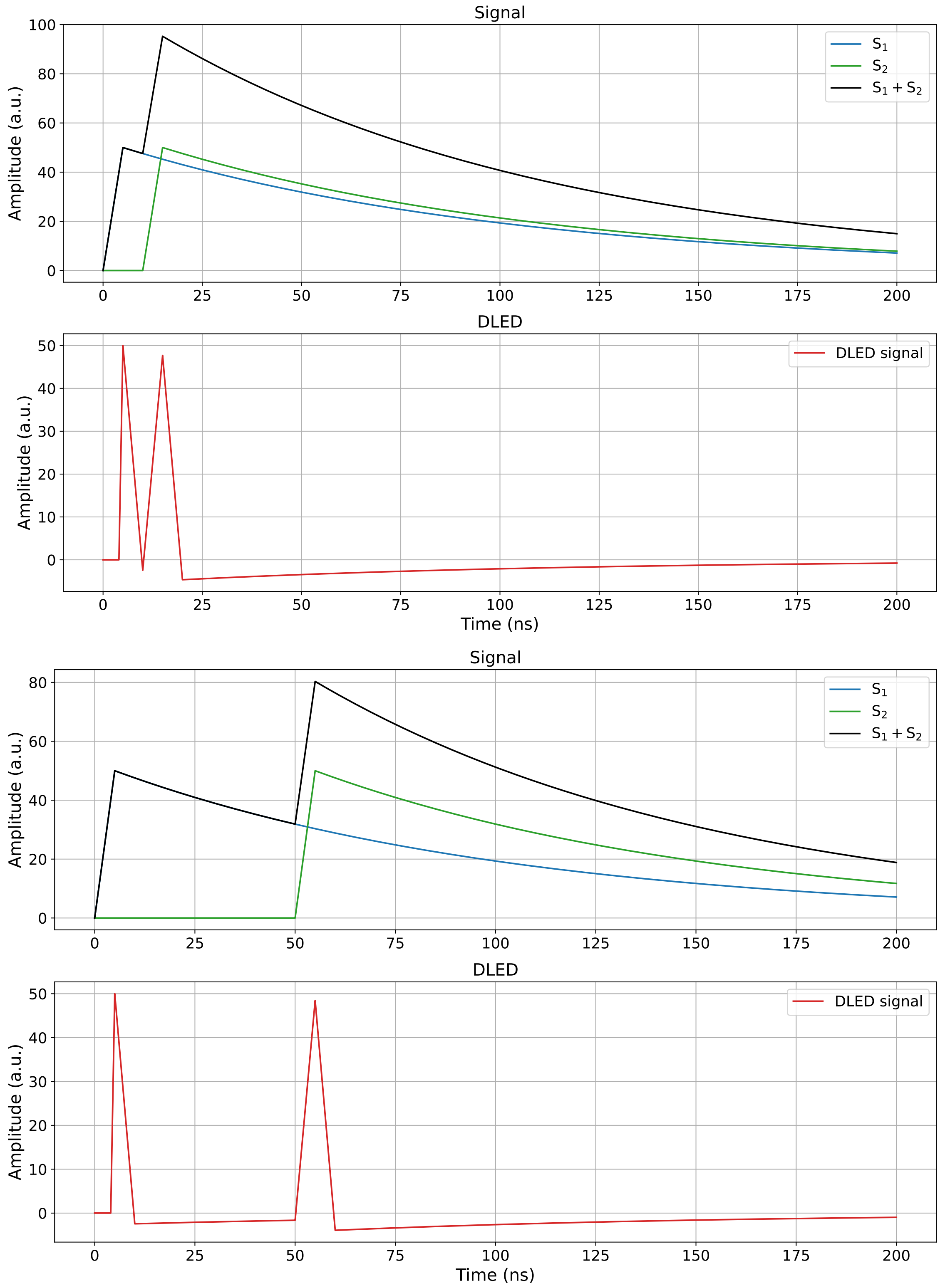

Figure 4.69: Simple DLED Simulation
(a) $t_{delay} = 2 \cdot t_{rise}$: the peaks are clearly distinguishable (boundary case)
(b) $t_{delay} > 2 \cdot t_{rise}$: the peaks are clearly distinguishable

Single Photoelectron Spectrum on SE Channel

Before calibrating the whole SiPM pixel, we need to calibrate the reference SiPM. For this purpose, dark count signals are acquired on the SE channel with the DAQ system (Tektronix MSO6 oscilloscope with 200 MHz bandwidth limit in our case). Afterwards a python program processes the signals using the DLED technique, runs a peak finding algorithm and fills a histogram with the found peaks amplitudes. An example of the obtained distribution is visible in Figure 4.70.

The 1 pe, 2 pe and 3 pe distributions are then fitted with three different Gaussian functions:

$$f_i = C_i e^{-\frac{(V-V_i)^2}{2\sigma_i^2}} \tag{4.65}$$

Fit boundaries are evaluated by the program as the ones which give the lowest chi-square value, in a given amplitude acceptance region. The gain is the difference between the mean of the 2nd pe distribution and the mean of the 1st one. It is clear that this value is the same as the difference between the mean of the 3rd pe distribution and the 2nd one; therefore, the gain is calculated as the mean value of the two differences:

$$g = \frac{1}{2}(g_{2,1} + g_{3,2}) = \frac{1}{2}\left[(V_2 - V_1) + (V_3 - V_2)\right] \tag{4.66}$$

The pedestal p is evaluated as the difference between the mean of the 1 pe distribution and the gain:

$$p = V_1 - g \tag{4.67}$$

The amplitude A of a pulsed LED signal is evaluated as the difference between the signal maximum in the pulsed LED window P_{LED} and the maximum of the signal in a time window prior to the LED signal P_{ped} ($A = P_{LED} - P_{ped}$). From the gain g and pedestal p values it is possible to evaluate the number of photoelectrons $n_{pe,SE}$ induced by the pulsed LED as:

$$n_{pe,SE} = \frac{A - p}{g} = \frac{P_{LED} - P_{ped} - p}{g} \tag{4.68}$$

Please remember that $n_{pe,SE}$ is the number of photoelectrons generated in the reference pixel. Please note that this Equation is valid only if the pixel response is linear.

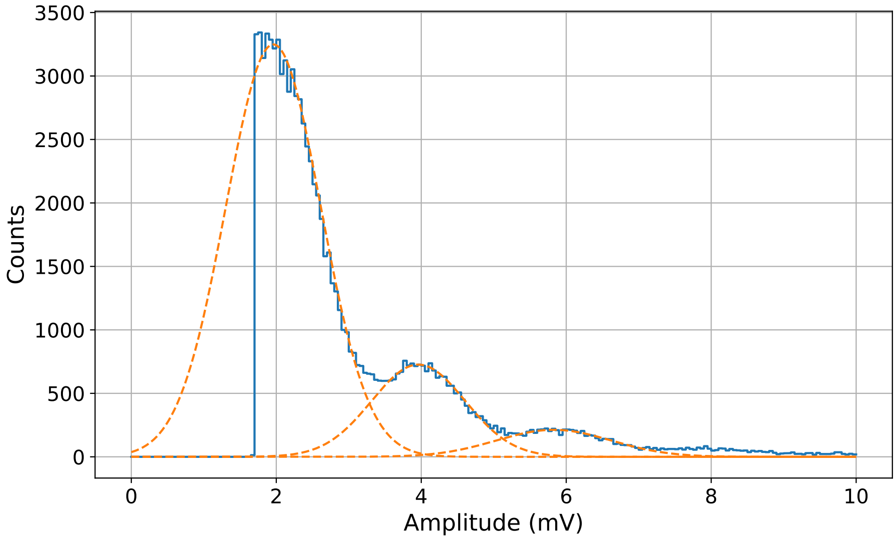

Figure 4.70: Single photoelectron spectrum on SE reference channel with the 1 pe, 2 pe and 3 pe distributions fitted with gaussian functions

Linearity of the SE Channel

Another fundamental aspect that must be known about the reference sensor is its linearity. To evaluate this quantity, we proceed as described below.

The SiPM pixel is flashed by a pulsed LED (Picoquant PDL 800-D with PLS 400 LED head) and the reference pixel SE signal is acquired with the DAQ system (Tektronix MSO6 oscilloscope with 200 MHz bandwidth limit), triggering on the LED. Between the LED and the sensor we place a black panel with two holes, which can be kept open or closed; a diffuser is placed between the panel and the pixel to facilitate the illumination of the latter one. The structure is shown in Figure 4.71. We have four different operation modes:

1. All holes closed; this condition is used to check whether there is or not light leakage from the closed holes
2. Hole 1 open, hole 2 closed
3. Hole 1 closed, hole 2 open
4. Both holes open

Once found that there are no light leaks with the holes closed, for each of the three remaining configurations we acquire 1000 waveforms with the oscilloscope, then we evaluate the peak values with the same software used to find the single photoelectron spectrum and finally we compute the average value of the peaks. The pixel is linear if the value obtained in the fourth operation mode is equal to the sum of the ones obtained in the second and third one. If L_i is the average peak value obtained with the hole i open and the other one closed, and L_{12} is the one obtained with both holes open, the sensor is linear if:

$$L_{12} = L_1 + L_2 \tag{4.69}$$

This is true only if the pulsed LED amplitude remains constant; since the acquisition is quite fast, as well as the change between the three configurations, this condition is safely respected after an appropriate pulsed LED warm-up time. To convert the peak amplitude

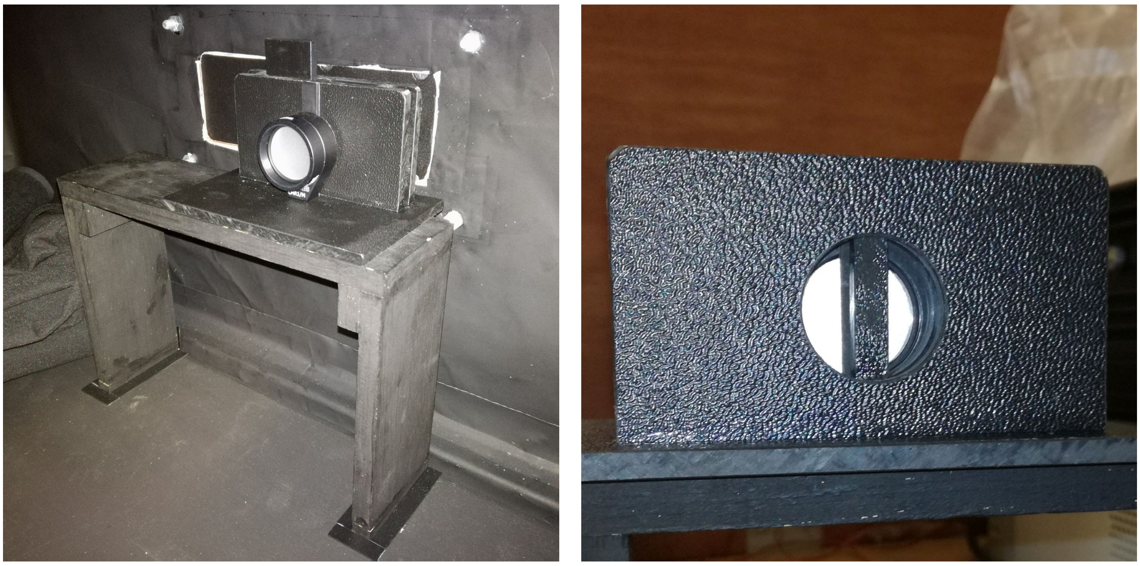

(a) (b)

Figure 4.71: The black panel with two holes used for linearity measurements

in photoelectrons (using Equation 4.68), we must be sure that the reference pixel is linear both in L_1 and in L_2: for this reason we perform the scan starting from a low pulsed LED amplitude (where we are sure the response is linear) and we gradually increase it, up to reach our desired dynamics.

Results are visible in Figure 4.72a; data are shown as blue dots and a dashed gray line is the ideal linear behaviour. At first glance, we can say that the pixel is linear up to just over 300 photoelectrons. To have a more precise indication of the pixel linearity, we can evaluate the deviation from linearity D_{lin} as:

$$D_{lin} = \left(\frac{L_{12}}{L_1 + L_2} - 1 \right) \tag{4.70}$$

Results are shown in Figure 4.72b, excluding measurements at more than 400 photoelectrons. Since the deviation is always less than 2 %, we can conclude that the reference pixel is linear below 300 photoelectrons (safe limit).

Given the high number of microcells in the SiPM (22 500), the deviation from linearity due to the sensor itself is quite negligible. Indeed by using Equation 3.17 and 4.70 we obtain a deviation of about 0.7 % at 300 photoelectrons. The clear deviation from linearity seen in Figure 4.72a is therefore due to the electronics (channel saturation). This measurement also shows us that the photons emitted by the pulsed LED are perfectly stacked, as the whole measurement was made by studying the signal peak.

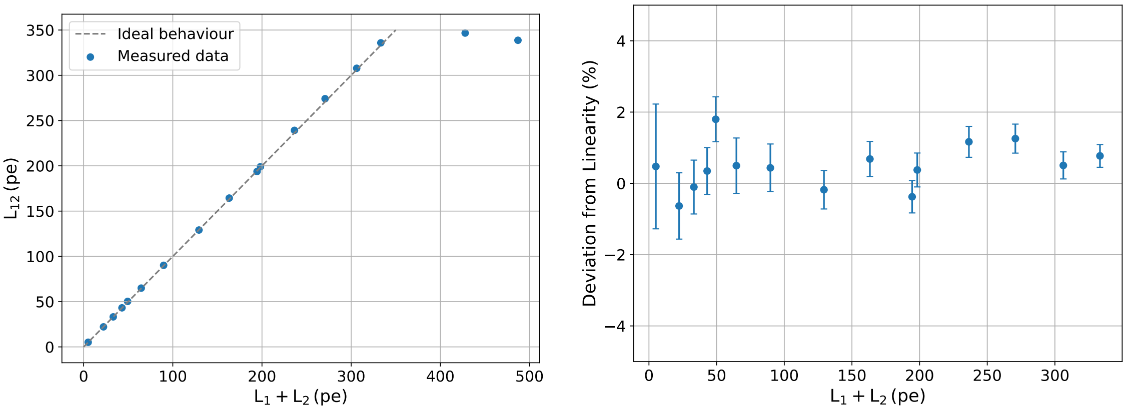

(a) (b)

Figure 4.72: Linearity (a) and deviation from linearity (b) of the reference pixel; see the text for more details

Light Uniformity

As anticipated, the calibration procedure is valid only if the pulsed LED light is uniform. The diffuser used in the setup is a Thorlabs ED1-S20-MD 20° Square Engineered Diffuser; in Figure 4.73 it is show its relative intensity versus the scatter angle.

To ensure maximum light uniformity, the pixel must be located at an angular distance of less than 10° from the center of the pulsed light. During the calibration procedure, the center of the SiPM array is held on axis with the LED spot, at a distance equal to 30 cm. At the same time reference and pixel sum signals are acquired, and later processed as previously described. To study the influence of the light non-uniformity, the calibration procedure is repeated moving the array by 3 cm on the axes perpendicular to the light beam. The scheme is shown in Figure 4.74. In each position, 10 000 waveforms from the Pixel signal (SUM of 12 SiPMs) and from the reference SiPM (SE) are acquired, and the gain is evaluated as in Equation 4.63. The error induced by the light non-uniformity is evaluated as the standard deviation of the five measurements. The procedure is repeated three times, and the error was always below 7 %. This value will be considered in the calculation of the gain uncertainty.

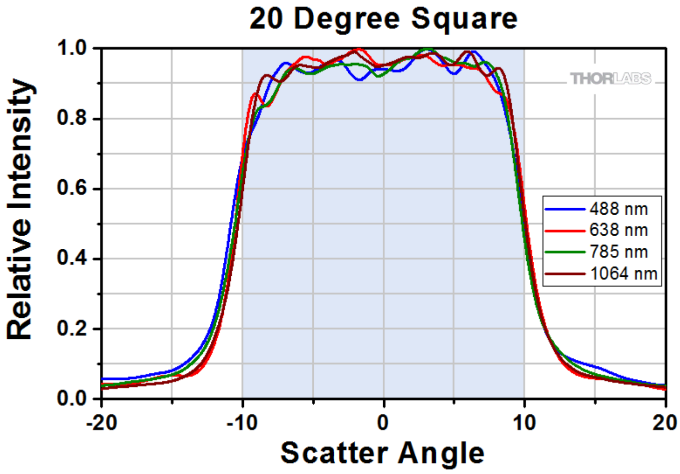

Figure 4.73: Relative intensity versus the scatter angle for the Thorlabs ED1-S20-MD 20° Square Engineered Diffuser [113]

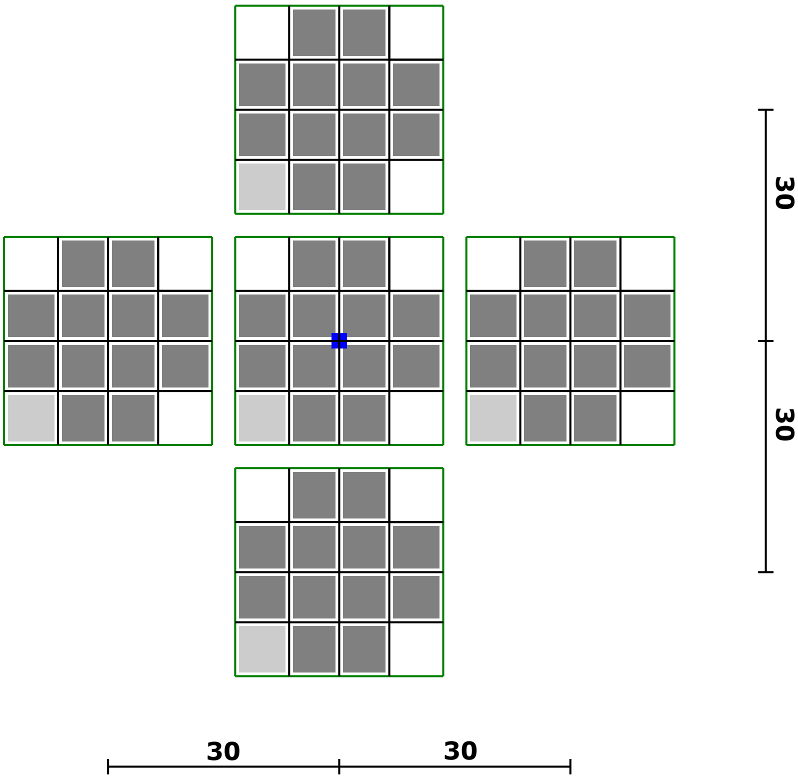

Figure 4.74: SiPM array position for light uniformity study; the blue square is the spot of pulsed LED light. Units in mm.

SUM Signal Calibration and Linearity

Once the reference pixel is calibrated and the light uniformity is studied, we can perform the calibration of the whole SiPM pixel.

In the same time, 10 000 waveforms from the pixel signals (High Gain and Low Gain) and from the reference pixel (SE) are acquired. From the number of photoelectrons measured in the reference pixel we obtain the number of photoelectrons generated in the 12 SiPMs ($n_{pe,SUM}$) by using Equation 4.62. Then we evaluate the area of the High Gain and Low Gain sum signals. Results are shown in Figure 4.75, where on the abscissa axis we have $n_{pe,SUM}$ and on the ordinate axis the sum signals area. The errors reported in the abscissa axis are the ones obtained propagating the errors on the $n_{pe,SUM}$ calculation. Comparing the plot with the PMT pixel one (Figure 4.10a), we observe that the two pixels can cover almost the same dynamic range.

Data in the linearity region are fitted with:

$$\begin{aligned} A_{HG} &= g_{HG}\, n_{pe,SUM} \\ A_{LG} &= g_{LG}\, n_{pe,SUM} \end{aligned} \tag{4.71}$$

where A_{HG} and A_{LG} are the High Gain and Low Gain SUM signal area and $n_{pe,SUM}$ the number of photoelectrons. The gains g_{HG} and g_{LG} obtained are:

$$\begin{aligned} g_{HG} &= (50.9 \pm 3.6)\ \text{ADC/pe} \\ g_{LG} &= (6.48 \pm 0.46)\ \text{ADC/pe} \end{aligned} \tag{4.72}$$

where the non-uniformity of the light is also taken into account in the errors evaluation. With these values it is possible to convert each signal acquired with the pixel into the corresponding number of photoelectrons.

However, we must keep in mind that the quantity thus obtained is not the "real" number of photoelectrons n_{pe} detected by the SiPM pixel, since we have the cross talk effect:

$$n_{pe} = \frac{n_{pe,SUM}}{1 + P_{CT}} \tag{4.73}$$

where P_{CT} is the cross talk probability.

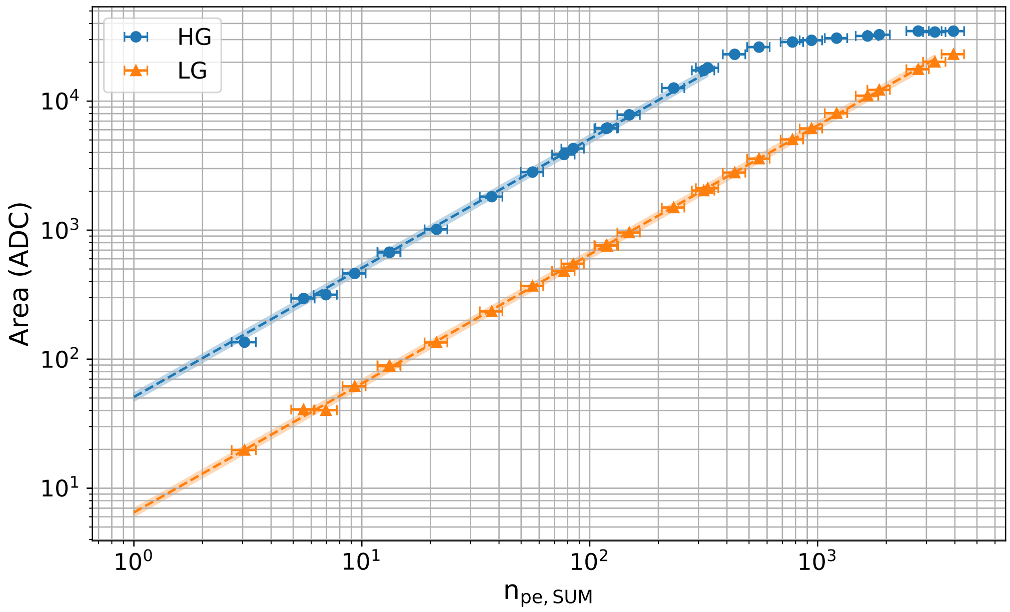

Figure 4.75: SiPM pixel calibration and linearity results

4.4.9 Pixel Power Consumption

As anticipated, the SiPM pixel is more power demanding than the PMT one. For this reason, the more power demanding parts, i.e. the MUSIC power lines and the SiPM Regulator input voltage, are connected to external power supplies. The power for the Regulator and Monitors is instead provided by DRS4 readout board.

Two different lines powers the MUSIC part of the SiPM pixel, corresponding to the 3V3 and the 5V0 MUSIC line:

- LVL: input voltage for the 3V3 LDO
- LVH: input voltage for the 5V0 LDO

In order to guarantee the correct functioning of the circuit, the LVL and LVH voltages are set in order to have about 1 V of voltage drop on the LDOs. These lines, together with the SiPM Regulator input voltage HV, are the main contributors to the power consumption.

The power consumption on the LV lines is:

$$\begin{aligned} P_{LV} &= V_{LVL} \cdot I_{LVL} + V_{LVH} \cdot I_{LVH} \simeq \\ &\simeq 4.3\,\mathrm{V} \cdot 100\,\mathrm{mA} + 6.0\,\mathrm{V} \cdot 0\,\mathrm{mA} \simeq \\ &\simeq 430\,\mathrm{mW} \end{aligned} \tag{4.74}$$

We can simply check this value, to see if it is reasonable. The main contributors on P_{LV} are the power consumption of the MUSIC ASIC P_{MUSIC} and the one of the 3V3 LDO $P_{3V3,LDO}$. By construction, the 3V3 LDO consumes:

$$P_{3V3,LDO} \simeq 1\,\mathrm{V} \cdot 100\,\mathrm{mA} = 100\,\mathrm{mW} \tag{4.75}$$

From the MUSIC datasheet [98], each channel consumes about 30 mW, and the summation block requires about 200 mW if all channels are summed together. Since only six channels are enabled and summed:

$$P_{MUSIC} < 30\,\mathrm{mW} \cdot 6 + 200\,\mathrm{mW} = 380\,\mathrm{mW} \tag{4.76}$$

Therefore the measured value is compatible with what is expected.

Instead, the power consumption on the HV line (set to 37 V) depends on the current flowing in the SiPM, which ranges from about 3.5 mA in dark condition to about 13 mA when the 10 mA current limit is reached:

$$\begin{aligned} P_{HV} &= V_{HV} \cdot I_{HV} \simeq \\ &\simeq 37\,\mathrm{V} \cdot (3.5\,\mathrm{mA} - 13\,\mathrm{mA}) \simeq \\ &\simeq 130\,\mathrm{mW} - 480\,\mathrm{mW} \end{aligned} \tag{4.77}$$

The power for the Regulators and Monitors is less easier to be measured, but its contribution is negligible when compared to the other lines. The total power consumption of a single pixel in dark condition is about 0.6 W, and can reach about 1 W in a very high background condition.

The SiPM pixel, as expected, is therefore more power demanding than the PMT one, which consumes less than 0.2 W (35 mW from the Cockcroft-Walton high voltage supply and 150 mW for the PACTA preamplifier).

4.4.10 Comparison with the PMT Pixel

As a comparison, the measurements carried out on the SiPM pixel are redone on the PMT pixel. The PMT biased at 1100 V using the LST slow control software, while the SiPM is biased at 6 V overvoltage thanks to the CaCoSiPM software. The CaCoSiPM software allows simultaneous measurements on both the SiPM pixel and the PMT one; the voltage adjust is done only on the SiPM pixel.

Waveforms

The pulsed LED light flashed simultaneously the two pixels, and the signals are acquired as previously described.

An example of the SiPM and PMT pixel waveforms, both for High Gain and Low Gain, are shown in Figure 4.76; on the left we have the SiPM signals, and on the right the PMT ones. In both gains we observe a clear time difference between the two pixel signals: the SiPM pixel offers a faster response when compared to the PMT one.

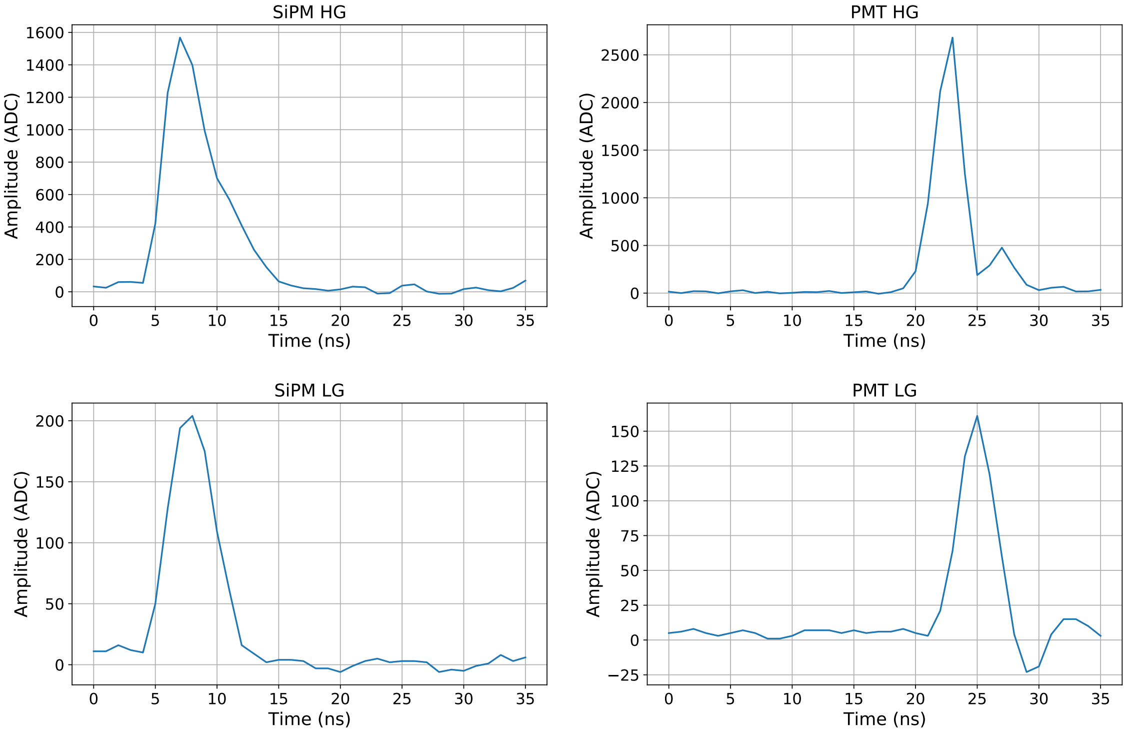

Figure 4.76: SiPM pixel and PMT pixel example waveforms

Full Width at Half Maximum

A comparison of the full width at half maximum (FWHM) for the SiPM and PMT pixels is shown in Figure 4.77, for both gains. It is clear that the PMT signals offers a shorter FWHM; in particular, for this specific acquisition run we have:

$$\begin{aligned} FWHM_{SiPM,HG} &\simeq 4.2\,\mathrm{ns} \\ FWHM_{SiPM,LG} &\simeq 4.3\,\mathrm{ns} \\ FWHM_{PMT,HG} &\simeq 3.0\,\mathrm{ns} \\ FWHM_{PMT,LG} &\simeq 3.5\,\mathrm{ns} \end{aligned} \tag{4.78}$$

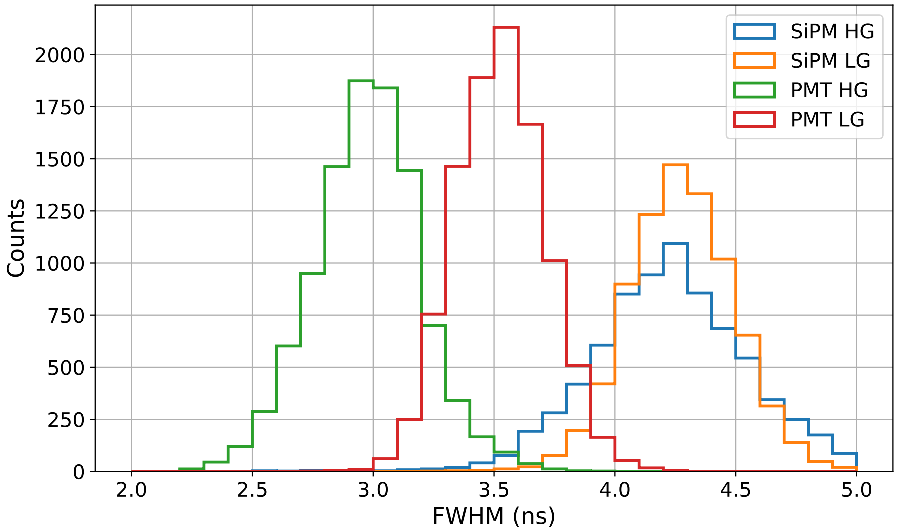

Figure 4.77: SiPM pixel and PMT pixel full width at half maximum distributions

Gain Dependance on Night Sky Background

The setup is the same used for the measurement carried out on the SiPM pixel; however, particular care must be paid not to let the current flowing in the photomultiplier exceed its safety limit value (100 µA), in order not to damage it. For a fair comparison, the same program is used to integrate the waveforms, but with d_{low} and d_{high} equal to 3 ns for both gains. Results are shown in Figures 4.78a and 4.78b for High Gain and Low Gain respectively, and should be compared with the results obtained with the SiPM pixel shown in Figures 4.62a and 4.62b. Especially by comparing the Low Gain channel, it is clear that the PMT has a bigger gain dependance as the night sky background varies. Noteworthy is also the different current flowing in the two sensor types: milliamps in the SiPMs, only tens of microamps in the PMTs.

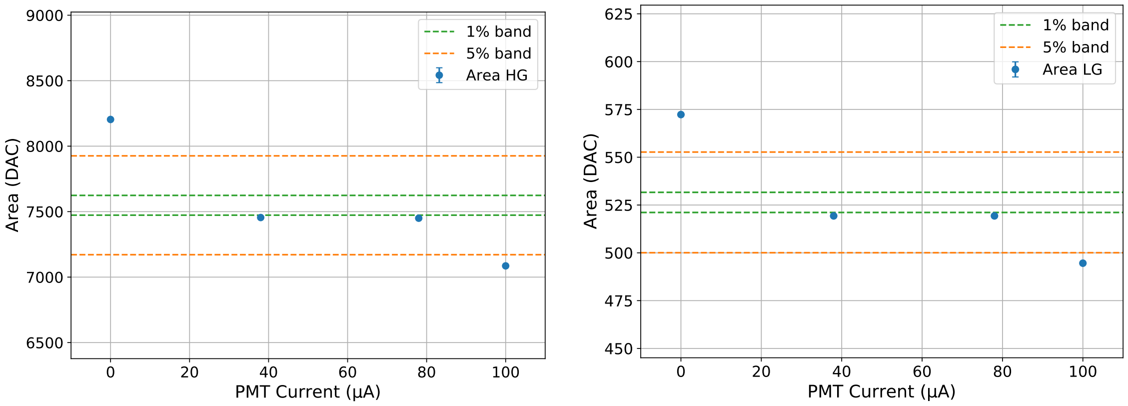

(a) **(b)**

Figure 4.78: PMT pixel gain dependance on night sky background measurement results for High Gain (a) and Low Gain (b)

4.5 Global Module

A complete module made by seven channels has been assembled; a picture can be found in Figures 4.79 and 4.80.

The operations reported in Appendix A have been repeated for all the modules, in order to load the proper MUSIC settings and to calibrate the MUSIC analog outputs offsets. The Voltage and Current Monitor have been calibrated as described in section 4.4.1 and 4.4.2; results are shown in Figures 4.81a and 4.81b respectively. The calibration results have been loaded in the CaCoSiPM software (the used configuration file is the one reported in Appendix B).

An example of signals acquired by flashing the module with a non-uniform pulsed light (Picoquant PDL 800-D with PLS 400 LED head) is shown in Figure 4.82; the channels are not calibrated. We can also observe that the ratio between the amplitudes of the High Gain and Low Gain channels is not constant between the pixels: this could be due to the MUSIC automatic calibration procedure implemented in the microcontroller firmware.

The SiPM arrays used for the construction of this module are those that have not passed the quality tests for the prototype of the SCT telescope, as they are not fully functional. For this reason, no qualitative measurements were carried out on the module.

Regarding the power consumption, on the LV lines:

$$\begin{aligned} P_{LV} &= V_{LVL} \cdot I_{LVL} + V_{LVH} \cdot I_{LVH} \simeq \\ &\simeq 4.3\,\mathrm{V} \cdot 700\,\mathrm{mA} + 6.0\,\mathrm{V} \cdot 0\,\mathrm{mA} \simeq \\ &\simeq 3\,\mathrm{W} \end{aligned} \tag{4.79}$$

The current flowing on the HV line ranges from about 25 mA in dark condition, to about 90 mA:

$$\begin{aligned} P_{HV} &= V_{HV} \cdot I_{HV} \simeq \\ &\simeq 37\,\mathrm{V} \cdot (25\,\mathrm{mA} - 90\,\mathrm{mA}) \simeq \\ &\simeq 0.9\,\mathrm{W} - 3.3\,\mathrm{W} \end{aligned} \tag{4.80}$$

The current flowing in the DRS4 readout board power line (set to 24 V) is measured as 0.6 A, corresponding to a power consumption of about 14.4 W

$$\begin{aligned} P_{24V} &= V_{24V} \cdot I_{24V} \simeq \\ &\simeq 24\,\mathrm{V} \cdot 0.6\,\mathrm{A} \simeq \\ &\simeq 14.4\,\mathrm{W} \end{aligned} \tag{4.81}$$

The total power consumption of the global module is therefore:

$$\begin{aligned} P &= P_{LV} + P_{HV} + P_{24V} \simeq \\ &\simeq 3\,\mathrm{W} + (0.9\,\mathrm{W} - 3.3\,\mathrm{W}) + 14.4\,\mathrm{W} \simeq \\ &\simeq 18.3\,\mathrm{W} - 20.7\,\mathrm{W} \end{aligned} \tag{4.82}$$

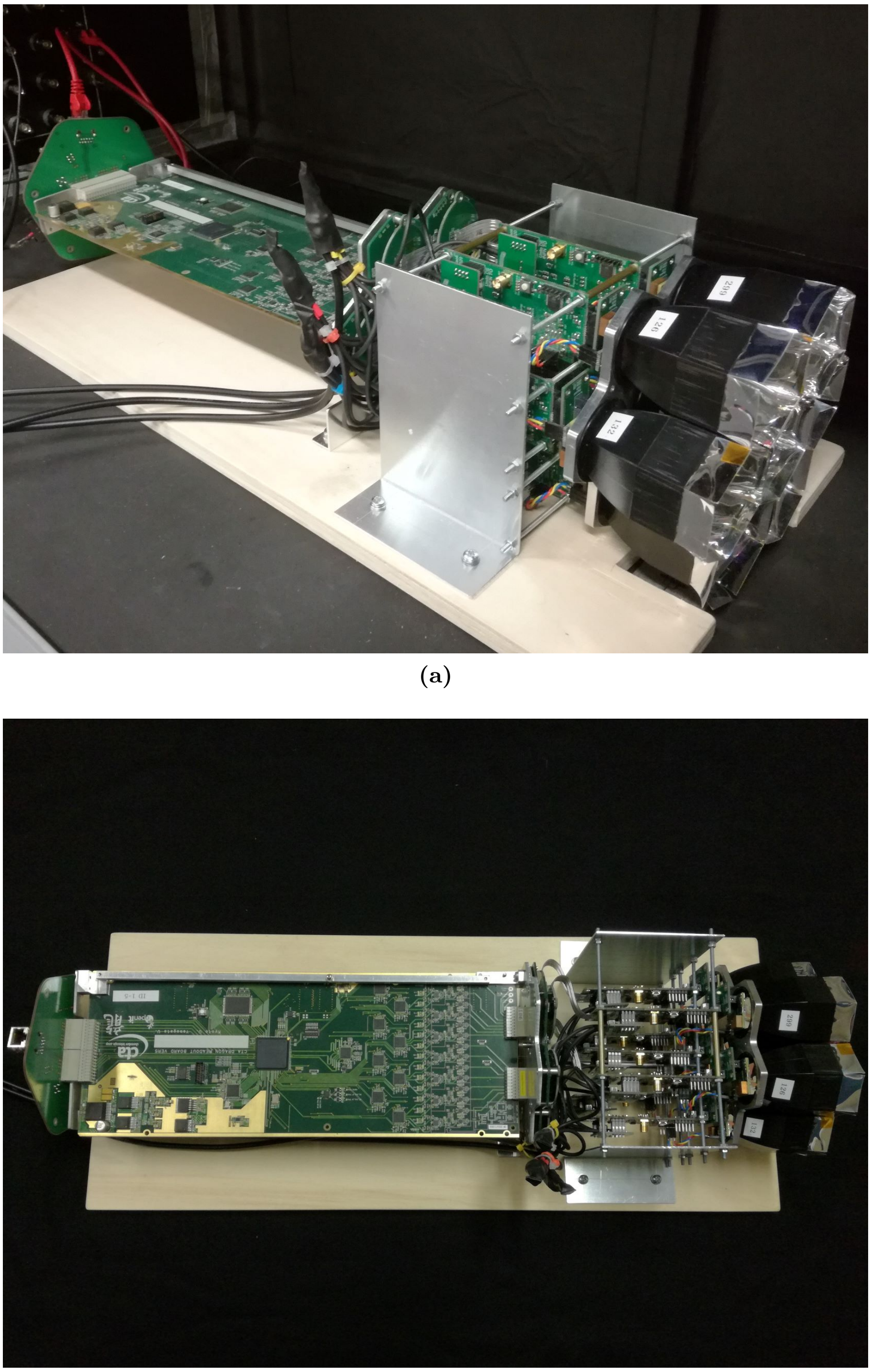

(a)

(b)

Figure 4.79: Pictures of the assembled seven-channels module

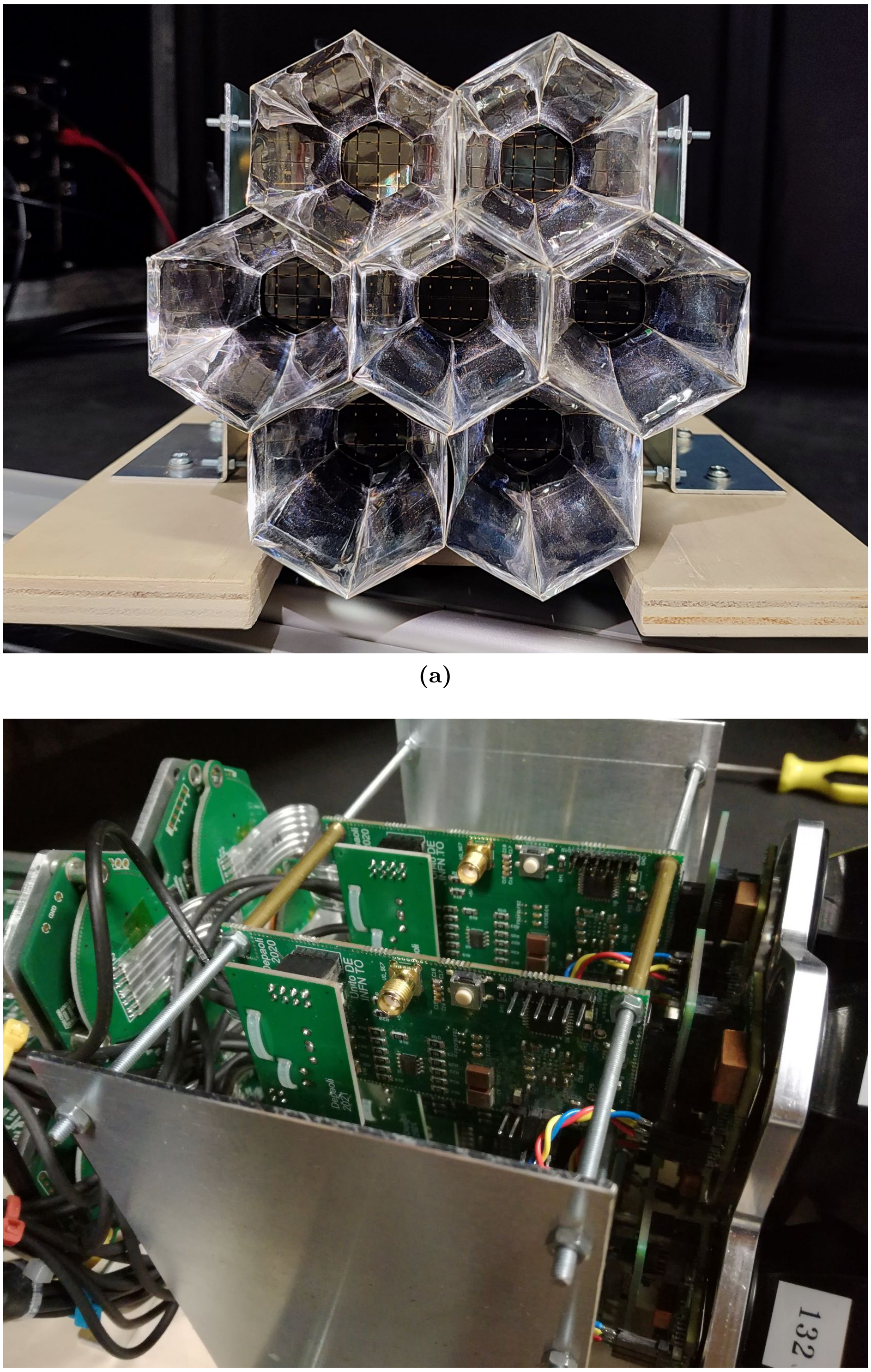

(a)

(b)

Figure 4.80: Pictures of the assembled seven-channels module

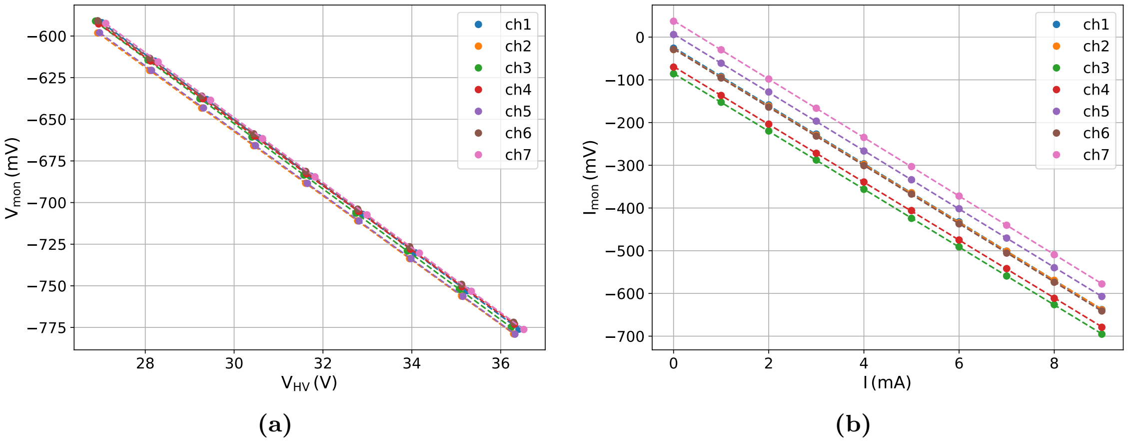

(a) **(b)**

Figure 4.81: Voltage Monitor (a) and Current Monitor (b) calibration results for the seven channels

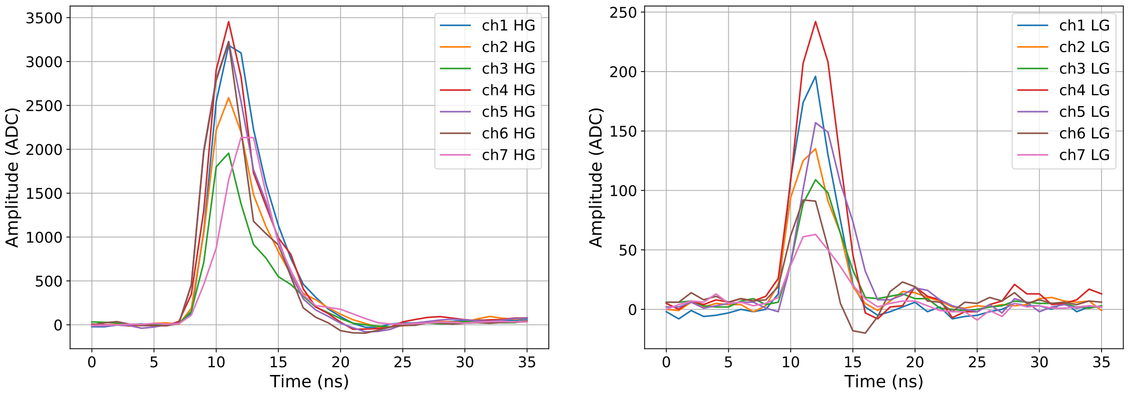

Figure 4.82: An example of signals acquired by the module for High Gain channel (left) and Low Gain one (right)

4.6 Other Possible Solutions

4.6.1 Test with Hamamatsu S13361

Before selecting the NUV HD3-4 FBK SiPMs, a fast test was also carried out on the Hamamatsu S13361-6050AS-04 SiPM array [114, 115]. These sensors however offer a much greater FWHM than the FBK SiPMs one, therefore they were discarded.

The array is composed of sixteen 6 mm × 6 mm SiPMs; a picture of the array can be found in Figure 4.83a. The SiPM cell size is equal to 50 µm, and each sensor has 14 336 cells in total. Its window is made of silicone resin. Its typical breakdown voltage is (53 ± 5) V and has a spectral response between 280 nm and 900 nm, with the peak sensitivity at 450 nm.

A PCB was designed to adapt the Samtec connector on the back of the Hamamatsu array to the connector on the back of the FBK array, connecting only the twelve inner SiPMs in the array in the 2P configuration. A picture of the array connected to the PCB is shown in Figure 4.83b.

Before proceeding with the signal acquisition, the average breakdown voltage of the array was measured, with the same procedure described in section 4.3.15. Given the connection, the I-V curves will be those of two SiPMs in parallel with each other. An example of the I-V characteristics of the same two SiPMs in parallel taken at different temperatures and the resulting V_{bd} dependance on the temperature is shown in Figure 4.84. The measured mean breakdown voltage of the six pixels at 20 °C is 51.24 V, with a standard deviation of 0.04 V. The obtained dV_{bd}/dT coefficient is 53 mV °C^{-1}. To perform a more detailed measurement of the breakdown voltage, pixel by pixel, it would have been necessary to develop a new PCB board, suitable for this purpose. However, since these sensors will not be used in the module, and given the complexity of soldering the mate connector of the one located on the back of the Hamamatsu array, this further measurement has not been carried out.

The different breakdown voltage value and the different dependence of the same on the temperature with respect to those obtained for the SiPM FBK depend on the different internal structure of the two sensors, as described in the previous chapter.

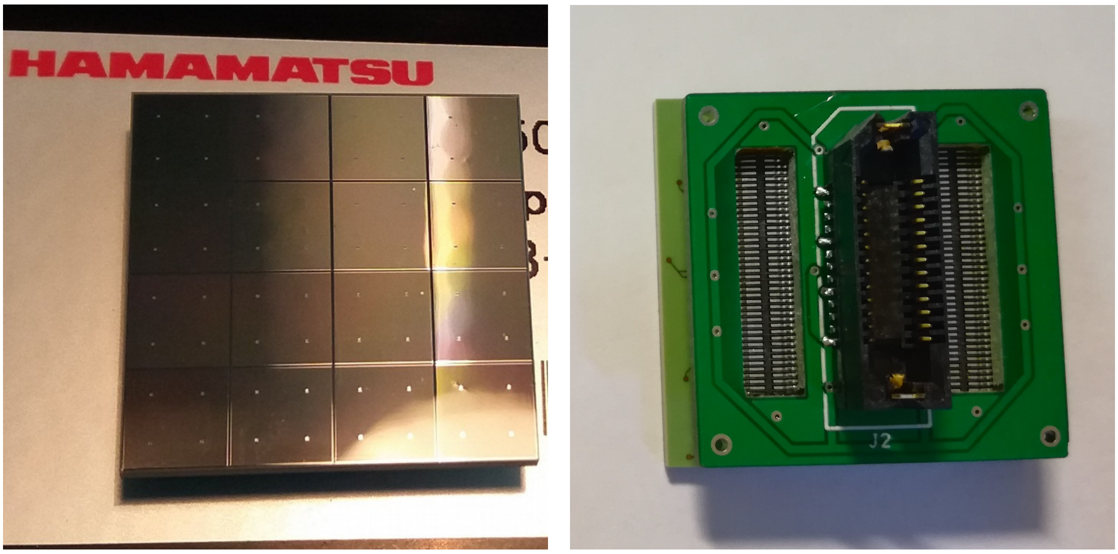

(a) (b)

Figure 4.83: (a) A picture of the Hamamatsu S13361-6050AS-04 SiPM array (a)
(b) A picture of the back of the Hamamatsu adapter seen from the back

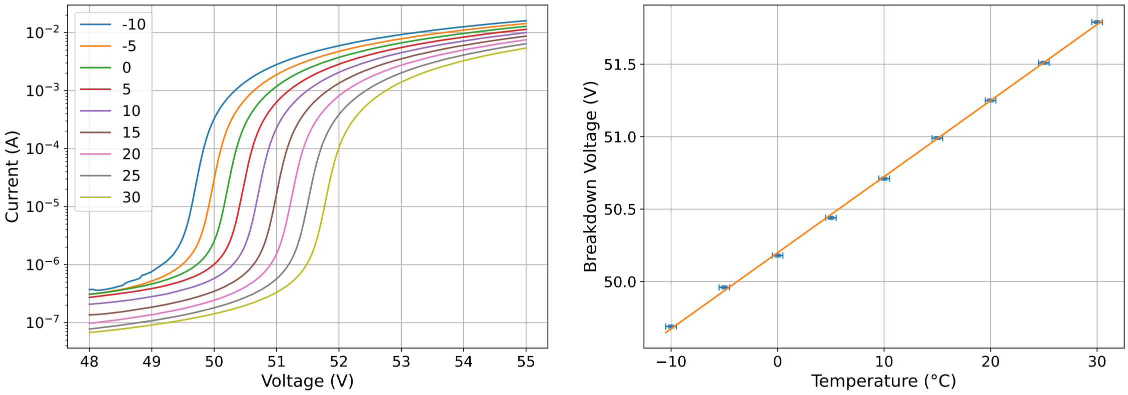

Figure 4.84: An example of the I-V characteristics of the same two SiPMs in parallel taken at different temperatures, and the resulting V_{bd} dependance on the temperature

We therefore proceed with the signal acquisition: the sensor is biased at 58 V, and the MUSIC is set with the same configurations used for the FBK SiPMs. The sensor is flashed with a Picoquant PDL 800-D with PLS 400 LED head. The High Gain sum of the 12 inner SiPMs is acquired by a Tektronix MSO6 Oscilloscope, triggering on the LED. The average of 1000 waveforms is shown in Figure 4.85. As done for the signals acquired with the DRS4 readout board, a python program interpolates with the `numpy` package the waveform and evaluates the FWHM; the obtained FWHM is greater than 12 ns. Although an improvement in FWHM can be expected by switching from MiniBoard to an all-in-one module, it is clearly impossible to obtain comparable values with the FBK SiPMs. In addition, given the higher bias voltage required, it would have been necessary to develop a different regulator. These sensors were therefore not used for our protopipe.

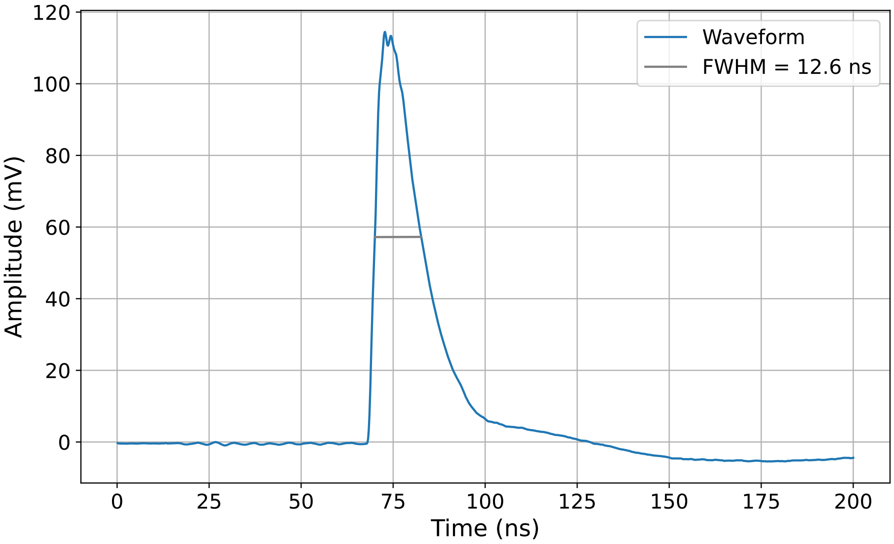

Figure 4.85: Average waveform with the FWHM measurement

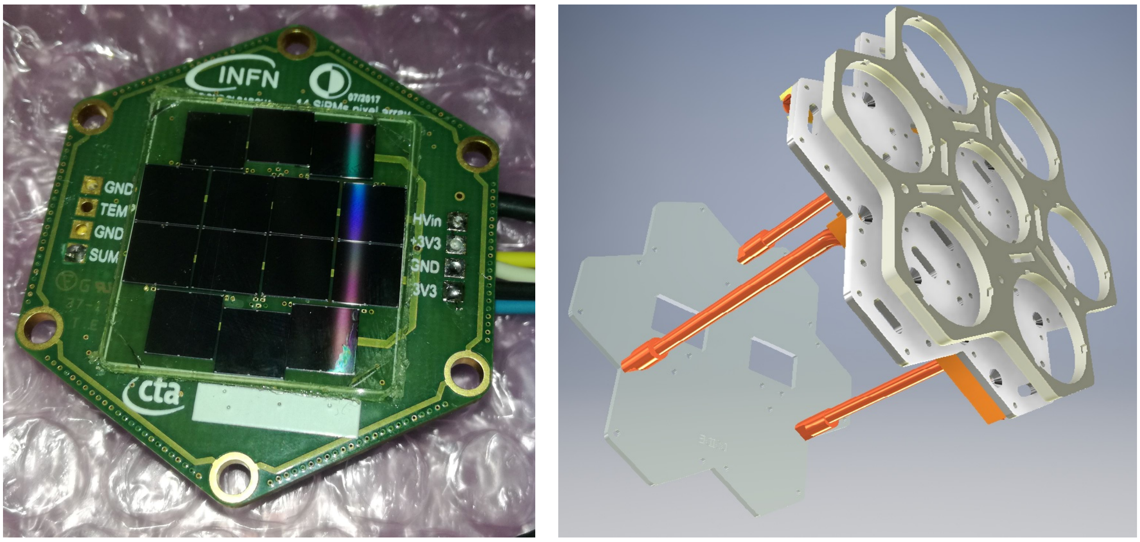

(a) (b)

Figure 4.86: (a) A picture of the discrete component SiPM pixel, composed of fourteen 6 mm × 6 mm FBK NUV SiPMs
(b) Mechanical design of the heat transfer system [116]

4.6.2 Discrete Components Solution

Alongside the reported development, a possible solution based on a discrete components circuit is also under study. This solution is taken into consideration above all if the chosen pixel dimension for the LST SiPM camera will be smaller than the PMT ones. In this way the circuit will have less channels, since less SiPM signals will be summed together.

A picture of the SiPM pixel is visible in Figure 4.86a. The active area is composed of fourteen 6 mm × 6 mm FBK NUV SiPMs glued and micro-bonded under a UV resin coating and a thin quartz film. On the back of the PCB we find the circuit: each SiPM output is connected to a fast BJT preamplifier, and all the 14 signals are summed together by a two-stage operational amplifier circuit. For this prototype, the output signal is single ended and only one gain is implemented.

If on the one hand it improves the signal integrity, the preamplifier circuit directly mounted on the back of the SiPMs causes the sensors to heat up considerably, increasing their dark count rate (the preamplifier consumes about 0.9 W). This heat must be taken away: the PCBs could be thermally connected to an Aluminum plate, and the heat could be carried away by heat pipes; the mechanical design of the heat transfer system can be seen in Figure 4.86b [116].

Full Width at Half Maximum

This circuit offers a very fast signal: a FWHM of 3.4 ns has been measured by averaging the FWHMs of 1000 waveforms acquired by means of a Tektronix MSO6 oscilloscope with 1 GHz bandwidth. In Figure 4.87a it is shown the output signal, obtained as the average of 1000 acquisitions, while in Figure 4.87b the distributions of the FWHMs.

Linearity

The linearity measurement on this pixel was carried out with a process similar to the one reported in section 4.4.8, but using two different LED heads instead of a double slit. The setup scheme is shown in Figure 4.88. A pulser independently operates two LED heads, flashing the SiPM pixel under test. Since with this system it is very difficult to align the signal peaks, we proceed to study the linearity of the signal area. In the other case, instead, it was necessary to study the linearity of the signal peak, since the signal was processed with the DLED technique, not ideal for area measurements. Since the slit used in the previous measurement is not controlled remotely, this method has the advantage that it is not necessary to open the black box during the measurement. Signals are acquired with a Tektronix MSO6 oscilloscope, with 1 GHz bandwidth. The area is evaluated by integrating the average of 100 waveforms with a 20 ns time window, wider than the signal duration. In this measurement L_i is the average signal area value obtained with the LED i on and the other one off, and L_{12} is the value obtained with the two LED flashing the pixel. To remove the baseline, the area value obtained with both LEDs off was subtracted to each L_{ij} value. Measurements are repeated covering a range of output signals up to more than 1 V, the maximum input value for the DRS4 board. The measurements were repeated by biasing the sensor at 30 V and at 35 V. The deviation from linearity is evaluated with Equation 4.70, and results are shown in Figure 4.89; this plot was obtained with the SiPM biased at 35 V, and similar results were obtained at 30 V.

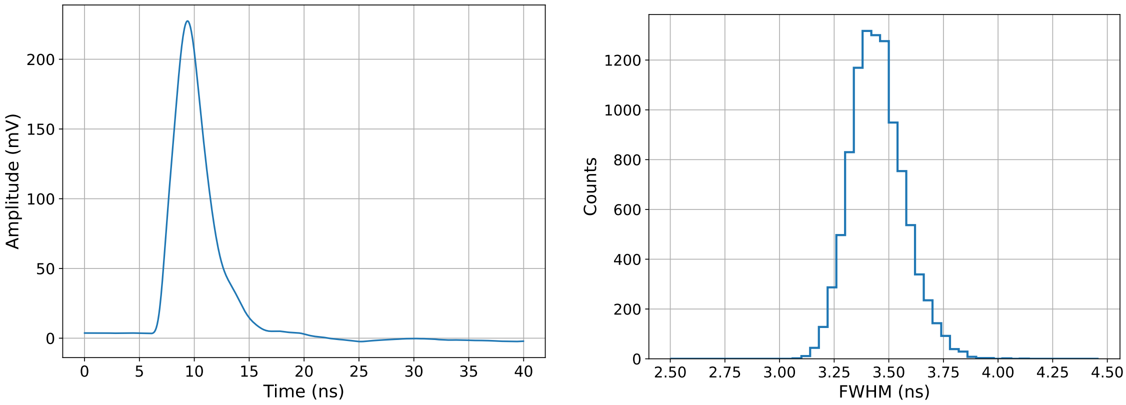

(a) (b)

Figure 4.87: (a) Discrete component SiPM pixel average signal of 1000 acquisitions
(b) Distributions of the signal FWHMs

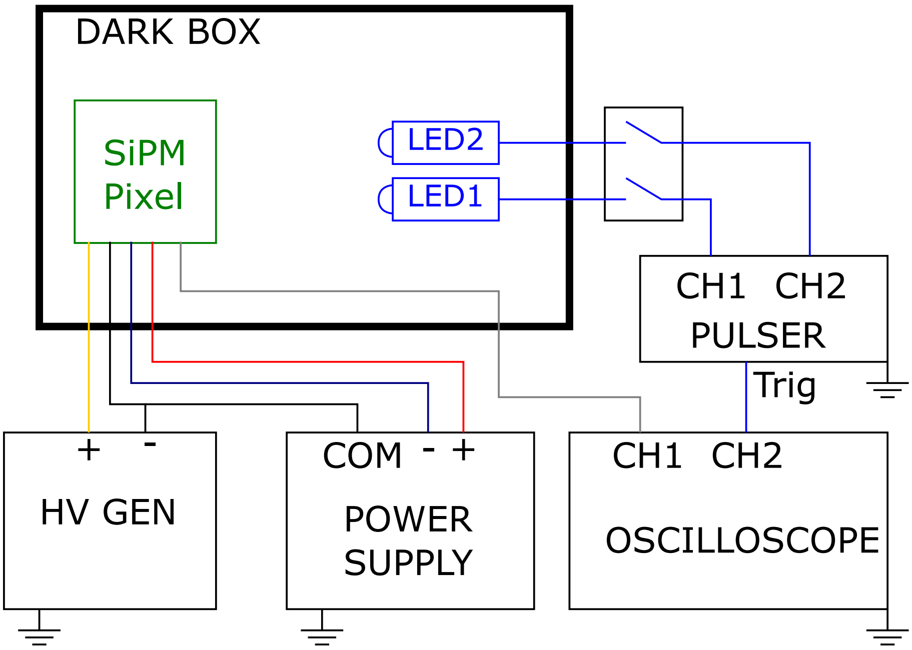

Figure 4.88: Setup for the linearity measurement

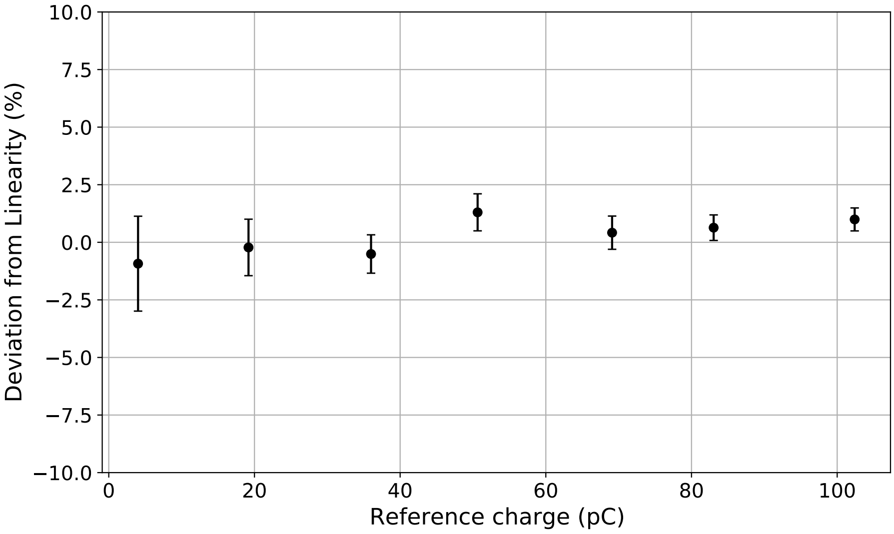

Figure 4.89: The SiPM pixel deviation from linearity, covering a range of output signals up to more than 1 V

4.7 Summary and Future Perspectives

In this chapter we described the development of a working SiPM module based on the LST nominal one. This work aimed at emphasizing one of the main advantages of SiPMs, i.e. their robustness and tolerance to high illumination levels. These features improve the reliability of the telescope and may allow us to work in illumination conditions that are not suitable for traditional photomultipliers, thus leading to an increase in the duty cycle.

Since the development was based on the LST module, we kept the same pixel size as the nominal PMT. To cover the required area with solid state sensors, we had to sum 12 SiPMs; for the amount of sensors composing the pixel the easiest solution was to rely on an ASIC instead of a discrete component circuit. The active current limiter for the SiPM bias and the AC filter on the SiPM output signals turned out to be the key solutions to detect pulsed light signals even in a high-background environment. Indeed, thanks to the current limiter, it is possible to keep the same bias voltage on the SiPMs using a proper slow control; on the other hand this would not have been possible if we had used a protection resistor. In addition, without the AC filter, the pixel would rapidly saturate as the signal increases, thus becoming unusable.

All the solutions studied and developed in this chapter are indeed independent from the pixel size. Hence, for the final SiPM camera using smaller pixels could be considered: they are easier to build, since a smaller number of sensors has to be summed together, and would also improve the angular resolution. Besides, if the pixels were smaller, less current would flow in the sensors at the same background, so it would be possible to operate with the same current limitation in presence of higher background values.

In order to fully exploit the advantages of SiPMs, the final circuit setup must be adjusted in the framework of the whole telescope system and the expected operating conditions. The resulting amount of extra observing time will depend on several factors, whose study is beyond the scope of this thesis, e.g. the final pixel size and the current limit (which could be a trade-off with SiPM lifetime). The circuit developed in this work can be adapted as needed and its final optimisation could be implemented in the future.

Chapter 5

Analysis of SiPM-Based Camera LSTs Simulations

As we have already discussed, Silicon Photomultipliers (SiPMs) are more and more emerging as promising competitors to standard PMTs in IACT applications: indeed, in CTA both small-sized telescopes and dual-mirror medium-sized ones will use them as photodetectors. An alternative to the current LST camera is therefore under study: the goal is to develop an "Advanced" camera achieving better performance than the PMT one [117]. This new camera will host SiPMs on its focal plane, most probably organized in smaller pixels providing higher granularity of the collected images, and the electronics design will follow a fully digital approach, in order to maximize its flexibility. In order to evaluate the potential performance improvement with respect to standard cameras and to start defining the key parameters to optimize it, a detailed simulation work is being performed. We thus simulated an array of four "Advanced" LSTs, comparing the results with the nominal LST array.

For the first simulation runs, the ones studied in this work, we started from the SST1-M focal plane, increasing the pixel number up to cover a surface comparable to the nominal LST camera (about $3\,\mathrm{m} \times 3\,\mathrm{m}$). We therefore used the SST-1M pixel size and shape; in this way the pixels are about a quarter the size of the LST PMTs. The simulated sensors are also the ones used in the SST-1M camera, i.e. Hamamatsu LCT5. Other simulations will follow, with different pixel sizes and SiPMs. For these runs no UV filter has been added to the focal plane, simulated with the nominal PMMA LST window; we therefore expect a higher night sky background rate than what we would have on the PMT camera. As discussed in section 3.5.1, the use of a filter would improve the signal-to-noise ratio; however, this would also result in a lower signal, and since in an IACT telescope the trigger and the analysis are based on the images which occur on the focal plane, having a lower signal can worsen the overall performances. New Monte Carlo productions will follow, to evaluate whether it is convenient to use a filter or not.

For these simulations the electronics and the trigger of the nominal LSTs have been kept, and only the focal plane has been changed. Data have been analysed with the same analysis pipeline, with standard algorithms (random forests) and without any specific optimization for SiPMs, therefore we anyway don't expect to see a big improvement in performance. On the other hand we expect that a more complex analysis, based on Deep Learning methods, could benefit the higher granularity of the images (with or without image parametrization). Two analysis pipelines have been used for this work: *magic-cta-pipe*, built for the MAGIC and LST combined analysis, and *protopipe*, the pipeline being developed for the analysis of the CTA observatory data. Both pipelines are under huge development, the results shown in this chapter must be therefore considered as preliminary.

	Gammas point	Gammas diffuse	Protons	Electrons
Number of showers	10 000	50 000	100 000	60 000
Shower reuse	10	10	10	10
Minimum energy	5 GeV	5 GeV	10 GeV	5 GeV
Maximum energy	50 TeV	50 TeV	100 TeV	5 TeV
Maximum scatter range	800 m	1000 m	1500 m	1000 m
Spectral index	−2°	−2°	−2°	−2°
Viewing cone radius	0°	6°	10°	6°

Table 5.1: Extensive Air Showers simulations settings

5.1 Monte Carlo Simulations

To evaluate the benefits of a SiPM-based camera for LST, we are performing a detailed simulation work. As a first step, we simulated an array of four LSTs which have the focal plane composed of 7987 hexagonal SiPMs, in order to compare its performance with the nominal LST array. The simulations were obtained with CORSIKA [118] for the simulation of the Extensive air showers and `sim_telarray` [119] for the telescopes' response.

5.1.1 Extensive Air Showers Simulations

As anticipated in the discussion of the electromagnetic and hadronic showers, their most accurate description is obtained through Monte Carlo simulations. These simulations are used to estimate the energy and direction of the detected gamma rays, and to discriminate between hadronic and electromagnetic showers. Usually at least three incoming particles are simulated:

- gammas
- positrons
- electrons

The gammas are simulated both coming from a point-like source or diffused, namely coming from a solid angle greater than the field of view of the telescope; protons and electrons are simulated only diffused. The pipeline handles both MAGIC and CTA simulations; for our aims, we will use only the last ones. We will analyse and compare simulations of an array of four nominal LSTs and an array of four SiPM-based camera LSTs.

Simulations are performed with standard NSB for extragalactic observations, at 20° of zenith. The simulated array is made by the four LSTs and the two MAGIC telescopes. The input parameters of the corsika EAS productions analysed in this thesis are listed in Table 5.1.

5.1.2 Telescopes Simulations

While the settings for extensive air showers simulations are the same for both arrays, clearly the telescopes settings differ.

The LST Nominal camera is composed of 1855 Hamamatsu R11920-100-2 PMTs; each pixel has a field of view of 0.1°. The PMT quantum efficiency is shown in Figure 5.1a. As we can see, two slightly different quantum efficiencies are used to simulate LST-1 (the first and currently only LST) and to simulate the other ones. The single photoelectron spectrum is visible in Figure 5.1b in blue. In Figure 5.1c we can see the High Gain and Low Gain normalized pulse shapes.

The LST Advanced camera focal plane is indeed composed of 7987 hexagonal SiPMs and is based on the SST-1M telescope one, with the same Hamamatsu LCT5 sensors and the same light guides. Each pixel has a field of view of 0.05° and no filter window is used on the focal plane. The SiPMs are biased at 7 V of overvoltage, bias at which they have a crosstalk equal to 15 %. Their Photon Detection Efficiency (PDE) is maximum at 470 nm and it is shown for $V_{OV} = 7\,\mathrm{V}$ in Figure 5.1a in green. Their single photoelectron spectrum is shown in Figure 5.1. Both plots are based on measurements made within the CTA collaboration by Andrii Nagai.

Its finer pixelation suggests to us that this camera will have a better angular resolution than the nominal one. The readout electronics and the trigger are the same as the one used in the nominal LST. The SiPM signal is shaped up to reach a FWHM of 3 ns. The used signal template for the simulation is shown in Figure 5.1c; the shape is derived from a 7 ns not-smoothed template and was developed by L. David M. Miranda from Andrii Nagai's measurements on LCT2 sensors within the CTA collaboration. Only one gain is simulated. Some comparison of the same event seen in the nominal camera and in the LST Advanced Camera is visible in Figure 5.2: the finer pixelation allows to see each shower with higher resolution.

For both simulations the safe trigger threshold is defined as the threshold at which the night sky background rate multiplied by 1.5 would be equal to twice the protons rate.

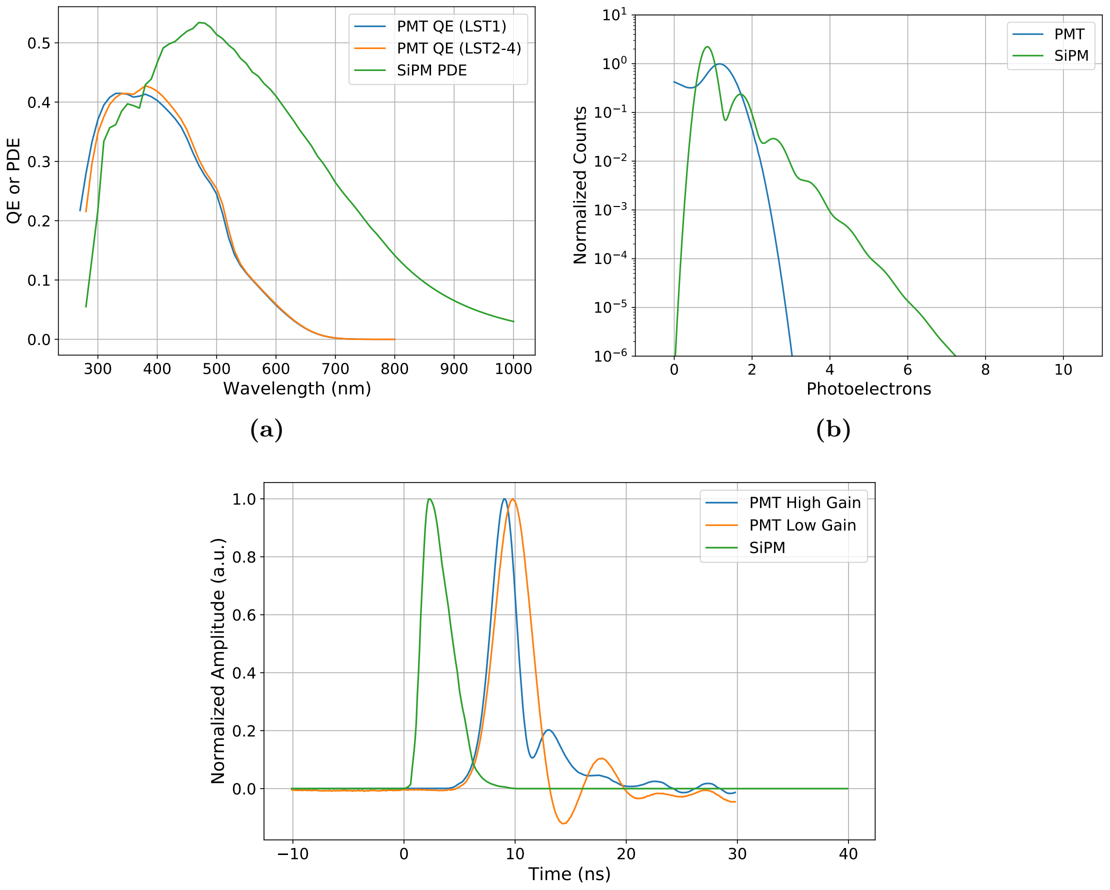

(a)

(b)

(c)

Figure 5.1: Telescope simulations settings:
(a) PMT quantum efficiency and LCT5 Hamamatsu SiPM Photon Detection Efficiency at $V_{OV} = 7\,\mathrm{V}$
(b) PMT and SiPM single photoelectron spectrum
(c) Signal template used for the simulations

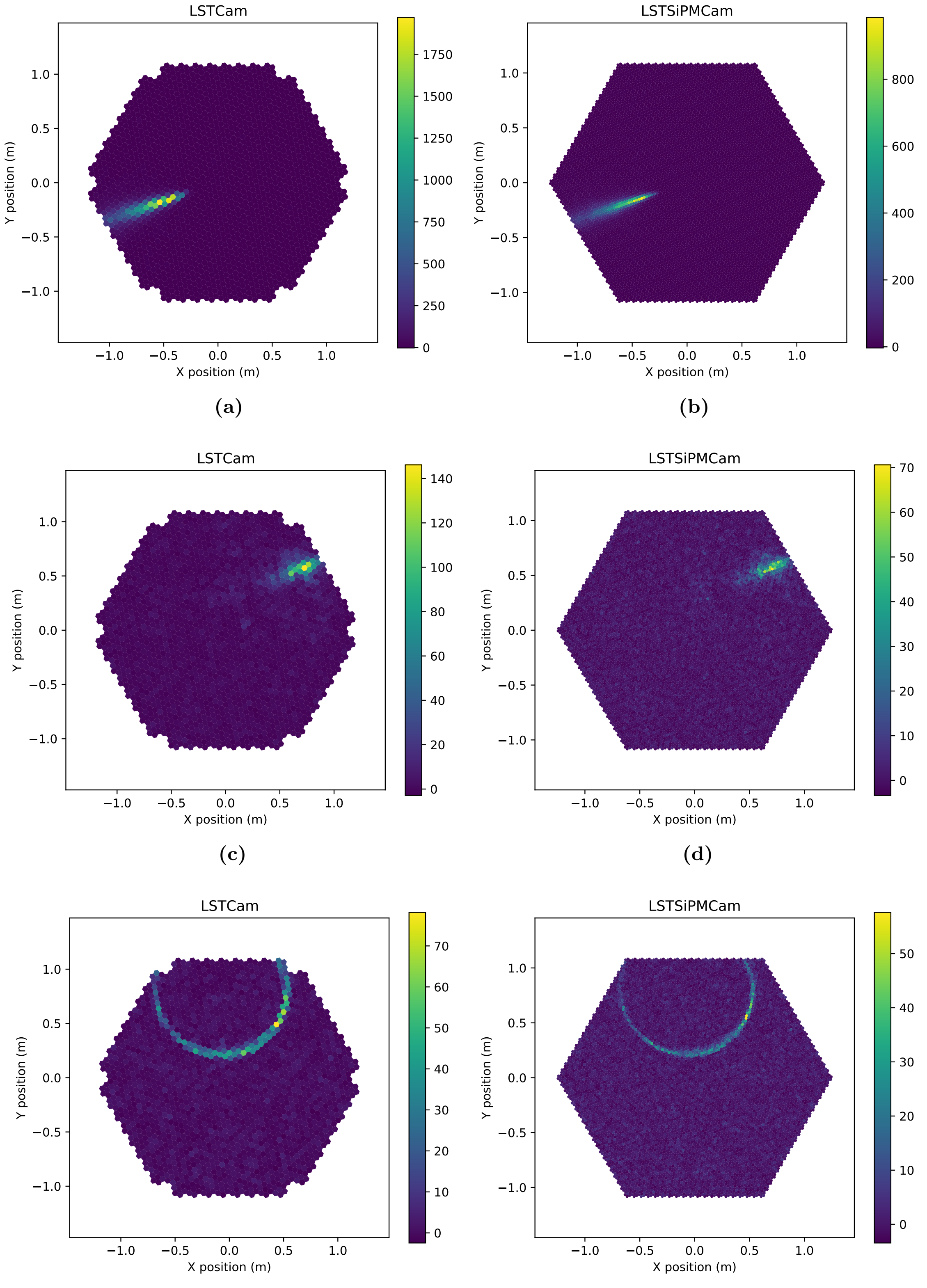

(a) (b) (c) (d) (e) (f)

Figure 5.2: The same event observed with the LST Nominal Camera (left) and with the SiPM-based camera (right): gamma-ray induced shower (a, b), proton induced shower (c, d) and a muon (e,f)

5.2 MAGIC and LST Analysis Pipeline: *magic-cta-pipe*

The *magic-cta-pipe* software package was born to analyse MAGIC and LST joint observations. The two facilities are indeed built very close together, and joint observations between the two MAGIC telescopes and LST-1 (the first and currently only LST) are already performed. Due to the improvement in angular resolution and in sensitivity, observing the same source with the two systems will allow us a better understanding of the physical processes that regulate its gamma-ray emission. MAGIC has indeed its own analysis software, the MAGIC Analysis Reconstruction Software (MARS) [120]. It is an object-oriented software based on the ROOT framework, developed since 2000. However, this software can't be used to analyse data from other telescopes, for example LST data. Therefore, to analyse MAGIC and LST joint observations it was necessary to develop a new software package, named *magic-cta-pipe*. The development started in 2019, and its main tasks are:

- Analyse coincident events between MAGIC and LST
- Cross-calibration of the two systems
- Science with MAGIC and LST

The pipeline is entirely written in python and is based on the *ctapipe* package [121], built for CTA analysis. It is made up of a set of scripts, based on common python scientific libraries (`numpy`, `pandas`, `scipy`, `scikit-learn`, ...). It has only one configuration file, written in `yaml` format. The pipeline handles both real data (MAGIC and LST) and Monte Carlo simulations. For our aim, we will focus only on the last ones. The pipeline uses the *Random Forest* (RF) method for the events classification and for determining their main parameters. Three different random forest types are trained:

- Gamma/hadron separation (classifier)
- Energy
- Direction

5.2.1 Input Files

The pipeline handles the following data:

- MAGIC real data
- MAGIC Monte Carlo simulations
- LST real data
- CTA Monte Carlo simulations

For our purposes, we will focus our attention on the last ones. In this case, input files are divided as follows:

- Train sample: Monte Carlo files used to train the random forests
  - Diffuse gamma rays: used to train classifier (gamma), energy and direction random forests
  - Protons: used to train classifier (hadrons)
- Test sample: files on which random forests are applied
  - Point-like gamma rays
  - Protons (different from the ones composing the train sample)
  - Electrons

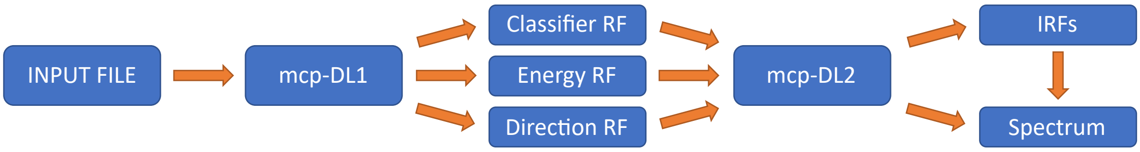

Figure 5.3: Workflow of the *magic-cta-pipe* pipeline

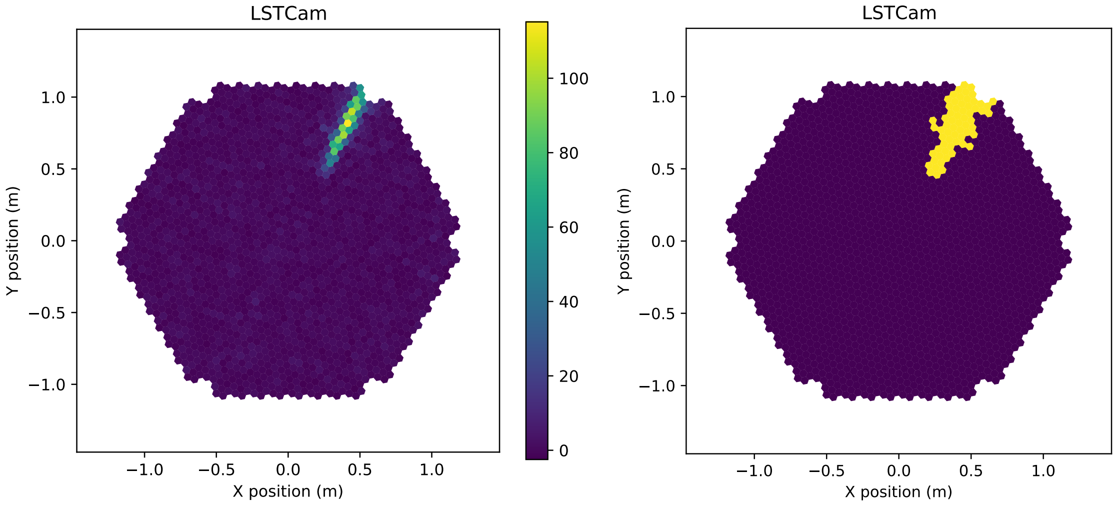

(a) **(b)**

Figure 5.4: An example of a LST calibrated images in photoelectrons (a) and its corresponding cleaning mask (b)

5.2.2 Pipeline Overview

The *magic-cta-pipe* steps are schematized Figure 5.3. Below we list them briefly; in the next sections each point will be explained in more detail.

- Hillas and stereo reconstruction: evaluation of hillas and stereo parameter; results are saved in *mcp-DL1* files
- Train random forests
- Apply random forests on *mcp-DL1*, obtaining *mcp-DL2* files
- Instrument response evaluation

The intermediate files are called *mcp-DL1* and *mcp-DL2* since they do not follow the official *DL1* and *DL2* CTA file format.

5.2.3 Hillas and Stereo Reconstruction

Raw data (*DL0*) are processed with the *ctapipe* `CameraCalibrator` class. This class performs the full camera calibration, integrating the pixel signals and converting the resulting charges into photoelectrons. An example of a calibrated image is visible in Figure 5.4 on the left; the colorbar represents the number of photoelectrons for each pixel.

It is clear that the interesting pixels are only the ones illuminated by the Cherenkov photons produced in the air shower. The other pixels instead contain only noise signals, whether induced by the night sky background or by the electronics. We therefore proceed with the cleaning of the image, to select only the interesting pixels. There are

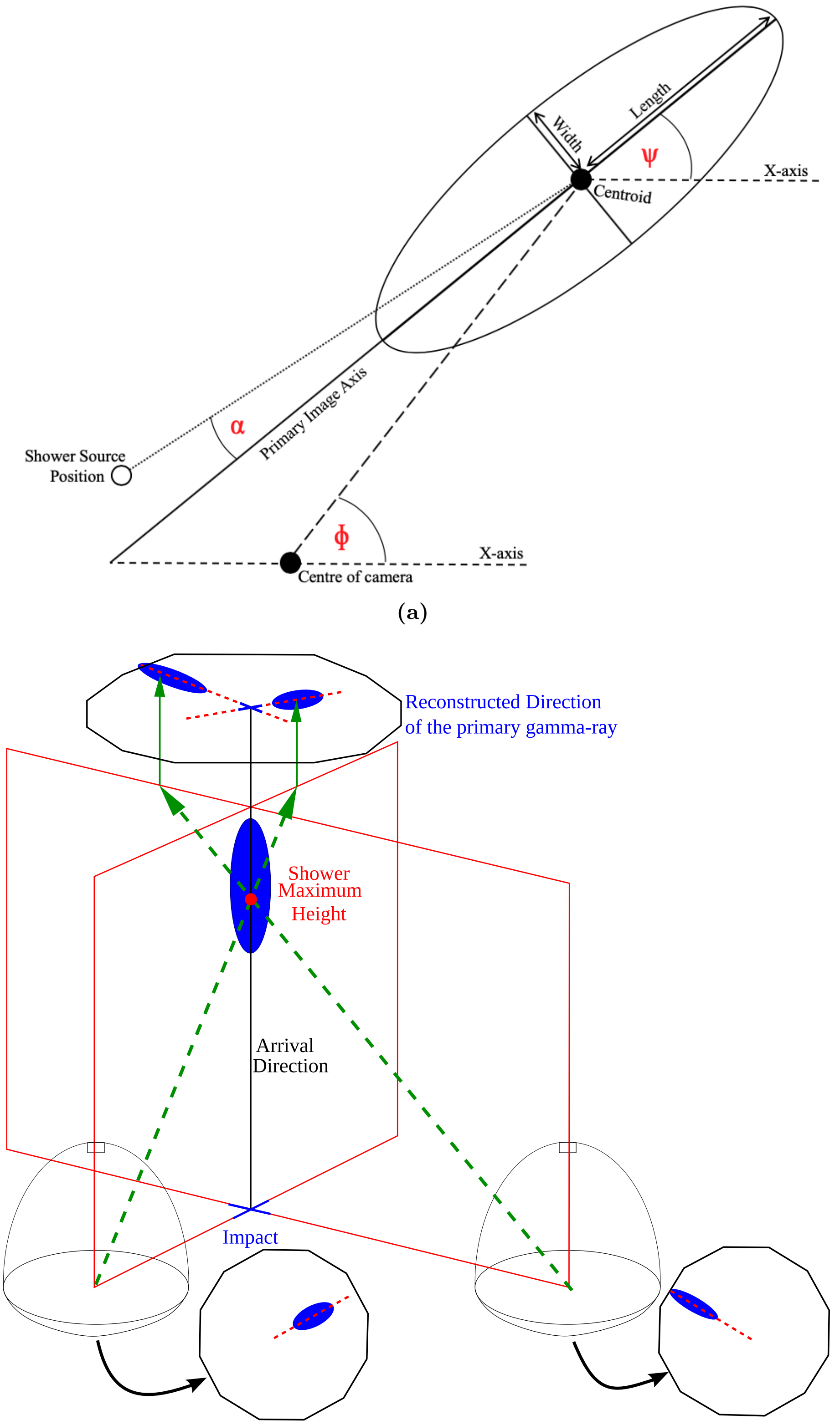

(a)

(b)

Figure 5.5: Visual representation of some Hillas [121] (a) and stereo [122] (b) parameters

many possible algorithms to carry out this process. The one used by *ctapipe* is the so-called *tailcuts cleaning*. It is a two-thresholds filter: it keeps all the pixels in the camera with a charge higher than a first given threshold (called `picture_thresh`), and then all their neighbors if they are above another given threshold (`boundary_thresh`). Logically, the second threshold is set lower than the first one. The two thresholds can be set via the configuration file. The standard settings used to clean the LST camera is 6-3 (`picture_thresh-boundary_thresh`) or 8-4; for our analyses we will use the second one. On the right in Figure 5.4 we can find the cleaning mask (i.e., the selected pixels for further image parametrization) of the picture under study.

Once obtained the cleaned calibrated images, it is possible to parametrize them. Some of them are still the ones used by Hillas in 1985 to discriminate between electromagnetic and hadronic showers [40]. The main parameters are:

- **intensity** (or **size**): total number of photoelectrons in the cleaned image; this parameter is strictly related to the primary particle energy
- **length**: half length of the major axis of the image ellipse (i.e., standard deviation along the major axis of the ellipse)
- **width**: half length of the minor axis of the image ellipse (i.e., standard spread along the minor axis of the ellipse)
- **center of gravity**: coordinates of the centroid of the shower images; with respect to the camera center, *ctapipe* evaluates:
    - **x**: x coordinate of the center of gravity
    - **y**: y coordinate of the center of gravity
    - **r**: radial coordinate of the center of gravity
    - **phi**: polar coordinate of the center of gravity
- **psi**: rotation angle of the ellipse, with respect to camera x-axis
- **skewness**: measure of the asymmetry of the ellipse
- **kurtosis**: measure of the tailedness of the ellipse
- **leakage 1**: fraction of the image that falls in the outermost camera ring, compared to the total size; this parameter is useful to discard images in which the shower is partially out of the camera
- **leakage 2**: as before, but considering the two outermost rings
- **slope**: angular coefficient of the linear function used to fit the arrival time distribution for each pixel with respect to the pixel coordinates projected on the major axis of the ellipse
- **number of islands**: number of not connected groups of pixels after image cleaning

The visual representation of some Hillas parameters can be seen in Figure 5.5a.

The parameters seen so far are related to individual telescope data (*mono mode*). However, if more telescopes are observing the same event, it is possible to combine their information, obtaining a three-dimensional reconstruction of the shower. This approach, referred to as *stereo mode*, is clearly more powerful than the first one. In this case, in addition to finding the hillas parameters for each telescope involved in the event, it is possible to find the stereo parameters, in particular:

- **shower maximum height**: as the name suggests, it is the height of the shower maximum
- **core**: coordinates of the impact point on the ground
- **impact**: distance between the shower axis and the telescope pointing axis

The visual representation of some stereo parameters are shown in Figure 5.5b.

5.2.4 Random Forests Training

The parameters obtained so far are necessary to determine the nature and the properties of the event. Finding the nature of the event is necessary to discriminate the gamma-induced events from the background (mostly hadrons). The other properties that we want to reconstruct are the gamma-ray energy and their arrival direction. In *magic-cta-pipe* the discrimination between gammas and hadrons and the determination of the other properties are based on *Random Forest* (RF) methods. The pipeline therefore produces three RFs for each telescope:

- Gamma/hadron separation
- Energy
- Direction

Each telescope has its own random forest. The training is performed on Monte Carlo simulations, both for showers induced by gamma rays and protons; in the next sections we will briefly describe how these random forests are obtained. The pipeline offers the possibility to train the RFs only on selected events which pass some quality cuts, given in the configuration file. However, it has been seen that the best results are obtained by training the RFs on all events, and then applying the cuts on the data to be analysed.

Gamma/Hadron Separation

The gamma/hadron separation relies on a discrete random forest. The random forest [123] is a simple machine learning method consisting of a set of decision trees, each one built through a number of random choices on a set of training samples. We will describe the basic functioning of a RF to classify an event in a discrete way (in our case to distinguish an event induced by a gamma from one induced by a hadron); however, this method can be generalized in the continuous case (energy and arrival direction).

For gamma/hadron separation, the training sample contains two classes: gammas and hadrons. Each element of the training sample is called *event*. Each event is characterized by a multidimensional vector whose components are the image parameters obtained in the previous analysis step (i.e., Hillas and stereo parameters). If we consider N parameters, the event will belong to a N-dimensional hypercube. The random forests training parameters are based on the ones used in MARS.

From this training sample we construct a binary decision tree. A first parameter is randomly chosen, and the cut on this parameter is computed. This cut is evaluated in order to optimize the sample into its classes (gammas and hadrons). The initial hypercube is therefore divided in two different nodes, and the previous operation is repeated for each one (considering other parameters). The procedure ends when a node contains only gammas (or hadrons), or if the number of events in a node is below a predefined value. A *gammaness* l value is therefore assigned to each node: $l = 1$ if the node contains only gammas, $l = 0$ if it contains only hadrons and a number between 0 and 1 if the node contains both. In the

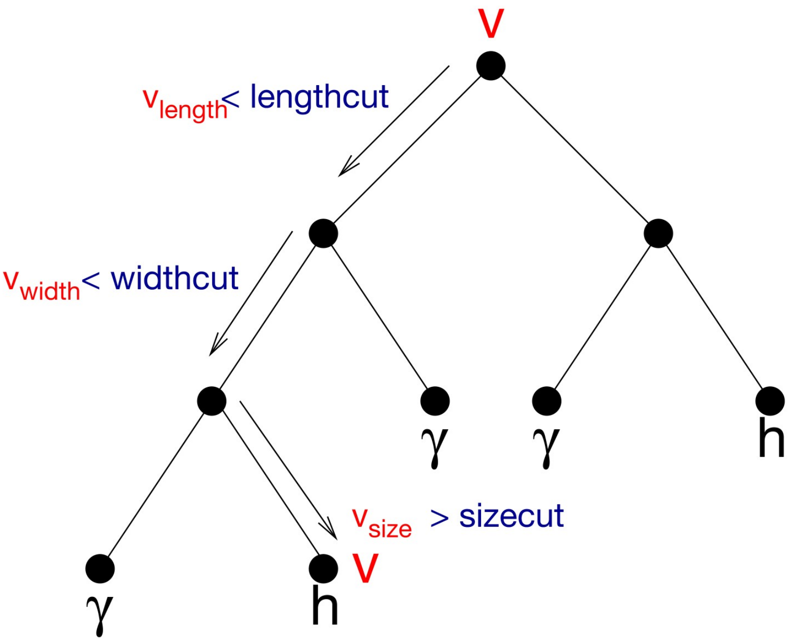

Figure 5.6: Tree structure for the classification of an event v with components v_{length}, v_{width}, and v_{size} [123].

latter case, the gammaness value is calculated considering the gamma fraction contained in the node:

$$l = \frac{N_\gamma}{N_\gamma + N_h} = \frac{N_\gamma}{N} \tag{5.1}$$

where N_γ and N_h are the numbers of gammas and hadrons in the node and N is the total node population:

$$N = N_\gamma + N_h \tag{5.2}$$

When all nodes have received a gammaness value, the tree has been built. For better performances, more trees are built, giving origin to a forest.

To evaluate the separation ability of a parameter and to optimize the cut value we use a quantity called *Gini index* Q_{Gini} . Introduced in the economic field, the Gini index measures the inequality of two distributions (gammas and hadrons in our case). In the RF case, the Gini index is:

$$Q_{Gini} = 4\frac{N_\gamma N_h}{N^2} \in [0,1] \tag{5.3}$$

If in a node only one class is present, then Q_{Gini} will be zero (since either $N_\gamma = 0$ or $N_h = 0$). The Gini index of the split is evaluated as the sum of the Gini indexes of the two successor nodes, called left and right, normalized to one:

$$Q_{Gini} = 2\left(\frac{N_{\gamma,left}N_{h,left}}{N^2_{left}} + \frac{N_{\gamma,right}N_{h,right}}{N^2_{right}}\right) \in [0,1] \tag{5.4}$$

Minimizing the Gini index corresponds to minimizing the variance of the population of gammas and hadrons in the sample.

An example of a binary decision tree of an event v with components v_{length}, v_{width}, and v_{size} is shown in Figure 5.6. The classification process works as follows. We consider a fully grown decision tree, such as the one reported in Figure 5.6. We have an event v, and we want to determine whether it is a gamma or a hadron. At the first node, we have a split over a parameter (length in our example): depending on whether this value is greater or less than the cut, we proceed to the right or to the left of the decision tree. The same process is repeated at each node. The event v therefore follows a track through the decision tree, depending on the values of its parameters. The process ends when we reach a terminal node, which assigns to the event v a gammaness value $l_i(v)$, where i is the tree number. The event v will be classified by all the trees of the forest; different trees will lead to different gammaness values. The gammaness value of the event $g(v)$ is evaluated as the mean of all the values obtained in each tree:

$$g(v) = \frac{\sum_{n=1}^{n_{trees}} l_i(v)}{n_{trees}} \tag{5.5}$$

where n_{trees} is the total number of trees in the forest.

Once the classifier RF is trained, the pipeline checks its efficiency by applying it to a Monte Carlo test sample, in which we know the true value we should reconstruct. The resulting plots for a Monte Carlo simulation of four nominal LSTs is shown in Figure 5.7a. In the first row we have the distribution of the gamma (blue) and hadron (orange) events of the test sample with respect to their reconstructed gammaness value. In the second row we have the respective cumulative distributions. In the first column, the gammaness is the average of the values obtained by applying the RFs, while in the following columns we have the individual telescope detail. The gammaness values given to the events by the pipeline are the ones shown in the first column. We clearly see how the gammaness distributions for gamma-ray or proton-induced events are well separated: this parameter is therefore excellent to find the nature of events. To do so, we need to decide a cut on this parameter, which will inevitably cause a signal loss and integration of some background. How we will see later, a possible way to define this cut is as the one that optimizes the sensitivity.

Energy Estimation

The random forest method is used also in the case of a continuous variable, in this case the energy of the primary gamma ray. The train sample contains only gammas, and the used algorithm is the one implemented in the `RandomForestRegressor` class of the `scikit-learn` python library. The training parameters are based on the ones used in MARS.

Also in this case, after the RFs are trained, they are applied on the test sample to check their reliability. The program evaluates the *migration matrices*, i.e. the two-dimensional histograms showing the distribution of the reconstructed energy (E_{est}) compared to the simulated one (E_{true}). The resulting plots for a Monte Carlo simulation of four PMT-based LSTs are visible in Figure 5.7b; in the last column the energy values are the mean of all the energy values obtained for each telescope for the same event, while in the other columns we have the individual telescope detail.

Arrival Direction Estimation

The arrival direction estimation relies on the so-called *DISP RF* method [122, 124]. This method takes into account the image shape and the timing information. For each telescope we compute the estimated distance *DISP* between the image center of gravity and the source position:

$$DISP = A(\text{size}) + B(\text{size}) \cdot \frac{\text{width}}{\text{length} + \eta(\text{size}) \cdot \text{leakage2}} \tag{5.6}$$

The optimization of the coefficients A, B and η is performed with a random forest method on a continuous quantity over a Monte Carlo gamma sample. Since the source position is assumed to lie on the line defined by the main axis of the ellipse, we have two possibilities.

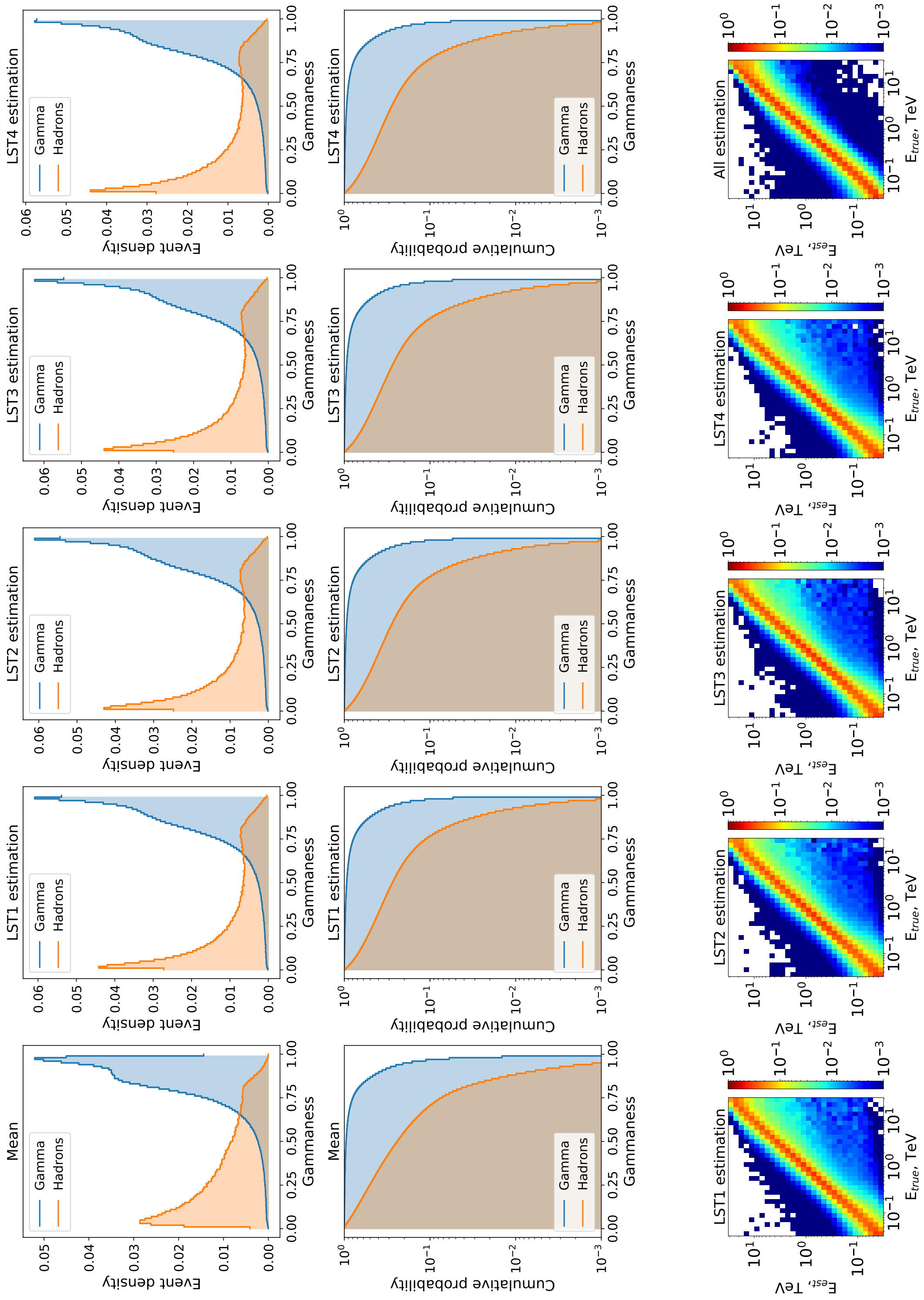

(a)

(b)

Figure 5.7: (a) Gamma/hadron separation RF check plots for events triggering the 4 PMT-based LSTs array
(b) Migration matrices for events triggering the 4 PMT-based LSTs array

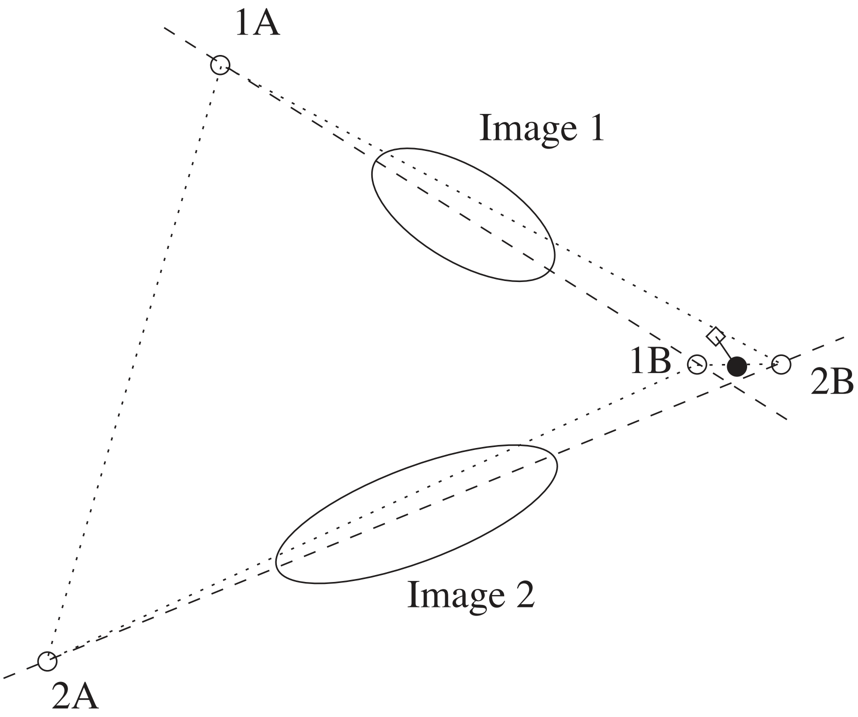

Figure 5.8: DISP RF method for two telescopes. The main axes of the ellipses are plotted with dashed lines, the distance between the reconstructed DISP RF positions in dotted lines. The diamond and the black dot shows the true source position and the final reconstructed source position, respectively.

This ambiguity is called head-tail discrimination and can be solved by considering the crossing points of the images (in the stereo case), or by taking into account the image asymmetry along the main axis of the ellipse. However, the first method will fail in case of almost parallel lines, and the second is not reliable at low energies, where the images are made up of a few pixels. It is therefore necessary to use a more robust method; below we explain it in the case of only two telescopes, but it can logically be extended in the general case. Referring to Figure 5.8, the DISP RF reconstructed positions are 1A and 1B for the first telescope, 2A and 2B for the second one. We compute the four distances between the reconstructed source positions (1A-2A, 1A-2B, 1B-2A, 1B-2B), and we consider the smallest one (1B-2B). The final reconstructed source position is the weighted average of 1B and 2B. Also in this case, the random forests training parameters are based on the ones used in MARS.

Again, after the RFs are obtained, they are applied to a test sample (or only to a subsample) to check their effectiveness. Resulting plots for events triggering the 4 PMT-based LSTs array are shown in Figure 5.9, where θ is the angular distance between the true and the reconstructed source position. The first column shows the θ^2 plot, the second one the corresponding θ cumulative distribution. In the first row we are considering the mean of the values obtained for each RF, while in the following rows we have the individual telescope detail.

5.2.5 Application of Random Forests

The next step is to apply all the RFs to the test sample, in order to obtain for each event its gammaness, arrival direction and energy. Since we have one RF for each telescope, these quantities are the average of the ones obtained from all the telescopes. The resulting files are the *mcp-DL2* ones.

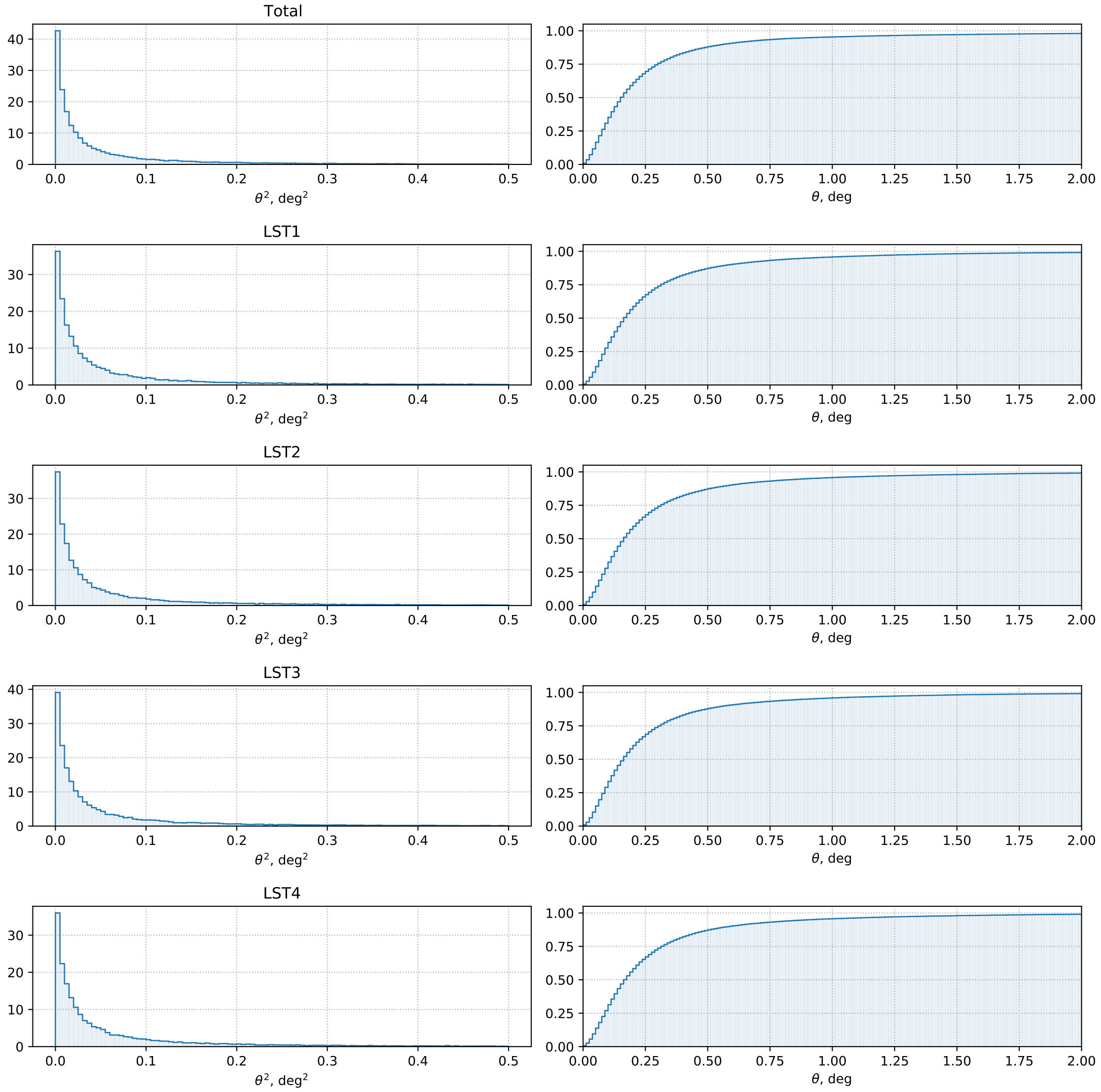

Figure 5.9: Direction estimation check plots for events triggering the 4 PMT-based LSTs array; the first column shows the θ^2 plot, the second one the corresponding θ cumulative distributions

5.2.6 Instrument Response Functions

Once the events have been reconstructed, it is possible to evaluate the Instrument Response Functions. Their evaluation is done using the *pyirf* package [125]. The used test samples are the simulated gamma rays and protons, and the pipeline evaluates:

- Effective collection area
- Angular resolution
- Energy resolution
- Sensitivity

It is possible to calculate these quantities only on events surviving some quality cuts, given in the configuration file. In addition to quality cuts, the program calculates cuts in direction and gammaness. These cuts are those used in the analysis of telescope data.

Analysis Cuts

We have two analysis cuts:

- Gammaness cut
- Direction cut

The gammaness cut is calculated to select only the gamma induced showers from the data sample being analysed. In this way, the main background contribution, namely the protons, can be eliminated from the analysis. However, in this way it is impossible to discard the electron-induced events: indeed, both an electron and a gamma ray originate an electromagnetic shower. However, the direction of the primary particle helps us: while gamma rays arrive from the source, electrons arrive from all directions. For this reason, a cut on the arrival direction improves the analysis.

The evaluation of the two cuts is done in a semi-recursive way. As a first step the program selects in the gamma sample the events that have a gammaness greater than a fixed value, set in the configuration file. The program then applies the direction cut on the selected events; such a cut is chosen so that only the 68 % of the events survives. Then the gammaness cut to be applied in each energy bin is evaluated as follows: after having tested different gammaness cut values, the one which provides the best sensitivity is selected. Finally the arrival direction cut is again evaluated for the events selected by the gammaness cuts.

Gammaness and direction cuts are applied to the MC sample used to evaluate the effective area the energy resolution and the sensitivity, while only gammaness cuts are used for the angular resolution.

Effective Collection Area

The Effective collection area is the geometrical area where a gamma-ray shower can be detected by the telescope array, folded with the gamma-ray efficiency given by the trigger conditions and the analysis cuts. If the telescope array is large, the collection area above the energy threshold for low zenith angle observation is approximately equal to the array physical size [126]. For small telescopes arrays instead the collection area is mainly determined by the size of the Cherenkov light pool, which has a radius of about 120 m [124]. The collection area as a function of the energy E is:

$$A_{eff}(E) = \pi r_{max}^2 \cdot \frac{N(E)}{N_0(E)} \tag{5.7}$$

where r_{max} is the maximum simulated shower impact, $N_0(E)$ is the number of simulated events and $N(E)$ is the number of events passing either the trigger condition or the analysis cuts.

The effective area increases with the gamma-ray energy, since more photons are produced in the shower, and falls rapidly below the energy threshold. This quantity depends also on the zenith angle: at higher zenith angles the effective area at low energies is smaller, due to the increase of the energy threshold; however, as the energy increases, the effective area will be greater since the light pool is bigger [124].

Angular Resolution

The angular resolution indicates the telescopes' capability to reconstruct the gamma-ray incident direction. It is defined as the angular separation from the source position in which we have 68% of the reconstructed gamma rays, per energy bin.

Energy Resolution

The energy resolution gives an indication of the goodness of the energy reconstruction and is defined as the standard deviation of the Gaussian function which fits the peak of the $(E_{est} - E_{true})/E_{true}$ distribution, where E_{est} is the estimated particle energy and E_{true} is the true one.

Sensitivity

The sensitivity is the most important IRF, since it measures the overall performance of the array. It is the most used quantity to compare different telescopes.

The sensitivity is defined as the minimum gamma-ray flux that an observed point-like source should emit to allow a detection of 5 standard deviations above the background in a 50 hour observation; the significance is calculated with the Li & Ma formula [127]. In addition, per energy bin, we require a gamma-ray excess higher than 10 and at least 5 % of the residual background. The first condition is relevant when the sensitivity is dominated by the signal (almost background free but low statistics), while the second one is the dominant condition in the low energy range, where the background rate is still high and the excess should not be due to fluctuation of the background.

5.3 Pipeline Prototype for CTA: *protopipe*

As a comparison, both the nominal LST simulations and the LST SiPM-based camera simulations are analysed with *protopipe*, the prototype pipeline for CTA [128]. Also this pipeline is based on *ctapipe* and, as *magic-cta-pipe*, it is under development.

5.3.1 Pipeline Overview

The pipeline workflow is depicted in Figure 5.10. After the stereo parameters and hillas reconstruction, part of the Monte Carlo gamma point events (usually 20 % of the total) are used to evaluate the energy model with an “AdaBoost” regressor. Another set of the Monte Carlo gamma point events (usually 20 % of the total) and a set of proton events (usually 40 % of the total) are used to build a classifier model, with a random forest method. These models are applied on the remaining dataset (60 % of the simulated gamma point events, 60 % of simulated proton events and all the simulated electron events). The arrival direction is obtained by intersecting the hillas planes. The IRFs are evaluated using the *pyirf* package, similarly to *magic-cta-pipe*. More information about the pipeline and on how it works can be found at [128].

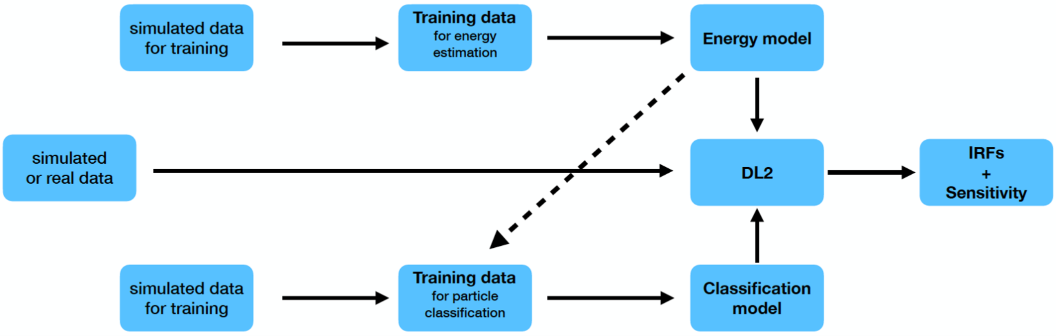

Figure 5.10: Workflow of the *protopipe* pipeline

5.4 Comparison Between the Two Pipelines

Now that we have introduced the two pipelines, we use them to analyse nominal LST Monte Carlo simulations.

The effective area, angular resolution, energy resolution and sensitivity of the nominal LSTs array analysed with *magic-cta-pipe* and with *protopipe* are shown in Figure 5.11a, 5.11b and 5.11d respectively. Concerning the quality cuts, for *magic-cta-pipe* events with a *leakage 1* higher than 0.15 or an intensity smaller than 50 photoelectrons are discarded. For *protopipe*, instead, events are considered if they have an intensity greater than 50 photoelectrons and an ellipticity between 0.1 and 0.6 (the ellipticity is defined as the ratio between width and length).

We immediately observe that there are great differences between the results obtained with the two pipelines. The effective area obtained with *protopipe* is slightly lower than the one obtained with *magic-cta-pipe*; on the other hand, the angular resolution is a bit better. Concerning the energy resolution, *magic-cta-pipe* offers a better performance when compared to *protopipe*. The sensitivity produced by *protopipe* worsen at lower energy, when compared to the *magic-cta-pipe* one: this is a known *protopipe* problem[1].

Clearly all these differences indicate that both pipelines are not completely reliable. In the comparison between nominal and SiPM-based LSTs, we will focus our attention on relative improvements, always bearing in mind that we must consider all these results as preliminary.

---

[1] Private communication with *protopipe* developers

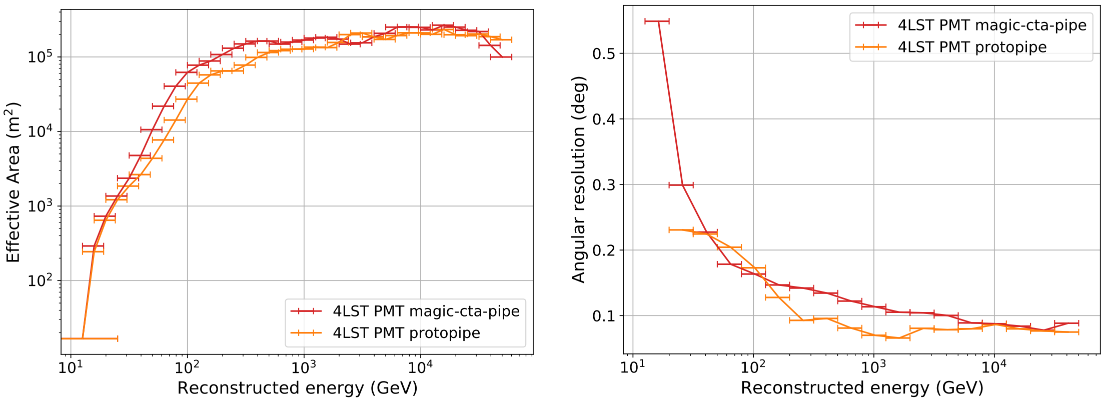

(a) (b)

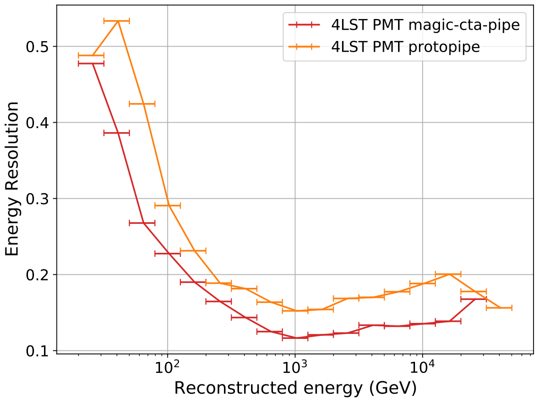

(c)

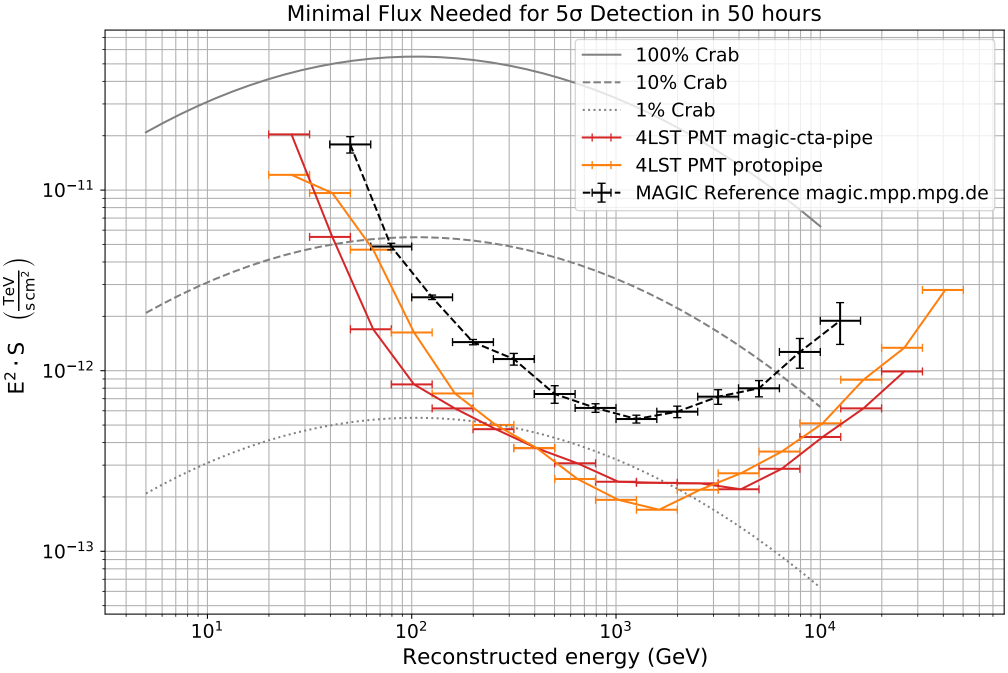

(d)

Figure 5.11: IRFs of the nominal LSTs array analysed with *magic-cta-pipe* and with *protopipe*: Effective area (a), angular resolution (b), energy resolution (c) and sensitivity (d)

5.5 Comparison Between Nominal and SiPM-Based LSTs Simulations

5.5.1 Analysis with *magic-cta-pipe*

The comparisons between the effective area, angular resolution, energy resolution and sensitivity of a four nominal LST array and a four LST SiPM-based camera array is shown in Figure 5.12a, 5.12b, 5.12c and 5.12d respectively.

In both cases it is required that the event triggered at least two telescopes. Concerning the quality cuts, events with a *leakage 1* higher than 0.15 or an intensity smaller than 50 photoelectrons are discarded.

No big differences are visible in the effective area plot. The angular resolution slightly benefits from the finer pixelation of the LST SiPM-based camera, although not in the whole considered energy range. A small improvement is also visible in the energy resolution. Concerning the sensitivities, the LST SiPM-based camera offers slightly better performances when compared to the PMT one.

5.5.2 Analysis with *protopipe*

The LST SiPM-based camera Monte Carlo simulations are analysed also with *protopipe*, using the same quality cuts described in the previous section: events are considered if they have an intensity greater than 50 photoelectrons and an ellipticity between 0.1 and 0.6. The obtained results (visible in Figure 5.13) are quite similar to the one obtained with *magic-cta-pipe*; in particular, we see a small improvement in the sensitivity.

5.5.3 Comparison Between the Two Analyses

In Figure 5.14 it is shown the ratio between the 4 LSTs SiPM-based camera sensitivity and the nominal camera one. Both analyses agree that the LST SiPM-based camera offers a slight improvement in performance than the nominal one, if they are analysed with the same pipeline.

However, we expect bigger performance improvement. Indeed, the analysis has not been optimized for the SiPM-based camera: the higher granularity of their images allows more complex analysis than the simple Hillas parametrization and random forests approach, with which its potential is not fully exploited. To maximize the benefits of smaller pixels, Deep Learning techniques are under study. In addition, for these simulations the electronics and the trigger of the nominal LSTs have been kept, while the LST Advanced camera will have a more efficient trigger and readout electronics. By adding a filter on the focal plane we could expect a performance improvement, since we would reduce the integrated night sky background. With this setup, on the other hand, we would reduce the integrated Cherenkov signal, resulting in a lower signal with the same number of incident photons, thus worsening the performance. We will therefore carefully study whether or not it is worthwhile to add a filter on the focal plane.

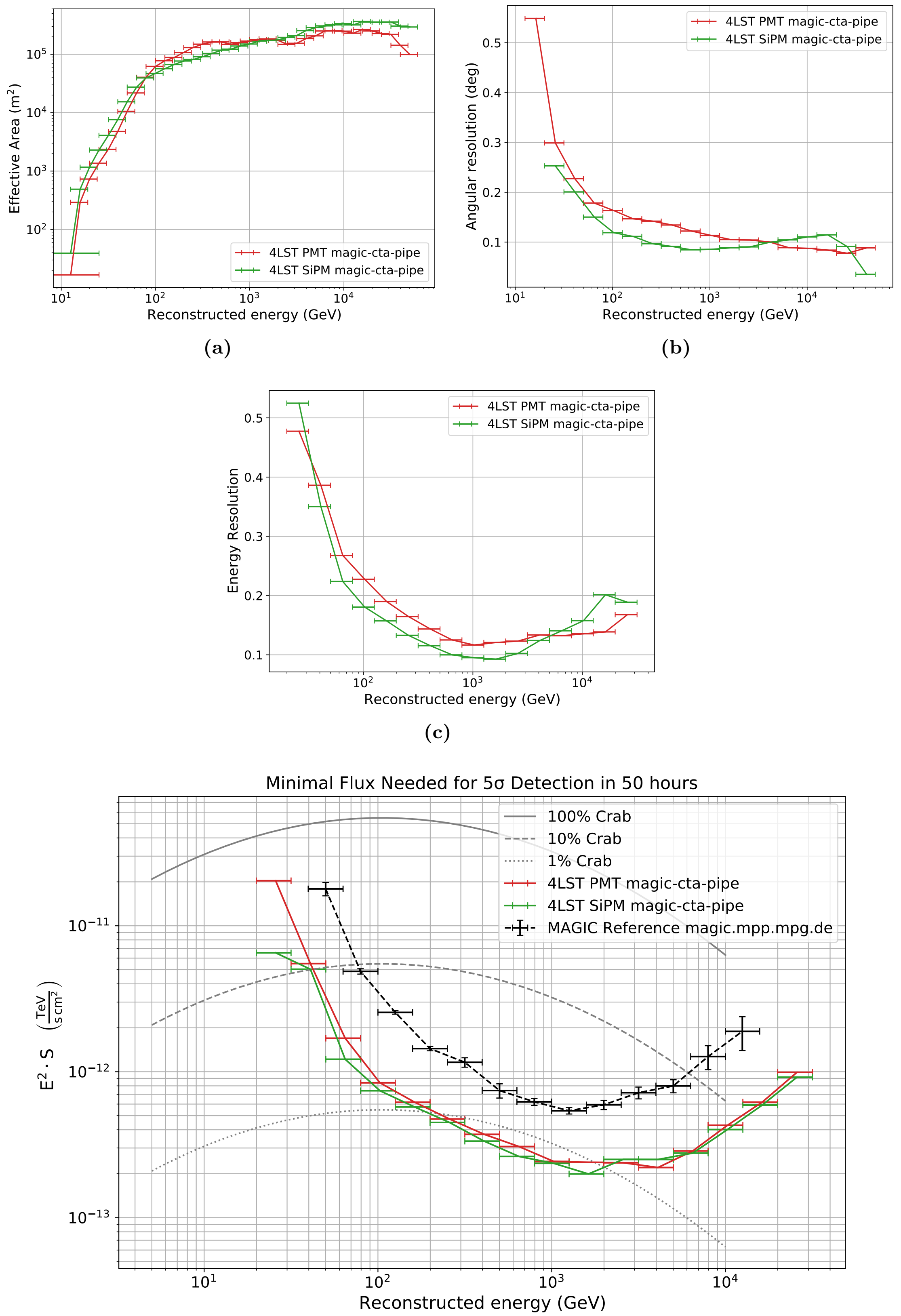

(a) **(b)**

(c)

(d)

Figure 5.12: IRFs of a four SiPM-based camera LSTs array compared to the nominal LSTs array: Effective area (a), angular resolution (b), energy resolution (c) and sensitivity (d)

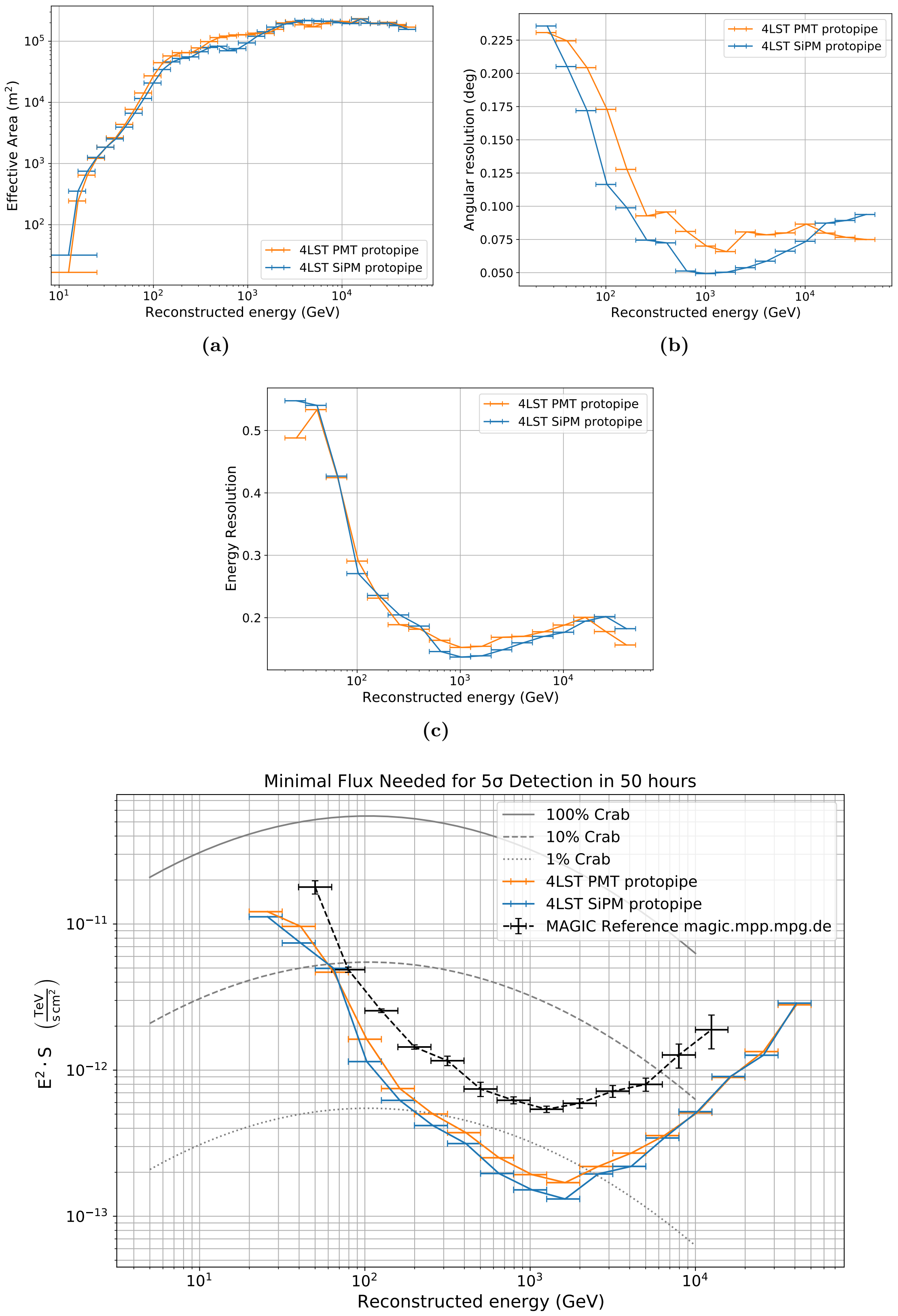

(a)

(b)

(c)

(d)

Figure 5.13: IRFs of a four SiPM-based camera LSTs array compared to the nominal LSTs array: Effective area (a), angular resolution (b), energy resolution (c) and sensitivity (d)

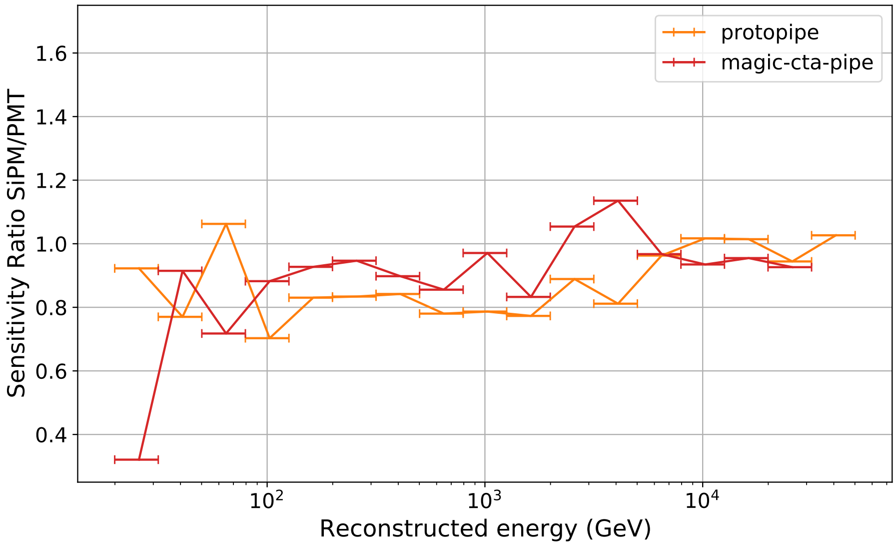

Figure 5.14: Sensitivity ratio of a four SiPM-based camera LSTs array compared to the nominal LSTs array, analysed both with *magic-cta-pipe* and *protopipe*

Chapter 6

Conclusions and Future Prospects

In this thesis we evaluated the possibility of using SiPMs in the focal plane of the Large Size Telescopes of the Cherenkov Telescope Array. A working light detector has been developed and built, starting from the study of the problem up to the realization of the detector itself. All the work needed, from the circuit design to the realization of the PCBs, was carried out by the Author.

The development was focused to emphasize the main advantages of SiPMs over PMTs for our application, i.e. their robustness and tolerance to high illumination levels. Indeed, with these sensors it is possible to observe in illumination conditions that are not suitable for traditional photomultipliers, thus leading to an increase in the duty cycle of the experiment. In addition, their robustness would improve the reliability of the telescope: indeed, exposing the PMTs to daylight, even with their high voltage off, can seriously damage them. All the solutions studied and developed are clearly suitable for any SiPM applications characterized by a high background noise and/or requiring the use of a medium-large pixel.

Since there is a technological limit to the single SiPM size, to cover a large area it is necessary to sum the signals from different sensors; this task must be carried out by a specific circuit. The choice of the MUSIC ASIC proved to be excellent for this purpose, in particular for the possibility of summing and shaping the SiPM signals within the same chip, reaching very short signals with the used FBK SiPMs. This is fundamental for our application, where high night sky background rate places constraints on the signal duration: indeed, the longer the signal, the higher the trigger threshold to be set in order not to be completely dominated by the background noise. However, like all electronic circuits, the MUSIC ASIC cannot support high current levels without being damaged. To make the most of the SiPM features, it is therefore necessary to include protection for the electronics. The most trivial solution to this problem is to use a protection resistor on the SiPM bias line: this approach is very simple and not space-consuming, but has the huge disadvantage of making the bias voltage dependent on the current flowing into the SiPM. Therefore, an alternative solution has been designed and tested: a simple two-BJTs active current limiter. This solution proved to be excellent: thanks to this circuit it is possible to bias the sensor at the desired operating voltage regardless of the current flowing into it. In addition, it is not enough to make sure that the pixel does not get damaged in high illumination conditions, but it is necessary to be able to see signals also in a high background environment. To solve this problem, the solution was to add an AC filter on the SiPM output signals. In the DC approach instead, as the background increases, the pixel would soon go into saturation, thus becoming unusable. Since most of the SiPM characteristics depend on its breakdown voltage, which in turn depends on the temperature, it is necessary to strictly monitor the sensor temperature, in order to properly correct the bias voltage. This task is accomplished by a digital thermometer in thermal contact with the SiPM array. A regulator and a current and voltage monitor are used to set and keep the sensor bias voltage at the desired value. The module is controlled by a slow control software, written by the Author, based on the one developed for the nominal LST module.

Many measurements have been carried out on the SiPM pixel, to study the slow control effectiveness, the possibility of operating in a high light background environment, up to the calibration of the pixel itself. It has been shown that the detector can work even in a very high light background environment, and covers the same dynamics as the PMT pixel.

Regarding the results obtained with Monte Carlo simulations, it has been shown that there could be a slight improvement in replacing the nominal PMT cameras with SiPM-based ones. However, the results reported here are preliminary, and more study is needed before any conclusions can be drawn. Results are however encouraging; in addition, we expect that more complex analysis, based on Deep Learning methods, could benefit the higher granularity of the images. This, combined with the other well-known SiPM advantages, among all their robustness and tolerance to high background light, make it desirable to continue the development of a SiPM camera for the LSTs. The use of these solid state sensors would indeed allow an increase in duty cycle, and their robustness goes well with an observatory that will be as automatic as possible.

In the LST collaboration an alternative to the current camera is therefore under study: the goal is to develop an “Advanced” camera achieving better performance than the current one. This new camera will host SiPMs on its focal plane and the electronics design will follow a fully digital approach, in order to maximize its flexibility and allow us to study different trigger solutions, which could lower the energy threshold. This camera can be used in the southern LSTs or can be an upgrade of the northern ones. The development is ongoing, and many aspects still need to be optimized, such as pixel size, maximum signal duration, trigger strategies, and so on. The solutions developed and described in this work could be useful for the realization of this novel camera.

Appendix A

SiPM Pixel Configuration Commands

As described in chapter 4, the MUSIC section of the SiPM Pixel Main Board is based on the circuit of the MUSIC MiniBoard, kindly made available by the developers. The MUSIC ASIC is controlled by an ATmega328P-AU microcontroller which runs the MUSIC MiniBoard [100] firmware.

To set the microcontroller, connect with an USB to UART adapter the SiPM pixel to a computer running the `mini_music.exe` software, the same one that controls the MUSIC MiniBoard. Below the main commands are described, for a more detailed discussion refer to [100].

The first step is to load the normal operation configuration file, with the following command:

```
mini_music.exe config_file -f <file_name>
```

An example of a MUSIC configuration file can be found in A.1. With this file the following settings are uploaded:

- Enable six channels (from 0 to 5)
- Sum the six enabled channels
- High trans-impedance configuration
- Pole-zero configuration:
  - $R_{lad} = 7$
  - $C_{lad} = 31$
  - Low Attenuation ON

The next step is to calibrate the offset of the analog outputs to maximize the rail-to-rail voltage swing:

```
mini_music.exe vdc_calib
```

Now the microcontroller has the correct settings. This step is not necessary if the configuration files already contains the correct settings for the MUSIC ASIC (each chip has its own).

In order for these settings to be loaded automatically every time the module is switched on, it is necessary to save them in the microcontroller's non-volatile EEPROM memory. To do so, run the following command:

```
mini_music.exe save_to_eeprom
```

For future reference, save the configuration on a local file:

```
mini_music.exe show_config -f <file_name>
```

To enter the calibration mode, copy the file saved during the last step, and do the following modifications in the channel 7 section:

- `EN_CH[7]      = 1`
- `EN_PZ_COMP[7] = 0`

In this way also the last channel is enabled, and the pole-zero compensation is skipped for its output. Then load the file as before (no need to save it in the EEPROM). Clearly, the value assigned to `EN_PZ_COMP[7]` does not matter for normal operating mode.

Listing A.1: MUSIC configuration file example

```
############################################################
##############   MiniMUSIC CALIBRATION FILE   ##############
############################################################

#File Version          : 1
#MiniMUSIC Chip ID     : 0

############################################################
# MiniMUSIC Bias Registers Parameters:
############################################################

LOW_AT_LAD     = 1
VDC_LG         = 0
VDC_HG         = 117
VDC_CH         = 124
VCM            = 144
IB_COMP        = 3
VBG_ADJ        = 6
IB_OP_SE       = 3
IB_AB_SE       = 15
!FASTOR_EN     = 0
HL_SUM         = 3
EN_DIFF_DRV_HL = 3
EN_BYPASS_HL   = 0
EN_PZ_HL       = 3
EN_CH_SUM      = 63
V_LIM          = 38
CAP_PZ         = 31
RLAD_PZ        = 7
IB_AB_DIFF     = 15
IB_OP_DIFF     = 3
IB_PAIR        = 4
IB_AB_PZ       = 4
IB_IN          = 25
IB_PZ_BUF      = 3

############################################################
#Channel #0 Parameters:
############################################################

EN_CH[0]      = 1
```

```
DIS_IN[0]      = 0
V_OFFSET[0]    = 255
HL[0]          = 1
EN_CH_SW[0]    = 1
EN_PZ[0]       = 1
EN_DRV_SE[0]   = 1
V_TH[0]        = 120
HL_COMP[0]     = 1
EN_COMP_SW[0] = 0
EN_PZ_COMP[0] = 1

############################################################
#Channel #1 Parameters:
############################################################

EN_CH[1]       = 1
DIS_IN[1]      = 0
V_OFFSET[1]    = 255
HL[1]          = 1
EN_CH_SW[1]    = 1
EN_PZ[1]       = 1
EN_DRV_SE[1]   = 1
V_TH[1]        = 120
HL_COMP[1]     = 1
EN_COMP_SW[1] = 0
EN_PZ_COMP[1] = 1

############################################################
#Channel #2 Parameters:
############################################################

EN_CH[2]       = 1
DIS_IN[2]      = 0
V_OFFSET[2]    = 255
HL[2]          = 1
EN_CH_SW[2]    = 1
EN_PZ[2]       = 1
EN_DRV_SE[2]   = 1
V_TH[2]        = 120
HL_COMP[2]     = 1
EN_COMP_SW[2] = 0
EN_PZ_COMP[2] = 1

############################################################
#Channel #3 Parameters:
############################################################

EN_CH[3]       = 1
DIS_IN[3]      = 0
V_OFFSET[3]    = 255
HL[3]          = 1
EN_CH_SW[3]    = 1
EN_PZ[3]       = 1
EN_DRV_SE[3]   = 1
V_TH[3]        = 120
HL_COMP[3]     = 1
EN_COMP_SW[3] = 0
EN_PZ_COMP[3] = 1
```

```
############################################################
#Channel #4 Parameters:
############################################################

EN_CH[4]       = 1
DIS_IN[4]      = 0
V_OFFSET[4]    = 255
HL[4]          = 1
EN_CH_SW[4]    = 1
EN_PZ[4]       = 1
EN_DRV_SE[4]   = 1
V_TH[4]        = 120
HL_COMP[4]     = 1
EN_COMP_SW[4] = 0
EN_PZ_COMP[4] = 1

############################################################
#Channel #5 Parameters:
############################################################

EN_CH[5]       = 1
DIS_IN[5]      = 0
V_OFFSET[5]    = 255
HL[5]          = 1
EN_CH_SW[5]    = 1
EN_PZ[5]       = 1
EN_DRV_SE[5]   = 1
V_TH[5]        = 120
HL_COMP[5]     = 1
EN_COMP_SW[5] = 0
EN_PZ_COMP[5] = 1

############################################################
#Channel #6 Parameters:
############################################################

EN_CH[6]       = 0
DIS_IN[6]      = 0
V_OFFSET[6]    = 255
HL[6]          = 1
EN_CH_SW[6]    = 1
EN_PZ[6]       = 1
EN_DRV_SE[6]   = 1
V_TH[6]        = 120
HL_COMP[6]     = 1
EN_COMP_SW[6] = 0
EN_PZ_COMP[6] = 1

############################################################
#Channel #7 Parameters:
############################################################

EN_CH[7]       = 0
DIS_IN[7]      = 0
V_OFFSET[7]    = 255
HL[7]          = 1
EN_CH_SW[7]    = 1
```

```
EN_PZ[7]        = 0
EN_DRV_SE[7]    = 1
V_TH[7]         = 120
HL_COMP[7]      = 1
EN_COMP_SW[7]   = 0
EN_PZ_COMP[7]   = 1
```

Appendix B

CaCoSiPM Configuration File

An example of a CaCoSiPM configuration file can be found below. See section 4.3.16 for the description of the various settings.

Listing B.1: CaCoSiPM configuration file example

```
script_dir: ’/home/cta-sipm/DRAGON/DRAGON_QCV7.04_DD/QCV7.04_Mod/’
log_dir: ’./log/’
IP: ’192.168.1.5’

R_ac: 16.67

V_MUSIC: 0

HV_sens: 0.050
I_MAX: 10
safe_DAC: 500
fix_DAC: [0, 0, 0, 0, 0, 0, 0]
max_DAC: 3050
k_DAC_HV: 85

wait_time: 1
timeout: 5

Def_Temp: 20

OV: 6

Vbd: [26.30, 26.34, 26.96, 27.06, 27.10, 27.05, 27.09]

dVbddT: 0.027

popt_HV:
  ch1: [-19.607980451778346, -62.07144842464561]
  ch2: [-19.304363425445917, -78.23377351054692]
  ch3: [-19.628543540827682, -63.71479199847292]
  ch4: [-19.296674379589643, -72.40465465547678]
  ch5: [-19.36134368477181, -75.76507834890245]
  ch6: [-19.340011574137517, -69.97481053040487]
  ch7: [-19.53060517616665, -63.034995311626815]

popt_I:
  ch1: [-68.15862083348418, -23.82266250005419]
  ch2: [-67.83670833348347, -26.77902500006066]
  ch3: [-67.74153750014993, -84.93371250018747]
```

```
  ch4: [-67.70248333348319, -68.81192500015229]
  ch5: [-68.25189583348438, 7.215162500013487]
  ch6: [-68.17037499498, -27.742487530774206]
  ch7: [-68.40887083333767, 38.43953749997152]
```

Acknowledgements

I thank my supervisor Professor Andrea Chiavassa and my co-supervisor Doctor Federico Di Pierro for giving me the opportunity to carry out this work and for their strong help and support.

I would also like to acknowledge Marco Aglietta for helping me in the realization of the laboratory setup and for his valuable suggestions. I am also grateful to Silvano Gallian for the assembly of the various PCB prototypes and more generally for his great help in all the practical issues that have been faced during the construction of the detector. I thank Daniele Corti for his valuable advices regarding high-speed PCB design. I want to express my gratitude to Takayuki Saito and to Seiya Nozaki for giving me relevant advices for the development of slow control software, and to Dirk Hoffmann and to Julien Houles for their help in setting up the LST data acquisition system. I also thank Sergio Gomez, David Gascon, Eduardo Picatoste and Joan Mauricio for assisting me in the configuration of the MUSIC ASIC and in its implementation in the detector PCB. I would like to thank Alessio Berti for helping me in the software analysis development and in overcoming software problems.

I thank my parents, my friends and all the people who have always been there by my side.

Bibliography

[1] Martin Lemoine and Guy Pelletier. “On the origin of very-high-energy photons in astrophysics: A short introduction to acceleration and radiation physics”. In: *Comptes Rendus Physique* 16.6-7 (Aug. 2015), pp. 628–640. DOI: `10.1016/j.crhy.2015.08.012`.

[2] M. S. Longair. *High Energy Astrophysics.* Cambridge University Press, 2011. ISBN: 9781139494540.

[3] MAGIC Collaboration et al. “Teraelectronvolt emission from the γ-ray burst GRB 190114C”. In: *Nature* 575.7783 (Nov. 2019), pp. 455–458. DOI: `10.1038/s41586-019-1750-x`. arXiv: `2006.07249 [astro-ph.HE]`.

[4] Meng Su and Christopher van Eldik. “Gamma rays from the Galactic Centre region”. In: *Comptes Rendus Physique* 16.6 (2015). Gamma-ray astronomy / Astronomie des rayons gamma, pp. 686–703. ISSN: 1631-0705. DOI: `https://doi.org/10.1016/j.crhy.2015.09.001`.

[5] F. A. Aharonian, L. O’C. Drury, and H. J. Voelk. “GeV/TeV gamma-ray emission from dense molecular clouds overtaken by supernova shells”. In: *Astronomy and Astrophysics* 285 (May 1994), pp. 645–647.

[6] R. U. Abbasi et al. “First Observation of the Greisen-Zatsepin-Kuzmin Suppression”. In: *Physical Review Letters* 100.10, 101101 (Mar. 2008), p. 101101. DOI: `10.1103/PhysRevLett.100.101101`. arXiv: `astro-ph/0703099 [astro-ph]`.

[7] J. Abraham et al. “Observation of the Suppression of the Flux of Cosmic Rays above 4×10^{19}eV”. In: *Physical Review Letters* 101.6, 061101 (Aug. 2008), p. 061101. DOI: `10.1103/PhysRevLett.101.061101`. arXiv: `0806.4302 [astro-ph]`.

[8] The Cherenkov Telescope Array Consortium. *Science with the Cherenkov Telescope Array.* 2017. arXiv: `1709.07997`.

[9] Eli Dwek and Frank Krennrich. “The extragalactic background light and the gamma-ray opacity of the universe”. In: *Astroparticle Physics* 43 (2013), pp. 112–133. ISSN: 0927-6505. DOI: `10.1016/j.astropartphys.2012.09.003`.

[10] Dieter Horns and Agnieszka Jacholkowska. “Gamma rays as probes of the Universe”. In: *Comptes Rendus Physique* 17.6 (2016), pp. 632–648. ISSN: 1631-0705. DOI: `10.1016/j.crhy.2016.04.006`.

[11] V. A. Acciari et al. “Bounds on Lorentz Invariance Violation from MAGIC Observation of GRB 190114C”. In: *Physical Review Letters* 125.2, 021301 (July 2020), p. 021301. DOI: `10.1103/PhysRevLett.125.021301`. arXiv: `2001.09728 [astro-ph.HE]`.

[12] H. Abdalla et al. “Sensitivity of the Cherenkov Telescope Array for probing cosmology and fundamental physics with gamma-ray propagation”. In: *Journal of Cosmology and Astroparticle Physics* 2021.2 (2021). DOI: `10.1088/1475-7516/2021/02/048`.

[13] R. D. Peccei and Helen R. Quinn. “CP conservation in the presence of pseudoparticles”. In: *Physical Review Letters* 38.25 (June 1977), pp. 1440–1443. DOI: `10.1103/PhysRevLett.38.1440`.

[14] Alessandro De Angelis, Giorgio Galanti, and Marco Roncadelli. “Relevance of axionlike particles for very-high-energy astrophysics”. In: *Physical Review D* 84.10, 105030 (Nov. 2011), p. 105030. DOI: `10.1103/PhysRevD.84.105030`. arXiv: `1106.1132 [astro-ph.HE]`.

[15] Glenn F. Knoll. *Radiation detection and measurement.* 4th. New York, NY: Wiley, 2010.

[16] M. J. Berger et al. *XCOM: Photon Cross Section Database (version 1.5).* National Institute of Standards and Technology, Gaithersburg, MD. 2021. DOI: `10.18434/T48G6X`. URL: `http://physics.nist.gov/xcom`.

[17] P.A. Zyla et al. “Review of Particle Physics”. In: *PTEP* 2020.8 (2020), p. 083C01. DOI: `10.1093/ptep/ptaa104`.

[18] Yung-Su Tsai. “Pair production and bremsstrahlung of charged leptons”. In: *Reviews of Modern Physics* 46.4 (Oct. 1974), pp. 815–851. DOI: `10.1103/RevModPhys.46.815`.

[19] Handel Davies, H. A. Bethe, and L. C. Maximon. “Theory of Bremsstrahlung and Pair Production. II. Integral Cross Section for Pair Production”. In: *Physical Review* 93.4 (Feb. 1954), pp. 788–795. DOI: `10.1103/PhysRev.93.788`.

[20] M. J. Berger and S. M. Seltzer. “Tables of Energy Losses and Ranges of Electrons and Positrons”. In: *Studies in Penetration of Charged Particles in Matter.* Jan. 1964, p. 205.

[21] Bruno Benedetto Rossi. *High-energy particles.* Prentice-Hall physics series. New York, NY: Prentice-Hall, 1952.

[22] V. Schoenfelder et al. “Instrument Description and Performance of the Imaging Gamma-Ray Telescope COMPTEL aboard the Compton Gamma-Ray Observatory”. In: *Astrophysical Journal Supplement* 86 (June 1993), p. 657. DOI: `10.1086/191794`.

[23] A. De Angelis et al. “Science with e-ASTROGAM. A space mission for MeV-GeV gamma-ray astrophysics”. In: *Journal of High Energy Astrophysics* 19 (Aug. 2018), pp. 1–106. DOI: `10.1016/j.jheap.2018.07.001`. arXiv: `1711.01265 [astro-ph.HE]`.

[24] W. B. Atwood et al. “The Large Area Telescope on the Fermi Gamma-Ray Space Telescope Mission”. In: *The Astrophysical Journal* 697.2 (June 2009), pp. 1071–1102. DOI: `10.1088/0004-637X/697/2/1071`. arXiv: `0902.1089 [astro-ph.IM]`.

[25] B. Bartoli et al. “The analog Resistive Plate Chamber detector of the ARGO-YBJ experiment”. In: *Astroparticle Physics* 67 (July 2015), pp. 47–61. DOI: `10.1016/j.astropartphys.2015.01.007`. arXiv: `1504.01510 [astro-ph.IM]`.

[26] A. U. Abeysekara et al. “Sensitivity of the high altitude water Cherenkov detector to sources of multi-TeV gamma rays”. In: *Astroparticle Physics* 50 (Dec. 2013), pp. 26–32. DOI: `10.1016/j.astropartphys.2013.08.002`. arXiv: `1306.5800 [astro-ph.HE]`.

[27] V. Marandon, A. Jardin-Blicq, and H. Schoorlemmer. “Latest news from the HAWC outrigger array”. In: *36th International Cosmic Ray Conference (ICRC2019).* Vol. 36. International Cosmic Ray Conference. July 2019, 736, p. 736. arXiv: `1908.07634 [astro-ph.IM]`.

[28] Miguel A. Mostafá. “The High-Altitude Water Cherenkov Observatory”. In: *Brazilian Journal of Physics* 44.5 (Oct. 2014), pp. 571–580. DOI: `10.1007/s13538-014-0225-7`. arXiv: `1310.7237 [astro-ph.HE]`.

[29] Zhen Cao et al. “Ultrahigh-energy photons up to 1.4 petaelectronvolts from 12 γ-ray Galactic sources”. In: *Nature* 594.7861 (Jan. 2021), pp. 33–36. DOI: `10.1038/s41586-021-03498-z`.

[30] Petra Huentemeyer et al. “The Southern Wide-Field Gamma-Ray Observatory (SWGO): A Next-Generation Ground-Based Survey Instrument”. In: *Bulletin of the American Astronomical Society.* Vol. 51. Sept. 2019, 109, p. 109. arXiv: `1907.07737 [astro-ph.IM]`.

[31] Walter Heitler. *The Quantum Theory of Radiation.* Monographs on Physics. Oxford University Press, 1954.

[32] J. Matthews. “A Heitler model of extensive air showers”. In: *Astroparticle Physics* 22.5-6 (Jan. 2005), pp. 387–397. DOI: `10.1016/j.astropartphys.2004.09.003`.

[33] Eve Curie. *Madame Curie translated by Vincent Sheean.* William Heineman Ltd, 1938.

[34] Mallet L. “The ultra-violet radiation of substances subjected to γ-rays”. In: (1929).

[35] Pavel Cherenkov. “Visible luminescence of pure liquids under the influence of γ-radiation”. In: *Dokl. Akad. Nauk SSSR* 2.8 (1934), pp. 451–454. DOI: `10.3367/UFNr.0093.196710n.0385`.

[36] P. M. S. Blackett. “A possible contribution to the night sky from the Cerenkov radiation emitted by cosmic rays”. In: *The Emission Spectra of the Night Sky and Aurorae.* International Conference held in London, July 1947. Ed. by The Physical Society. 1948, p. 34.

[37] W. Galbraith and J.V. Jelley. “Light Pulses from the Night Sky associated with Cosmic Rays”. In: *Nature* 171.4347 (Feb. 1953), pp. 349–350. ISSN: 1476-4687. DOI: `10.1038/171349a0`.

[38] E. Lorenz and R. Wagner. “Very-high energy gamma-ray astronomy. A 23-year success story in high-energy astroparticle physics”. In: *European Physical Journal H* 37.3 (Aug. 2012), pp. 459–513. DOI: `10.1140/epjh/e2012-30016-x`. arXiv: `1207.6003 [physics.hist-ph]`.

[39] Trevor C. Weekes. “The Atmospheric Cherenkov Technique in Very High Energy Gamma-Ray Astronomy”. In: *Space Science Reviews* 75.1-2 (Jan. 1996), pp. 1–15. DOI: `10.1007/BF00195020`.

[40] A. M. Hillas. “Cerenkov Light Images of EAS Produced by Primary Gamma Rays and by Nuclei”. In: *19th International Cosmic Ray Conference (ICRC19), Volume 3.* Vol. 3. International Cosmic Ray Conference. Aug. 1985, p. 445.

[41] T. C. Weekes et al. “Observation of TeV Gamma Rays from the Crab Nebula Using the Atmospheric Cerenkov Imaging Technique”. In: *Astrophysical Journal* 342 (July 1989), p. 379. DOI: `10.1086/167599`.

[42] The VERITAS Collaboration. *VERITAS Website.* Online; accessed 09 November 2021. URL: `https://veritas.sao.arizona.edu/`.

[43] T. C. Weekes et al. “The Very Energetic Radiation Imaging Telescope Array System (VERITAS)”. In: *AIP Conference Proceedings* 510.1 (2000), pp. 637–641. DOI: `10.1063/1.1303279`.

[44] The HESS Collaboration. *HESS Website.* Online; accessed 09 November 2021. URL: `https://www.mpi-hd.mpg.de/hfm/HESS/`.

[45] Chia-Chun Lu and H. E. S. S. Collaboration. “Improvement on the H.E.S.S. Angular Resolution by the Disp Method”. In: *International Cosmic Ray Conference*. Vol. 33. International Cosmic Ray Conference. Jan. 2013, p. 3147. arXiv: `1310.1200 [astro-ph.IM]`.

[46] NASA, Wikipedia Commons. *Atmospheric electromagnetic transmittance or opacity*. Online; accessed 09 November 2021. 2007. URL: `https://commons.wikimedia.org/wiki/File:Atmospheric_electromagnetic_opacity.svg`.

[47] M. Doering et al. “Measurement of the Cherenkov light spectrum and of the polarization with the HEGRA-IACT-system”. In: *arXiv e-prints*, astro-ph/0107149 (July 2001), astro–ph/0107149. arXiv: `astro-ph/0107149 [astro-ph]`.

[48] The CTA Consortium. *CTA Website*. Online; accessed 09 November 2021. URL: `https://www.cta-observatory.org/`.

[49] *TeVCat*. Online; accessed 09 November 2021. URL: `http://tevcat.uchicago.edu/`.

[50] B. S. Acharya et al. “Introducing the CTA concept”. In: *Astroparticle Physics* 43 (Mar. 2013), pp. 3–18. DOI: `10.1016/j.astropartphys.2013.01.007`.

[51] B. P. Abbott et al. “Observation of Gravitational Waves from a Binary Black Hole Merger”. In: *Physical Review Letters* 116.6, 061102 (Feb. 2016), p. 061102. DOI: `10.1103/PhysRevLett.116.061102`. arXiv: `1602.03837 [gr-qc]`.

[52] B. P. Abbott et al. “Astrophysical Implications of the Binary Black-hole Merger GW150914”. In: *The Astrophysical Journal Letters* 818.2, L22 (Feb. 2016), p. L22. DOI: `10.3847/2041-8205/818/2/L22`. arXiv: `1602.03846 [astro-ph.HE]`.

[53] B. P. Abbott et al. “GW151226: Observation of Gravitational Waves from a 22-Solar-Mass Binary Black Hole Coalescence”. In: *Physical Review Letters* 116.24, 241103 (June 2016), p. 241103. DOI: `10.1103/PhysRevLett.116.241103`. arXiv: `1606.04855 [gr-qc]`.

[54] G. Bertone, D. Hooper, and J. Silk. “Particle dark matter: evidence, candidates and constraints.” In: *Physics Reports* 405 (Jan. 2004), pp. 279–390.

[55] P. Cushman et al. “Snowmass CF1 Summary: WIMP Dark Matter Direct Detection”. In: *arXiv e-prints*, arXiv:1310.8327 (Oct. 2013), arXiv:1310.8327. arXiv: `1310.8327 [hep-ex]`.

[56] M. Cahill-Rowley et al. “Complementarity and Searches for Dark Matter in the pMSSM”. In: *arXiv e-prints*, arXiv:1305.6921 (May 2013), arXiv:1305.6921. arXiv: `1305.6921 [hep-ph]`.

[57] M. Ackermann et al. “Searching for Dark Matter Annihilation from Milky Way Dwarf Spheroidal Galaxies with Six Years of Fermi Large Area Telescope Data”. In: *Physical Review Letters* 115.23, 231301 (Dec. 2015), p. 231301. DOI: `10.1103/PhysRevLett.115.231301`. arXiv: `1503.02641 [astro-ph.HE]`.

[58] H. Abdallah et al. “Search for Dark Matter Annihilations towards the Inner Galactic Halo from 10 Years of Observations with H.E.S.S.” In: *Physical Review Letters* 117.11, 111301 (Sept. 2016), p. 111301. DOI: `10.1103/PhysRevLett.117.111301`. arXiv: `1607.08142 [astro-ph.HE]`.

[59] Planck Collaboration et al. “Planck 2015 results. XIII. Cosmological parameters”. In: *Astronomy & Astrophysics* 594, A13 (Sept. 2016), A13. DOI: `10.1051/0004-6361/201525830`. arXiv: `1502.01589 [astro-ph.CO]`.

[60] IceCube Collaboration et al. "Multimessenger observations of a flaring blazar coincident with high-energy neutrino IceCube-170922A". In: *Science* 361.6398, eaat1378 (July 2018), eaat1378. DOI: `10.1126/science.aat1378`. arXiv: `1807.08816 [astro-ph.HE]`.

[61] MAGIC Collaboration et al. "Observation of inverse Compton emission from a long γ-ray burst". In: *Nature* 575.7783 (Nov. 2019), pp. 459–463. DOI: `10.1038/s41586-019-1754-6`. arXiv: `2006.07251 [astro-ph.HE]`.

[62] John M. Davies and Eugene S. Cotton. "Design of the quartermaster solar furnace". In: *Solar Energy* 1.2-3 (Apr. 1957), pp. 16–22. DOI: `10.1016/0038-092X(57)90116-0`.

[63] Karl Schwarzschild. "Untersuchungen zur geometrischen Optik II". In: *Astronomische Mitteilungen der Universitaets-Sternwarte zu Goettingen* 10 (Jan. 1905), p. 1.

[64] A Couder. "Sur un type nouveau de télescope photographique". In: *Comptes Rendus* 183 (1926), pp. 1276–1279.

[65] J. Cortina and M. Teshima. "Status of the Cherenkov Telescope Array Large Size Telescopes". In: *34th International Cosmic Ray Conference (ICRC2015)*. Vol. 34. International Cosmic Ray Conference. July 2015, 943, p. 943. arXiv: `1508.06438 [astro-ph.IM]`.

[66] K. Kobayashi A. Ghassemi K. Sato. *MPPC Characterization, Hamamatsu Technical Note.*

[67] Simon M. Sze and Kwok K. Ng. *Physics of Semiconductor Devices.* Wiley, 2006. ISBN: 9780470068304.

[68] Fabio Acerbi and Stefan Gundacker. "Understanding and simulating SiPMs". In: *Nuclear Instruments and Methods in Physics Research A* 926 (May 2019), pp. 16–35. DOI: `10.1016/j.nima.2018.11.118`.

[69] Massimo Mazzillo et al. "Electro-Optical Performances of p-on-n and n-on-p Silicon Photomultipliers". In: *IEEE Transactions on Electron Devices* 59.12 (Dec. 2012), pp. 3419–3425. DOI: `10.1109/TED.2012.2218250`.

[70] Adam Nepomuk Otte et al. "Characterization of three high efficiency and blue sensitive silicon photomultipliers". In: *Nuclear Instruments and Methods in Physics Research A* 846 (Feb. 2017), pp. 106–125. DOI: `10.1016/j.nima.2016.09.053`. arXiv: `1606.05186 [physics.ins-det]`.

[71] A. N. Otte et al. "A measurement of the photon detection efficiency of silicon photomultipliers". In: *Nuclear Instruments and Methods in Physics Research A* 567.1 (Nov. 2006), pp. 360–363. DOI: `10.1016/j.nima.2006.05.145`.

[72] Roger Newman. "Visible Light from a Silicon p-n Junction". In: *Physical Review* 100.2 (Oct. 1955), pp. 700–703. DOI: `10.1103/PhysRev.100.700`.

[73] A. L. Lacaita et al. "On the bremsstrahlung origin of hot-carrier-induced photons in silicon devices". In: *IEEE Transactions on Electron Devices* 40.3 (Mar. 1993), pp. 577–582. DOI: `10.1109/16.199363`.

[74] Patrick Eckert et al. "Characterisation studies of silicon photomultipliers". In: *Nuclear Instruments and Methods in Physics Research A* 620.2-3 (Aug. 2010), pp. 217–226. DOI: `10.1016/j.nima.2010.03.169`. arXiv: `1003.6071 [physics.ins-det]`.

[75] *LTspice®*. Analog Devices.

[76] D. Marano et al. "Silicon Photomultipliers Electrical Model Extensive Analytical Analysis". In: *IEEE Transactions on Nuclear Science* 61.1 (Feb. 2014), pp. 23–34. DOI: `10.1109/TNS.2013.2283231`.

[77] H. Anderhub et al. “Design and operation of FACT - the first G-APD Cherenkov telescope”. In: *Journal of Instrumentation* 8.6, P06008 (June 2013), P06008. DOI: `10.1088/1748-0221/8/06/P06008`. arXiv: `1304.1710 [astro-ph.IM]`.

[78] A. Biland et al. “Calibration and performance of the photon sensor response of FACT — the first G-APD Cherenkov telescope”. In: *Journal of Instrumentation* 9.10, P10012 (Oct. 2014), P10012. DOI: `10.1088/1748-0221/9/10/P10012`. arXiv: `1403.5747 [astro-ph.IM]`.

[79] C. R. Benn and S. L. Ellison. “Brightness of the night sky over La Palma”. In: *New Astronomy Reviews* 42.6-8 (Nov. 1998), pp. 503–507. DOI: `10.1016/S1387-6473(98)00062-1`. arXiv: `astro-ph/9909153 [astro-ph]`.

[80] C. Alispach et al. “Large scale characterization and calibration strategy of a SiPM-based camera for gamma-ray astronomy”. In: *Journal of Instrumentation* 15.11 (Nov. 2020), P11010. DOI: `10.1088/1748-0221/15/11/P11010`. arXiv: `2008.04716 [astro-ph.IM]`.

[81] E. J. Schioppa et al. “The SST-1M camera for the Cherenkov Telescope Array”. In: *arXiv e-prints*, arXiv:1508.06453 (Aug. 2015), arXiv:1508.06453. arXiv: `1508.06453 [astro-ph.IM]`.

[82] M. L. Knoetig et al. “FACT Long-Term Stability and Observations during Strong Moon Light”. In: *International Cosmic Ray Conference.* Vol. 33. International Cosmic Ray Conference. Jan. 2013, p. 1132. arXiv: `1307.6116 [astro-ph.IM]`.

[83] Riccardo Rando et al. “Silicon Photomultiplier Research and Development Studies for the Large Size Telescope of the Cherenkov Telescope Array”. In: *34th International Cosmic Ray Conference (ICRC2015).* Vol. 34. International Cosmic Ray Conference. July 2015, 940, p. 940. arXiv: `1508.07120 [astro-ph.IM]`.

[84] J. Biteau et al. “Performance of Silicon Photomultipliers for the Dual-Mirror Medium-Sized Telescopes of the Cherenkov Telescope Array”. In: *34th International Cosmic Ray Conference (ICRC2015).* Vol. 34. International Cosmic Ray Conference. July 2015, 963, p. 963. arXiv: `1508.06245 [astro-ph.IM]`.

[85] C. B. Adams et al. “Detection of the Crab Nebula with the 9.7 m prototype Schwarzschild-Couder telescope”. In: *Astroparticle Physics* 128, 102562 (Mar. 2021), p. 102562. DOI: `10.1016/j.astropartphys.2021.102562`. arXiv: `2012.08448 [astro-ph.IM]`.

[86] S. Lombardi et al. “First detection of the Crab Nebula at TeV energies with a Cherenkov telescope in a dual-mirror Schwarzschild-Couder configuration: the ASTRI-Horn telescope”. In: *Astronomy and Astrophysics* 634, A22 (Feb. 2020), A22. DOI: `10.1051/0004-6361/201936791`. arXiv: `1909.12149 [astro-ph.IM]`.

[87] R. White. “The Small-Sized Telescopes for the Southern Site of the Cherenkov Telescope Array”. In: *arXiv e-prints*, arXiv:2110.14527 (Oct. 2021), arXiv:2110.14527. arXiv: `2110.14527 [astro-ph.IM]`.

[88] A. Hahn et al. “Development of three silicon photomultiplier detector modules for the MAGIC telescopes for a performance comparison to PMTs”. In: *Nuclear Instruments and Methods in Physics Research A* 912 (Dec. 2018), pp. 259–263. DOI: `10.1016/j.nima.2017.11.071`.

[89] S. Masuda et al. “Development of the photomultiplier tube readout system for the first Large-Sized Telescope of the Cherenkov Telescope Array”. In: *34th International Cosmic Ray Conference (ICRC2015).* Vol. 34. International Cosmic Ray Conference. July 2015, 1003, p. 1003. arXiv: `1509.00548 [astro-ph.IM]`.

[90] A. Sanuy et al. “Wideband (500 MHz) 16 bit dynamic range current mode PreAmplifier for the CTA cameras (PACTA)”. In: *Journal of Instrumentation* 7.1 (Jan. 2012), p. C01100. DOI: `10.1088/1748-0221/7/01/C01100`.

[91] LST team for the CTA consortium. *Large Size Telescope Technical Design Report.* Tech. rep. LST-TDR/140408. CTA consortium, Apr. 2019.

[92] Takeshi Toyama et al. “Novel Photo Multiplier Tubes for the Cherenkov Telescope Array Project”. In: *International Cosmic Ray Conference.* Vol. 33. International Cosmic Ray Conference. Jan. 2013, p. 1178. arXiv: `1307.5463 [astro-ph.IM]`.

[93] D. Hadasch et al. “Development of Slow Control Boards for the Large Size Telescopes of the Cherenkov Telescope Array”. In: *arXiv e-prints*, arXiv:1509.01364 (Sept. 2015), arXiv:1509.01364. arXiv: `1509.01364 [astro-ph.IM]`.

[94] J. Adam et al. “The MEG detector for μ $^{+}{\rightarrow}$e^{+} γ decay search”. In: *European Physical Journal C* 73, 2365 (Apr. 2013), p. 2365. DOI: `10.1140/epjc/s10052-013-2365-2`. arXiv: `1303.2348 [physics.ins-det]`.

[95] S. Ritt. *DRS4 - 9 Channel, 5 GSPS Switched Capacitor Array.* Rev. 0.9. Paul Scherrer Institute. Nov. 2008.

[96] *ADA4927-1/ADA4927-2 - Ultralow Distortion Current Feedback Differential ADC Driver.* Rev. B. Analog Devices. 2016.

[97] Sergio Gómez et al. “MUSIC: An 8 channel readout ASIC for SiPM arrays”. In: *Optical Sensing and Detection IV.* Ed. by Francis Berghmans and Anna G. Mignani. Vol. 9899. Society of Photo-Optical Instrumentation Engineers (SPIE) Conference Series. Apr. 2016, 98990G, 98990G. DOI: `10.1117/12.2231095`.

[98] *MUSICR1 Datasheet - MUSICR1: 8 channel Multiple Use IC for SiPM anode readout.* Rev. B. Institute of Cosmos Sciencies - University of Barcelona. 2013.

[99] LST team for the CTA consortium. *cta-lstchain.* Online; accessed 09 November 2021. URL: `https://github.com/cta-observatory/cta-lstchain/tree/v0.6.3`.

[100] *eMUSIC MiniBoard User Guide.* Version 2. Rev. 2.5a. Institute of Cosmos Sciencies - University of Barcelona. Feb. 2019.

[101] A. Nagai et al. “SiPM behaviour under continuous light”. In: *Journal of Instrumentation* 14.12 (Dec. 2019), P12016. DOI: `10.1088/1748-0221/14/12/P12016`. arXiv: `1910.00348 [physics.ins-det]`.

[102] Fabio Acerbi et al. “NUV Silicon Photomultipliers With High Detection Efficiency and Reduced Delayed Correlated-Noise”. In: *IEEE Transactions on Nuclear Science* 62.3 (June 2015), pp. 1318–1325. DOI: `10.1109/TNS.2015.2424676`.

[103] R. W. Erickson. “Optimal single resistors damping of input filters”. In: *APEC ’99. Fourteenth Annual Applied Power Electronics Conference and Exposition. 1999 Conference Proceedings (Cat. No.99CH36285).* Vol. 2. Mar. 1999, 1073–1079 vol.2. DOI: `10.1109/APEC.1999.750502`.

[104] *MIC5205, 150 mA Low-Noise LDO Regulator.* Rev. A. Microchip Technology. May 2017.

[105] *MIC5225, Ultra-Low Quiescient Current 150 mA uCap Low Dropout Regulator.* Microchip Technology. July 2008.

[106] *DS28EA00, 1-Wire Digital Thermometer with Sequence Detect and PIO.* Rev. 2. Maxim Integrated Products. June 2019.

[107] *3M Twin Axial Cable SL8800 Series.* 3M. 2011.

[108] C. Adams et al. “Status of the development of NUV SiPMs for INFN optical modules for the SCT medium sized telescope proposed for the CTA observatory”. In: *Nuclear Instruments and Methods in Physics Research A* 982, 164486 (Dec. 2020), p. 164486. DOI: `10.1016/j.nima.2020.164486`.

[109] G. Ambrosi et al. “Characterization and development of NUV SiPMs for INFN optical modules for the SCT Medium Size Telescope proposed for the CTA Observatory”. In: *2019 IEEE 8th International Workshop on Advances in Sensors and Interfaces (IWASI)*. 2019, pp. 37–41. DOI: `10.1109/IWASI.2019.8791342`.

[110] *LM5002 Wide Input Voltage Switch Mode Regulator*. Rev. F. Texas Instruments. May 2021.

[111] *AD9637, Octal, 12-Bit, 40/80 MSPS, Serial LVDS, 1.8 V Analog-to-Digital Converter*. Rev. A. Analog Devices. Apr. 2013.

[112] Alberto Gola, Claudio Piemonte, and Alessandro Tarolli. “The DLED Algorithm for Timing Measurements on Large Area SiPMs Coupled to Scintillators”. In: *IEEE Transactions on Nuclear Science* 59.2 (Apr. 2012), pp. 358–365. DOI: `10.1109/TNS.2012.2187927`.

[113] *Thorlabs Website*. Online; accessed 09 November 2021. URL: `https://www.thorlabs.com/`.

[114] *MPPC® (Multi-Pixel Photon Counter) arrays - S13361-6050 series*. Hamamatsu Photonics K.K. Apr. 2016.

[115] *MPPC (S13361-6050AS-04) Reference*. Hamamatsu Photonics K.K. May 2018.

[116] A. Berti et al. “Development and test of a SiPM cluster for a SiPM version of the Cherenkov Telescope Array LST camera”. In: *Nucl. Instrum. Meth. A* 982 (2020), p. 164373. DOI: `10.1016/j.nima.2020.164373`.

[117] Hyuga Abe et al. “Development of an advanced SiPM camera for the Large Size Telescope of the Cherenkov Telescope Array Observatory”. In: *Proceedings of 37th International Cosmic Ray Conference — PoS(ICRC2021)*. Vol. 395. 2021, p. 889. DOI: `10.22323/1.395.0889`.

[118] D. Heck et al. *CORSIKA: a Monte Carlo code to simulate extensive air showers.* 1998.

[119] Konrad Bernlöhr. “Simulation of imaging atmospheric Cherenkov telescopes with CORSIKA and sim_telarray”. In: *Astroparticle Physics* 30.3 (Oct. 2008), pp. 149–158. DOI: `10.1016/j.astropartphys.2008.07.009`. arXiv: `0808.2253 [astro-ph]`.

[120] Roberta Zanin et al. “MARS, The MAGIC Analysis and Reconstruction Software”. In: *International Cosmic Ray Conference*. Vol. 33. International Cosmic Ray Conference. Jan. 2013, p. 2937.

[121] The CTA Consortium. *CTA Website*. Online; accessed 09 November 2021. URL: `https://github.com/cta-observatory/ctapipe`.

[122] Alessio Berti. “Study of astrophysical transients with the MAGIC telescopes”. PhD thesis. 2018.

[123] J. Albert et al. “Implementation of the Random Forest method for the Imaging Atmospheric Cherenkov Telescope MAGIC”. In: *Nuclear Instruments and Methods in Physics Research A* 588.3 (Apr. 2008), pp. 424–432. DOI: `10.1016/j.nima.2007.11.068`. arXiv: `0709.3719 [astro-ph]`.

[124] J. Aleksić et al. “The major upgrade of the MAGIC telescopes, Part II: A performance study using observations of the Crab Nebula”. In: *Astroparticle Physics* 72 (Jan. 2016), pp. 76–94. DOI: `10.1016/j.astropartphys.2015.02.005`. arXiv: `1409.5594 [astro-ph.IM]`.

[125] Maximilian Nöthe et al. *pyirf*. Nov. 2020. DOI: `10.5281/zenodo.4304466`.

[126] K. Bernlöhr et al. “Monte Carlo design studies for the Cherenkov Telescope Array”. In: *Astroparticle Physics* 43 (Mar. 2013), pp. 171–188. DOI: `10.1016/j.astropartphys.2012.10.002`. arXiv: `1210.3503 [astro-ph.IM]`.

[127] T. Li and Y. Ma. “Analysis methods for results in gamma-ray astronomy.” In: *Astrophysical Journal* 272 (Sept. 1983), pp. 317–324. DOI: `10.1086/161295`.

[128] Michele Peresano. *protopipe*. Mar. 2021. DOI: `10.5281/zenodo.4586755`.